Fall 2017

Identification of physical parameters of biological and mechanical systems under whole-body vibration

Guandong Qiao
University of Iowa

Recommended Citation

Qiao, Guandong. "Identification of physical parameters of biological and mechanical systems under whole-body vibration." PhD (Doctor of Philosophy) thesis, University of Iowa, 2017.
https://doi.org/10.17077/etd.dpegr0hb

Follow this and additional works at: https://ir.uiowa.edu/etd
Part of the Civil and Environmental Engineering Commons

IDENTIFICATION OF PHYSICAL PARAMETERS OF BIOLOGICAL AND MECHANICAL SYSTEMS UNDER WHOLE-BODY VIBRATION

by

Guandong Qiao

A thesis submitted in partial fulfillment
of the requirements for the Doctor of Philosophy
degree in Civil and Environmental Engineering in the
Graduate College of
The University of Iowa

December 2017

Thesis Supervisor: Associate Professor Salam Rahmatalla

Graduate College
The University of Iowa
Iowa City, Iowa

CERTIFICATE OF APPROVAL

PH.D. THESIS

This is to certify that the Ph.D. thesis of

Guandong Qiao

has been approved by the Examining Committee for
the thesis requirement for the Doctor of Philosophy degree
in Civil and Environmental Engineering at the December 2017 graduation.

Thesis Committee:

Salam Rahmatalla, Thesis Supervisor

Jasbir S. Arora

M. Asghar Bhatti

Jia Lu

Colby C. Swan

ACKNOWLEDGMENTS

Since I entered the University of Iowa in the fall of 2012, a lot of things have happened that encouraged me or disappointed me. However, all these things will be my life’s fortune.

I would like to express my sincere gratitude to my advisor, Dr. Salam Rahmatalla, for the continuous support of my Ph. D study and research with patience, inspiration, guidance, and expertise.

My appreciation also goes to my thesis committee members, Dr. Jasbir S. Arora, Dr. M. Asghar Bhatti, Dr. Jia Lu, and Dr. Colby C. Swan, for their guidance and suggestions.

Furthermore, I would like to thank Jonathan DeShaw for the experiments and data processing. I also would like to thank Ulysses Grant for his assistance on the experiments. Without them, I could not have run my experiments or built my data so smoothly.

Additionally, I would like to express my special thanks to my parents, Junmei Qiao and Yulan Fu. I can feel love and support from them, even if over more than ten thousand kilometers.

Finally, my sincere thanks to all my friends for your appearances in my life and sharing happiness with me.

ABSTRACT

The identification of the physical parameters (mass, stiffness, and damping) of structural, mechanical, and biomechanical systems is a major challenge in many applications, especially when dealing with old systems and biological systems with heavy damping and where environmental noises are presented. This work presents a novel methodology called eigenvector phase correction (EVPHC) to solve for the physical parameters of structural and biomechanical systems even with the existence of a significant amount of noise. The method was first tested on structural/mechanical systems and showed superior results when compared with an iterative method from the literature. EVPHC was then developed and used to identify the physical parameters of supine humans under vertical whole-body vibration. Modal parameters of fifteen human subjects, in the supine position, were first identified in this work using experimentation under vertical whole-body vibration. EVPHC was then used to solve an inverse modal problem for the identification of the stiffness and damping parameters at the cervical and lumbar areas of supine humans. The results showed that the resulting physical parameters were realistically close to those presented in the literature. The proposed human model was able to predict the time histories of the acceleration at the head, chest, pelvis, and legs very closely to those of the experimental measured values. A scaling methodology is also presented in this work, where an average human model was scaled to an individual subject using the body mass properties.

PUBLIC ABSTRACT

The purpose of the work presented is to introduce a novel methodology to identify the unknown physical properties of structural, mechanical, and biomedical systems. Data is collected from vibration experiments on human beings. Then the collected data is utilized to characterize the vibration of the supine human and further identify the physical properties of the supine human.

TABLE OF CONTENTS

LIST OF TABLES

LIST OF FIGURES

CHAPTER 1. INTRODUCTION

The process of identifying the physical parameters (mass, stiffness, and damping) of a structural, mechanical, and biomechanical system is a major challenge in many applications such as those involving old structures and biological systems. The identification of the physical parameters can be essential in developing new systems and in the evaluation and health monitoring of existing systems. While the mass and stiffness parameters can be characterized, to a certain degree, under static and quasi-static environments, damping parameters can only be identified by dynamic testing. Much work has been done toward estimating the physical parameters of structural and mechanical systems, however, limited work has been done in the area of biomechanical systems. While some existing parameter identification methods have shown some success, most existing methods can produce a significant amount of error when noises are introduced in the systems. This thesis introduces novel methodologies that can predict the physical parameters of structural, mechanical, and biomechanical systems under whole-body vibration (WBV), even with the existence of a considerable amount of system and environmental noise.

This thesis proposal comprises six chapters. Chapters 2-5 present the related background, discussion, and conclusion sections. A novel approach for the solution of the inverse modal problem is introduced in Chapter 2 using viscous damped spring-mass systems. The proposed method, called eigenvector phase correction (EVPHC), solves for the unknown physical parameters of systems. EVPHC uses the phase of the complex eigenvector components as design variables inside an optimization problem that minimizes the differences between the experimental and predicted transfer functions. An analytical four-degree-of-freedom (four-DOF) system with known physical parameters is used in Chapter 2 to demonstrate the efficacy of EVPHC. Three cases with 1, 5, and 10% added white noise were considered. The results showed the superiority of EVPHC to retrieve the analytical physical parameters when compared with an iterative method from the literature.

In Chapter 3, experimental modal analysis was conducted on fifteen supine humans using sine-sweep and random vertical WBV rides. The chapter includes a detailed analysis of the process of extracting the modal parameters of the supine human using frequency and time domain analyses. Methodologies to fill the missing components and average of the modal parameters from the fifteen subjects are also introduced. The chapter ends with tables demonstrating the resulting supine human modal parameters.

In Chapter 4, EVPHC is developed and used to identify the stiffness and damping parameters at the cervical and lumbar areas of the spine using the modal parameters of the fifteen human subjects extracted in Chapter 3. EVPHC was used to solve the inverse modal analysis of supine humans under vertical sine-sweep WBV. A four-DOF human model was suggested based on the resulting modal parameters. The resulting physical parameters showed close values when compared with those in the literature. Also, the predicted acceleration by the model at the head, chest, pelvis, and legs showed trends very close to those of the experiments. A scaling method, where the physical parameters of an average human model were scaled to an individual human subject, is also introduced toward the end of this chapter.

Chapter 5 investigates the effect of separating the feet from the legs and considering the feet as an additional lumped-mass component of the human body, by the use of the experimental modal analysis, transmissibility, and wavelet transform. The analysis demonstrated that these two human body segments, the legs and feet, can be viewed as rigidly connected and then can be considered as one supine human body segment for further analysis under vertical WBV.

The thesis ends with Chapter 6, where future work is presented.

CHAPTER 2. EIGENVECTORS PHASE CORRECTION IN INVERSE MODAL PROBLEM

2.1. Introduction

A major challenge in modeling and assessing the health condition of damped systems, such as old structures and biomechanical systems, is in predicting the related unknown spatial mass, stiffness, and damping parameters. Traditionally, these physical parameters are approximately identified by solving an inverse modal problem. The modal parameters of the modal problem (frequency, damping ratio, and mode shape) are first obtained by conducting experimental modal analyses on the system [1] using transfer functions constructed from measured input force/motion and output motion at selected points on the system. Due to measurement noises, nonlinearity, and boundary conditions, the resulting modal parameters will normally inherit some level of noise [2]. This noise will introduce significant uncertainty in the resulting physical parameters when solving the inverse modal problem for the spatial parameters [3, 4].

The solution of the inverse modal problem, with complex modes, for the spatial parameters is an area of extensive study [5-11]. In an article by Lancaster in 1961 [5], the author proposed a methodology to solve the inverse modal problem of viscous-type systems. His method required the normalization of the complex eigenvectors, a process that requires a prior knowledge of the mass and damping matrices, which the algorithm is solving for. Pilkey and Inman [6] presented a method to characterize damping parameters from a lightly damped system. The method starts with an initial damping matrix and a known mass matrix and then offers an iterative method to normalize the eigenvectors, instead of requiring the normalization of the eigenvector as a prior, and simultaneously solves for the stiffness and damping matrices. The authors claimed that the method performed well even with a moderate level of noise. In a review article by Pilkey and Inman [12], the authors presented different methods that solve the inverse modal problem for the damping matrix. They classified the methods into those that work in the frequency, Laplace, and time domains. They did not promote any method presented in this review, but in general, all methods were sensitive to a certain degree to the amount of noise presented in the data. Adhikari [13] revisited Lancaster's method of damping identification and presented a methodology that mitigates the strict requirement of Lancaster's method of a prior knowledge of the damping matrix. The method is based on the poles and residues that are derived from the measured transfer function. The method worked very effectively in reconstructing accurate mass, stiffness, and damping matrices. However, the methodology showed some drawbacks when noise was presented in the data.

This work presents a new methodology to mitigate the effect of noise in the resulting modal shapes on the solution of the inverse modal problem. The modal parameters are assumed to be complex [14-16]. The method will be called eigenvector phase correction (EVPHC) throughout this article. EVPHC uses the eigenvectors' phase components as design variables inside an optimization problem, but preserves the norm of the eigenvectors. The optimization problem minimizes a cost function that tracks the difference between the analytical and calculated transfer functions. The equivalent point frequency response function (EPFRF), which is a ratio between an equivalent input force to the system and the output motion of the system, will be used as a transfer function in this work. While preserving the inter-connectivity, the numeric sign of the elements, and the positive and semi-positive definiteness of the spatial matrices (mass, stiffness, and damping) [17, 18] that are essential in dynamics problems, additional constraints are imposed on the spatial matrices during the optimization process in order to achieve these specific requirements.

2.2. Theoretical Background

2.2.1. Inverse modal problem of viscous damped system

The equation of motion for an underdamped viscous vibrating system with *N* degrees of freedom (DOF) can be given as:

$$\mathbf{M}\ddot{\mathbf{u}}(t) + \mathbf{C}\dot{\mathbf{u}}(t) + \mathbf{K}\mathbf{u}(t) = \mathbf{0} \tag{2.1}$$

where **M**, **C**, and **K** are $N \times N$ mass, damping, and stiffness matrices, respectively. All three matrices can be assumed to be symmetric real matrices. For a general case, the damping matrix doesn't need to satisfy the proportionality of the mass and stiffness condition. $\mathbf{u}(t)$ is the $N \times 1$ column vector for displacement.

For a vibrating system, **M** and **K** are positive definite, and **C** may be positive definite or positive semi-definite.

The equation of motion is a differential equation that can be transformed to the algebraic form,

$$(\lambda_i^2 \mathbf{M} + \lambda_i \mathbf{C} + \mathbf{K})\boldsymbol{\psi}_i = \mathbf{0} \tag{2.2}$$

where λ_i is the eigenvalue and $\boldsymbol{\psi}_i$ is the corresponding eigenvector.

In this work, it is assumed that all eigenvalues are complex and simple, i.e., there are no repeated eigenvalues in the analysis, $\lambda_i \in \Im$ and $\boldsymbol{\psi}_i \in \Im^{N \times 1}$, where $\Im$ represents the complex domain.

The following second-order equation can be derived from Eq.(2.2):

$$\mathbf{Q}(\lambda) = (\lambda^2 \mathbf{M} + \lambda \mathbf{C} + \mathbf{K}) \tag{2.3}$$

Eq. (2.3) can be defined as "quadratic λ matrix" [11]. The physical parameters **M**, **C**, and **K** in Eq. (2.3) are unknown and should be solved for simultaneously.

All eigenvalues with a positive imaginary part of $\mathbf{Q}(\lambda)$ can constitute a $N \times N$ diagonal matrix.

$$\boldsymbol{\Lambda} = diag(\lambda_1, \lambda_2, \cdots, \lambda_N) \tag{2.4}$$

The eigenvalue λ_j and its conjugate $\bar{\lambda}_j$ can be written as:

$$\lambda_j = \alpha_j + i\beta_j; \qquad \bar{\lambda}_j = \alpha_j - i\beta_j \tag{2.5}$$

where α_j and $\beta_j \in \Re, \beta_j > 0$, and $\Re$ represents the real domain. The corresponding eigenvectors $\boldsymbol{\psi}_j$ and their conjugate $\bar{\boldsymbol{\psi}}_j$ can be written as

$$\boldsymbol{\psi}_j = \boldsymbol{\psi}_{jR} + i\boldsymbol{\psi}_{jI}; \quad \bar{\boldsymbol{\psi}}_j = \boldsymbol{\psi}_{jR} - i\boldsymbol{\psi}_{jI} \tag{2.6}$$

where $\boldsymbol{\psi}_{jR}$ represents the real part of eigenvector ($\boldsymbol{\psi}_j$) for mode j, and $\boldsymbol{\psi}_{jI}$ is the imaginary part.

Here $\boldsymbol{\psi}_j \in \Im^{N\times 1}, \boldsymbol{\psi}_{jR}$ and $\boldsymbol{\psi}_{jI} \in \Re^{N\times 1}$. The eigenvalue λ_i and the corresponding eigenvector $\boldsymbol{\psi}_i$ form an eigenpair. All eigenpairs can form the following 2*N*×2*N* eigenvalue matrix $\boldsymbol{\psi}_i$ (Eq. (2.7)) and the *N*×2*N* eigenvector matrix $\boldsymbol{\psi}_t$ (Eq. (2.8)). The subscript t in $\boldsymbol{\Lambda}_t$ and $\boldsymbol{\psi}_t$ means total.

$$\boldsymbol{\Lambda}_t = \begin{bmatrix} \boldsymbol{\Lambda} & \mathbf{0} \\ \mathbf{0} & \bar{\boldsymbol{\Lambda}} \end{bmatrix} \tag{2.7}$$

$$\boldsymbol{\psi}_t = [\boldsymbol{\psi} \ \bar{\boldsymbol{\psi}}] \tag{2.8}$$

The matrices in Eq. (2.7) and Eq. (2.8) can be rearranged as shown in Eqs. (2.9) and (2.10).

$$\boldsymbol{\Lambda}_t = diag(\lambda_1, \lambda_2, \cdots, \lambda_{2k-1}, \lambda_{2k}, \cdots \lambda_{2N}) \tag{2.9}$$

$$\boldsymbol{\psi}_t = \left[\boldsymbol{\psi}_1, \boldsymbol{\psi}_2, \cdots, \boldsymbol{\psi}_{2k-1}, \boldsymbol{\psi}_{2k}, \cdots, \boldsymbol{\psi}_{2N-1}, \boldsymbol{\psi}_{2N}\right] \tag{2.10}$$

For this case, λ_{2k} and $\boldsymbol{\psi}_{2k}$ are the complex conjugates of λ_{2k-1} and $\boldsymbol{\psi}_{2k-1}$, respectively. A mapping is presented in Eq. (2.11) that can transform the complex-value eigenpairs into real-value eigenpairs [11].

$$\mathbf{R} = diag(\frac{1}{\sqrt{2}}\begin{bmatrix} 1 & 1 \\ i & -i \end{bmatrix} \ , \cdots, \ \frac{1}{\sqrt{2}}\begin{bmatrix} 1 & 1 \\ i & -i \end{bmatrix}) \tag{2.11}$$

$\mathbf{R} \in \Im^{2N\times 2N}$ and $i = \sqrt{-1}$.

The relationship between the new real-value eigenpairs $\tilde{\mathbf{\Lambda}}_t \in \Re^{2N\times 2N}$ and $\tilde{\boldsymbol{\psi}}_t \in \Re^{N\times 2N}$ and the previous complex-value ones ($\mathbf{\Lambda}_t$ and $\boldsymbol{\psi}_t$) are given in Eqs. (2.12) and (2.13).

$$\mathbf{\Lambda}_t = \mathbf{R}^H \tilde{\mathbf{\Lambda}}_t \mathbf{R} \tag{2.12}$$

$$\boldsymbol{\psi}_t = \tilde{\boldsymbol{\psi}}_t \mathbf{R} \tag{2.13}$$

The superscript H represents the Hermitian transpose.

Eq. (2.2) can be written in terms of the real-value eigenpairs,

$$\mathbf{M}\tilde{\boldsymbol{\psi}}_t \tilde{\mathbf{\Lambda}}_t^{\,2} + \mathbf{C}\tilde{\boldsymbol{\psi}}\tilde{\mathbf{\Lambda}}_t + \mathbf{K}\tilde{\boldsymbol{\psi}}_t = \mathbf{0} \tag{2.14}$$

In order to solve the inverse modal problem of Eq. (2.14) for **M**, **C**, and **K**, such that the matrices satisfy the positive definite and semi-definite requirements and other required constraints, the following semi-definite programming approach (SDP) will be used in this work.

2.2.2. Semi-definite programming

The SDP is an extension of linear programming (LP), which deals with symmetric matrices instead of scalars or vectors as unknowns. With SDP, it is possible to impose the requirements on the symmetric spatial matrices to be positive definite or positive semi-definite, which presents an obvious advantage over many other optimization methods. Linear inequality or linear equality constraints and different types of constraints can be easily implemented in this approach.

The SDP problem in primal standard form [19] is:

$$\begin{aligned} &\text{minimize } B \bullet \mathbf{X} \\ &\text{subject to } A_i \bullet \mathbf{X} = b_i,\ i = 1,\cdots,m \\ &\qquad\qquad\quad \mathbf{X} \geq 0 \end{aligned} \tag{2.15}$$

$\mathbf{X} \in \Re_S^{nxn}$ are the design variables. $A_i \in \Re_S^{nxn}$, $b \in \Re^m$, and $B \in \Re_S^{nxn}$ are given. $\Re_S^{nxn}$ denotes the space of real symmetric matrices with order *n*. $B \bullet \mathbf{X}$ denotes the inner product between these two matrices and is used here as an objective function in SDP. The constraints can be given in a similar form of $A_i \bullet \mathbf{X} = b_i$. $\mathbf{X} \geq 0$ means $\mathbf{X}$ is a positive semi-definite matrix.

The implementation of the constraint functions and the specification of their parameters inside SDP is an involved process because the programming language inside SDP is not user friendly. YALMIP [20], which is a plug-in software with SDP, is used in this work because it can provide a more user-friendly programming language for entering the equations and their parameters, such as rewriting the motion equation, Eq. (2.14) into the form of Eq. (2.15) conveniently. With YALMIP, the description of an SDP optimization problem and constraints can be achieved by applying several lines of code in MATLAB style. The solver named SDPT3 [21], which is designed to solve primal and dual semi-definite quadratic linear conic programming problems, will be used to solve the inverse eigenvalue problem.

2.2.3. Solution of inverse modal problem using SDP

In this process, SDP will use Eq. (2.14) as a constraint and then solve for **M**, **C**, and **K**. However, the inherent errors in the modal parameters due to noise and other effects could affect the equality conditions of Eq. (2.14). Furthermore, an over-determinate problem [22] will arise when the number of prescribed eigenvalues is more than the requirement for solving Eq. (2.14), which will lead to trivial solutions. Therefore, a new constraint is presented in this work that is based on the following inequality condition:

$$\mathbf{M}\tilde{\boldsymbol{\psi}}_t\tilde{\boldsymbol{\Lambda}}_t{}^2 + \mathbf{C}\tilde{\boldsymbol{\psi}}\tilde{\boldsymbol{\Lambda}}_t + \mathbf{K}\tilde{\boldsymbol{\psi}}_t \leq \mathbf{T} \qquad (2.16)$$

where **T** is the tolerance matrix, and

$$\mathbf{T} = t\mathbf{I} \qquad (2.17)$$

where $\mathbf{I}_{N\times 2N}$ is the unit matrix and t is a real scalar.

SDP is a feasible optimization problem instead of a minimum-maximum problem. If the modal information is accurate, theoretically, the objective function or cost function are not necessarily needed, and SDP will provide accurate values of the **M**, **C**, and **K** matrices with the value of t equal to zero. However, under noisy conditions, it is expected that the modal parameters will not be accurate and therefore the value of t will not be equal to zero. If t is set to zero, then SDP will produce a solution where the **M**, **C**, and **K** matrices will have elements with very small and unrealistic values. In order to circumvent this problem, the value of t will be selected based on the minimization of an objective function ($(M_{11}-1)^2$) inside SDP that forces the first element in the mass matrix (M_{11}) to go to one. With this normalization process, the solution of the SDP is forced to produce more realistic values of **M**, **C**, and **K**.

The inverse modal problem is expected to generate unrealistic solutions if no constraints are applied on the inner structure of the spatial model [17]. Besides the positive and semi-positive definiteness requirements of the **M**, **C**, and **K** matrices, other inner-structure requirements such as the inter-connectivity between the different DOF and the numeric signs of the elements in the **M**, **C**, and **K** matrices should be also included. Meanwhile, these structured requirements [18] present major challenges when solving the inverse modal problem. However, with YALMIP, these structured requirements can be considered as constraints and can be easily dealt with [23].

The mass matrix of the system is assumed to be unknown in this work. Meanwhile, based on prior knowledge regarding the relationship between the different masses of the system and a reasonable estimation of the first mass of the system, it is suggested that constraints be imposed on the ratio between the individual masses of the system relative to the first mass. The full spatial parameters can be retrieved by multiplying the magnitude of the first element in the mass matrix by the spatial parameters. Accordingly, the following constraint (Eq. (2.18)) will be used inside SDP. The numbers a and b in Eq. (2.18) are relevant to the system and should be selected realistically for different systems.

$$a \le \frac{m_n^o}{m_1^o} \le b \tag{2.18}$$

where m_1^o is the first element (M_{11}) in the unknown mass matrix of the system, and m_n^o are the other masses of the system.

2.2.4. Equivalent point frequency response function

Vibration enters most mechanical systems through their supports. The EPFRF is introduced in this work as a measure of the dynamic response of the system due to the equivalent input force on the supports (base). The EPFRF can be calculated as the ratio, in the frequency domain, between the output acceleration of the masses of the system and the input acceleration at the base. The EPFRF is similar to the frequency response function (FRF) but is multiplied by the mass matrix and a vector of ones as described in the following paragraphs. The expression for the FRF ($\mathbf{H}(\omega)$) can be introduced in terms of the mass (**M**), damping (**C**), and stiffness (**K**) matrices as shown below:

$$\mathbf{H}(\omega) = (\mathbf{K} + i\omega\mathbf{C} - \omega^2\mathbf{M})^{-1} \tag{2.19}$$

Under base motion, the output acceleration of the masses of the system in the frequency domain can be expressed in terms of the transfer function as:

$$\mathbf{U}_r = -\omega^2\mathbf{H}(\omega)\mathbf{F} = -\omega^2\mathbf{H}(\omega)\mathbf{M}\mathbf{U}_g \tag{2.20}$$

where $\mathbf{F}$ is the input force to the system, $\mathbf{U}_r$ is the output acceleration of the masses of the system, and $\mathbf{U}_g$ is the acceleration of the base.

The base motion vector can be expressed as follows:

$\mathbf{U}_g = \mathbf{e}U_g$, where **e** is a column vector with all components equal to one and U_g is a scalar. In this case $\mathbf{U}_r$ can be written as:

$$\mathbf{U}_r = -\omega^2 \mathbf{H}(\omega)\mathbf{Me}U_g \tag{2.21}$$

Let $\mathbf{EPFRF}(\omega) = -\omega^2 \mathbf{H}(\omega)\mathbf{Me}$, then EPFRF for each mass can be expressed as:

$$\text{EPFRF}_{(n)} = \frac{U_r^{(n)}}{U_g} \tag{2.22}$$

2.2.5. Correcting the phase of the eigenvectors

The work by Adhikari [13] showed that the error presented in the residues, which contains the eigenvector information, of the transfer function due to noise can induce considerable inaccuracy when solving the inverse modal problem for mass, stiffness, and damping matrices. The present work proposes a methodology (EVPHC) that mitigates the effect of the error in the complex eigenvectors when solving the inverse modal problem for the spatial parameters. EVPHC is based on modifying the phase information in each component of the eigenvectors, such that the calculated EPFRF approaches the analytical or experimental EPFRF.

For a system with order N, the mode shape of mode j is given as:

$$\boldsymbol{\psi}_j = \begin{bmatrix} \psi_{1j} & \psi_{2j} & \cdots & \psi_{Nj} \end{bmatrix}^T \tag{2.23}$$

Each component in this mode is a complex value, which can be represented by its real and imaginary parts (Eq.(2.16)). Another way to represent these components is to use the polar form, where the eigenvectors can be written in terms of their magnitudes and arguments.

$$\boldsymbol{\psi}_j = \begin{bmatrix} M_{1j}e^{i\varphi_{1j}} & M_{2j}e^{i\varphi_{2j}} & \cdots & M_{nj}e^{i\varphi_{nj}} & \cdots & M_{Nj}e^{i\varphi_{Nj}} \end{bmatrix}^T \tag{2.24}$$

where M_{nj} is the magnitude of component n for mode j, and φ_{nj} is the corresponding argument. The upper and lower boundaries on these arguments are given as

$$-180^\circ \le \varphi_{nj} \le 180^\circ \tag{2.25}$$

Changing the magnitude and phase of the components of the eigenvectors may lead to a variety of eigenvectors that may be not well related to the system. Therefore, this work preserves the norm of the eigenvectors and uses the phase of its components as design variables inside an optimization problem. The cost function $f_{\cos t}$ (Eq. (2.26)) minimizes the errors between the analytical $EPFRF_n^A$ at degree *n* and the calculated $EPFRF_n^C$ (within EVPHC) at degree *n*.

$$f_{\cos t} = \sum_{n=1}^{4} \left| EPFRF_n^A - EPFRF_n^C \right| \tag{2.26}$$

In the general form, the cost function can be written in terms of a weighted-sum multi-objective function with four cost functions representing the four masses. However, in this work, we chose similar weights (weight = 1) for each cost function and then summed the four cost functions in one cost function as shown in Eq. (2.26).

For demonstration purposes, Figure (2.1a) shows the polar representation of an eigenvector of a four-DOF system. Each arrow inside the circles represents the magnitude and phase of each component of an eigenvector. As mentioned above, the magnitude of each arrow will be kept constant, and the directions of the arrow will be used as design variables that minimize the cost function in Eq. (2.26).

In this work, the mode shape shown in Figure (2.1a) was normalized. The mode shape normalization process was done in two steps. In the first step, the norm of each mode shape was scaled to one as shown in Figure (2.1b). In the next step, the last component of the mode shape was set to align with the real positive axis, and the rest of the eigenvector components were rotated without affecting their magnitude and the angles between them as shown in Figure (2.1c) [24]. The latter arrangement was done in this work to reduce the number of design variables from 4 to 3.

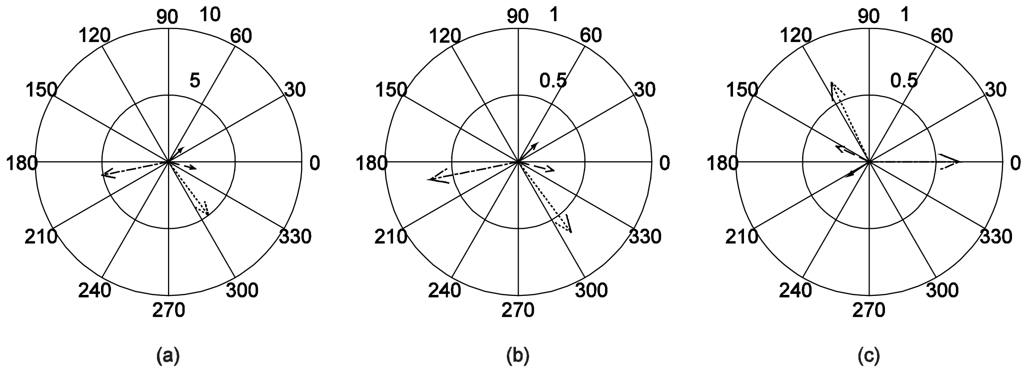

Figure (2.1) Schematic representation of the components of an eigenvector of a four-DOF system in polar plane (‘—’ – comp1, ‘– –’ – comp2, ‘- - ’ – comp3, ‘– -’ – comp4), (a) components of an eigenvector before normalization, (b) normalized components, and (c) last component aligned with the positive real axis

2.2.6. Solution algorithm using EVPHC

In EVPHC, two nested optimization problems are solved with the goal of minimizing the error between the analytical $EPFRF_n^A$ and the experimental $EPFRF_n^C$. In the inner problem, SDP solves an optimization problem to predict **M**, **C**, and **K**, and it is defined as follows:

$$\text{Minimize } (M_{11}-1)^2$$

$$\text{Subject to } \mathbf{M}\tilde{\boldsymbol{\psi}}_t\tilde{\boldsymbol{\Lambda}}_t^{2}+\mathbf{C}\tilde{\boldsymbol{\psi}}\tilde{\boldsymbol{\Lambda}}_t+\mathbf{K}\tilde{\boldsymbol{\psi}}_t\le\mathbf{T},\ \mathbf{T}=t\mathbf{I}$$

$$a\le\frac{m_n^o}{m_1^o}\le b$$

The difference between $EPFRF_n^C$ and $EPFRF_n^A$ is then calculated and used as an objective function in the outer optimization problem to update the phase of the eigenvectors.

The outer optimization problem is defined as:

$$\text{Minimize } f_{\cos t}=\sum_{n=1}^{4}\left|EPFRF_n^A-EPFRF_n^C\right|$$

$$\text{Subject to } -180^\circ \le \varphi_{nj} \le 180^\circ$$

For each iteration, the interior point algorithm [25] utilizes the combination of two gradient step types to update the design variables (φ); the two types are direct step (Hessian matrix) and conjugate gradient step. All computation was done in MATLAB. Figure (2.2) shows a flow chart of how EVPHC works. The final solution for the spatial parameters will be achieved when the number of optimization iterations exceeds 50 or the difference (ε) between $EPFRF_n^C$ and $EPFRF_n^A$ ($\sum_{n=1}^{4}\left|EPFRF_n^A - EPFRF_n^C\right|$) becomes $\varepsilon \le 0.05$.

As can be seen in Section 2.2.4, EPFRF is very similar to FRF, and both can be specified in terms of the spatial or modal parameters or the response. So, we anticipate that minimizing the objective function in Eq. (2.26), using the mode shape as design variables, can ensure the causality of the response.

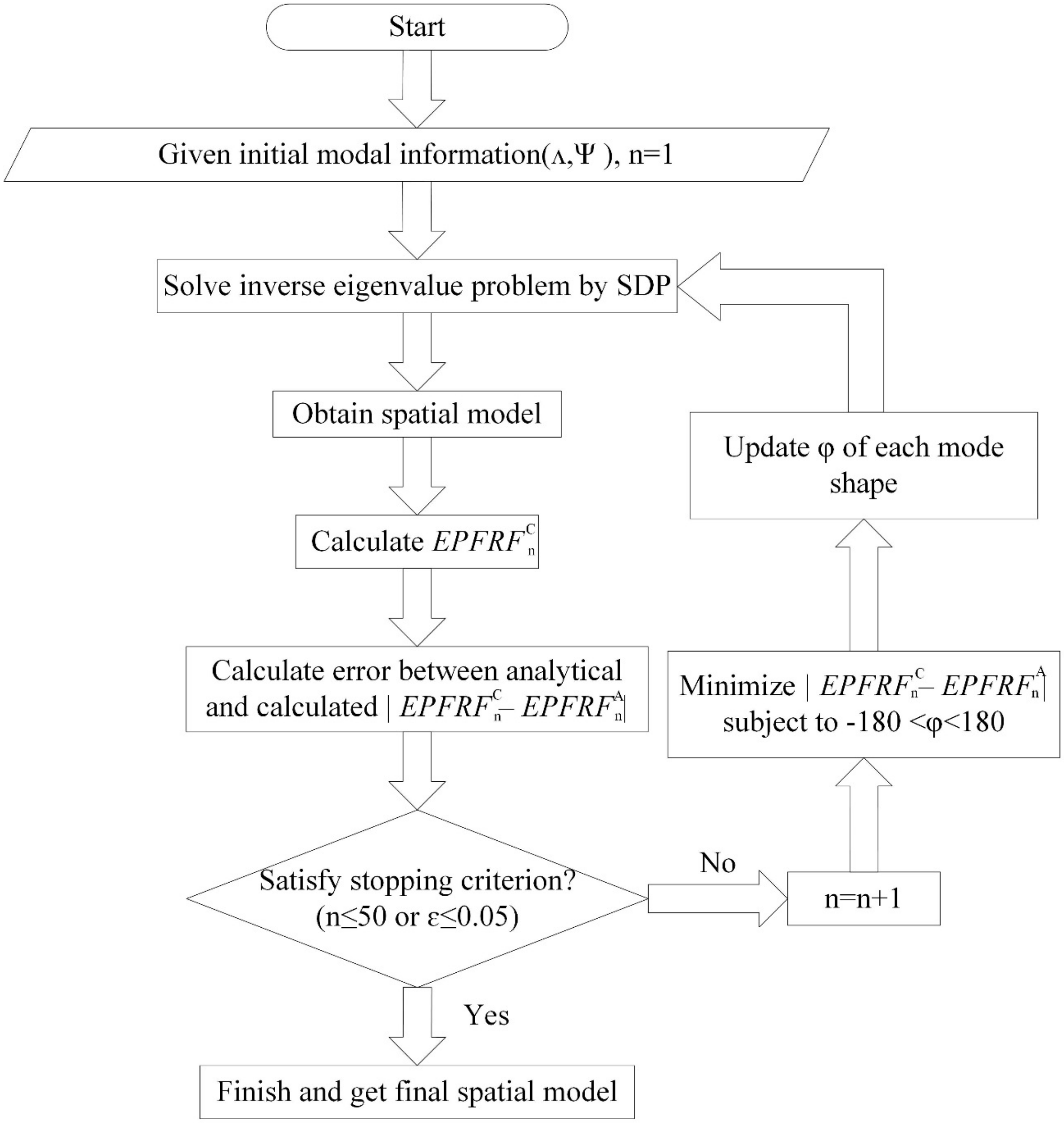

Figure (2.2) Flow chart showing the inverse modal problem solution algorithm using EVPHC

2.3. Results

A four-DOF linear lumped mass system with dashpots and springs will be used in this section to demonstrate the efficacy of the proposed EVPHC method. The analytical solution of the modal parameters and the associated $EPFRF_n^A$ will be first presented in Section 2.3.1. This solution will be considered as a "baseline" for subsequent comparison with EVPHC and another method from the literature (Pilkey and Inman's iterative algorithm [6]). For convenience, the method from the literature will be called PIA. PIA was selected for the comparison with the proposed method because it is considered a good method in the literature that can deal with noisy modal parameters, and it is easy to implement. Noise will be added to the eigenvectors in Section 2.3.2 to investigate the performance of EVPHC under different levels of noise. The solution of the inverse modal problem using EVPHC will be compared with the analytical (baseline) and PIA methods in Section 2.3.2. An example of a system with lower damping ratios, as compared to those presented in Section 2.3.2, will be presented in Section 2.3.3.

2.3.1. Analytical solution

Figure (2.3) shows a four-DOF mass-spring system with dashpots. The system is subjected to a ground input motion in the horizontal direction. All DOF of the system can only move in the horizontal direction.

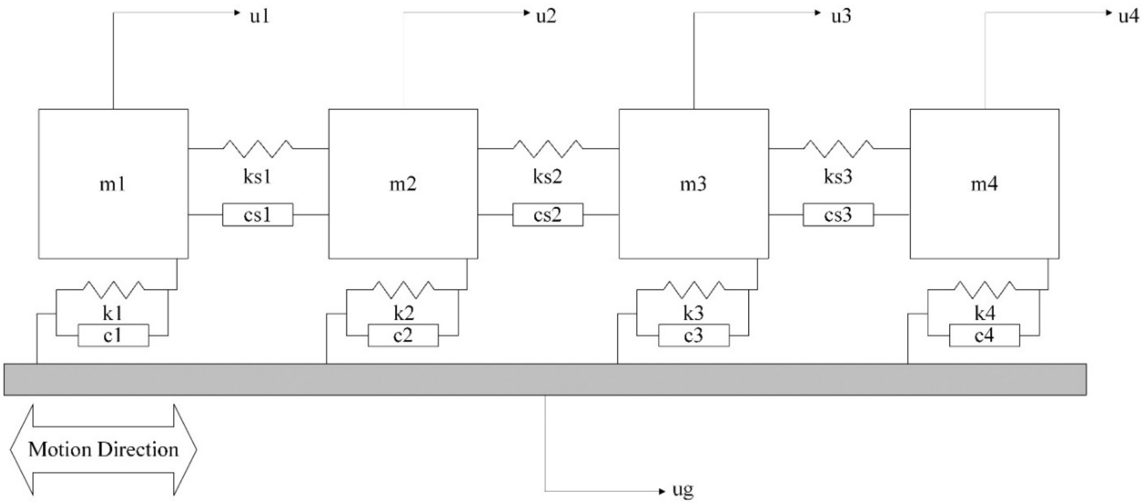

Figure (2.3) Four-DOF mass-spring system with dashpots with base motion (ug)

The mass matrix **M**, damping matrix **C**, and stiffness matrix **K** are as shown.

$$\mathbf{M} = \begin{bmatrix} 6 & 0 & 0 & 0 \\ 0 & 14 & 0 & 0 \\ 0 & 0 & 22 & 0 \\ 0 & 0 & 0 & 9 \end{bmatrix} \mathbf{C} = \begin{bmatrix} 500 & -80 & 0 & 0 \\ -80 & 753 & -163 & 0 \\ 0 & -163 & 1183 & -165 \\ 0 & 0 & -165 & 211 \end{bmatrix}$$

$$\mathbf{K} = \begin{bmatrix} 88000 & -14000 & 0 & 0 \\ -14000 & 59000 & -17000 & 0 \\ 0 & -17000 & 148800 & -11000 \\ 0 & 0 & -11000 & 13400 \end{bmatrix}$$

The undamped natural frequencies and damping ratios of this four-DOF system are presented in Table (2.1). Figure (2.4) shows the magnitude of the components of each eigenvector in this system, while Figure (2.5) shows their respective magnitude and phase in the polar plane. Figure (2.6) shows $EPFRF_n^A$ (baseline) of each DOF based on the input base motion.

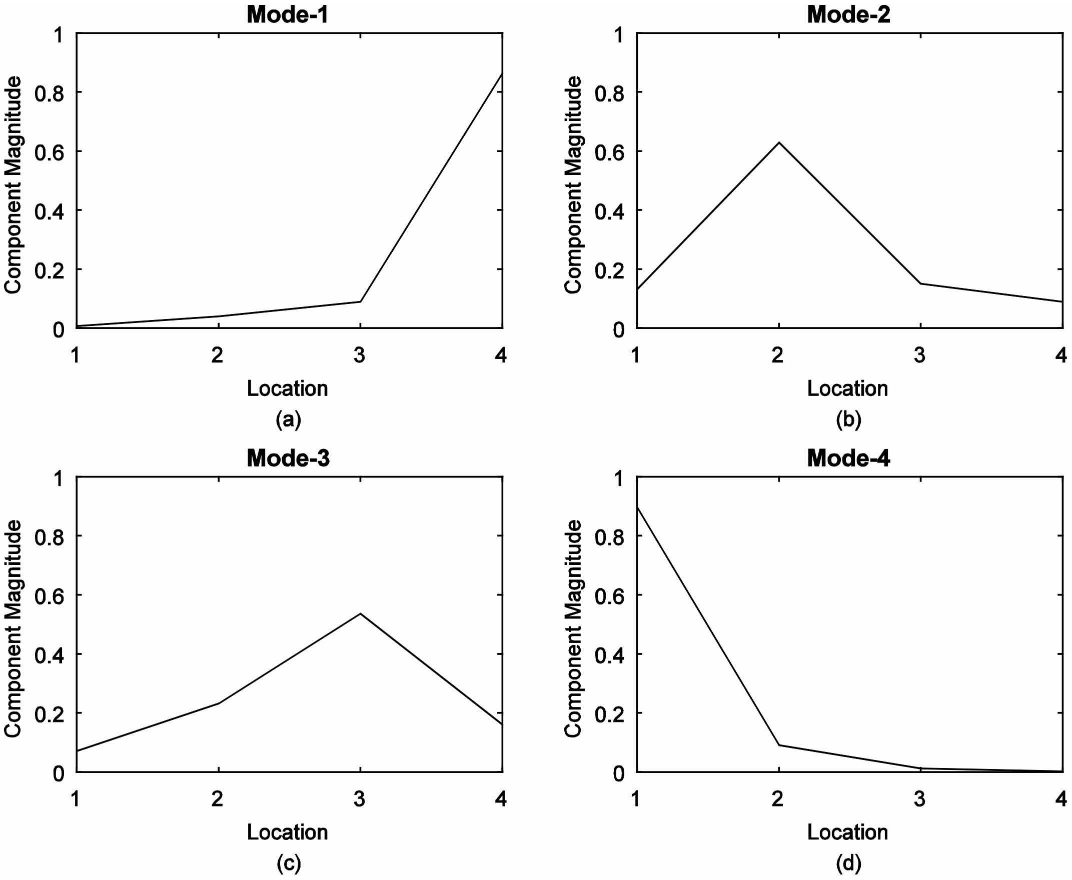

Figure (2.4) Magnitude information of the eigenvectors of the four-DOF system: (a) Mode-1, (b) Mode-2, (c) Mode-3, and (d) Mode-4

Table (2.1) Analytical frequencies and damping ratios of the four-DOF system

Mode order	1	2	3	4
Undamped natural frequency(Hz)	5.92	9.77	13.33	19.40
Damping ratio	0.28	0.39	0.36	0.35

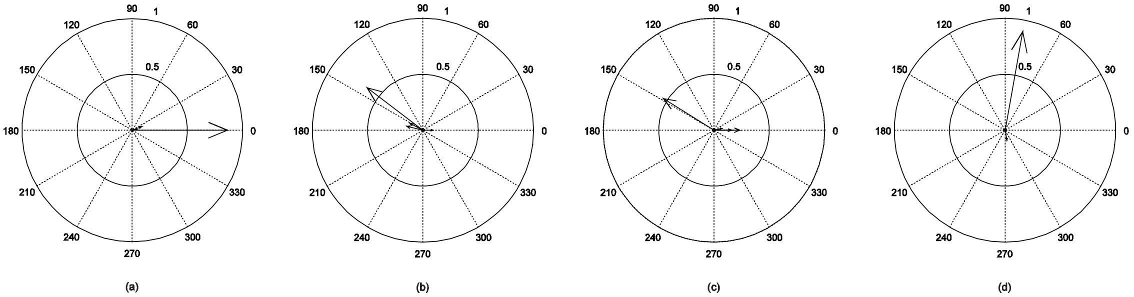

Figure (2.5) Phase and magnitude of the components of the eigenvectors of the four-DOF system in the polar plane: (a) Mode-1, (b) Mode-2, (c) Mode-3, and (d) Mode-4

Please note that each mode has four components represented by four arrows inside each circle in Figure (2.5). Some of these components are very small relative to the other components and may be hard to see.

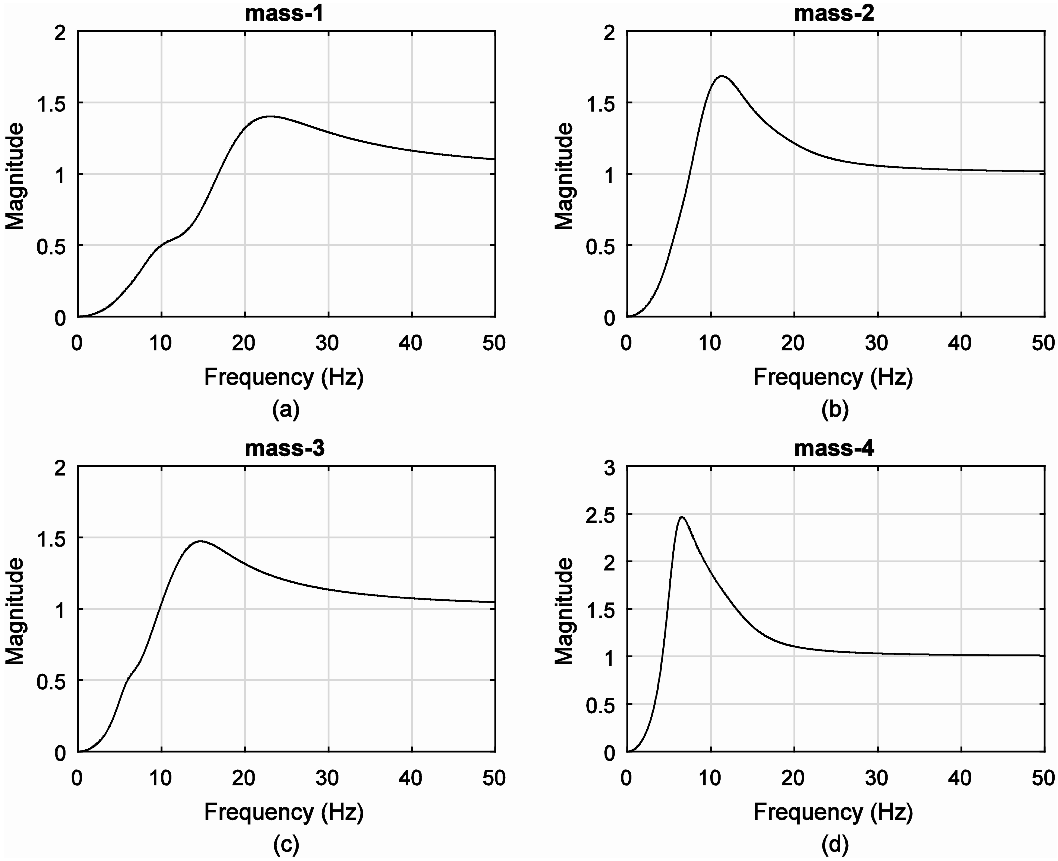

Figure (2.6) Analytical $EPFRF_n^A$ (baseline) of the four-DOF spring-mass system with dashpots: (a) mass-1, (b) mass-2, (c) mass-3, and (d) mass-4

With lightly damped systems, the EPFRF plots generally show obvious peaks at the resonance frequencies, and the function reduces significantly when the frequency is much higher than the highest resonance. Due to the amount of damping used in this work, the peaks in the EPFRF (Figure (2.6)) became less prominent, and the EPFRF slowly dropped after the last natural frequency.

2.3.2. Eigenvectors with added noise

Three cases of added white noise of 1%, 5%, and 10% to the eigenvectors and their effects on the resulting spatial matrices (**M**, **C**, and **K**) will be presented in the following subsections. The following constraint will be imposed on the element of the mass matrix during the solution process of EVPHC.

$$1.0 \le \frac{m_2^o}{m_1^o} \le 2.5,\ 3.0 \le \frac{m_3^o}{m_1^o} \le 5,\ 1.0 \le \frac{m_4^o}{m_1^o} \le 2$$

where m_1^o , m_2^o , m_3^o , and m_4^o are the unknown masses.

2.3.2.1. Case 1: 1% white noise added to the eigenvectors

Figure (2.7) shows the resulting $EPFRF_n^C$ using the EVPHC method and the analytical $EPFRF_n^A$ for each mass of the four-DOF system when 1% noise was added to the eigenvectors.

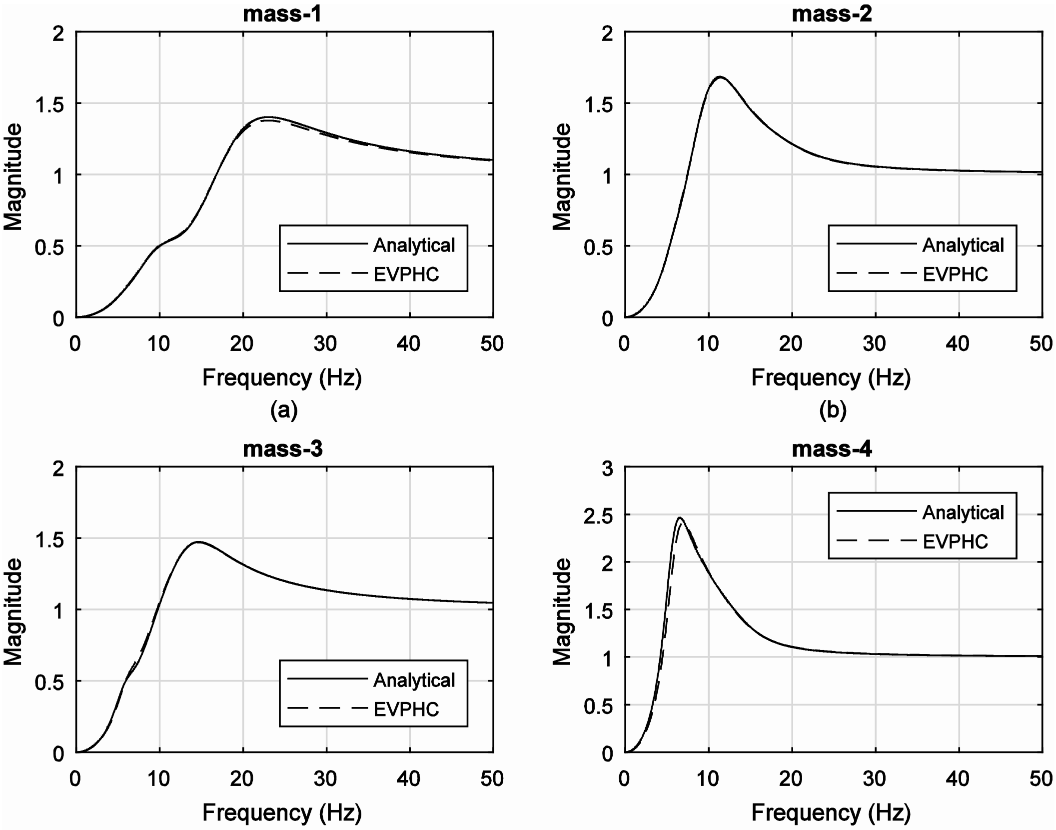

(a)

(b)

(c)

(d)

Figure (2.7) The resulting $EPFRF_n^C$ using the EVPHC method and the analytical $EPFRF_n^A$ for each mass, when 1% noise level was added to the analytical eigenvectors: (a) mass-1, (b) mass-2, (c) mass-3, and (d) mass-4

The resulting modal information using EVPHC and PIA and the percentage deviation from the analytical values (Table (2.1)) are given in Table (2.2). Figure (2.8) shows the comparison between the resulting eigenvectors using EVPHV, PIA, and the analytical baseline.

Table (2.2) Modal frequencies and damping ratios as predicted by EVPHC and PIA under 1% noise; the values in parentheses represent the percentage deviation from the baseline analytical values

	Mode order	1	2	3	4
EVPHC	Frequency (Hz)	6.24	9.80	13.40	19.19
		(5.52%)	(0.39%)	(0.54%)	(-1.05%)
	Damping ratio	0.28	0.39	0.37	0.36
		(1.07%)	(1.83%)	(1.72%)	(1.81%)
PIA	Frequency (Hz)	6.03	9.84	13.69	19.31
		(1.87%)	(0.73%)	(2.73%)	(-0.46%)
	Damping ratio	0.28	0.34	0.42	0.31
		(-0.71%)	(-12.14%)	(17.38%)	(-11.02%)

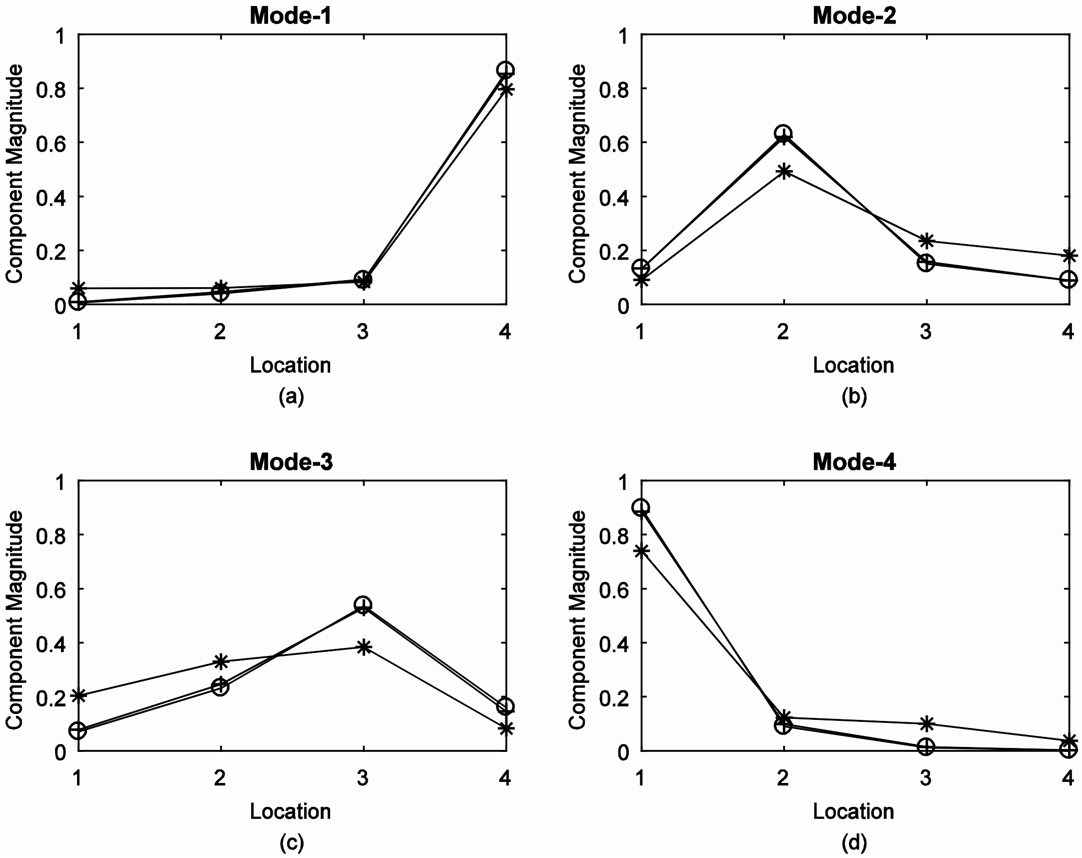

Figure (2.8) Modal shapes magnitude of the four-DOF system (○ - analytical, + - EVPHC, * - PIA), (a) Mode-1, (b) Mode-2, (c) Mode-3, and (d) Mode-4

2.3.2.2. Case 2: 5% white noise added to the eigenvectors

Figure (2.9) shows the resulting $EPFRF_n^C$ using the EVPHC method and the analytical $EPFRF_n^A$ for each mass of the four-DOF system when 5% noise was added to the eigenvectors.

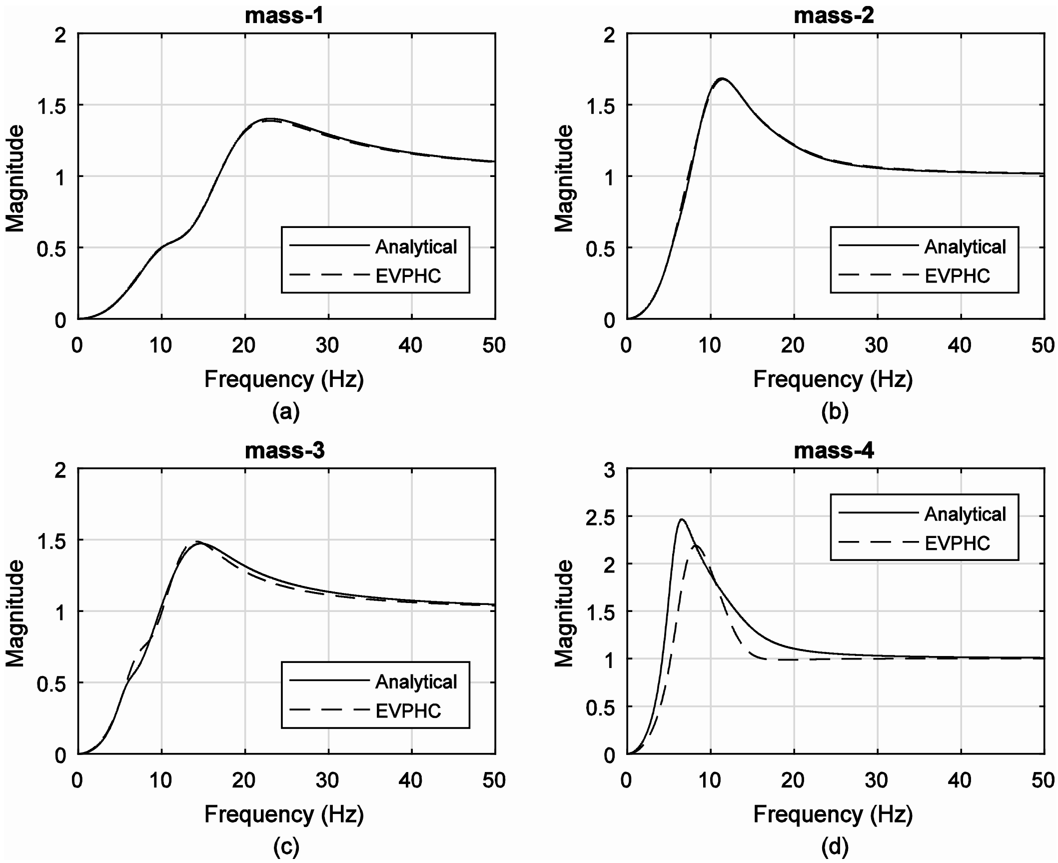

(a)
(b)
(c)
(d)

Figure (2.9) The resulting $EPFRF_n^C$ using EVPHC and analytical $EPFRF_n^A$ for each mass under 5% noise level: (a) mass-1, (b) mass-2, (c) mass-3, and (d) mass-4

The resulting modal frequency and damping ratio from EVPHC and PIA in comparison with the analytical solution are given in Table (2.3). Figure (2.10) shows a comparison between the resulting eigenvectors based on PIA, EVPHC, and the analytical baseline.

Table (2.3) Modal frequencies and damping ratios as predicted by EVPHC and PIA with 5% noise; the values in parentheses represent the percentage deviation from the baseline analytical values

	Mode order	1	2	3	4
EVPHC	Frequency (Hz)	7.26	9.79	12.61	19.21
		(22.74%)	(0.22%)	(-5.38%)	(-0.96%)
	Damping ratio	0.34	0.40	0.32	0.35
		(21.36%)	(1.19%)	(-12.14%)	(0.72%)
PIA	Frequency (Hz)	6.62	9.96	18.55	21.22
		(11.92%)	(2.02%)	(39.20%)	(9.37%)
	Damping ratio	0.45	0.34	0.33	0.19
		(61.66%)	(-12.03%)	(-8.86%)	(-45.41%)

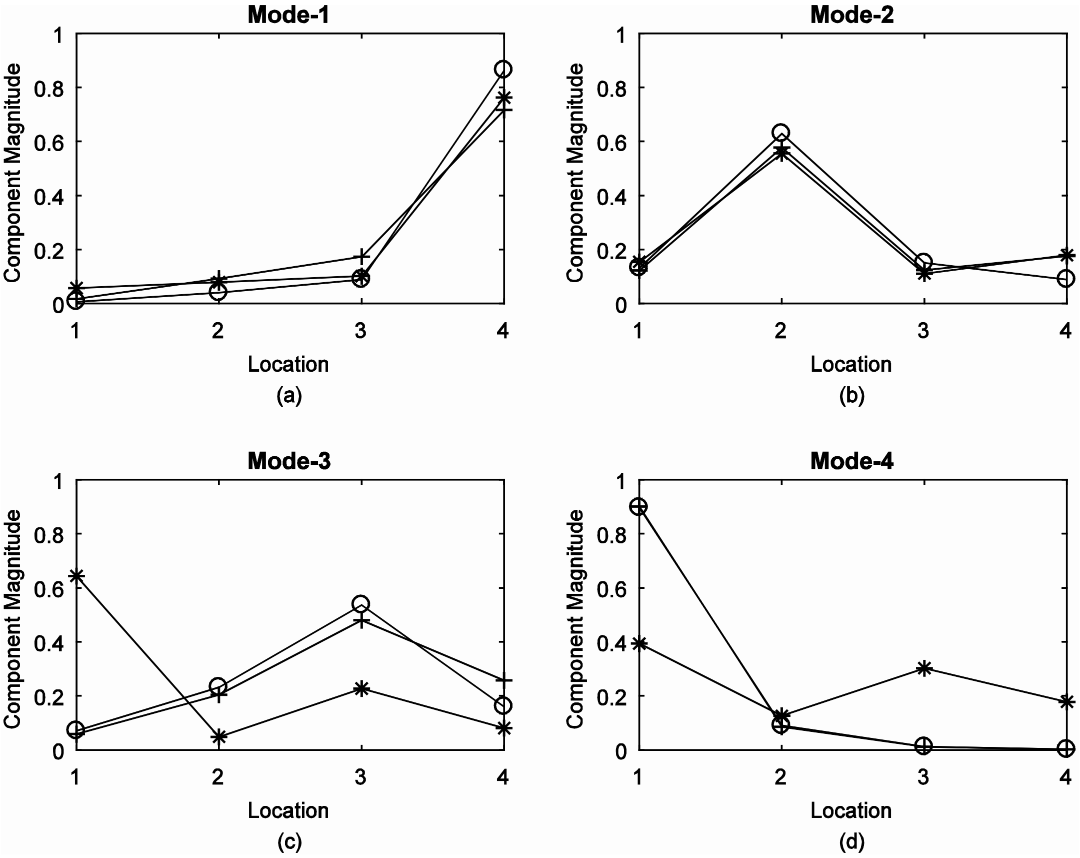

Figure (2.10) Modal shapes magnitude of the four-DOF system (○ - analytical, + - EVPHC, * - PIA): (a) Mode-1, (b) Mode-2, (c) Mode-3, and (d) Mode-4

2.3.2.3. *Case 3: 10% white noise added to the eigenvectors*

Figure (2.11) shows the resulting $EPFRF_n^C$ using the EVPHC method and the analytical $EPFRF_n^A$ for each mass of the four-DOF system when 10% noise was added to the eigenvectors. It can be seen that $EPFRF_n^C$ was very close to the analytical $EPFRF_n^A$ for masses 2 and 3, but showed some difficulties matching those for masses 1 and 4. However, all graphs showed trends similar to those of the analytical.

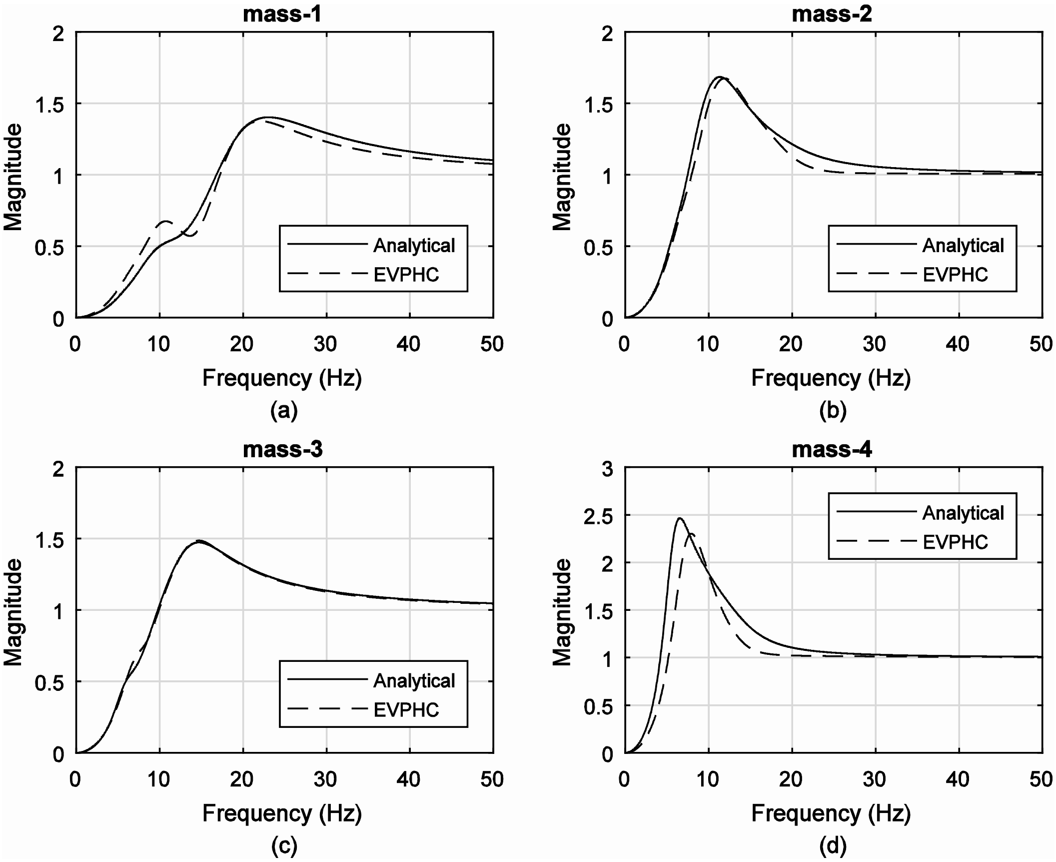

Figure (2.11) The resulting $EPFRF_n^C$ using EVPHC and analytical $EPFRF_n^A$ for each mass under 10% noise level: (a) mass-1, (b) mass-2, (c) mass-3, and (d) mass-4

The modal information predicted by EVPHC and PIA, compared with the baseline analytical solution, are given in Table (2.4). It can be seen that the error in the predicted values using EVPHC was much smaller than in those predicted by PIA.

Table (2.4) Modal frequencies and damping ratios as predicted by EVPHC and PIA under 10% noise; the values in parentheses represent the percentage deviation from the baseline analytical values

	Mode order	1	2	3	4
EVPHC	Frequency (Hz)	7.28	10.25	13.98	18.68
		(22.99%)	(4.92%)	(4.85%)	(-3.68%)
	Damping ratio	0.30	0.37	0.29	0.28
		(6.32%)	(-5.00%)	(-19.13%)	(-20.15%)
PIA	Frequency (Hz)	8.24	8.68	11.95	35.12
		(39.33%)	(-11.12%)	(-10.34%)	(81.04%)
	Damping ratio	0.95	0.21	0.26	0.12
		(241.15%)	(-46.44%)	(-27.69%)	(-65.42%)

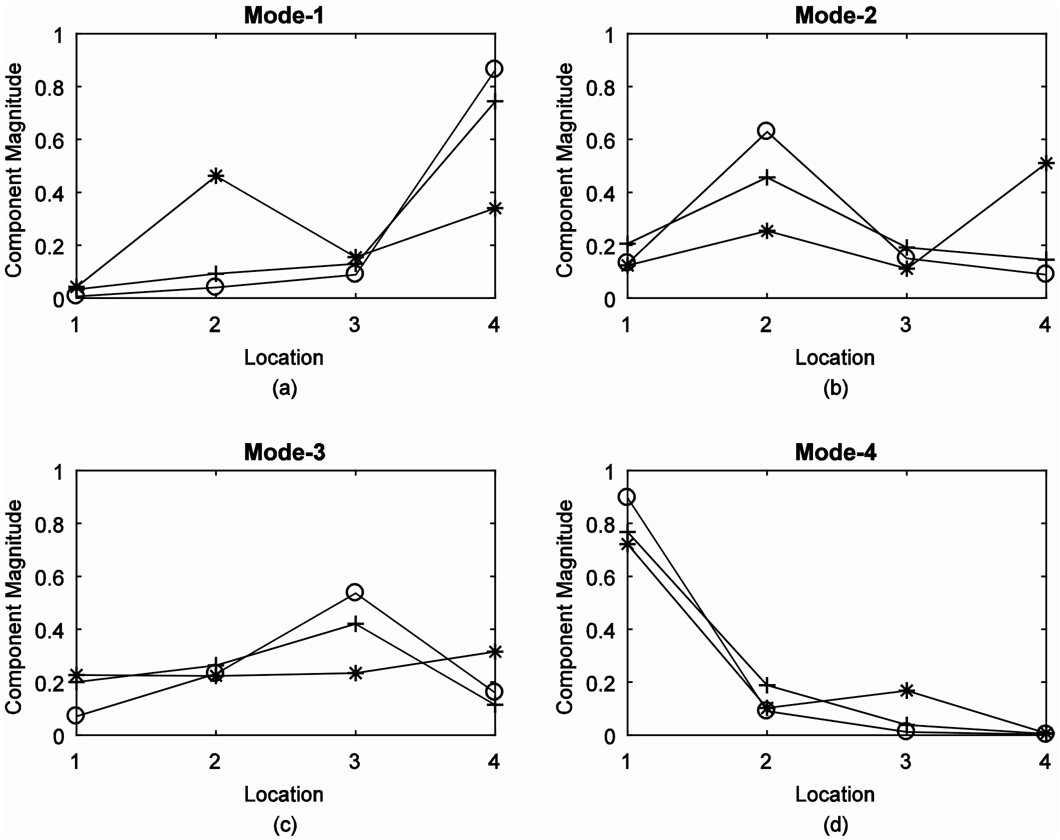

Figure (2.12) Eigenvector magnitudes of the four-DOF system (○ - analytical, + - EVPHC, * - PIA): (a) Mode-1, (b) Mode-2, (c) Mode-3, and (d) Mode-4

Figure (2.12) shows a comparison between the resulting eigenvectors based on PIA, EVPHC, and the analytical baseline. The physical parameters of the spatial matrices (stiffness and damping) of the baseline system and those produced by the EVPHC and PIA methods are shown schematically in Figure (2.13). It is clear from Figure (2.13) that the magnitudes of the elements in the **C** and **K** matrices predicted by EVPHC were closer to those of the analytical as compared with PIA. The detailed values of the resulting damping and stiffness matrices with 10% noise, as predicted by the PIA method, are shown in the following **C** and **K** matrices.

$$\mathbf{C}=\begin{bmatrix} 317 & -457 & (87) & (5) \\ -457 & 1408 & -474 & (-98) \\ (87) & -474 & 911 & -1000 \\ (5) & (-98) & -100 & 169 \end{bmatrix} \mathbf{K}=\begin{bmatrix} 263950 & -59780 & (-168690) & (-2885) \\ -59780 & 69456 & 33934 & (15368) \\ (-168690) & 33934 & 260210 & -27381 \\ (-2885) & (15368) & -27381 & 25329 \end{bmatrix}$$

The values in parentheses inside **C** and **K** denote the elements that should have zero values (as shown in the baseline analysis values in Section 2.3.1). It can be seen that some of the values in the parentheses are relatively large when compared with the diagonal elements; see for example (-98) in the **C** matrix and (-168690) in the **K** matrix. Also, the predicted values in the **K** matrix can exceed three times those in the baseline analytical values. The predicted values in the **C** matrix can exceed four times those in the baseline analytical values.

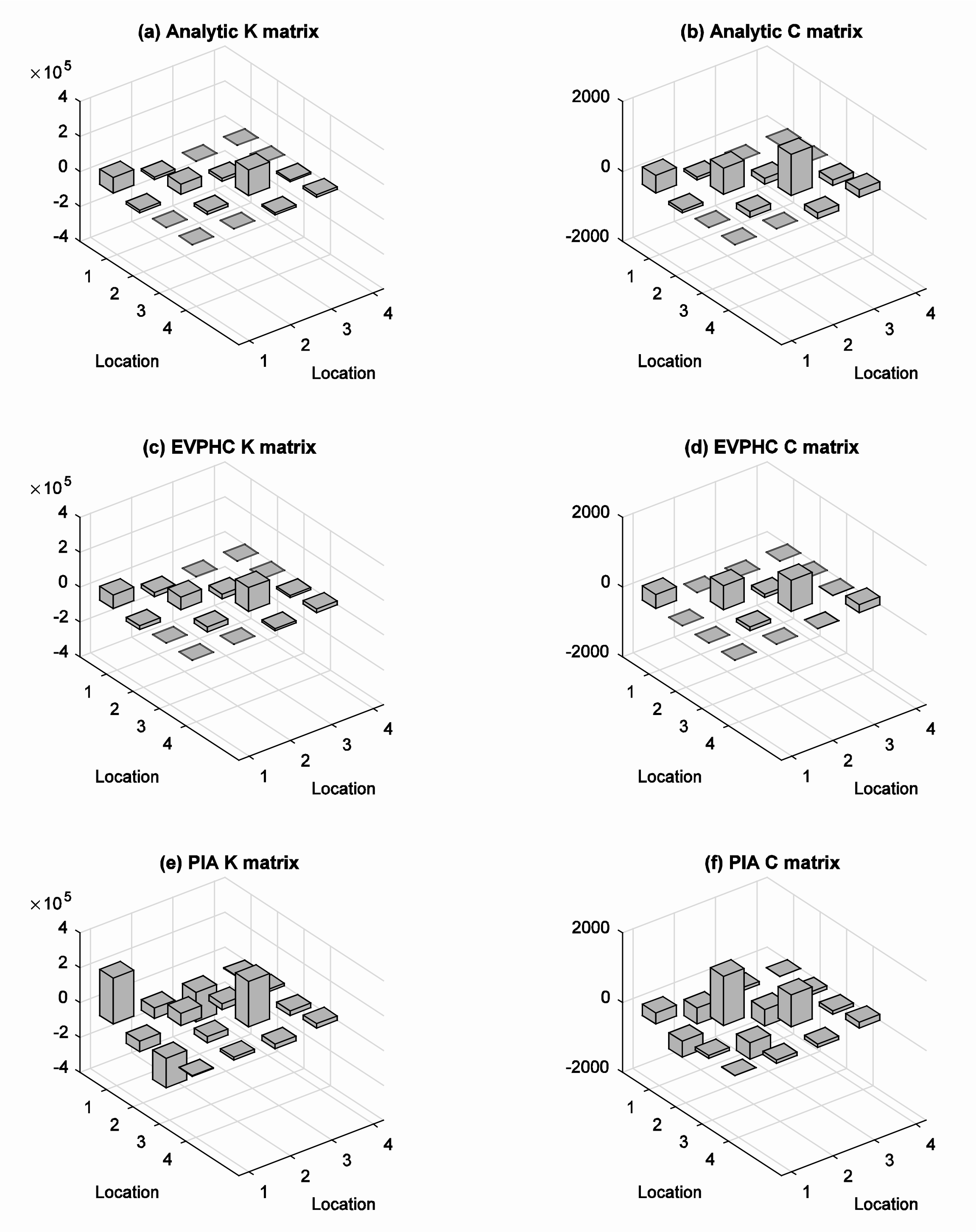
(a) Analytic K matrix

(b) Analytic C matrix

(c) EVPHC K matrix

(d) EVPHC C matrix

(e) PIA K matrix

(f) PIA C matrix

Figure (2.13) Baseline analytical stiffness and damping matrices and those predicted by EVPHC and PIA with 10% added noise: (a-b) Analytical, (c-d) EVPHC, and (e-f) PIA

2.3.3. System with lower damping

In the previous examples, the four-DOF mass-spring system with dashpots of Figure (2.3) was solved under damping ratios that can reach 0.4. The reason behind choosing such relatively high damping ratios was to show the validity of the proposed EVPHC in dealing with engineering applications in biomechanical systems such as the human body as well applications on old structural systems with heavy damping [26, 27]. In order to show the applicability of the proposed EVPHC method on more general mechanical systems, the same four-DOF mass-spring system with dashpots of Figure (2.3) is solved in this example using relatively lower damping. Table (2.5) demonstrates the undamped natural frequencies and damping ratios of this four-DOF system.

Table (2.5) Analytical frequencies and damping ratios of the four-DOF system

Mode order	1	2	3	4
Undamped natural frequency(Hz)	5.89	9.71	13.46	19.42
Damping ratio	0.0256	0.0224	0.0240	0.0192

Figure (2.14) shows the resulting $EPFRF_n^C$ using the EVPHC method and the analytical $EPFRF_n^A$ for each mass of the four-DOF system when 1% noise was added to the eigenvectors. It can be seen that $EPFRF_n^C$ was very close to the analytical $EPFRF_n^A$ for all masses but showed some difficulty matching the first peak associated with mass-4.

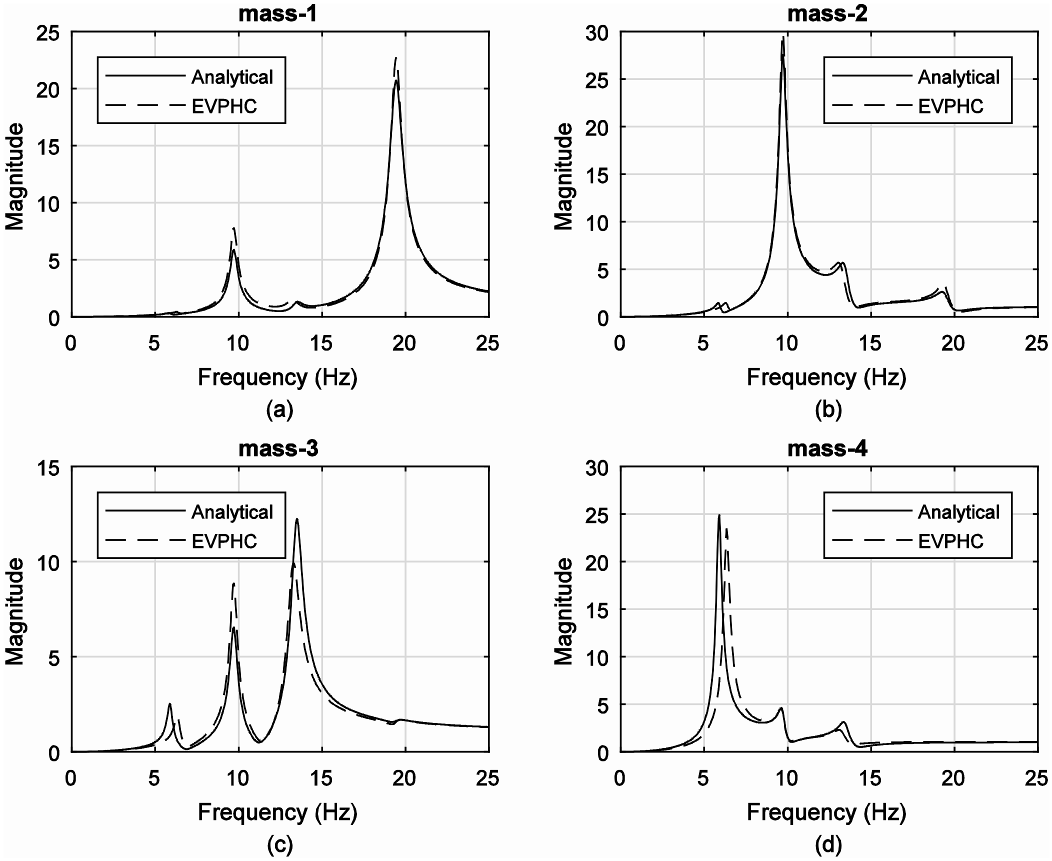

Figure (2.14) The resulting $EPFRF_n^C$ using EVPHC and analytical $EPFRF_n^A$ for each mass under 1% noise level: (a) mass-1, (b) mass-2, (c) mass-3, and (d) mass-4

The modal information predicted by EVPHC and PIA, compared with the baseline analytical solution, is presented in Table (2.6). The table shows that the errors in the predicted damping values using EVPHC were smaller than those predicted by PIA.

Table (2.6) Modal frequencies and damping ratios as predicted by EVPHC and PIA under 1% noise; the values in parentheses represent the percentage deviation from the baseline analytical values

	Mode order	1	2	3	4
EVPHC	Frequency (Hz)	6.34	9.70	13.25	19.42
		(7.76%)	(-0.04%)	(-1.63%)	(0.03%)
	Damping ratio	0.0260	0.0215	0.0270	0.0164
		(1.32%)	(-3.85%)	(12.56%)	(-14.77%)
PIA	Frequency (Hz)	5.95	9.68	13.64	20.01
		(1.01%)	(-0.30%)	(1.32%)	(3.03%)
	Damping ratio	0.0239	0.0324	0.0206	0.0153
		(-6.81%)	(44.50%)	(-14.33%)	(-20.32%)

Figure (2.15) shows a comparison between the resulting eigenvectors based on PIA, EVPHC, and the analytical baseline. As shown in the figure, EVPHC was closer to the analytical solution than PIA in all modes.

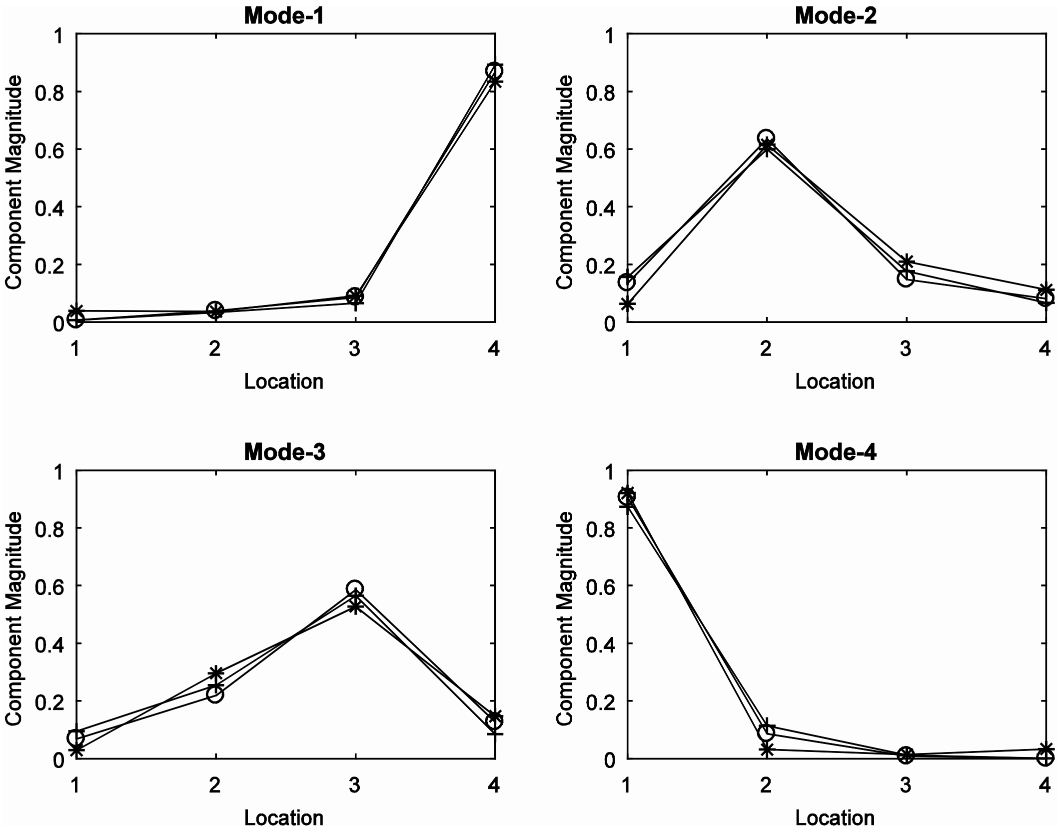

Figure (2.15) Eigenvector magnitudes of the four-DOF system (○ - analytical, + - EVPHC, * - PIA): (a) Mode-1, (b) Mode-2, (c) Mode-3, and (d) Mode-4

2.4. Discussion

A new methodology (EVPHC) is presented in this work to solve the inverse modal problem for the spatial parameters (mass, stiffness, and damping) using noisy eigenvector data. The methodology showed very encouraging results for identifying the spatial parameters of the system. The numerical examples showed realistic values of the resulting system spatial matrices, even when 10% Gaussian white noise was added to the complex eigenvectors. While adding noise to the complex eigenvectors can affect their magnitude and phase, the process of correcting the phase and reserving the norms of the eigenvector still showed very encouraging results when compared with the PIA method. It should be noted here that the PIA method requires a prior knowledge of the mass matrix, while this is less of a strict requirement in EVPHC.

When 1% Gaussian noise level was added to the eigenvectors, the resulting stiffness and damping matrices of EVPHC were comparable to those of PIA. EVPHC kept the original inter-connectivity and the numeric signs associated with the elements of the spatial matrices, while PIA produced full stiffness and damping matrices with out-of-diagonal elements that do not have any physical meaning. The number of iterations and the time consumed for each method varied in different cases. Numerical testing showed that PIA is much faster than EVPHC. For the 1% noise level case, as an example, PIA under tolerance of 0.0001 took 25 iterations and 0.69 second to converge to its final solution; EVPHC took 37 minutes and 50 iterations to reach a solution. At 5% added noise, the PIA method generated 39.20% and 61.66% error in the predicted undamped natural frequency and damping ratio, respectively, while the error in EVPHC reached 22.74% and 21.36%, respectively. At 10% noise, EVPHC generated 22.99% error in the undamped natural frequency and 20.15% error in the damping ratio, while the PIA method generated 81.04% and 241.15% relative error in the undamped natural frequency and damping ratio, respectively.

Because there are no inherent requirements regarding the inner structures of the damping and stiffness matrices for PIA, the non-zero terms in the stiffness and damping matrices spread around all the elements. For 10% added Gaussian noise, the PIA method generated a large negative value (-168690 instead of zero) in the third element of the first column of the stiffness matrix K_{31}. This number is 143% larger than the second diagonal element K_{22} and 566% larger than the fourth diagonal element K_{44}. Also, element C_{42} in the damping matrix has a value of -98 instead of zero, which represents 49% of the diagonal element C_{44}. Such errors in the resulting **K** and **C** matrices in the PIA method will produce a new system with different modal parameters than those of the original system, as can be seen in Figures (2.10) and (2.12). On the other hand, the resulting spatial matrices of EVPHC generated realistic **K** and **C** matrices and preserved the numeric signs and the inner connectivity of the elements in the **K** and **C** matrices as can be seen in Figure (2.13). Also, the resulting eigenvectors have similar trends to those of the original system.

With the 10% added noise, the predicted $EPFRF_n^C$ by EVPHC showed some difficulties matching those of the analytical $EPFRF_n^A$ for masses 1 and 4 (Figure (2.11)). That could be related to the effect of the added noise on the magnitude of the eigenvectors, which was not considered in the correction process. Interestingly, the magnitudes of the resulting eigenvectors were closer to the analytical ones for modes 1 and 4 than to those of modes 2 and 3. PIA showed clear deviation from the analytical solutions for all modes.

It should be noted that under the close spacing natural frequencies condition, the EVPHC method still works and can offer a reasonable solution. However, numerical testing showed that close spacing of natural frequencies affected the performance of the method and produced spatial parameters with less accurate results. In addition, numerical testing showed that tighter constraints on the mass ratios didn't have considerable effects on the resulting EPFRF plots.

2.5. Conclusion

A new methodology called EVPHC is presented in this work. It solves the inverse eigenvalue problem for the spatial parameters when noise is added to the eigenvectors. The method showed very promising results when tested on mass-spring systems with viscous damping, even when 10% noise was added to the eigenvectors. The finding of this work will provide key damping and stiffness information for conducting analysis and modeling on existing mechanical and biological systems.

CHAPTER 3. ENHANCED EXPERIMENTAL MODAL ANALYSIS OF SUPINE HUMANS UNDER VERTICAL WHOLE-BODY VIBRATION

3.1. Introduction

During supine transport, such as that involved in train sleeping berths or emergency transport, humans become sensitive to certain frequencies, especially those that can excite the resonance frequencies of the body, where large unintentional motions can be generated. The resulting motions can cause discomfort and can exacerbate injuries during emergency transport. The quantification of the magnitude and nature of these frequencies and the associated mode shapes and damping ratios are critical to the safety and comfort of the humans during transport. There have been many attempts over the past decades to conduct experimental modal analysis on seated and standing humans to determine the modal parameters of humans [28-33]. The findings from these efforts have shown promising results in identifying the natural frequencies of the human body under these postures. Due to the complexity of the human response in whole-body vibration (WBV) and the unknown damping parameters, however, the undamped natural frequencies, damping ratios, and associated mode shapes are still not very well defined for seated and standing humans.

On the other hand, limited work has been done to investigate the modal parameters of supine humans under WBV. The focus of these investigations was on finding the resonance frequencies of the supine human. Kraus and Lang [34] measured the changes in body strain at the trunk, neck, and limbs of a supine human under vertical WBV. They showed that the strain magnitudes at different parts of the body peaked at 7 Hz. The authors also investigated the changes in the mechanical impedance of the human body with frequency and showed a main natural frequency around 7 Hz, which is consistent with their strain findings. The same authors found another peak at 11 Hz. They used a single mass-spring system and estimated a damping ratio of 0.3-0.4 at 7 Hz. While the 7 Hz natural frequency of the human body is an important finding, the authors emphasized the need to characterize the natural frequencies of the individual body parts of the supine human in any future work. Vogt et al. [35] investigated the nonlinearity of the supine human under vertical WBV using the mechanical impedance function. Ten human subjects were tested under sustained sinusoidal vibration of 0.5 g in the range between 2-20 Hz. The authors found a fundamental frequency around 6 Hz and detected smaller peaks in their impedance curve at 8 and 10 Hz.

The characterization of the modal parameters of the human body has normally been done in the frequency domain. Different types of transfer functions correlated with the input forcing motion, and the output motion in the frequency domain was determined and used to predict the modal parameters during seated and standing postures. These transfer functions included the apparent mass, impedance, and transmissibility [36-40]. Human natural frequencies, usually the damped natural frequencies, have traditionally been determined from the peaks in the experimental transfer functions. However, this approach may present many challenges, as there is a tendency for the transfer function to have many artificial peaks that do not associate with resonance but can be by-product anomalies related to a lack of input energy at certain frequencies. This can also happen as a result of transforming the signal from the time domain to the frequency domain using the fast Fourier transform (FFT), where different types of filters and windows can be applied.

After estimating the resonance frequencies from the peaks of the transfer function using different types of curve fitting [1], the next step is calculating the associated modal shapes and modal damping ratios. The modal shapes and modal damping ratios of the human body are normally solved using a multi-degree-of-freedom human model that represents the human at a certain posture. While the human body can have many degrees of freedom (DOF), the number of DOF in these models are normally subjectively selected based on the number of segments that show large motions. This process is normally followed by solving an inverse problem and using optimization or curve-fitting techniques, where the human model's physical parameters (mass, stiffness, and damping) are updated such that the human model's response mostly matches the experimental data at the natural frequencies. Several human models have been presented in the literature [41-43].

The current state of the art in the area of modal analysis of supine humans demonstrates the limited information available at this time regarding the modal parameters of supine humans. According to Matsumoto and Griffin [31], there is no information available about the stiffness and damping matrix parameters of a living human body in the literature. Therefore, researchers have used different types of approximations, such as those based on proportional damping, that can only give reasonable results for lightly damped systems. Also, there is no current information available on the modal characteristics of the individual body segments [34].

This work presents modal analyses of supine humans under vertical WBV, with the goal of determining the magnitudes and locations of the resonance frequency, the associated mode shape, and the modal damping ratio of the supine human body and at different body segments, including the head, chest, pelvis, and legs. The autoregressive moving average model with exogenous excitation (ARMAX) [44-46] will be used in this work as an attractive time domain approach for characterizing the modal parameters of a supine human body. ARMAX can deal with systems with different levels of damping. Besides finding the damped natural frequencies of the system, the time domain analysis can also give good estimations of the mode shapes and modal damping parameters associated with the natural frequencies. Due to damping and the low energy at some input frequencies, the modal shapes are sometimes incomplete in terms of their components. A methodology is proposed in this work to enhance the missing components of the eigenvectors using the transmissibility function. Because most supine human testing is conducted using a shaker table with a rigid platform, this work presents a transfer function that uses base acceleration as an equivalent input force instead of measuring the actual input forces.

3.2. Methods

3.2.1. Participants

The subject group for this study consisted of fifteen males. Table (3.1) presents the age, mass, and height of the subjects, as well as their mean value and standard deviation (SD). All subjects were generally healthy and reported no musculoskeletal conditions. The protocol was approved by the University of Iowa Institutional Review Board prior to testing.

Table (3.1) Basic anthropometric information of the subjects

Subject	Age (years)	Mass (kg)	Height (m)
1	22	97.52	1.83
2	20	72.58	1.83
3	21	74.84	1.88
4	19	74.84	1.78
5	30	63.50	1.78
6	21	79.38	1.83
7	21	79.38	1.80
8	20	80.74	1.70
9	27	72.00	1.78
10	21	77.11	1.78
11	27	70.76	1.73
12	26	70.00	1.65
13	22	89.81	1.85
14	21	83.92	1.80
15	32	68.04	1.70
Mean Value	23.33	76.96	1.78
SD	4.01	8.71	0.06

3.2.2. Experiments

The subjects were exposed to two types of vertical excitation, a sine-sweep vibration with increasing power (from 0.5 to 20 Hz) and random vibration with frequency content (from 0.5 to 28 Hz), using a motion simulator (Moog ECU-624-1800, Moog-FCS, Ann Arbor, MI, USA). Subjects lay freely on a rigid platform on top of a thin rubber mat to avoid slippage on the metal surface of the platform as shown in Figure (3.1). Vertical translational vibration motions transmitted to the subject’s head, chest, pelvis, and lower leg regions were measured using inertial sensors [47]. Figure (3.2a) shows the time history profile of the input sine-sweep vibration during a 120 second ride, while Figure (3.2b) shows the power spectral density (PSD) of the signal for the frequency range from 0-30 Hz. Figure (3.3a) shows the time history profile of the input random vibration during a 120 second ride, while Figure (3.3b) shows the power spectral density (PSD) of the signal for the frequency range from 0-30 Hz.

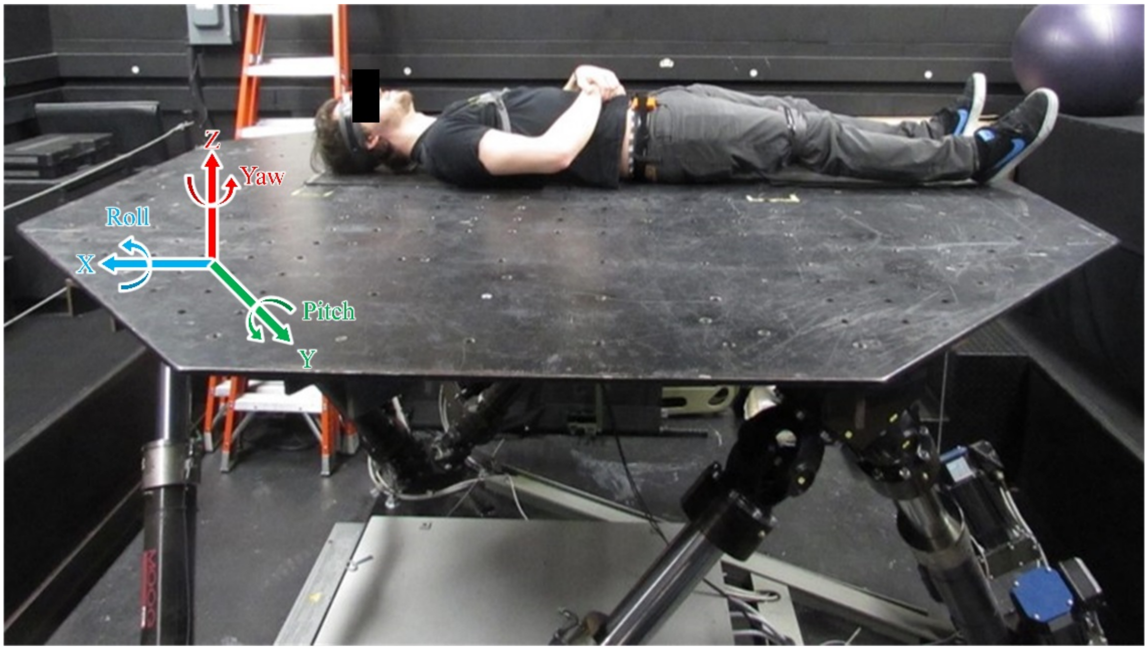
[redacted]

Figure (3.1) Profiles of the supine human testing: the human subject lay on the rigid platform of the motion simulator, and vibrations were generated in the vertical Z direction

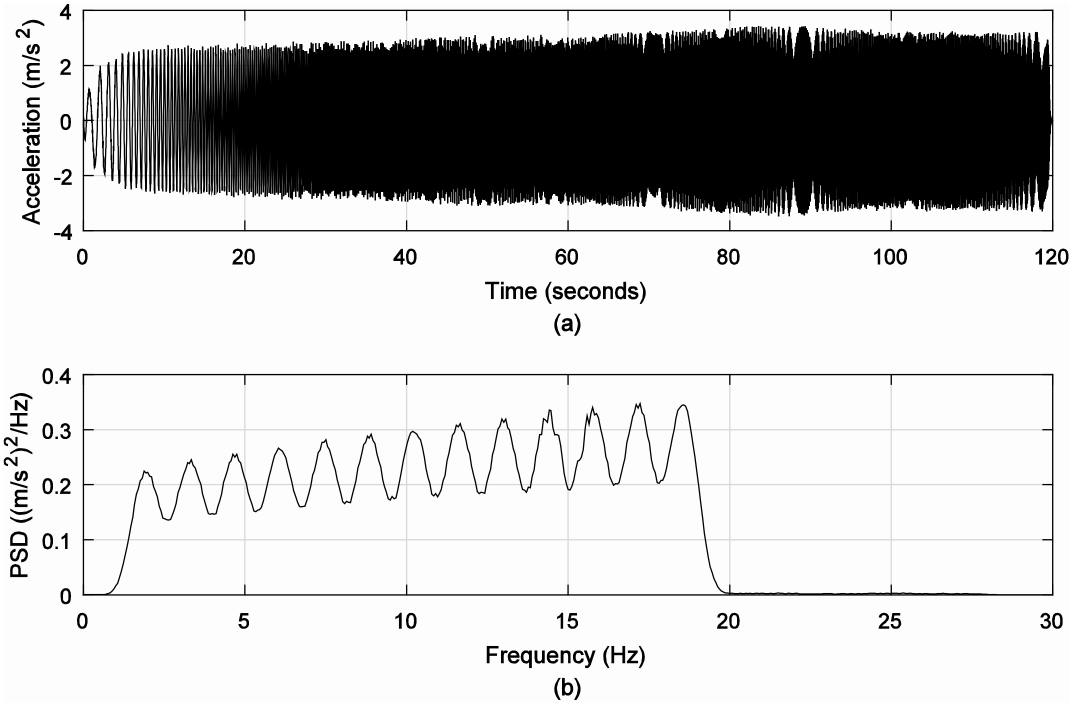

(a)

(b)

Figure (3.2) The input sine-sweep vibration during the 120 second ride: (a) the time history profile, (b) the power spectral density (PSD) of the signal for the frequency range from 0-30 Hz

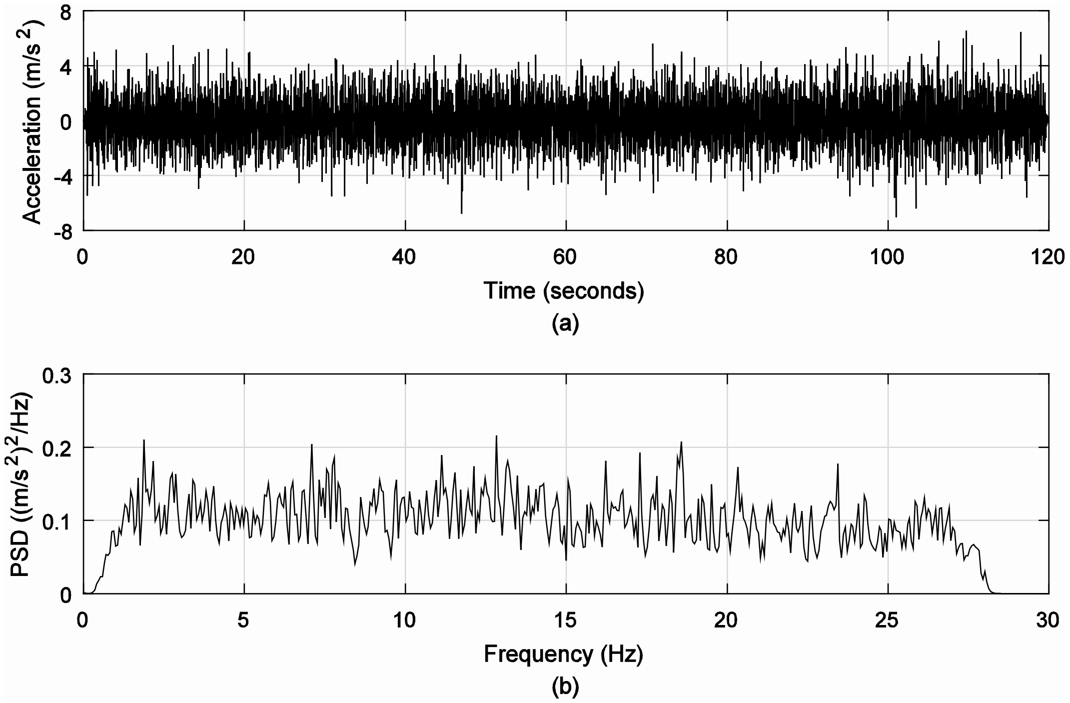

(a)

(b)

Figure (3.3) The input random vibration during the 120 second ride: (a) the time history profile, (b) the power spectral density (PSD) of the signal for the frequency range from 0-30 Hz

3.2.3. Data collection and processing

Four wireless inertial sensors (MTw, Xsens Technologies, Enschede, Netherlands) were used to measure the motion at the different segments of the supine human, including the head, chest, pelvis, and legs. The sensor on the head was placed on the forehead, just between the eyebrows. The sensor on the chest was attached at the flattest location of the sternum. The sensor on the pelvis was attached to a belt tightened over the right anterior superior iliac spine. The fourth sensor was attached to the leg above the patella of the right knee. A fifth sensor was attached to the rigid surface of the motion platform and used as a reference for the input motion. The sensors were adhered to the human body using double-sided tape and were further secured by banded strips of athletic and duct tapes. The MTw sensor recorded motion data at 60 Hz to a desktop computer, then trimmed and post-processed it using a low-pass filter at 28 Hz. Correction methods were used to adjust for the errors that can result when attaching sensors on curved regions of the human body [47].

3.3. Theory

A brief description of the theoretical background behind the modal analysis in the frequency and time domains will be presented in this section. Analysis in the frequency domain is normally presented in terms of transfer functions that correlate the input force/motion with the output motion. The modal analysis in the time domain is conceptually similar to that in the frequency domain, as both domains are based on the concept of a transfer function. In this section, the modal analysis in the frequency domain will be presented first; this will be followed by the modal analysis in the time domain.

3.3.1. Frequency domain analysis

The equations of motion of a viscous underdamped *N*-DOF system with external force are given in form of matrix, as shown in Eq. (3.1)

$$\mathbf{M}\ddot{\mathbf{u}}(t)+\mathbf{C}\dot{\mathbf{u}}(t)+\mathbf{K}\mathbf{u}(t)=\mathbf{f}(t) \tag{3.1}$$

where **M**, **C,** and **K** are the N×N mass, damping, and stiffness matrices, respectively. All three matrices can be assumed to be symmetric real matrices. For the general case, the damping matrix doesn’t need to satisfy the proportional assumption to the mass and stiffness matrices. $\mathbf{u}(t)$ is the N×1 vector for displacement, and $\mathbf{f}(t)$ is the excitation vector at each DOF.

Eq. (3.1) can be rewritten in the Laplace space based on the eigenvalues and eigenvectors as:

$$\mathbf{U}(s)=\sum_{n=1}^{N}\left(\frac{\boldsymbol{\psi}_n\boldsymbol{\psi}_n^T}{a_n(s-\lambda_n)}+\frac{\boldsymbol{\psi}_n^*\boldsymbol{\psi}_n^H}{a_n^*(s-\lambda_n^*)}\right)\mathbf{F}(s) \tag{3.2}$$

where $\mathbf{U}(s)$ and $\mathbf{F}(s)$ are the Laplace transforms of $\mathbf{u}(t)$ and $\mathbf{f}(t)$, respectively; s is the Laplace variable; λ_n is the eigenvalue of order n; and $\boldsymbol{\psi}_n$ is the corresponding eigenvector. Superscript T represents the transpose operation, $*$ the conjugate operator, H the Hermitian transpose operation, and a_n the diagonal elements of a diagonal matrix.

$$\begin{aligned}\mathbf{a}&=diag(a_1,a_2,\cdots,a_N,a_1^*,a_2^*,\cdots a_N^*)\\&=\begin{bmatrix}\boldsymbol{\psi} & \boldsymbol{\psi}^*\\ \boldsymbol{\psi}\boldsymbol{\Lambda} & \boldsymbol{\psi}^*\boldsymbol{\Lambda}^*\end{bmatrix}^T\begin{bmatrix}\mathbf{C} & \mathbf{M}\\ \mathbf{M} & \mathbf{0}\end{bmatrix}\begin{bmatrix}\boldsymbol{\psi} & \boldsymbol{\psi}^*\\ \boldsymbol{\psi}\boldsymbol{\Lambda} & \boldsymbol{\psi}^*\boldsymbol{\Lambda}^*\end{bmatrix}\end{aligned} \tag{3.3}$$

where $\boldsymbol{\psi}=[\boldsymbol{\psi}_1 \quad \boldsymbol{\psi}_2 \quad \cdots \quad \boldsymbol{\psi}_N]$ is the eigenvector matrix, $\boldsymbol{\Lambda}=diag(\lambda_1,\lambda_2,\cdots,\lambda_N)$ is the eigenvalue matrix, and $\mathbf{0}$ is N×N null matrix.

Using Eq. (3.2), the transfer function ($\mathbf{H}(s)$) in the matrix form [48] can be written as:

$$\mathbf{H}(s)=\sum_{n=1}^{N}\left(\frac{\boldsymbol{\psi}_n\boldsymbol{\psi}_n^T}{a_n(s-\lambda_n)}+\frac{\boldsymbol{\psi}_n^*\boldsymbol{\psi}_n^H}{a_n^*(s-\lambda_n^*)}\right) \tag{3.4}$$

The corresponding frequency response function (FRF) can be obtained by substituting $s=i\omega$ in Eq. (3.4). The eigenvalue λ_n can be determined using the following equation.

$$\lambda_n = -\xi_n \varpi_n + i\varpi_n \sqrt{1-\xi_n^2} \tag{3.5}$$

where ϖ_n is the undamped natural frequency for order n, and ξ_n is the corresponding damping ratio. For convenience, Eq. (3.4) can be written by using the residue matrix as:

$$\mathbf{H}(s) = \sum_{n=1}^{N} \left(\frac{\mathbf{R}_n}{(s-\lambda_n)} + \frac{\mathbf{R}^*_n}{(s-\lambda_n^*)} \right) \tag{3.6}$$

where $\mathbf{R}_n = \dfrac{\boldsymbol{\Psi}_n \boldsymbol{\Psi}_n^T}{a_n}$ is the residue matrix.

The corresponding impulse responses function (IRF) is the inverse Laplace transform of Eq. (3.4) as shown below [48].

$$h_{ij}(t) = \sum_{n=1}^{N} (R_{ijn} e^{\lambda_n t} + R_{ijn}^* e^{\lambda_n^* t}) \tag{3.7}$$

where $R_{ijn} = \dfrac{\psi_{in} \psi_{jn}}{a_n}$.

Eq. (3.7) can be transformed to the Z-domain as shown in Eq.(3.8)

$$H_{ij}(\mathrm{z}) = \sum_{n=1}^{N} \left(\frac{R_{ijn}}{1-\mu_n \mathrm{z}^{-1}} + \frac{R_{ijn}^*}{1-\mu_n^* \mathrm{z}^{-1}} \right) \tag{3.8}$$

where $\mu_n = e^{\lambda_n \Delta t}$, and Δt is the time interval.

3.3.2. Time domain analysis

The ARMAX was used in this work to solve for the modal parameters of the supine human. The discrete time system of Eq. (3.1) can be rewritten by the ARMAX [44-46] with orders (na, nb, nc) as

$$\mathbf{A}(q)\mathbf{u}[t] = \mathbf{B}(q)\mathbf{f}[t] + \mathbf{C}(q)\mathbf{e}[t] \tag{3.9}$$

where $t = 1, 2, \cdots$ represents the sample interval, $\mathbf{u}[t]$ is the $N\times1$ output vector, $\mathbf{f}[t]$ is the $M\times1$ input column vector and $\mathbf{e}[t]$ is the $N\times1$ stochastic column vector. $\mathbf{A}(q)$ is the $N\times N$ output parameter matrix for the autoregressive part (AR), $\mathbf{C}(q)$ is the $N\times N$ parameter matrix for the moving average part (MA). $\mathbf{B}(q)$ is the $N\times M$ input parameter matrix for the exogenous excitation (X). q is the forward shift operation as $qu[t] = u[t+1]$, and the backward shift operation is q^{-1}. All matrices $\mathbf{A}(q)$, $\mathbf{B}(q)$, and $\mathbf{C}(q)$ can be formed in polynomial matrix as

$$\begin{aligned} \mathbf{A}(q) &= \mathbf{E} + \mathbf{A}_1 q^{-1} + \mathbf{A}_2 q^{-2} + \cdots + \mathbf{A}_{n_a} q^{-n_a} \\ \mathbf{B}(q) &= \mathbf{B}_0 + \mathbf{B}_1 q^{-1} + \mathbf{B}_2 q^{-2} + \cdots + \mathbf{B}_{n_b} q^{-n_b} \\ \mathbf{C}(q) &= \mathbf{E} + \mathbf{C}_1 q^{-1} + \mathbf{C}_2 q^{-2} + \cdots + \mathbf{C}_{n_c} q^{-n_c} \end{aligned} \tag{3.10}$$

When the feedback from output responses to input can be ignored, the output can be assumed to be diagonal as

$$A_n(q) = 1 + A_1^n q^{-1} + A_2^n q^{-2} + \cdots A_{n_a}^n q^{-n_a} \tag{3.11}$$

According to Eq.(3.10), the output function form can be written as:

$$u_n(t) = \frac{\mathbf{B}_n(q)}{A_n(q)}\mathbf{f}(t) + \frac{\mathbf{C}_n(t)}{A_n(q)}e_n(t) = \mathbf{G}_n(q)\mathbf{f}(t) + H_n(q)e_n(t) \tag{3.12}$$

where $\mathbf{G}_n(q)$ represents a transfer function.

$$\mathbf{G}_n(q) = [G_{n1}(q) \quad G_{n2}(q) \quad \cdots \quad G_{nM}(q)] \tag{3.13}$$

and $G_{nm}(q) = \dfrac{B_{nm}(q)}{A_n(q)}$.

Similar to Eq.(3.8), the transfer function $G_{nm}(q)$ in Eq. (3.12) can be also rewritten in the partial fraction form [45].

$$G_{nm}(q) = \frac{B_{nm}(q)}{A_n(q)} = \sum_{k=1}^{n_a} \left(\frac{R_{nmk}}{1-\mu_k q^{-1}} + \frac{R_{nmk}^*}{1-\mu_k^* q^{-1}} \right) \tag{3.14}$$

By solving for the zeros of $A_n(q)$ at location *n*, μ_n can be determined. The undamped natural frequency (f_n) of order *n* and the corresponding damping ratio (ξ_n) can be calculated using the following equations [49]:

$$f_k = \frac{1}{2\pi\Delta t}\sqrt{\left(\frac{\ln(\mu_k\mu_k^*)}{2}\right)^2 + \left(\arccos\left(\frac{\mu_k+\mu_k^*}{2\sqrt{\mu_k\mu_k^*}}\right)\right)^2}\,(Hz) \tag{3.15}$$

$$\xi_k = \sqrt{\frac{(\ln(\mu_k\mu_k^*))^2}{(\ln(\mu_k\mu_k^*))^2 + 4\left(\arccos\left(\frac{\mu_k+\mu_k^*}{2\sqrt{\mu_k\mu_k^*}}\right)\right)^2}} \tag{3.16}$$

The modal shape for order k can be determined by the residues in Eq. (3.14).

$$\boldsymbol{\psi}_k = \begin{bmatrix} R_{1mk} & R_{2mk} & \cdots & R_{Nmk} \end{bmatrix}^T \tag{3.17}$$

It should be noted that the derivation so far was based on the displacement response. When it comes to velocity and acceleration responses, the proper representation of ARMAX can be found in the literature [49]. The modal parameter extraction process for velocity and acceleration is similar to that of displacement. Due to external influences such as environmental noise and calibration errors, a higher order of AR is necessary [50]. At the same time, too high a value of n_a will increase the computational cost in the calculation and analysis [51] and may lead to artificial modes. So, the value of n_a should be carefully selected so that only the frequency range of interest is taken into consideration. The prediction-error method [46] is adopted here to estimate the parameters of ARMAX. The calculations were conducted in MATLAB.

3.3.3. Transfer function under base motion

During supine transport, vibration is normally transferred to the supine human body from the supporting surfaces (the rigid base of the motion platform). With such a setup, it becomes more complicated and expensive to construct transfer functions that are based on the input forces at the different locations of the supine human body. While the input motion entering the human body through the rigid base can be considered to be similar to all body segments, this work uses an equivalent force represented by the product of the acceleration and mass of the supine human segment. The resulting transfer function using this equivalent force is called the equivalent point frequency response function (EPFRF). The EPFRF is calculated as the ratio between the motion of the body's segment at the input port and the input acceleration at the input port in frequency domain.

The equation of motion in the global reference frame can be expressed as:

$$\mathbf{M}\ddot{\mathbf{u}} + \mathbf{C}\dot{\mathbf{u}} + \mathbf{K}\mathbf{u} = \mathbf{0} \tag{3.18}$$

$\mathbf{u}$ can be written as:

$$\mathbf{u} = \mathbf{u}_g + \mathbf{u}_r \tag{3.19}$$

where $\mathbf{u}_g$ is the motion of the rigid base of the motion platform, and $\mathbf{u}_r$ is the motion of the human body relative to the rigid base of the platform. Eq. (3.18) can be written as

$$\mathbf{M}\ddot{\mathbf{u}}_r + \mathbf{C}\dot{\mathbf{u}}_r + \mathbf{K}\mathbf{u}_r = -\mathbf{M}\ddot{\mathbf{u}}_g = \mathbf{f}_{eq} \tag{3.20}$$

where $\mathbf{f}_{eq}$ represents the equivalent force on base motion. The mass matrix is diagonal as

$$\mathbf{M} = \begin{bmatrix} m_1 & 0 & \cdots & 0 \\ 0 & m_2 & \cdots & 0 \\ \vdots & \vdots & \ddots & \vdots \\ 0 & 0 & \cdots & m_N \end{bmatrix} \tag{3.21}$$

$$\mathbf{f}_{eq} = -\mathbf{M}\ddot{\mathbf{u}}_g = -\begin{bmatrix} m_1 & 0 & \cdots & 0 \\ 0 & m_2 & \cdots & 0 \\ \vdots & \vdots & \ddots & \vdots \\ 0 & 0 & \cdots & m_N \end{bmatrix} \begin{bmatrix} \ddot{u}_g \\ \ddot{u}_g \\ \vdots \\ \ddot{u}_g \end{bmatrix} = -\begin{bmatrix} m_1\ddot{u}_g \\ m_2\ddot{u}_g \\ \vdots \\ m_N\ddot{u}_g \end{bmatrix} = -\begin{bmatrix} m_1 \\ m_2 \\ \vdots \\ m_N \end{bmatrix} \ddot{u}_g \qquad (3.22)$$

where the acceleration of the base motion is considered as the input. The output motion can be expressed in terms of the transfer function as:

$$\begin{aligned} u_i(\omega) &= \sum_{j=1}^{N} H_{ij}(\omega) f_j(\omega) \\ &= \sum_{j=1}^{N} H_{ij}(\omega) m_j \ddot{u}_g(\omega) \\ &= \sum_{j=1}^{N}\sum_{n=1}^{N} \left(\frac{R_{ijn}}{i\omega-\lambda_n} + \frac{R_{ijn}^*}{i\omega-\lambda_n^*}\right) m_j \ddot{u}_g(\omega) \\ &= \sum_{n=1}^{N} \left(\frac{\psi_{in}\sum_{j=1}^{N}\psi_{jn}m_j}{a_n(i\omega-\lambda_n)} + \frac{\psi_{in}^*\sum_{j=1}^{N}\psi_{in}^*m_j}{a_n^*(i\omega-\lambda_n^*)}\right) \ddot{u}_g(\omega) \end{aligned} \qquad (3.23)$$

Let

$$M_{in} = \frac{\psi_{in}\sum_{j=1}^{N}\psi_{jn}m_j}{a_n} \qquad (3.24)$$

Then Eq. (3.23) can be written as

$$u_i(\omega) = \sum_{n=1}^{N} \left(\frac{M_{in}}{(i\omega-\lambda_n)} + \frac{M_{in}^*}{(i\omega-\lambda_n^*)}\right) \ddot{u}_g(\omega) \qquad (3.25)$$

$$EPFRF_i(\omega) = \sum_{n=1}^{N} \left(\frac{M_{in}}{(i\omega-\lambda_n)} + \frac{M_{in}^*}{(i\omega-\lambda_n^*)}\right) \qquad (3.26)$$

The output can also be measured in terms of velocity and acceleration. Eq. (3.26) has a structure and function similar to the FRF given in Eq. (3.6). Therefore, the model shape extraction method based on Eq. (3.6) can be used in the base excitation case. Furthermore, the base excitation case can be considered as a single-input ARMAX model when the diagonal property of $\mathbf{A}(q)$ can be achieved by Eq. (3.11). In this case, the modal identification process of a multi-DOF system can be simplified as a series of single-input single-output (SISO) systems.

3.3.4. Modal shape supplement from transmissibility

In human testing, due to damping, noise, and low energy at some input frequencies, it is common to see incomplete eigenvectors, i.e., eigenvectors with missing components. In this work, a method based on the transmissibility function that supplements the missing components of the eigenvectors is presented. The equation of motion in Eq. (3.1) can be transferred in the Laplace domain with zero initial condition.

$$(\mathbf{M}s^2 + \mathbf{C}s + \mathbf{K})\mathbf{U}(\mathrm{s}) = \mathbf{F}(s) \tag{3.27}$$

where s is the Laplace variable, and $\mathbf{U}(\mathrm{s})$ and $\mathbf{F}(s)$ are the Laplace transformations of $\mathbf{u}(\mathrm{t})$ and $\mathbf{f}(\mathrm{t})$, respectively. The dynamical stiffness can be defined as

$$\mathbf{U}(\mathrm{s}) = \mathbf{D}^{-1}(s)\mathbf{F}(s) = \mathbf{H}(s)\mathbf{F}(s) \tag{3.28}$$

Transmissibility can be defined in the Laplace domain as the ratio between two responses at locations k and l due to a single input force, such as

$$T_{kl}(s) = \frac{U_k(s)}{U_l(s)} \tag{3.29}$$

$$T_{kl}(s) = \frac{U_k(s)}{U_l(s)} = \frac{H_{kj}(s)F_j(s)}{H_{lj}(s)F_j(s)} = \frac{H_{kj}(s)}{H_{lj}(s)} \tag{3.30}$$

So the transmissibility is also a ratio between two transfer functions under a single input force. With the base motion input and using the concept of the equivalent input force, Eq. (3.29) can be written as:

$$T_{kl}(s)=\frac{U_k(s)}{U_l(s)}=\frac{\sum_{j=1}^{N}H_{kj}(s)m_j\ddot{u}_g(s)}{\sum_{j=1}^{N}H_{lj}(s)m_j\ddot{u}_g(s)}=\frac{\sum_{n=1}^{N}\left(\frac{\psi_{kn}\sum_{j=1}^{N}\psi_{jn}m_j}{a_n(s-\lambda_n)}+\frac{\psi_{kn}^{*}\sum_{j=1}^{N}\psi_{in}^{*}m_j}{a_n^{*}(s-\lambda_n^{*})}\right)}{\sum_{n=1}^{N}\left(\frac{\psi_{ln}\sum_{j=1}^{N}\psi_{jn}m_j}{a_n(s-\lambda_n)}+\frac{\psi_{ln}^{*}\sum_{j=1}^{N}\psi_{in}^{*}m_j}{a_n^{*}(s-\lambda_n^{*})}\right)} \qquad (3.31)$$

Taking the limit as *s* approaches λ_r,

$$\lim_{s\to\lambda_r}T_{kl}(s)\approx\frac{\psi_{kr}\sum_{j=1}^{N}\psi_{jr}m_j}{\psi_{lr}\sum_{j=1}^{N}\psi_{jr}m_j} \qquad (3.32)$$

Eq. (3.32) shows that the modal shape components ratio can be obtained from the transmissibility function. While the response is given here by the displacement, the velocity and acceleration can be used as well [52]. When the noise effect is considered, Eq. (3.32) can still be viewed as a reasonable way to approximate the model shape ratio. Eq. (3.32) can be written in the frequency domain using a similar approach.

$$\lim_{\omega\to\omega_r}T_{kl}(\omega)\approx\frac{\psi_{kr}}{\psi_{lr}} \qquad (3.33)$$

where ω_r represents the damped natural frequency for mode *r*, $\omega_r=\bar{\omega}_r\sqrt{1-\xi_r^2}$, and $\bar{\omega}_r$ and ξ_r are the corresponding undamped natural frequency and damping ratio, respectively [52].

When the partial modal shape is obtained, the unknown part for this mode can be enhanced using the following expression:

$$\phi_{pr}=T_{pl}^{r}s_{ql}^{r}\phi_{lr} \qquad (3.34)$$

where $T_{pl}^{r}=\lim_{\omega\to\omega_r}T_{pl}(\omega)$, similarly $T_{ql}^{r}=\lim_{\omega\to\omega_r}T_{ql}(\omega)$.

Here $s_{ql}^{r} = \left|\frac{\phi_{qr}}{\phi_{lr}}\right| / \left|T_{ql}^{r}\right|$ is a scalar function to reduce influence from neighboring modes. ϕ_{pr} is the unknown mode shape component at location *p* for mode *r*, and ϕ_{qr} and ϕ_{lr} are the neighboring known mode shape components at *q* and *l*, respectively.

3.4. Results

Figure (3.4) shows the time history of the vertical acceleration at the head, chest, pelvis, and legs of Subject 3 as a result of the vertical input sinusoidal motion at the rigid-platform level. The time history of the other fourteen subjects is given in Appendix A. While the horizontal axis in the graphs represents time, the time can be correlated with the frequencies. All graphs showed large motion with peaks at certain times/frequencies, and that can be related to the resonance of the segments.

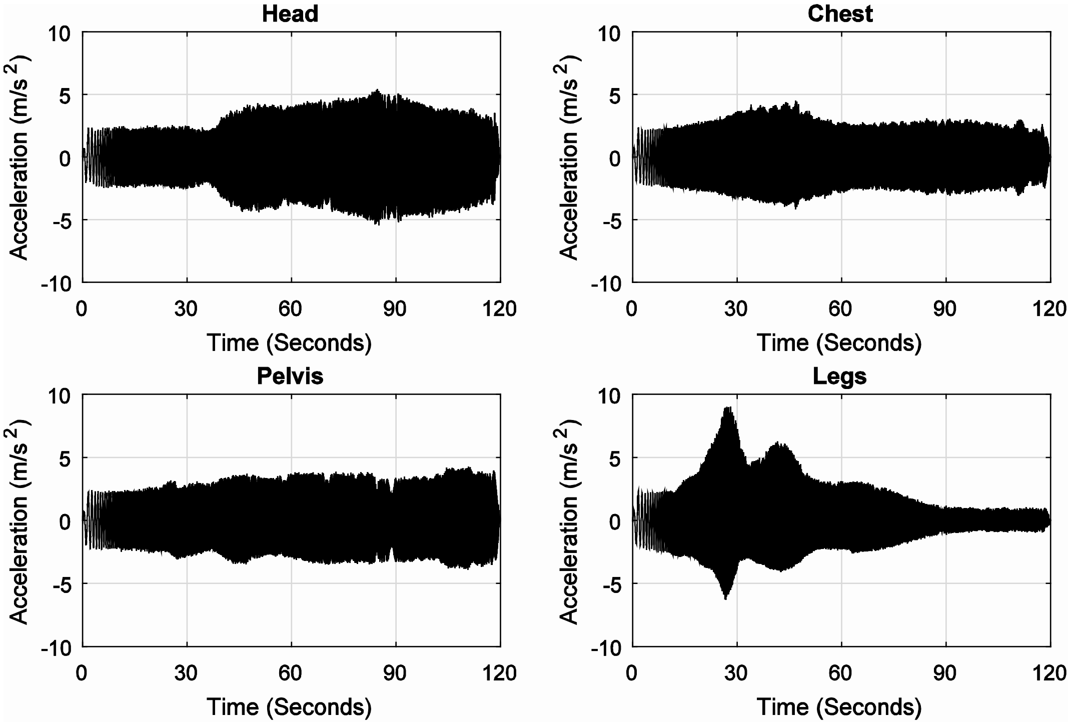

Figure (3.4) Time history of the resulting vertical acceleration signals measured at the head, chest, pelvis, and legs as a result of the vertical input sinusoidal motion of Subject 3

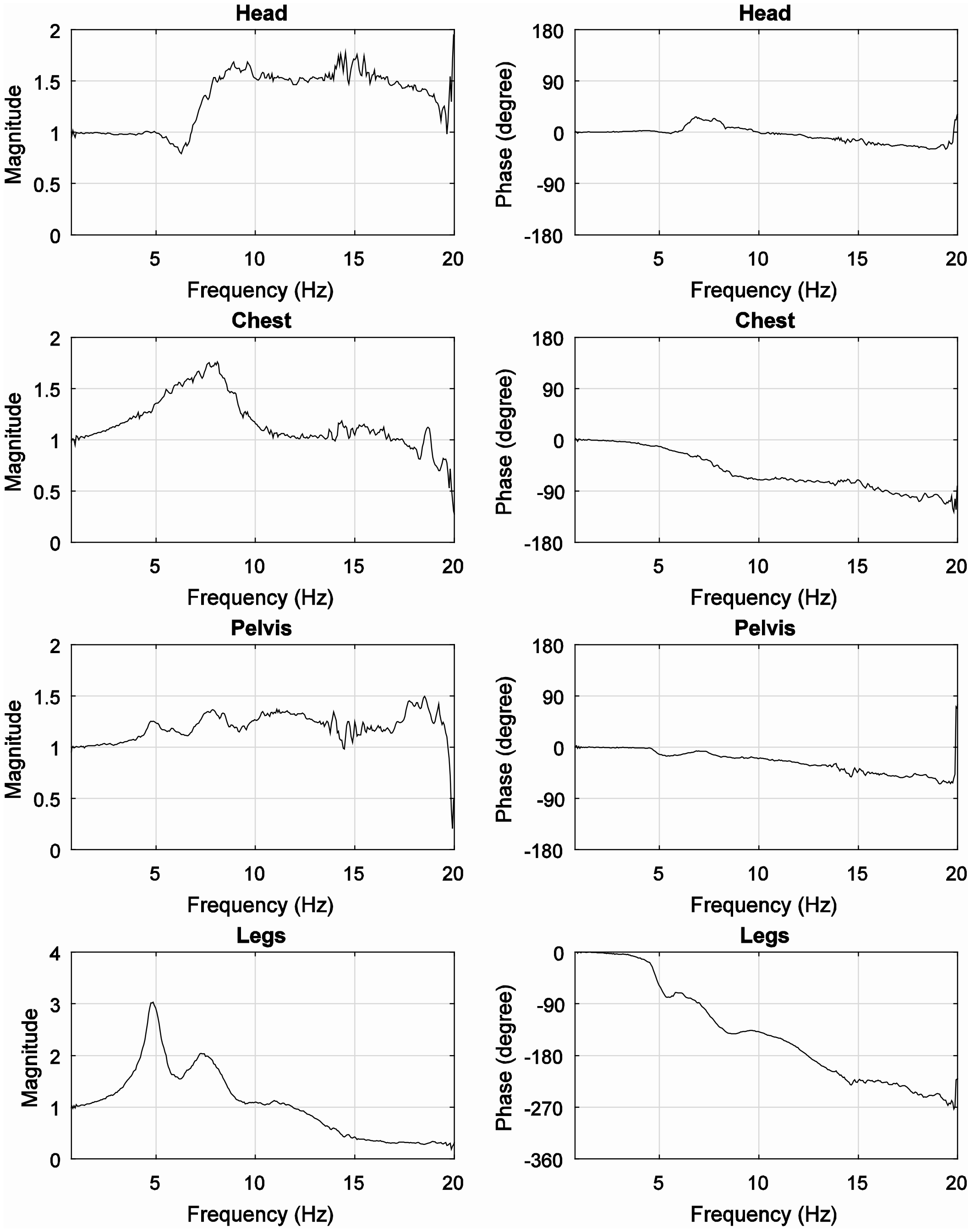

Figure (3.5) Transmissibility magnitude and phase between the vertical output motion at the head, chest, pelvis, and legs of Subject 3, and the vertical input sinusoidal motion at the rigid-base level

The transmissibility magnitude and phase graphs of the individual segments are shown in Figure (3.5). The transmissibility presents the ratio between the input motion at the rigid platform level and the output motion at the individual segments such as the head, chest, pelvis, and legs. The transmissibility graphs would give a better picture of how the input motion is magnified at different frequencies. For example, the transmissibility magnitude at the legs of this subject clearly showed three peaks where the motion of the body was amplified under the input motion.

Figure (3.6) shows the relationships between the ARMAX model prediction and those of the experiments in the frequency domain for the different body segments for Subject 3. The vertical axis represents the magnitude of an EPFRF. It can be seen that, at low frequency, the EPFRF gives zero values at the head, while the transmissibility, on the other hand, gives a value of one at this range of frequencies, as shown in Figure (3.5). The information of the other fourteen subjects is given in Appendix B.

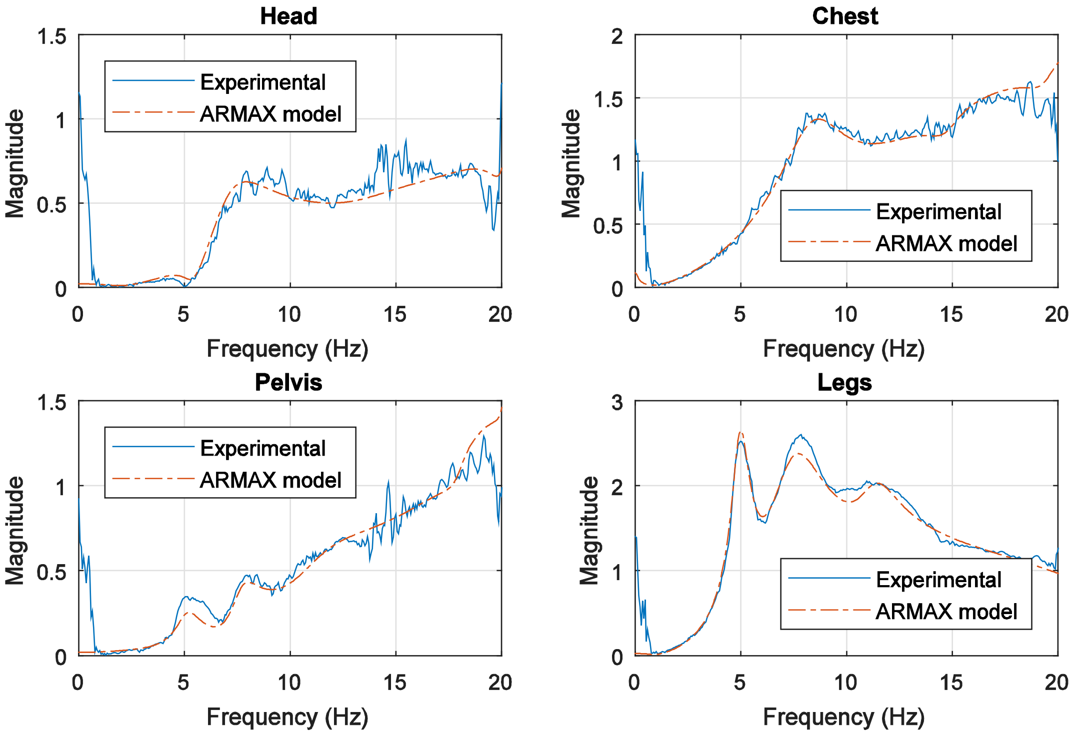

Figure (3.6) EPFRF magnitude predicted by ARMAX at the head, chest, pelvis, and legs, and those measured by the experiments of Subject 3

Table (3.2) Damped and undamped natural frequencies and damping ratios at the head, chest, pelvis, and legs levels of the fifteen participants

Subject	Mode / Loc.	Undamped Natural Frequency (Hz)				Damping Ratio				Damped Natural Frequency (Hz)			
		1	2	3	4	1	2	3	4	1	2	3	4
Sub1	Head	5.9552	8.2812	X	14.3309	0.1173	0.1630	X	0.3457	5.9141	8.1705	X	13.4472
	Chest	6.1187	7.3690	9.9324	14.9849	0.2425	0.0532	0.3728	0.1760	5.9361	7.3585	9.2165	14.7510
	Pelvis	5.8843	X	9.9442	12.7517	0.2871	X	0.4356	0.0606	5.6365	X	8.9514	12.7283
	Legs	5.4875	X	9.2420	14.2958	0.1763	X	0.1692	0.1532	5.4016	X	9.1088	14.1271
Sub2	Head	3.8807	8.4614	X	16.6460	0.0466	0.3167	X	0.2101	3.8765	8.0258	X	16.2743
	Chest	4.2199	7.4608	9.0787	15.6718	0.0701	0.2674	0.1672	0.2281	4.2095	7.1892	8.9509	15.2585
	Pelvis	5.2701	X	10.1912	17.6698	0.0714	X	0.1780	0.1751	5.2567	X	10.0284	17.3967
	Legs	4.2696	8.0512	X	18.5928	0.1107	0.1442	X	0.1003	4.2434	7.9671	X	18.4991
Sub3	Head	5.7193	7.1315	X	14.4896	0.2251	0.2238	X	0.1915	5.5725	6.9506	X	14.2213
	Chest	X	8.5563	X	14.7368	X	0.1953	X	0.0669	X	8.3915	X	14.7038
	Pelvis	5.1368	7.6972	11.3466	X	0.1166	0.0917	0.2032	X	5.1018	7.6647	11.1099	X
	Legs	4.9718	7.4259	11.2842	X	0.0865	0.1869	0.0999	X	4.9532	7.2951	11.2278	X
Sub4	Head	6.0138	8.1589	X	17.8112	0.1747	0.1688	X	0.3433	5.9214	8.0419	X	16.7290
	Chest	6.6035	7.7228	X	13.7582	0.0970	0.2208	X	0.1340	6.5724	7.5322	X	13.6342
	Pelvis	4.9769	X	9.6653	12.2624	0.0724	X	0.4471	0.1194	4.9638	X	8.6454	12.1747
	Legs	5.0941	8.5298	11.1798	17.6906	0.1220	0.1465	0.1356	0.1743	5.0560	8.4378	11.0766	17.4197
Sub5	Head	5.3058	6.9873	8.7531	13.4326	0.1169	0.1414	0.1376	0.1651	5.2694	6.9171	8.6698	13.2483
	Chest	5.1875	6.9621	X	13.9282	0.1926	0.3393	X	0.1160	5.0903	6.5490	X	13.8342
	Pelvis	X	7.0537	11.4702	X	X	0.2612	0.2602	X	X	6.8088	11.0750	X
	Legs	5.4230	7.3598	12.0276	X	0.1357	0.3203	0.0484	X	5.3729	6.9721	12.0134	X
Sub6	Head	4.0740	6.5001	X	14.2719	0.3204	0.2846	X	0.7135	3.8593	6.2313	X	9.9992
	Chest	4.5481	7.7686	11.3460	14.4497	0.3549	0.2735	0.1185	0.1182	4.2520	7.4724	11.2660	14.1914
	Pelvis	5.6095	8.2626	12.7421	X	0.1124	0.1444	0.3405	X	5.5739	8.1760	11.9806	X
	Legs	5.4096	6.8169	9.7782	15.2144	0.1182	0.3825	0.1440	0.1969	5.3717	6.2985	9.6763	14.9166
Sub7	Head	3.4491	7.6007	X	17.5394	0.1620	0.2227	X	0.2546	3.4035	7.4098	X	16.9616
	Chest	X	6.5165	9.2214	15.1961	X	0.2870	0.7603	0.0233	X	6.2424	5.9896	15.1923
	Pelvis	5.3943	7.1685	11.7013	X	0.1163	0.2719	0.3370	X	5.3578	6.8985	11.0169	X
	Legs	5.0437	7.0361	11.2084	13.3257	0.1065	0.0221	0.3238	0.1181	5.0150	7.0344	10.6047	13.2324
Sub8	Head	3.6877	7.4190	9.1490	14.0546	0.1021	0.2456	0.0842	0.2022	3.6684	7.1918	9.1165	13.7643
	Chest	3.9310	8.6696	10.7360	X	0.1842	0.1823	0.0709	X	3.8637	8.5243	10.7090	X
	Pelvis	4.6570	6.6233	11.7139	X	0.1531	0.2924	0.2438	X	4.6021	6.3339	11.3606	X
	Legs	3.9657	9.5960	X	16.7086	0.1377	0.2319	X	0.0173	3.9279	9.3345	X	16.7061

Table (3.2.continued) Damped and undamped natural frequencies and damping ratios at the head, chest, pelvis, and legs levels of the fifteen participants

Sub9	Head	3.9430	8.5976	X	16.4058	0.1160	0.1736	X	0.4230	3.9164	8.4670	X	14.8656
	Chest	4.4394	7.2559	12.7486	X	0.1477	0.3629	0.2697	X	4.3906	6.7613	12.2761	X
	Pelvis	4.7069	7.2801	11.1423	X	0.0767	0.0611	0.2776	X	4.6930	7.2665	10.7043	X
	Legs	4.7679	9.5520	13.2596	16.2376	0.1350	0.1216	0.2599	0.0923	4.7243	9.4811	12.8040	16.1682
Sub10	Head	X	8.2254	X	15.1439	X	0.3706	X	0.2934	X	7.6397	X	14.4772
	Chest	3.8627	6.9284	12.8276	16.2877	0.1012	0.2301	0.2904	0.1238	3.8428	6.7426	12.2748	16.1625
	Pelvis	5.0805	8.4072	13.8884	X	0.0763	0.1397	0.1885	X	5.0657	8.3248	13.6395	X
	Legs	4.8817	7.4278	10.4331	14.5080	0.1504	0.3080	0.1620	0.1978	4.8262	7.0666	10.2952	14.2214
Sub11	Head	4.2593	6.7424	8.8304	15.8906	0.1063	0.1446	0.1679	0.4305	4.2352	6.6715	8.7051	14.3424
	Chest	3.4758	7.5509	X	14.7284	0.1536	0.2759	X	0.0426	3.4346	7.2578	X	14.7150
	Pelvis	4.6095	X	10.3772	13.7045	0.0356	X	0.4545	0.0939	4.6066	X	9.2434	13.6440
	Legs	4.9279	8.0581	10.2457	16.8876	0.1135	0.1323	0.0994	0.3601	4.8961	7.9873	10.1949	15.7544
Sub12	Head	6.5357	X	10.3767	15.6271	0.1890	X	0.0344	0.0953	6.4179	X	10.3709	15.5559
	Chest	6.6180	8.5520	X	X	0.1651	0.4908	X	X	6.5272	7.4513	X	X
	Pelvis	4.9642	7.9292	10.6042	X	0.1753	0.1458	0.0616	X	4.8874	7.8444	10.5840	X
	Legs	5.1270	10.6549	11.6448	17.0070	0.1420	0.4273	0.0431	0.0196	5.0750	9.6331	11.6340	17.0037
Sub13	Head	4.5824	6.4917	9.3900	17.7374	0.1309	0.2433	0.5688	0.1868	4.5430	6.2966	7.7233	17.4250
	Chest	X	6.5662	10.8843	15.9415	X	0.4371	0.0899	0.2051	X	5.9058	10.8403	15.6026
	Pelvis	4.7469	7.3736	10.4138	16.4177	0.1035	0.1210	0.2755	0.0902	4.7214	7.3195	10.0108	16.3508
	Legs	4.8448	X	11.1430	16.9164	0.1334	X	0.1396	0.1930	4.8016	X	11.0340	16.5984
Sub14	Head	5.8617	8.5102	X	X	0.0752	0.2894	X	X	5.8451	8.1461	X	X
	Chest	X	6.6033	11.1640	14.2646	X	0.2950	0.1825	0.3243	X	6.3094	10.9766	13.4935
	Pelvis	5.8876	8.7782	11.7061	X	0.0805	0.2771	0.2336	X	5.8684	8.4343	11.3821	X
	Legs	6.0264	X	9.8997	14.7042	0.1046	X	0.1523	0.2375	5.9933	X	9.7842	14.2833
Sub15	Head	5.5471	7.2561	X	12.7373	0.1107	0.2014	X	0.4176	5.5130	7.1075	X	11.5736
	Chest	4.9168	8.8410	X	X	0.3426	0.4015	X	X	4.6192	8.0973	X	X
	Pelvis	5.2214	6.8074	12.2428	X	0.1126	0.1352	0.3088	X	5.1882	6.7449	11.6446	X
	Legs	5.3237	7.4295	10.5491	13.6407	0.1762	0.1493	0.1541	0.2056	5.2404	7.3463	10.4231	13.3494

Table (3.3) Average of the undamped natural frequencies, damping ratios, and damped natural frequencies of the head, chest, pelvis, and legs of the fifteen supine human subjects with their standard deviation (SD)

Mode / Subject	Undamped Natural Frequency (Hz)				Damping Ratio				Damped Natural Frequency (Hz)			
	1	2	3	4	1	2	3	4	1	2	3	4
Sub1	5.7480	8.1363	9.8456	14.2988	0.2053	0.1455	0.3770	0.2438	5.6256	8.0496	9.1190	13.8675
Sub2	4.2896	7.8828	9.8628	16.9895	0.1084	0.2507	0.1748	0.1839	4.2643	7.6311	9.7109	16.6997
Sub3	5.1909	7.6597	11.3091	14.6065	0.1271	0.1950	0.1410	0.1326	5.1488	7.5126	11.1960	14.4776
Sub4	5.4348	8.0596	10.1002	17.0228	0.1294	0.1854	0.3576	0.2381	5.3891	7.9199	9.4322	16.5331
Sub5	5.3890	7.1576	10.7109	13.5626	0.1417	0.3151	0.1436	0.1522	5.3346	6.7930	10.5999	13.4046
Sub6	5.0496	7.1635	11.7524	14.4954	0.2042	0.3146	0.2588	0.4513	4.9432	6.7996	11.3520	12.9356
Sub7	5.0305	6.9894	10.3053	16.5492	0.1101	0.1886	0.5362	0.2170	4.9999	6.8640	8.6989	16.1549
Sub8	3.9958	8.8048	11.4552	14.9223	0.1419	0.2194	0.2142	0.1417	3.9553	8.5904	11.1894	14.7717
Sub9	4.7380	8.0569	12.8226	16.3769	0.1333	0.2673	0.2658	0.3661	4.6957	7.7636	12.3613	15.2397
Sub10	4.8669	7.7138	12.6320	15.1035	0.1448	0.2903	0.2318	0.2393	4.8156	7.3817	12.2879	14.6647
Sub11	4.8400	7.4722	10.1365	16.5344	0.1140	0.2302	0.3906	0.3684	4.8085	7.2716	9.3311	15.3715
Sub12	5.5889	9.5558	11.1890	16.1642	0.1564	0.4144	0.0490	0.0658	5.5201	8.6965	11.1756	16.1291
Sub13	4.8288	6.5801	10.2300	16.8020	0.1323	0.3609	0.3395	0.1886	4.7863	6.1367	9.6224	16.5006
Sub14	6.0096	7.6085	10.9834	14.5427	0.1017	0.2910	0.1931	0.2694	5.9785	7.2793	10.7766	14.0049
Sub15	5.2609	8.2426	11.7630	13.2547	0.1977	0.3172	0.2650	0.2962	5.1571	7.8168	11.3426	12.6600
Average	5.0841	7.8056	11.0065	15.4150	0.1432	0.2657	0.2625	0.2370	5.0282	7.5004	10.5464	14.8943
SD	0.5293	0.7404	0.9566	1.2806	0.0341	0.0734	0.1224	0.1023	0.5184	0.6894	1.1532	1.3395

Table (3.2) shows the resulting damped and undamped natural frequencies and damping ratios at the head, chest, pelvis, and leg levels of the fifteen subjects. It can be seen that the table is missing several components marked by (X). The time domain analysis was unable to identify the information at the missing components, and that can be contributed to the experimental noises. While averaging the transfer functions of the different subjects may assist in finding these missing components, the averaging process may still lead to diminishing the peaks or shifting them to new locations. A better way is to take the average of the peak locations and magnitudes from different segments and subjects and use that as a representative of the tested group [53]. Based on this approach, Table (3.3) shows the average resonance frequencies and the SD of the four segments from the fifteen subjects.

The averaging process for each mode in Table (3.2) was achieved in two steps. In the first step, the weighted average resonance frequencies and damping ratios of the different body segments (head, chest, pelvis, and legs) for each subject were calculated using Eq. (3.35) and Eq. (3.36). The weighting factors in these two equations were chosen based on the residue term M_{ij} in Eq. (3.25), which reflected to some extent the energy level associated with a resonance frequency [51]. The missing components marked by (X) in Table (3.2) were not included in the calculations of the weighted average resonance frequencies and damping ratios for each subject. Then the second step involved calculating the average and the SD among the different subjects.

$$f_i^w = \frac{\sum_j^N f_i^j \left|M_{ij}\right|}{\sum_j^N \left|M_{ij}\right|} \qquad (3.35)$$

$$\xi_i^w = \frac{\sum_j^N \xi_i^j \left|M_{ij}\right|}{\sum_j^N \left|M_{ij}\right|} \qquad (3.36)$$

Here $N = 4$ means all four DOF. f_i^j and ξ_i^j are the natural frequency and damping ratio, respectively, from location *j* for mode *i*. The values of missing terms in Table (3.2) are set as zero. In Table (3.3), for each subject, the weighted natural frequencies and weighted damping ratios are given. The corresponding mean value and the SD over these fifteen subjects are also offered at the end of Table (3.3). It's easy to find that, compared with damping ratios, the natural frequencies have smaller relative SD.

Figure (3.7) shows the resulting mode shapes of the fifteen tested subjects at the different locations (segments) on the human body. The horizontal axis represents the head (1), torso (2), pelvis (3), and legs (4) segments. The vertical axis represents the magnitude of the component of each modal shape. In this figure, the geometrical mean modal shape of each mode is also plotted by black solid lines.

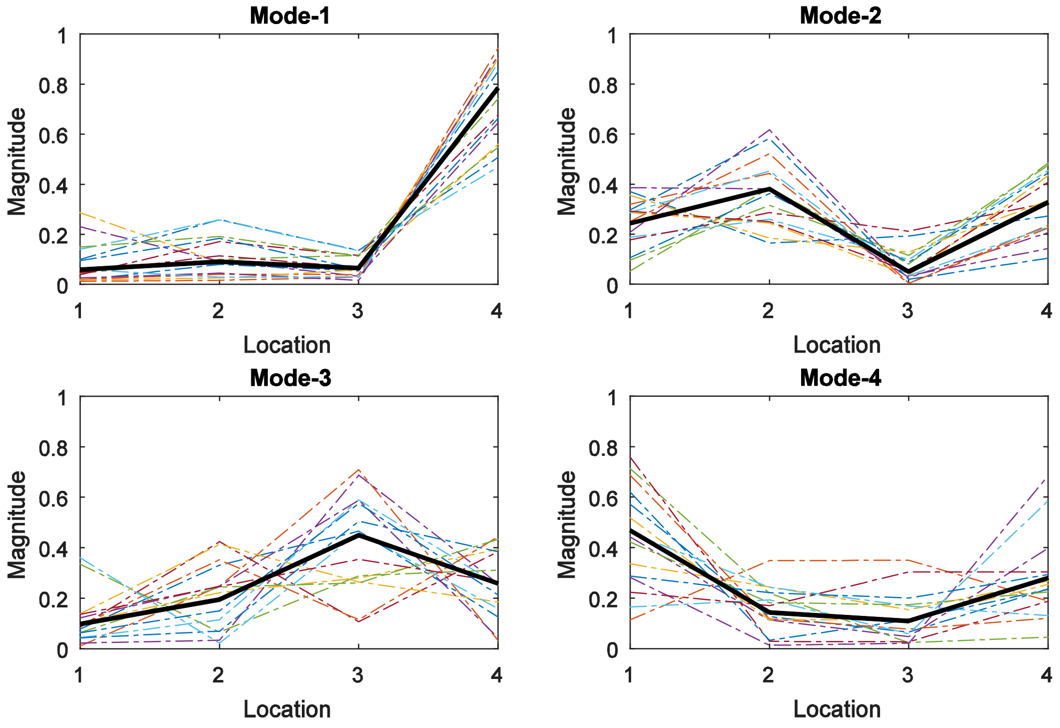

Figure (3.7) Mode shape components at the head (1), chest (2), pelvis (3), and legs (4) at the four resonance frequencies; dashed lines represent the individual subjects, and black solid lines represent the geometrical mean of the subjects

3.5. Discussion

The laboratory visual observations showed that the rocking motion of the legs and pelvis seemed to play a major role in generating the peak motions at different segments of the supine human during vertical input vibrations. The legs/pelvis started showing a large rocking motion at a frequency of around 4-5 Hz. This extreme motion was then transferred across the body, generating large motions at the chest and head of the subject. Around 5 Hz, the body moved in a global mode-like motion. Another peak was then seen at the chest level around 8 Hz. The chest moved with extreme motions, forcing the head and the rest of the body to move in a global mode. Extreme motions were seen at higher frequencies, but it was hard to accurately identify the resonance frequencies at which the extreme motions took place from the visual inspection.

The transmissibility magnitude and phase graphs in Figure (3.5) of the different body segments of one subject may provide a better estimate of the locations of the damped natural frequencies. The head showed a small peak around 5 Hz, a peak around 8-9 Hz, and another peak around 14-16 Hz. The chest showed a large peak around 8 Hz, followed by another peak around 14-16 Hz. The magnification in the chest motion at 8 Hz was much bigger than in the other segments, implying that the chest is a primary generator of this motion. Also, the transmissibility phase of the chest at 8 Hz showed a phase change from 0° to -90°, another indication of a local mode. The pelvis and legs showed clear peaks around 5 Hz, 7-8 Hz, 12 Hz, and 17 Hz. The corresponding graphs for the transmissibility phase of the legs demonstrated clear jumps at these frequencies. The previous information led to the perception of local modes at the different segments. However, some of these did not necessarily represent local modes but rather can be considered a by-product of the resonance motion of the other segments. In general, the peak motions of the different body segments didn’t occur at exactly the same frequency, and that could be related to the effects of damping, nonlinearity, and the weak connections between the different segments. Still, all segments moved in a global-like motion around resonance frequencies that approximately represent the average resonance frequencies of the body segments. A recent study [54] showed that the inter-subject variability outweighed the effect of the nonlinearity that can take place due to the changes in the vibration magnitude entering the human body during the standing posture.

The time domain analysis produced resonance frequencies in Table (3.2) and Table (3.3) comparable to those of the frequency domain. These time domain results demonstrated that different subjects can produce different resonance frequencies at various segments. This can be attributed to the differences in the subjects' anthropometry and body-mass index, subtle differences in postures and how they lay on the rigid platform, as well as other forms of experimental noises and uncertainties. But a closer look at Table (3.3) with the different modes considering the average frequencies from different subjects showed 5 Hz for Mode 1, 8 Hz for Mode 2, 11 Hz for Mode 3, and 15 Hz for Mode 4, with their SD. With these four average natural frequencies, the resulting average damping ratios and mode shapes can be calculated as seen in Table (3.3) and Figure (3.7).

While a complete set of resonance frequencies and damping ratios can be calculated, the components of the corresponding mode shapes at these resonance frequencies may not be complete. This can be explained by the differences between the subjects and the experimental noises. The missing components of the mode shapes can also be attributed to the lack of local resonance motion of some segments for some subjects and the weak connectivity between the different segments. However, for the sake of analysis and in order to provide the complete information to solve for the physical parameters (mass, stiffness, and damping) of the supine human body, the complete set of modal parameters was needed. The proposed transmissibility-based enhancement method of this work was used to fill the missing components of the individual mode shapes, by utilizing the motion information of the neighboring segments.

The input signal of the sine-sweep vibration with constant energy at the different frequencies was not able to generate adequate energy to significantly move the body segments at higher frequencies. The low energy at the higher frequencies can generate numerical anomalies when calculating the transfer functions. The increase in the input energy with higher frequencies, on the other hand, can produce some nonlinearity in the human response and may affect the linearity assumption that was used to conduct the modal analysis. It was assumed, however, that the differences between the responses of the subjects may come from the subtle changes in their postures that can outweigh the generated nonlinearity if it were presented. The input signal of the random vibration can generate higher frequencies from the view of its power spectrum shown in Figure (3.3b). However, it seemed doubtful that the body segments had significant movement at higher frequencies. So the measured data under the random base excitation was used as a supplement of the sine-sweep base excitation when the abnormal data appeared.

Figure (3.7) showed the four modal shapes at the four resonance frequencies. The behavior shown in the figure seemed consistent among the fifteen subjects. Several subjects, though, behaved in a different manner at some modes. This could be related to the subject’s anthropometry or the way the subject lay on the rigid platform, or it could be error resulting from the experimental measurements and noises. The average damping ratios at the end of Table (3.3) were in the range of 0.14 – 0.27, which were close to those identified by Krause and Lang [34], around 7 Hz.

3.6. Conclusion

The supine human body under WBV behaved as a weakly coupled non-linear system, where each body segment generated a large magnification at different frequencies. It was possible to identify global frequencies where the whole body moved as a linear system at the different modes. Other segmental peak frequencies took place at different locations and did not have a defined global mode shape. The supine human body showed four natural frequencies in the range between 0-20 Hz, and that may provide useful information on the number of segments required when modeling a human in such a configuration. Laboratory observations showed considerable pelvis and leg rocking motions, which were very clear at a frequency of 4-6 Hz.

CHAPTER 4. IDENTIFICATION OF DAMPING AND STIFFNESS PARAMETERS OF SUPINE HUMANS UNDER VERTICAL WHOLE-BODY VIBRATION

4.1. Introduction

The motion of the cervical and lumbar spines of humans is to some extent determined by the collective physical properties of the intervertebral disc, facet joints, ligaments, surrounding tissues, and muscles. With no existing direct way of measuring these physical properties of humans in vivo, the current traditional research is based on in-vitro testing of cadaver or animal models, mostly under static or quasi-static loading [55]. The characterization of the damping and stiffness parameters of human joints at the cervical and lumbar areas is a significant component in many applications, such as the development of biomaterials, the design of prosthetic devices, and the development of medical transport systems. Due to the complex interactions between the different components of the human body, the measurements of the physical properties, especially damping, must be done under dynamic loading conditions. The information about damping in the area of biomechanics is not as well established in the literature as it is in the area of structural dynamics, where damping can be approximated by different models, including proportional damping, in which the damping is expressed in terms of mass and stiffness. Still, finding appropriate damping parameters for aerospace and advanced materials in structural dynamics remains a challenging area of research [5, 6, 12].

Experimental modal analysis, a well-established area in structural and mechanical systems and a relatively new one in biological systems, is another way to predict the dynamic properties of systems under vibrational loading in terms of their natural frequencies (large response at certain frequencies), damping ratios, and eigenvectors (global distorted shapes at natural frequencies). Van Englen et al. [56] used experimental modal analysis on human lumbar motion segments and showed a good correlation between the stiffness obtained from static testing and that obtained from modal analysis. Van Englen et al. [57] also showed the validity of using vibration testing to estimate the modal parameters of goat lumbar vertebral segments and the feasibility of using vibration to study the mechanical properties of spinal segment motion in vivo. While the modal parameters represent the dynamic characteristics of the system, they do not represent the real physical damping and stiffness parameters. Therefore, work has been done to use the modal parameters to solve for the physical parameters through a process called the inverse modal problem.

The solution of the inverse modal problem for the physical parameters is an area of intense research. Different methods have been proposed [6, 13] with success. However, most existing methods suffer from short outcomes when experimental error and noise are presented in the modal parameters. Qiao and Rahmatalla [58] proposed a new methodology, which was presented in Chapter 2, to determine more accurate and sound damping and stiffness parameters for structural and mechanical systems by correcting the phase of the eigenvectors (mode shapes) when solving the inverse modal problem. The method will be developed in this work to solve for the unknown damping and stiffness parameters at the cervical and lumbar areas of supine humans under vertical WBV. In this work, the modal parameters described in this chapter, including natural frequencies, damping ratios, and mode shapes, will be used inside an inverse modal problem to determine the stiffness and damping parameters.

4.2. Methodology

4.2.1. Participants

The subject group for this study consisted of fifteen male participants. The averages and standard deviations (SD) of the age, height, and mass of these subjects are 23.33 ± 4.01 years, 1.78 ± 0.06 m, and 76.96 ± 8.71 kg, respectively. The biomechanical details about these participants are offered in Table (3.1).

4.2.2. Experiments

The subjects were exposed to two types of vertical excitation, a sine-sweep vibration with increasing power (from 0.5 to 20 Hz) and a random vibration with frequency content (from 0.5 to 28 Hz), using a motion simulator (Moog ECU-624-1800, Moog-FCS, Ann Arbor, MI, USA). Subjects lay freely on a rigid platform on top of a thin rubber mat to avoid slippage on the metal surface of the platform as shown in Figure (4.1). Vertical translational vibration motions (Z-direction) transmitted to the subject's head, chest, pelvis, and lower leg regions were measured using inertial sensors [47]. Information on these two types of vertical excitation is given in Figure (3.2) and Figure (3.3).

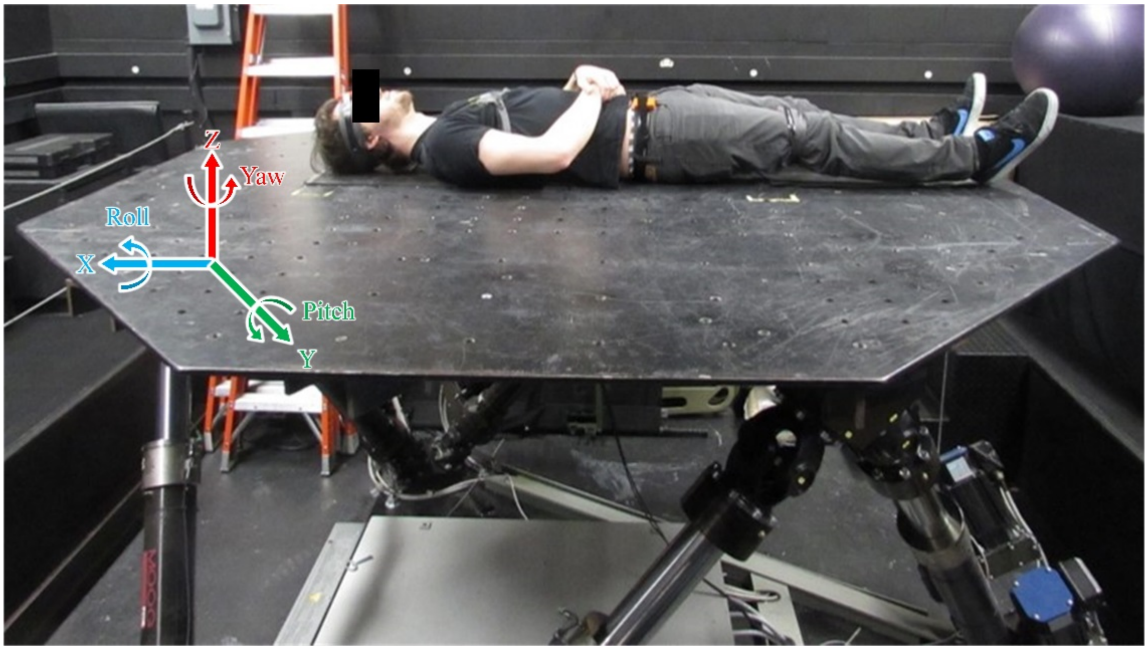

Figure (4.1) Profiles of the supine human testing: the human subject lay on the rigid platform of the motion simulator, and vibrations were generated in the vertical Z direction

4.2.3. Data collection

Experimental modal analysis was then conducted on the data collected from the fifteen human subjects, which is presented in Chapter 3. Table (4.1) shows the resulting average undamped natural frequencies, the damping ratios, and the damped natural frequencies of the fifteen subjects. Meanwhile, the details of each subject can be found in Table (3.7). Figure (4.2) shows the resulting mode shapes of the fifteen tested subjects at the different locations (segments) on the human body. The vertical axis represents the magnitude of the component of each modal shape. The horizontal axis represents the magnitude at the head (1), torso (2), pelvis (3), and legs (4) segments. In this figure, the geometrical mean modal shape of each mode is also given by black solid lines.

Table (4.1) Average of the undamped natural frequencies, damping ratios, and damped natural frequencies of the head, chest, pelvis, and legs of the fifteen supine human subjects

Mode Order	1	2	3	4
Undamped Natural Frequency (Hz)	5.0841	7.8056	11.0065	15.4150
Damping Ratio	0.1432	0.2657	0.2625	0.2370
Damped Natural Frequency (Hz)	5.0282	7.5004	10.5464	14.8943

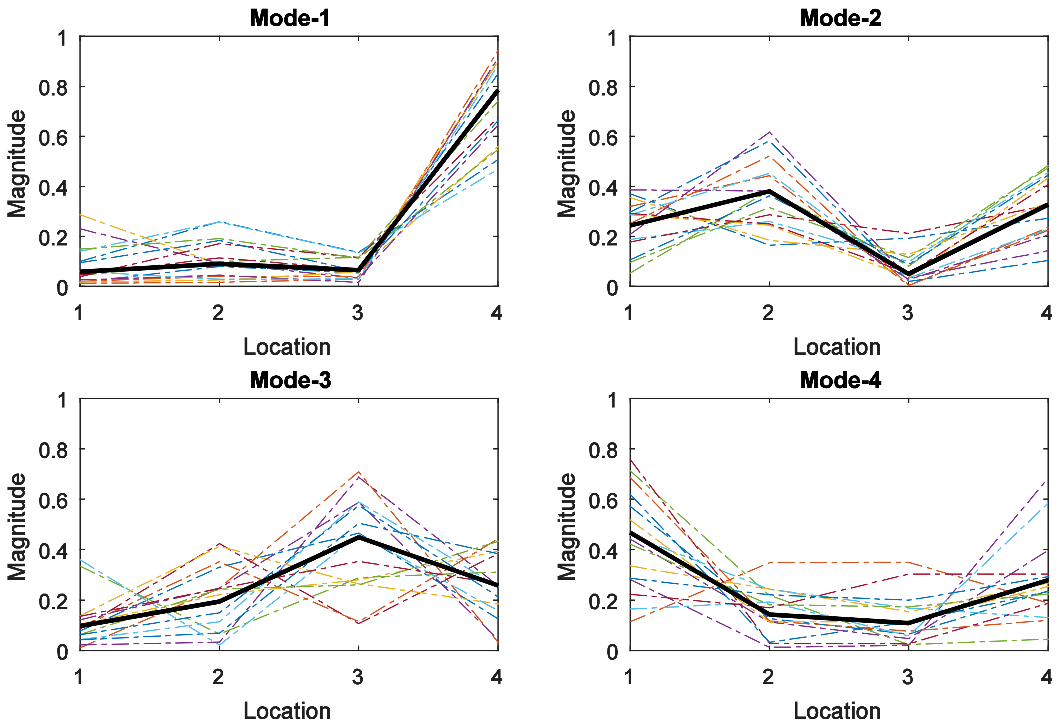

Figure (4.2) Mode shape components at the head (1), chest (2), pelvis (3), and legs (4) at the four resonance frequencies; dashed lines represent the individual subjects, and black solid lines represent the geometrical mean of the subjects

4.3. Inverse Modal Problem

4.3.1. Theoretical background

The equation of motion for a vibrating underdamped system with N degrees of freedom (DOF) can be written as

$$\mathbf{M}\ddot{\mathbf{u}}(t)+\mathbf{C}\dot{\mathbf{u}}(t)+\mathbf{K}\mathbf{u}(t)=\mathbf{0} \tag{4.1}$$

The mass matrix **M** and stiffness matrix **K** are real, symmetric, and positive definite, and the damping matrix **C** is real, symmetric, but can be positive definite or positive semi-definite.

The equation of motion is a differential equation that can be transformed to the algebraic form.

$$(\lambda_i^2\mathbf{M}+\lambda_i\mathbf{C}+\mathbf{K})\boldsymbol{\psi}_i=\mathbf{0} \tag{4.2}$$

where λ_i is the eigenvalue and $\boldsymbol{\psi}_i$ is the corresponding eigenvector.

It is assumed that all eigenvalues are complex and simple (non-repeated). Eq. (4.3) presents a transformation that changes the complex-value eigenpairs into real-value eigenpairs [11].

$$\mathbf{R} = diag\left(\frac{1}{\sqrt{2}}\begin{bmatrix} 1 & 1 \\ i & -i \end{bmatrix} \;, \cdots, \; \frac{1}{\sqrt{2}}\begin{bmatrix} 1 & 1 \\ i & -i \end{bmatrix}\right) \tag{4.3}$$

Eq. (4.2) can be written in terms of the real-value eigenpairs,

$$\mathbf{M}\tilde{\boldsymbol{\psi}}_t\tilde{\boldsymbol{\Lambda}}_t^{\,2} + \mathbf{C}\tilde{\boldsymbol{\psi}}\tilde{\boldsymbol{\Lambda}}_t + \mathbf{K}\tilde{\boldsymbol{\psi}}_t = \mathbf{0} \tag{4.4}$$

The semi-definite programming approach (SDP) was used in this work to solve the inverse modal problem of Eq. (4.4) for **M**, **K**, and **C**, such that the physical matrices satisfy certain requirements [58]. The SDP is an extension of linear programming (LP), which deals with symmetric matrices instead of scalars or vectors as unknowns [19].

4.3.2. Supine human model

A multi-DOF human model is used in this work as a basis for the computational analysis and validation. The results of the experimental modal analysis (shown in Table (4.1) and Figure (4.2)) indicated that the supine humans demonstrated four recognizable resonance frequencies in the vertical direction, in the frequency range of 0-20 Hz, where all body segments moved together. This information provided a guideline on the number of DOF that the supine human can have under this condition. Based on these results, a human model with four-DOF is presented in Figure (4.3).

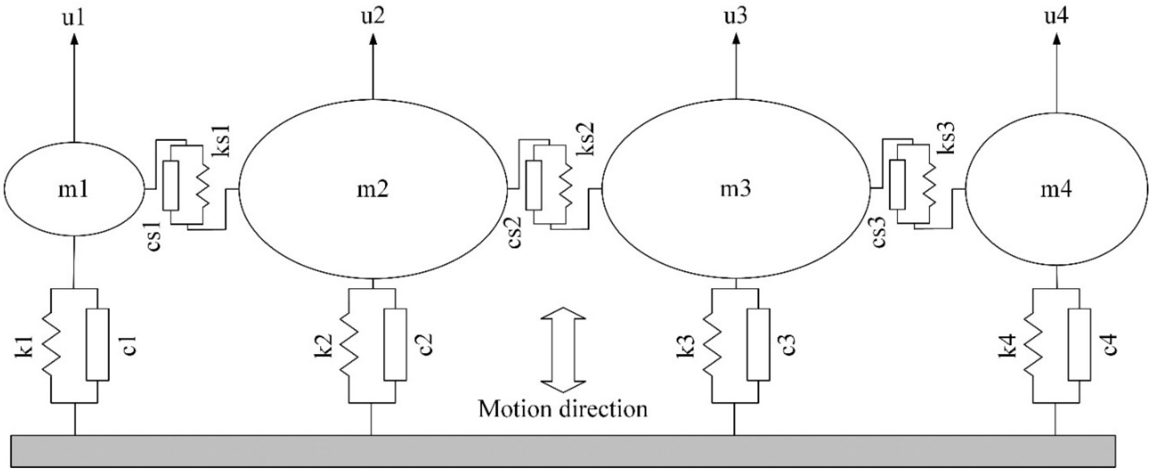

Figure (4.3) A four-DOF multi-body model of a supine human under vertical whole-body vibration

In this model, m_1, m_2, m_3, and m_4 represent the mass of the head, chest, pelvis, and legs, respectively. k_1, k_2, k_3, and k_4 represent the stiffness of the interface between the human body and the rigid support surface. c_1, c_2, c_3, and c_4 represent the damping coefficient of the interface surfaces. k_{s1}, k_{s2}, and k_{s3} represent the stiffness, in the vertical shear direction of the joints between the head and chest, chest and pelvis, and pelvis and legs, respectively. c_{s1}, c_{s2}, and c_{s3} represent the damping of the latter joints. The individual masses of the model are allowed to move in the vertical direction only in response to the input vertical vibration.

The unknown mass matrix **M**, damping matrix **C**, and stiffness matrix **K** of the proposed human model are shown in the following:

$$\mathbf{M}=\begin{bmatrix} m_1 & 0 & 0 & 0 \\ 0 & m_2 & 0 & 0 \\ 0 & 0 & m_3 & 0 \\ 0 & 0 & 0 & m_4 \end{bmatrix} \mathbf{C}=\begin{bmatrix} c_1+c_{s1} & -c_{s1} & 0 & 0 \\ -c_{s1} & c_2+c_{s1}+c_{s2} & -c_{s2} & 0 \\ 0 & -c_{s2} & c_3+c_{s2}+c_{s3} & -c_{s3} \\ 0 & 0 & -c_{s3} & c_4+c_{s3} \end{bmatrix}$$

$$\mathbf{K}=\begin{bmatrix} k_1+k_{s1} & -k_{s1} & 0 & 0 \\ -k_{s1} & k_2+k_{s1}+k_{s2} & -k_{s2} & 0 \\ 0 & -k_{s2} & k_3+k_{s2}+k_{s3} & -k_{s3} \\ 0 & 0 & -k_{s3} & k_4+k_{s3} \end{bmatrix}$$

4.3.3. Solution of the inverse modal problem for the physical parameters

Two nested optimization problems are solved [58] with the goal of minimizing the error between the calculated transfer functions (TR^C) and the experimental transfer function (TR^E). In the inner problem, SDP solves an optimization problem to predict **M**, **C**, and **K**, and it is defined as follows:

$$\text{Minimize } (M_{11}-1)^2$$

subject to: $\mathbf{M}\tilde{\boldsymbol{\psi}}_t\tilde{\boldsymbol{\Lambda}}_t^{\,2}+\mathbf{C}\tilde{\boldsymbol{\psi}}\tilde{\boldsymbol{\Lambda}}_t+\mathbf{K}\tilde{\boldsymbol{\psi}}_t \le \mathbf{T}$, $\mathbf{T}=t\mathbf{I}$, and the following constraints on the mass magnitude:

$$2.35 \le \frac{\text{torso mass}}{\text{head mass}} \le 4.03,\ \ 2.81 \le \frac{\text{pelvis mass}}{\text{head mass}} \le 4.81,\ \ 2.78 \le \frac{\text{legs mass}}{\text{head mass}} \le 4.77$$

where M_{11} represents the first element in the mass matrix, $\mathbf{I}_{N\times 2N}$ is the unit matrix, and *t* is a real scalar.

The upper and lower constraints on the different masses of the human body were selected based on the relationship between the different masses of the human body and the mass distribution [59] given in Table (4.2). The selection of the upper and lower limits is arbitrary, however, it encompasses the calculated magnitude of the mass ratio. For example, the ratio between the mass of the torso and head, based on the information in Table (4.2), is 3.358. Accordingly, the lower and upper limits were chosen to be 2.35 and 4.03 respectively.

Table (4.2) Mass distribution of human body

Segment	Description	Segment Mass/ Total Mass
Head	Head & Neck	0.081
Chest	Thorax, Shoulder & Upper Arms	0.272
Pelvis	Abdomen, Pelvis, Forearm Arms & Hands	0.325
Legs	Total Legs and Feet	0.322

The outer optimization problem is defined as:

$$\text{Minimize} \quad f_{\cos t} = \sum_{n=1}^{N} \left| Mag(TR_n^C) - Mag(TR_n^E) \right|$$

$$\text{Subject to} \quad -180^\circ \le \varphi_{mj} \le 180^\circ$$

where N is the segment's number, and φ_{mj} is the component j of the eigenvector phase angles for mode m.

All computations were done in MATLAB. Figure (4.4) shows a flow chart of the solution steps. The final solution for the physical parameters will be achieved when the number of optimization iterations exceeds 50 or the magnitude of $f_{\cos t}$ and the difference between TR^C and TR^E becomes $\varepsilon \le 0.05$.

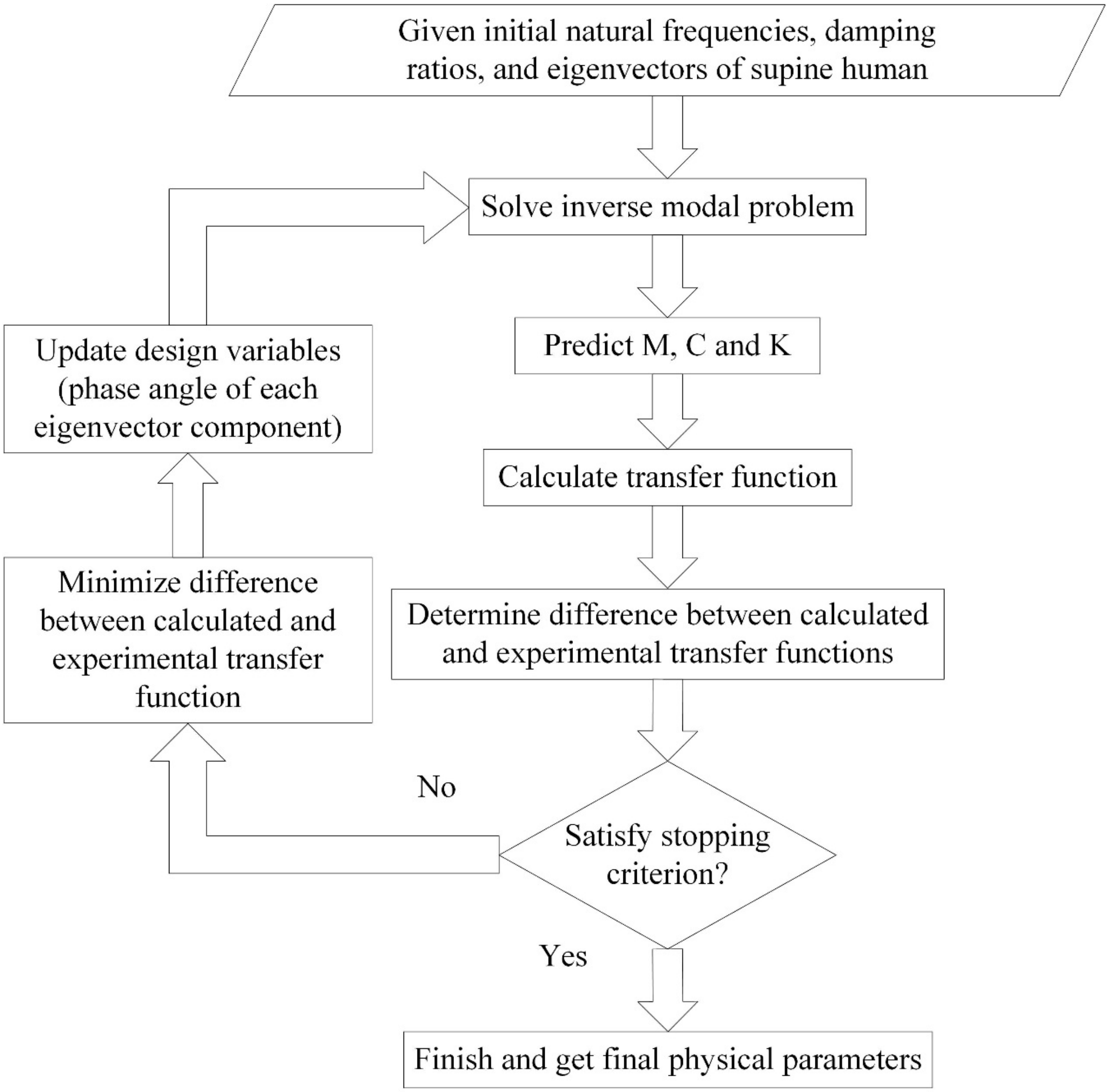

Figure (4.4) Flow chart showing the solution algorithm

4.4. Results

Figure (4.5) shows the geometrical mean of the magnitude of TR^E of the fifteen subjects and TR^E of the individual subjects [60]. The average mass (76.96 kg), the average natural frequencies, the average damping ratios, and the geometrical mean of the four mode shapes of the fifteen subjects were used as bases for the comparison with the predictive (calculated) model.

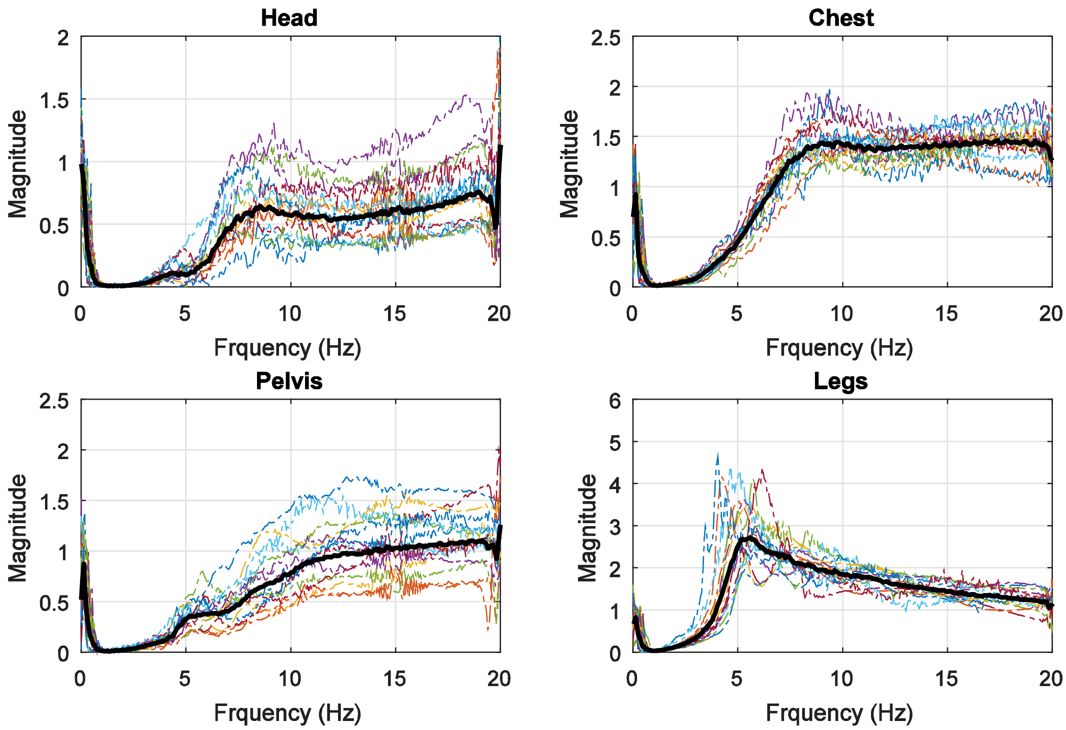

Figure (4.5) The magnitude TR^E of the individual subjects and the geometrical means (solid black line) of TR^E of the fifteen subjects across the frequency range of 0-20 Hz

The results of the proposed solution method show the following values for the damping and stiffness matrices.

$$\mathbf{M} = \begin{bmatrix} 6.2338 & 0 & 0 & 0 \\ 0 & 21.3693 & 0 & 0 \\ 0 & 0 & 30.0144 & 0 \\ 0 & 0 & 0 & 19.9488 \end{bmatrix} \mathbf{C} = \begin{bmatrix} 341.13 & -40.29 & 0 & 0 \\ 0 & 813.18 & -50.30 & 0 \\ 0 & -50.30 & 1434.80 & -266.96 \\ 0 & 0 & -266.96 & 428.26 \end{bmatrix}$$

$$\mathbf{K} = \begin{bmatrix} 61699 & -20992 & 0 & 0 \\ -20992 & 76065 & -36921 & 0 \\ 0 & -36921 & 190627 & -37109 \\ 0 & 0 & -37109 & 38169 \end{bmatrix}$$

Figure (4.6) shows the comparison between the experimental TR^E and the calculated TR^C transfer functions at the head, chest, pelvis, and legs based on the average physical parameters of the fifteen subjects.

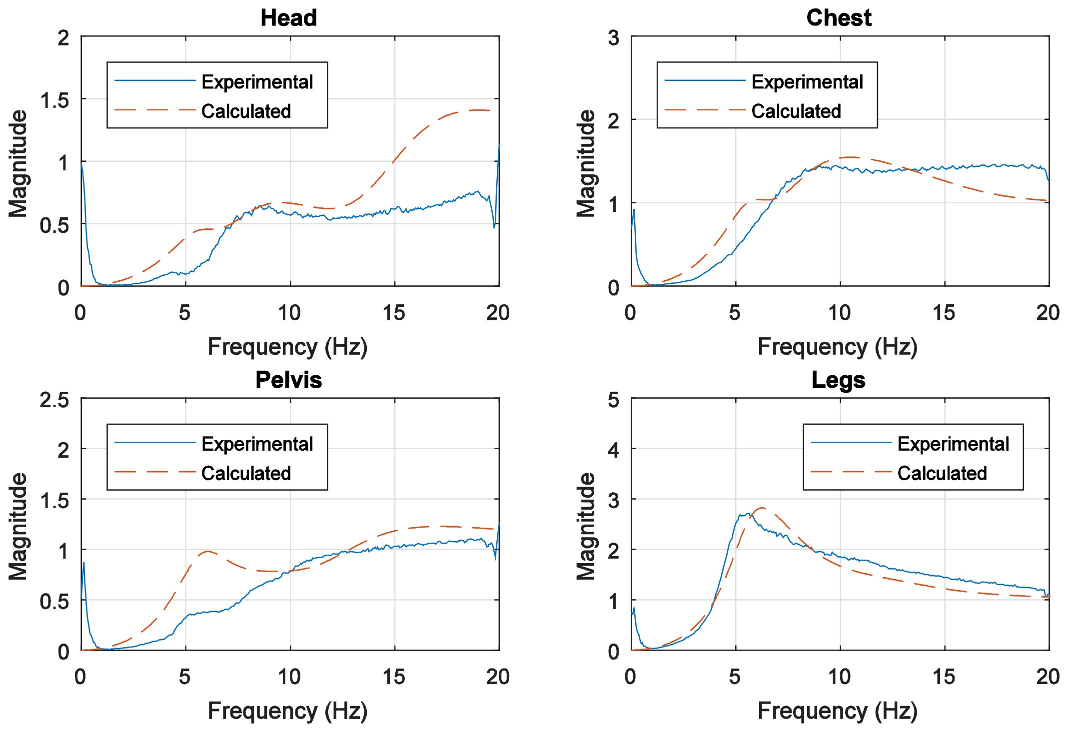

Figure (4.6) The experimental TR^E and the calculated TR^C transfer functions based on the average physical parameters of the fifteen subjects across the frequency range of 0-20 Hz

Table (4.3) shows the resulting resonance frequencies and damping ratios that are predicted by the model using the average physical parameters of the fifteen human subjects.

Table (4.3) The resulting modal frequency and damping ratio; the values in parentheses represent the resulting error with respect to the experimental solution

Mode Order	1	2	3	4
Undamped Natural Frequency (Hz)	5.8317 (14.7%)	8.3052 (6.4%)	13.5045 (22.7%)	16.2457 (5.4%)
Damping ratio	0.2568 (79.3%)	0.3518 (32.4%)	0.3015 (14.9%)	0.2711 (14.4%)
Damped Natural Frequency (Hz)	5.6361 (12.1%)	7.7742 (3.7%)	12.8761 (22.1%)	15.6373 (5.0%)

The magnitudes of the experimental and calculated eigenvectors predicted by the model are shown in Figure (4.7).

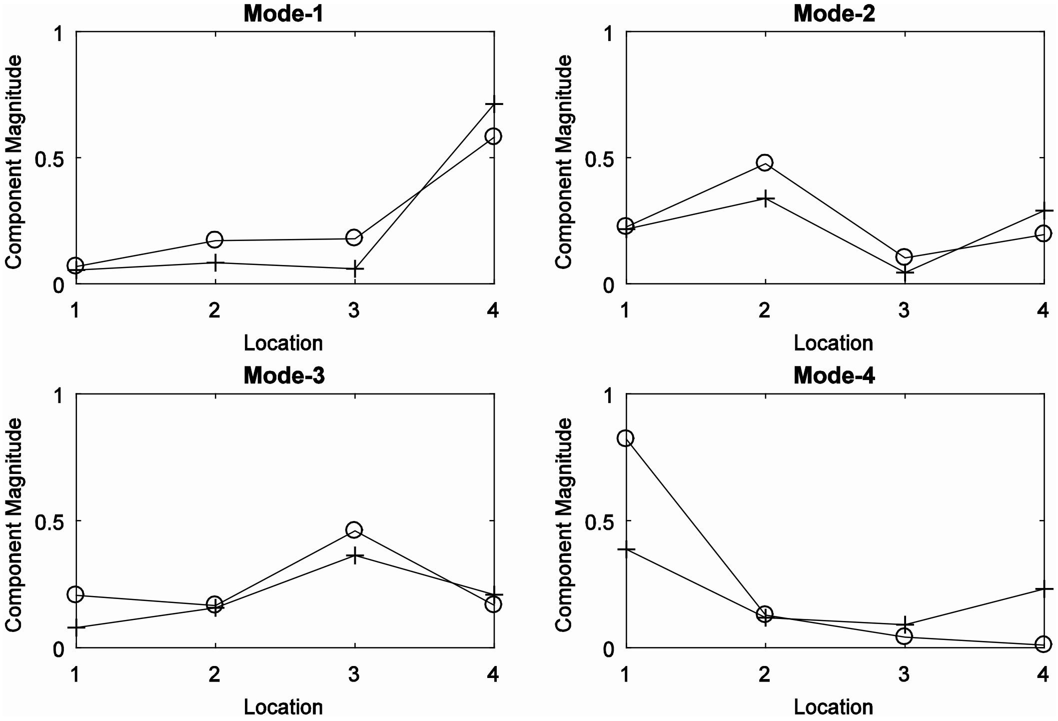

Figure (4.7) Magnitude of the experimental and calculated eigenvectors (○ - Calculated, + - experiment)

4.5. Validation

4.5.1. Physical parameters

In this section, the resulting predicted stiffness and damping coefficients of the supine human, shown in Table (4.4), will be compared to those available in the literature. To the author's knowledge, there is no information available in the literature regarding the damping parameters in the shear direction of the spine joints under dynamics loading. Therefore, the comparison will be based on the shear stiffness coefficients.

Table (4.4) The resulting predicted stiffness and damping components of the supine human body

Stiffness	k_1	k_2	k_3	k_4	k_{s1}	k_{s2}	k_{s3}
N/m	40707	18152	116596	1059	20992	36921	37109
Damping	c_1	c_2	c_3	c_4	c_{s1}	c_{s2}	c_{s3}
N·s/m	300.8	727.6	1122.5	161.3	40.3	45.3	267.0

Table (4.5) shows the average shear stiffness coefficients in different regions of the human spine based on the study by [61-64]. It should be noted that these values were based on experiments conducted on a bony spine, where the effects of muscles, viscera, and soft tissue were neglected.

Table (4.5) The average shear stiffness coefficients in the different regions of the spine

Regions of the Spine	Anterior Shear (N/m)	Posterior Shear (N/m)
Cervical	50000	53000
Thoracic	110000	110000
Lumbar	121000	170000
Lumbosacral	108000	189000

Table (4.6) shows the corresponding values of the shear stiffness coefficients of the intervertebral disc based on the studies by Markolf [65] and Moroney et al. [63].

Table (4.6) The shear stiffness coefficient of the intervertebral disc

Authors	Spine Region	Shear Stiffness (N/m)
Moroney et al., 1988	Cervical	60000
Markolf, 1970	Thoracic and lumbar	260000

4.5.2. Motion

The resulting stiffness and damping coefficients given in Table (4.4) are based on the average model. A methodology is presented in this section to scale the physical parameters of the average model to a specific subject as follows.

A biomechanical system can be described by its physical model by the mass matrix **M**, damping matrix **C**, and stiffness matrix **K**. The equation of motion of this system without external force can be given in a matrix form, as shown in Eq. (4.5).

$$\mathbf{M}\ddot{\mathbf{u}}(t) + \mathbf{C}\dot{\mathbf{u}}(t) + \mathbf{K}\mathbf{u}(t) = \mathbf{0} \tag{4.5}$$

If Eq. (4.5) is multiplied by a scalar α, then,

$$\alpha\mathbf{M}\ddot{\mathbf{u}}(t) + \alpha\mathbf{C}\dot{\mathbf{u}}(t) + \alpha\mathbf{K}\mathbf{u}(t) = \mathbf{0} \tag{4.6}$$

This new system keeps the same modal and frequency characters. So, if the mass of a specific subject is known, then the scaling parameter α can be calculated as shown in Eq. (4.7).

$$\alpha = m_s / m_a \tag{4.7}$$

where m_s and m_a are the mass of the specific subject and average model, respectively.

The response of the human's head, chest, pelvis, and legs under vertical random input acceleration will be used to validate the predicted values in the time domain using one subject. Figure (4.8) shows a comparison between the predicted acceleration and experimental acceleration at the head, chest, pelvis, and legs, for a specific subject during a period of 120 seconds.

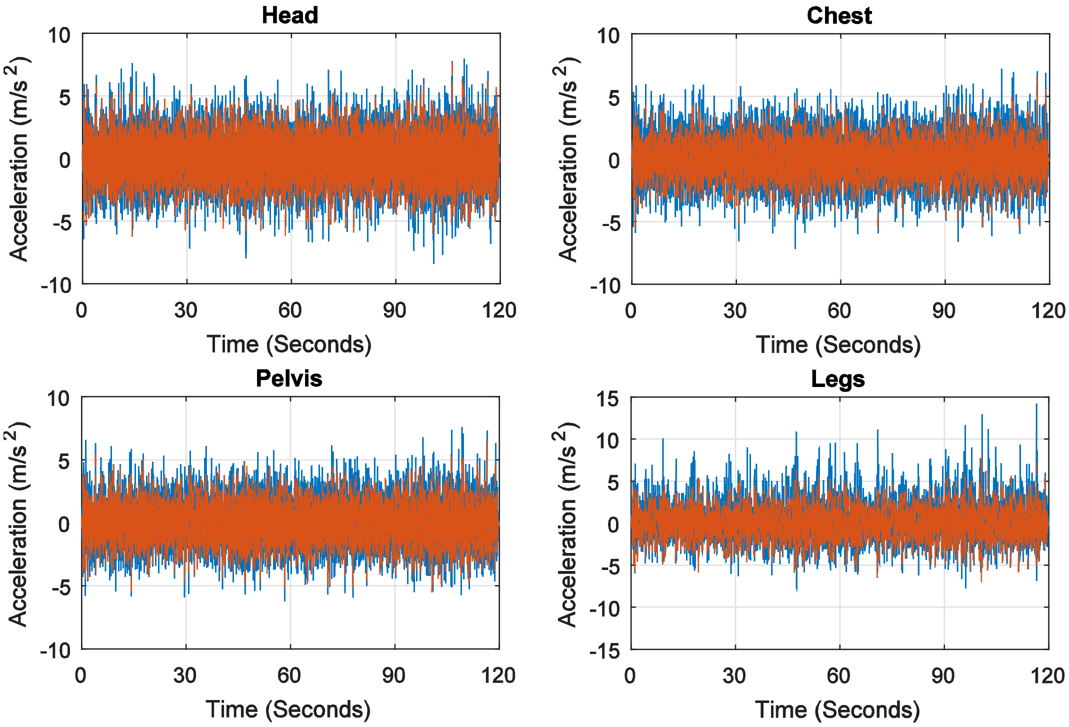

Figure (4.8) Time history of predicted acceleration and experimental acceleration at the head, chest, pelvis, and legs due to the input random vibration during the 120 second ride (blue solid line for experimental data, red dashed line for predicted data)

Figure (4.9) shows the resulting predicted acceleration time history for the time period of 10-13 seconds and the experimental acceleration at the head, chest, pelvis, and legs, respectively.

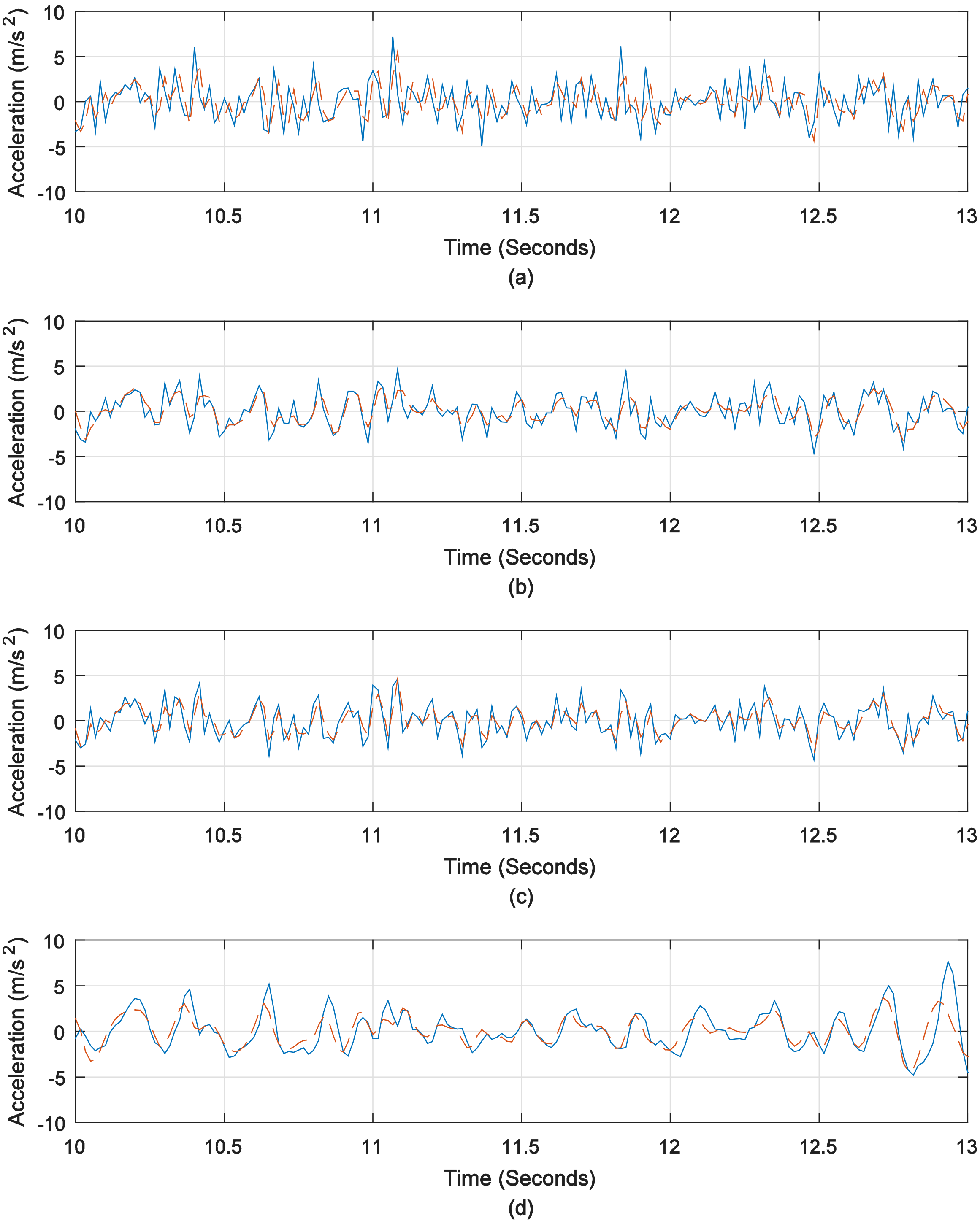

Figure (4.9) The resulting time history of predicted acceleration and experimental acceleration at the head, chest, pelvis, and legs, for the time period of 10-13 seconds (blue solid line for experimental data, red dashed line for predicted data)

4.6. Discussion and Conclusion

A methodology is presented in this work to predict the physical damping and stiffness parameters of supine humans under vertical whole-body vibration (WBV). The tested humans appeared to be relaxed during the experimentation, so it is likely that fewer muscle contributions were involved in the process and that the resulting physical parameters were closer to the passive values of the physical parameters. In addition, most human subjects followed the posture instructions during the experiments, so it is expected that the postures have less effect on the resulting modal parameters.

The modal analysis presents an excellent guide [53] to figure out how many DOF are required to model a supine human body. The experiments were very clear in pointing out four resonance frequencies in the frequency range of 0-20 Hz. Therefore, a four-DOF model, to a certain degree, is a realistic representation of how the supine human body responds to vertical vibration.

The resulting mass, stiffness, and damping matrices from the inverse modal problem preserve the positive or positive semi-definiteness, which presents a crucial requirement for any dynamics system. Also, the proposed method correctly preserved the out-of-diagonal zero elements in these physical matrices. This is an important contribution of the proposed method as the out-of-diagonal zero elements, which do not have any physical meaning, are presented in most of the predicted physical parameters in the literature.

The assumption of proportional damping, as normally used in the literature, can lead to normal modes and an easy way to normalize the eigenvectors. However, this assumption can be good for lightly damped systems but can lead to a loss of phase information and, ultimately, inaccurate physical information when used on biological systems. The usage of the complex modal shapes in this work is very important and is an obvious addition to the human response to vertical WBV, as the human body has considerable damping that can't be modeled using a proportional model.

The comparisons between the resulting modal parameters, which are based on the predicted damping and stiffness parameters of this work, have shown reasonable agreement with the experimental ones. The predicted transfer functions were close to those of the experiments at the different masses. The comparisons between the predicted acceleration of the model at the different masses have shown a very close trend to those of the experimental data. Considering the approximation that can take place during the modal analysis of the supine human and the error that was generated during this process, the proposed methodology of this work was able to find reasonable solutions.

The results demonstrated that the resulting shear stiffness coefficients at the cervical, thoracic, and lumbar spine were lower than those found in the literature. This comparison gives some idea about the physical parameters; however, it is by no means a direct comparison, as most parameters presented in the literature were based on the properties of the vertebras without the inclusion of the muscles, tissues, damping, and other living human materials that contribute to the shear stiffness of the human joints. Also, the literature provided a wide range of values due to the inconsistency between the different specimens and setups used in different works. Additionally, the current work goes beyond what is available in the literature in terms of predicting the damping properties of the human joints at the cervical, thoracic, and lumbar regions.

The proposed scaling process of this work successfully scaled the average model to different subjects and therefore can be considered a useful tool for subject-specific testing and comparison studies in future work. It should be noted that the scaling process is based on the assumption that the modal frequencies and mode shapes will remain the same for all subjects. This can be a weak assumption if the subject population has a large variance in the mass and shape of the subjects. More work will be done in the future to test the validity of this assumption.

CHAPTER 5. TIME AND FREQUENCY DOMAIN ANALYSIS OF SUPINE HUMANS UNDER VERTICAL WHOLE-BODY VIBRATION CONSIDERING THE FEET

5.1. Introduction

In Chapter 3 and Chapter 4, experimental modal analysis was conducted on the data measured at the head, chest, pelvis, and legs from fifteen human subjects. A four-degree-of-freedom (four-DOF) mass-damping-spring system was used to model the supine human in the analysis. With the latter format, the foot was considered as a part of the leg. This chapter investigates the effect of separating the foot from the leg and considering it as an additional lumped-mass component of the human body, i.e., considering the supine human as a five-DOF mass-damping-spring system. Natural frequencies, damping ratios, and mode shapes of the human body, including the feet, are determined using the time domain analysis. Analysis is conducted to investigate the differences between the motions of the feet and the legs and to determine whether there is value in considering the feet as a separate mass.

5.2. Methods

Referring to Chapter 3, the subjects were exposed to two types of vertical excitation, a sine-sweep vibration with increasing power (from 0.5 to 20 Hz, shown in Figure (3.2)) and a random vibration with frequency content (from 0.5 to 28 Hz, shown in Figure (3.3)), using a motion simulator (Moog ECU-624-1800, Moog-FCS, Ann Arbor, MI, USA). Subjects lay freely on a rigid platform on top of a thin rubber mat to avoid slippage on the metal surface of the platform as shown in Figure (5.1). In this chapter, the subjects will be tested under same conditions but with an additional inertial sensor attached at the medial malleolus of the right foot to measure its motion. The latter arrangement was done on ten out of the fifteen subjects used in this thesis.

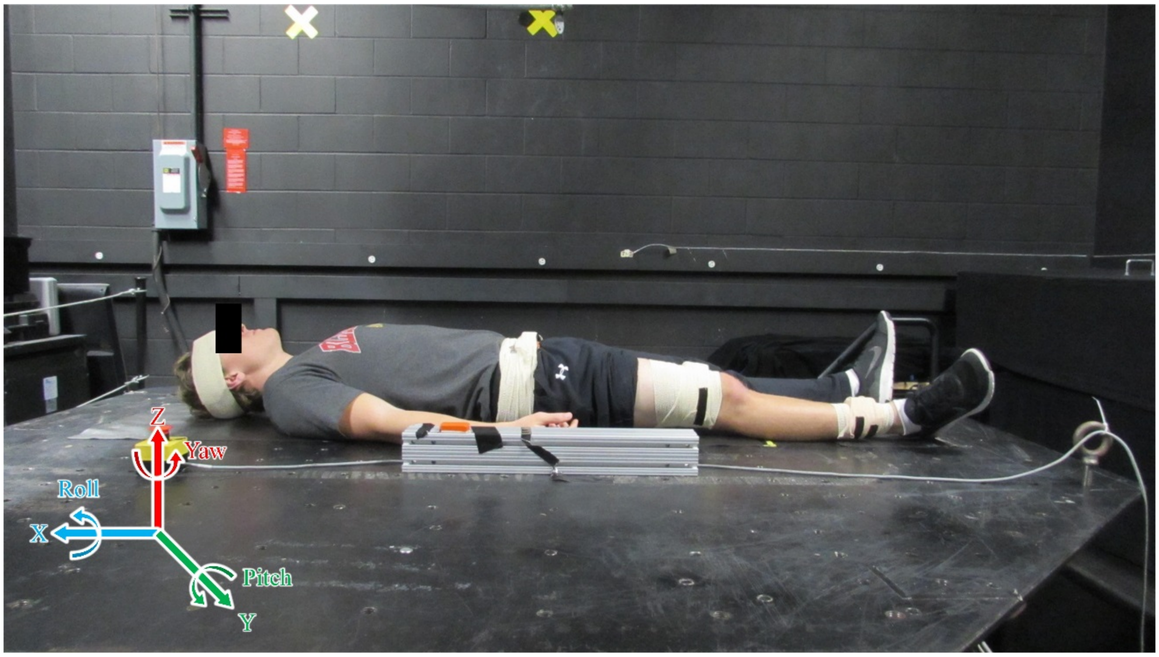

[redacted]

Figure (5.1) Profiles of the supine human testing: the human subject lay on the rigid platform of the motion simulator, and vibrations were generated in the vertical Z direction

A description of the theoretical background behind the experimental modal analysis can be found in Chapter 3. The transmissibility between different body segments is used here to evaluate their response to vibration, including the head, chest, pelvis, legs, and feet. The relative motion between the legs and the feet will be used here as a measure of the similarity and difference between their motions. The hypothesis here is that if the feet are moving in a similar way to that of the legs, then they can be lumped together and considered as one mass during modeling.

5.2.1. Analysis in the frequency domain

Transmissibility is a widely used transfer function for the biomechanical response under vibration [36, 39, 66-69]. In the case of base motion, the transmissibility between two output locations *k* and *l* can be defined in the frequency domain as the ratio between two responses at locations *k* and *l* relative to the base motion, such as

$$T_{kl}(\omega) = \frac{A_{kr}(\omega)}{A_{lr}(\omega)} \tag{5.1}$$

where $A_{kr}(\omega)$ is the Fourier transform of the acceleration $a_{kr} = a_{kg} - a_g$. a_{kr} is the acceleration at location *k* relative to the base motion, a_{kg} is its global acceleration, and a_g is the acceleration of base motion. In the same sense, $A_{lr}(\omega)$ is the Fourier transform of the acceleration $a_{lr} = a_{lg} - a_g$ at location *l*.

5.2.2. Analysis by Wavelet Transform

The Fourier transform is a great tool to transform a signal from the time domain into the frequency domain. However, it can only offer the overall frequency content of the signal. When the content of frequency in time domain needs to be considered, the wavelet transform presents a powerful way to locally decompose a signal into a time and frequency domain. The study of the wavelet is an extensive ongoing research area [70] and has been widely applied in different academic fields [71, 72].

The continuous wavelet transform (CWT) of a time series *f* can be defined as [73]

$$\tilde{f}(s,t) = \int_{-\infty}^{\infty} f(u)\bar{g}(\frac{u-t}{s})du \qquad (5.2)$$

where $\bar{g}(\frac{u-t}{s})$ is the complex conjugate of basic wavelet $g(u)$ localization at the time (*t*) and the scale (frequency, *s*).

The Morlet wavelet, as one type of CWT [70], is used here.

$$g(u) = \pi^{-1/4} e^{i\omega_0 u} e^{-u^2/2} \qquad (5.3)$$

where ω_0 is taken as 5 in practice.

The wavelet coherence can inspect the relationship in the time and frequency domain between two signals. The wavelet coherence *R* of two signals *x* and *y* can be defined as [74-76]

$$R^2 = \frac{\left|S(\tilde{f}_x^*(t,s)\,\tilde{f}_y(t,s))\right|^2}{S(\left|\tilde{f}_x(t,s)\right|^2)S(\left|\tilde{f}_y(t,s)\right|^2)} \tag{5.4}$$

where S is the smoothing operation in both the time and frequency domains [76].

Its wavelet coherence phase lag ϕ_{xy} is

$$\phi_{xy} = \arctan\left(\frac{\mathrm{Real}(S(\tilde{f}_x^*(t,s)\,\tilde{f}_y(t,s)))}{\mathrm{Imag}(S(\tilde{f}_x^*(t,s)\,\tilde{f}_y(t,s)))}\right) \tag{5.5}$$

where Real and Imag represent the real and imaginary parts, respectively.

5.3. Results

Figure (5.2a) shows the time history of the vertical acceleration at the feet of one subject, Subject 8, as a result of the vertical input sinusoidal motion at the rigid-platform level. Figure (5.2b) shows the relationship between the ARMAX model prediction and those of the experiments in the frequency domain for the feet for Subject 8. The information of the other nine subjects is given in Appendix C. For the experimental modal analysis including the feet, the measured data under the random excitation was used as supplement of the sine-sweep excitation when abnormal data appeared in the sine-sweep files.

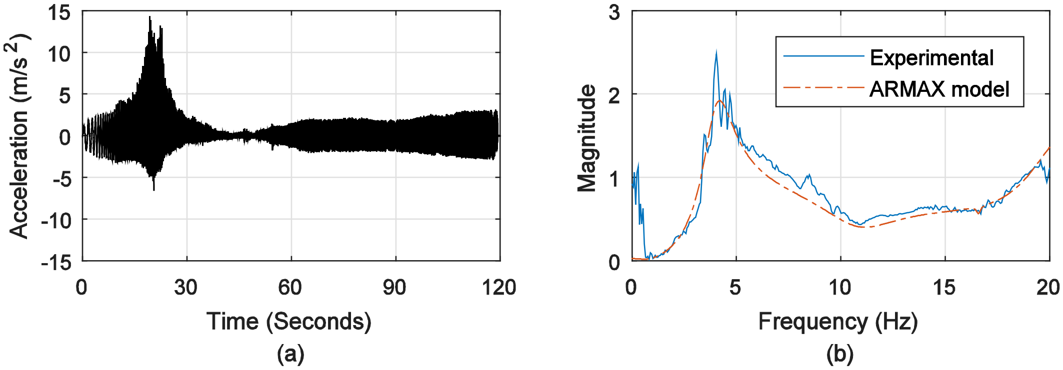

Figure (5.2) (a) Time history of the resulting vertical acceleration signals measured at the feet as a result of the vertical input sinusoidal motion of Subject 8, (b) EPFRF magnitude predicted by ARMAX and measured by the experiment

Table (5.1) Damped and undamped natural frequencies and damping ratios at the head, chest, pelvis, legs and feet levels of the ten participants

Subject	Mode Loc.	Undamped Natural Frequency (Hz)				Damping Ratio				Damped Natural Frequency (Hz)			
		1	2	3	4	1	2	3	4	1	2	3	4
Sub6	Head	4.0740	6.5001	X	14.2719	0.3204	0.2846	X	0.7135	3.8593	6.2313	X	9.9992
	Chest	4.5481	7.7686	11.3460	14.4497	0.3549	0.2735	0.1185	0.1182	4.2520	7.4724	11.2660	14.1914
	Pelvis	5.6095	8.2626	12.7421	X	0.1124	0.1444	0.3405	X	5.5739	8.1760	11.9806	X
	Legs	5.4096	6.8169	9.7782	15.2144	0.1182	0.3825	0.1440	0.1969	5.3717	6.2985	9.6763	14.9166
	Feet	5.1453	8.8488	X	17.3590	0.1931	0.2638	X	0.2259	5.0485	8.5355	X	16.9103
Sub7	Head	3.4491	7.6007	X	17.5394	0.1620	0.2227	X	0.2546	3.4035	7.4098	X	16.9616
	Chest	X	6.5165	9.2214	15.1961	X	0.2870	0.7603	0.0233	X	6.2424	5.9896	15.1923
	Pelvis	5.3943	7.1685	11.7013	X	0.1163	0.2719	0.3370	X	5.3578	6.8985	11.0169	X
	Legs	5.0437	7.0361	11.2084	13.3257	0.1065	0.0221	0.3238	0.1181	5.0150	7.0344	10.6047	13.2324
	Feet	4.7920	6.2543	10.9905	14.6654	0.1933	0.1305	0.1944	0.2710	4.7016	6.2008	10.7808	14.1166
Sub8	Head	3.6877	7.4190	9.1490	14.0546	0.1021	0.2456	0.0842	0.2022	3.6684	7.1918	9.1165	13.7643
	Chest	3.9310	8.6696	10.7360	X	0.1842	0.1823	0.0709	X	3.8637	8.5243	10.7090	X
	Pelvis	4.6570	6.6233	11.7139	X	0.1531	0.2924	0.2438	X	4.6021	6.3339	11.3606	X
	Legs	3.9657	9.5960	X	16.7086	0.1377	0.2319	X	0.0173	3.9279	9.3345	X	16.7061
	Feet	4.0547	X	10.8517	16.5943	0.1813	X	0.2526	0.0069	3.9875	X	10.4997	16.5939
Sub9	Head	3.9430	8.5976	X	16.4058	0.1160	0.1736	X	0.4230	3.9164	8.4670	X	14.8656
	Chest	4.4394	7.2559	12.7486	X	0.1477	0.3629	0.2697	X	4.3906	6.7613	12.2761	X
	Pelvis	4.7069	7.2801	11.1423	X	0.0767	0.0611	0.2776	X	4.6930	7.2665	10.7043	X
	Legs	4.7679	9.5520	13.2596	16.2376	0.1350	0.1216	0.2599	0.0923	4.7243	9.4811	12.8040	16.1682
	Feet	4.6697	9.1507	13.1557	X	0.1465	0.1301	0.1058	X	4.6193	9.0729	13.0818	X
Sub10	Head	X	8.2254	X	15.1439	X	0.3706	X	0.2934	X	7.6397	X	14.4772
	Chest	3.8627	6.9284	12.8276	16.2877	0.1012	0.2301	0.2904	0.1238	3.8428	6.7426	12.2748	16.1625
	Pelvis	5.0805	8.4072	13.8884	X	0.0763	0.1397	0.1885	X	5.0657	8.3248	13.6395	X
	Legs	4.8817	7.4278	10.4331	14.5080	0.1504	0.3080	0.1620	0.1978	4.8262	7.0666	10.2952	14.2214
	Feet	5.2149	X	10.8226	13.4523	0.1066	X	0.1459	0.0746	5.1852	X	10.7068	13.4149
Sub11	Head	4.2593	6.7424	8.8304	15.8906	0.1063	0.1446	0.1679	0.4305	4.2352	6.6715	8.7051	14.3424
	Chest	3.4758	7.5509	X	14.7284	0.1536	0.2759	X	0.0426	3.4346	7.2578	X	14.7150
	Pelvis	4.6095	X	10.3772	13.7045	0.0356	X	0.4545	0.0939	4.6066	X	9.2434	13.6440
	Legs	4.9279	8.0581	10.2457	16.8876	0.1135	0.1323	0.0994	0.3601	4.8961	7.9873	10.1949	15.7544
	Feet	4.8414	7.3563	9.4189	13.0506	0.1195	0.1401	0.0795	0.1932	4.8067	7.2837	9.3891	12.8048

Table (5.1.continued) Damped and undamped natural frequencies and damping ratio at the head, chest, pelvis, legs and feet levels of the ten participants

Sub12	Head	6.5357	X	10.3767	15.6271	0.1890	X	0.0344	0.0953	6.4179	X	10.3709	15.5559
	Chest	6.6180	8.5520	X	X	0.1651	0.4908	X	X	6.5272	7.4513	X	X
	Pelvis	4.9642	7.9292	10.6042	X	0.1753	0.1458	0.0616	X	4.8874	7.8444	10.5840	X
	Legs	5.1270	10.6549	11.6448	17.0070	0.1420	0.4273	0.0431	0.0196	5.0750	9.6331	11.6340	17.0037
	Feet	4.9798	X	10.0240	13.1562	0.1360	X	0.1730	0.2146	4.9335	X	9.8729	12.8496
Sub13	Head	4.5824	6.4917	9.3900	17.7374	0.1309	0.2433	0.5688	0.1868	4.5430	6.2966	7.7233	17.4250
	Chest	X	6.5662	10.8843	15.9415	X	0.4371	0.0899	0.2051	X	5.9058	10.8403	15.6026
	Pelvis	4.7469	7.3736	10.4138	16.4177	0.1035	0.1210	0.2755	0.0902	4.7214	7.3195	10.0108	16.3508
	Legs	4.8448	X	11.1430	16.9164	0.1334	X	0.1396	0.1930	4.8016	X	11.0340	16.5984
	Feet	4.9327	X	9.0569	14.2113	0.1366	X	0.1554	0.1926	4.8865	X	8.9469	13.9452
Sub14	Head	5.8617	8.5102	X	X	0.0752	0.2894	X	X	5.8451	8.1461	X	X
	Chest	X	6.6033	11.1640	14.2646	X	0.2950	0.1825	0.3243	X	6.3094	10.9766	13.4935
	Pelvis	5.8876	8.7782	11.7061	X	0.0805	0.2771	0.2336	X	5.8684	8.4343	11.3821	X
	Legs	6.0264	X	9.8997	14.7042	0.1046	X	0.1523	0.2375	5.9933	X	9.7842	14.2833
	Feet	6.0367	7.5090	11.0628	16.1228	0.1032	0.2891	0.0866	0.1983	6.0045	7.1884	11.0213	15.8027
Sub15	Head	5.5471	7.2561	X	12.7373	0.1107	0.2014	X	0.4176	5.5130	7.1075	X	11.5736
	Chest	4.9168	8.8410	X	X	0.3426	0.4015	X	X	4.6192	8.0973	X	X
	Pelvis	5.2214	6.8074	12.2428	X	0.1126	0.1352	0.3088	X	5.1882	6.7449	11.6446	X
	Legs	5.3237	7.4295	10.5491	13.6407	0.1762	0.1493	0.1541	0.2056	5.2404	7.3463	10.4231	13.3494
	Feet	5.5098	6.2200	11.1196	17.6482	0.1314	0.1418	0.1027	0.0890	5.4620	6.1571	11.0608	17.5782

Table (5.1) shows the resulting damped and undamped natural frequencies and damping ratios at the head, chest, pelvis, legs, and feet of the ten subjects under consideration. The missing components in Table (5.1) are marked by (X).

Figure (5.3) shows the resulting mode shapes of the ten tested subjects at the different segments on the human body. The horizontal axis represents the head (1), torso (2), pelvis (3), legs (4), and feet (5) segments. The vertical axis represents the magnitude of the component of each modal shape. In this figure, the geometrical mean modal shape of each mode is also given by black solid lines.

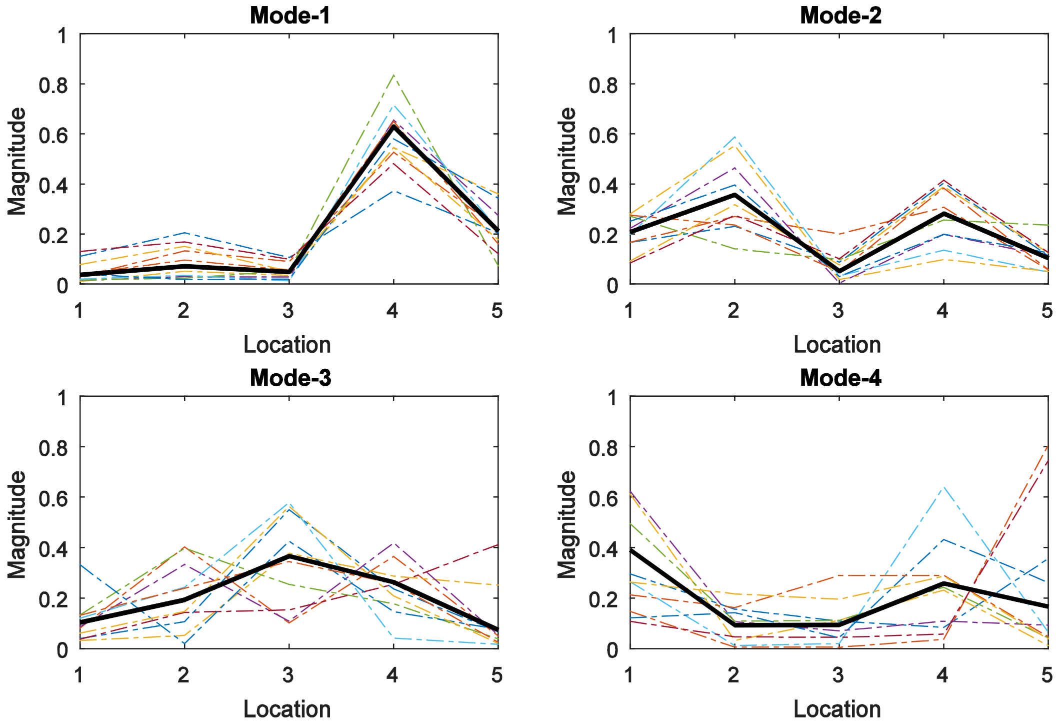

Figure (5.3) Mode shape components at the head (1), chest (2), pelvis (3), legs (4), and feet (5) at the four resonance frequencies. Dashed lines represent the individual subjects, and black solid lines represent the geometrical mean of the subjects

There are ten cases of transmissibility between different body segments, shown in Table (5.2). For example, Head-Chest represents the transmissibility of head to chest. Referring to Eq. (5.1), *k* is chest, *l* is head. At the same time, Chest-Head is not given because of the similar characteristics to that of the Head-Chest in Table (5.2). (X) in Table (5.2) means that the information will not be included in the study.

Table (5.2) Ten cases of transmissibility between different body segments including head, chest, pelvis, legs and feet of the supine human under vertical whole-body vibration

Location	Head	Chest	Pelvis	Legs	Feet
Head	X	Head-Chest	Head-Pelvis	Head-Legs	Head-Feet
Chest	X	X	Chest-Pelvis	Chest-Legs	Chest-Feet
Pelvis	X	X	X	Pelvis-Legs	Pelvis-Feet
Legs	X	X	X	X	Legs-Feet
Feet	X	X	X	X	X

The magnitude and phase of transmissibility for six subjects (Subjects 7-12) under vertical sine-sweep base motion of the different body segments (shown in Table (5.2)), are given in Figure (5.4) and Figure (5.5).

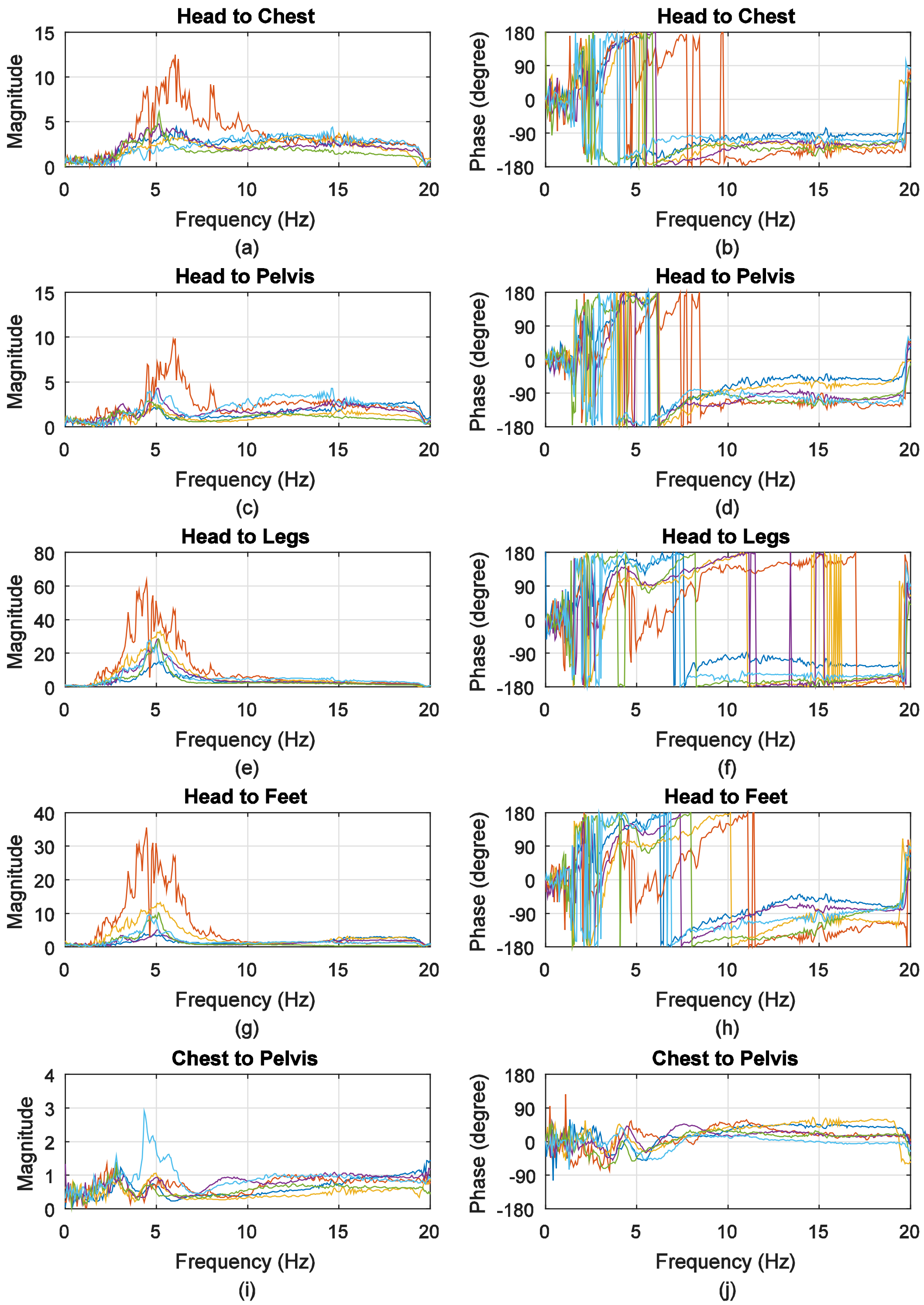

Figure (5.4) Transmissibility of, head to chest (a, b), head to pelvis (c, d), head to legs (e, f), head to feet (g, h), and chest to pelvis (i, j) of the six subjects

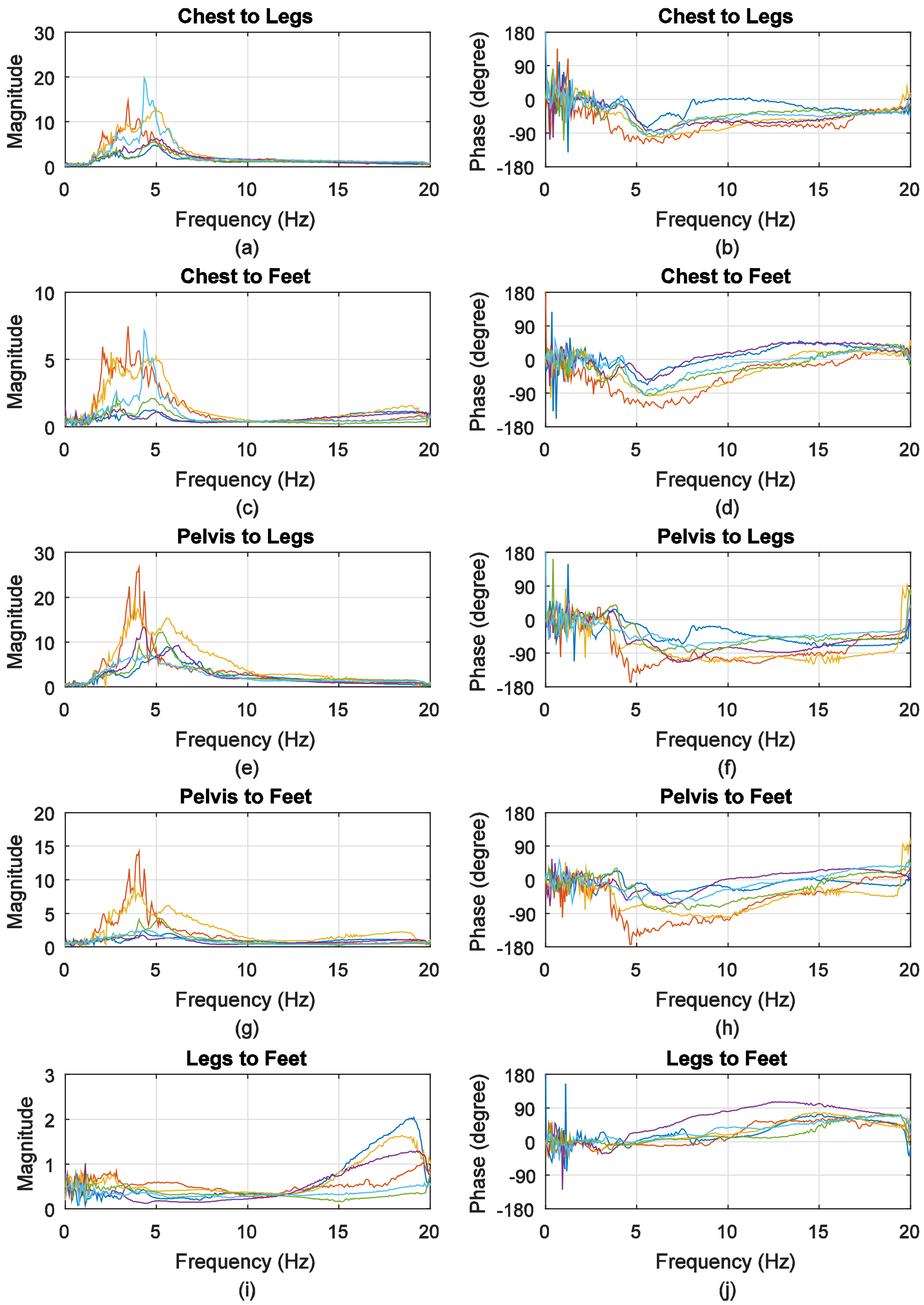

(a) (b) (c) (d) (e) (f) (g) (h) (i) (j)

Figure (5.5) Transmissibility of, chest to legs (a, b), chest to feet (c, d), pelvis to legs (e, f), pelvis to feet (g, h) and legs to feet (i, j) of the six subjects

Figure (5.6) shows the time history profile and its PSD of the input sine-sweep base motion.

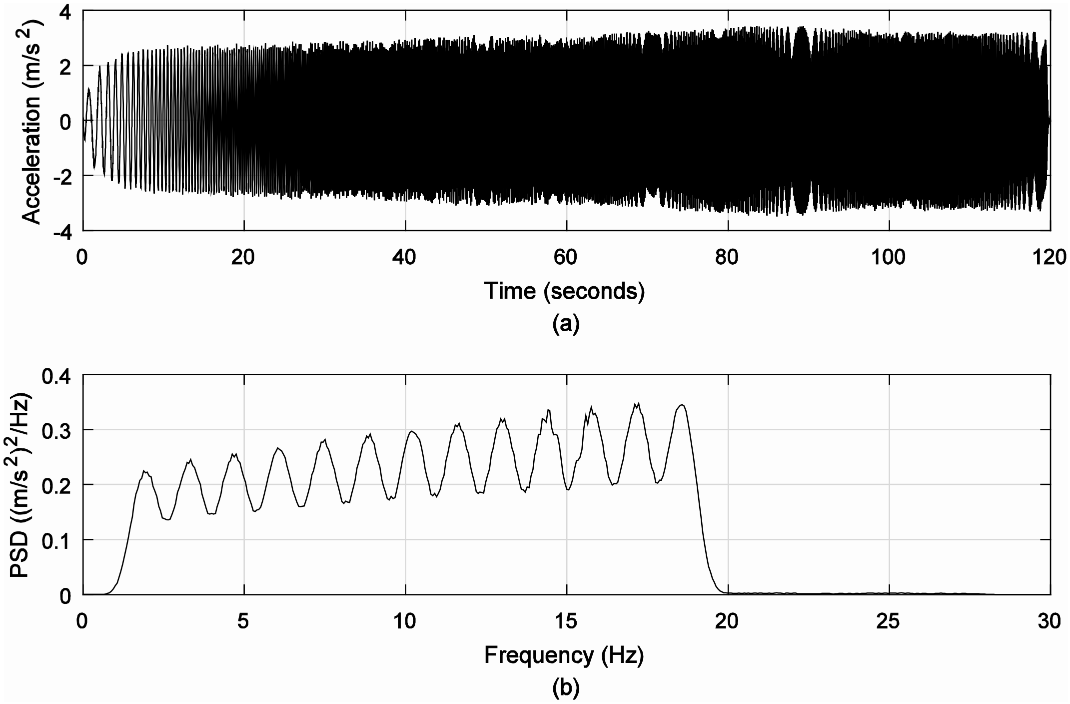

Figure (5.6) The input sine-sweep vibration during the 120 second ride: (a) the time history profile, (b) the power spectral density (PSD) of the signal for the frequency range from 0-30 Hz

Figure (5.7) shows the magnitude scalograms with the Morlet wavelet of the base motion acceleration and the head, chest, pelvis, legs, and feet accelerations relative to the base motion for Subject 8. The white dashed curve in each figure shows the cone of influence (COI), which indicates the edge effects [77]. The magnitude scalograms of other subjects are given in Appendix D.

Figure (5.7) also shows the locations of frequency intensity with time. For example, the base graph shows a continuous band of frequencies (the yellow band) that starts from 0.5 Hz and ends at 20 Hz. The head shows frequencies at the end side, indicating that it is more sensitive to that range of frequencies. The chest and pelvis show activities above 6 Hz, and the legs and feet show very similar activities.

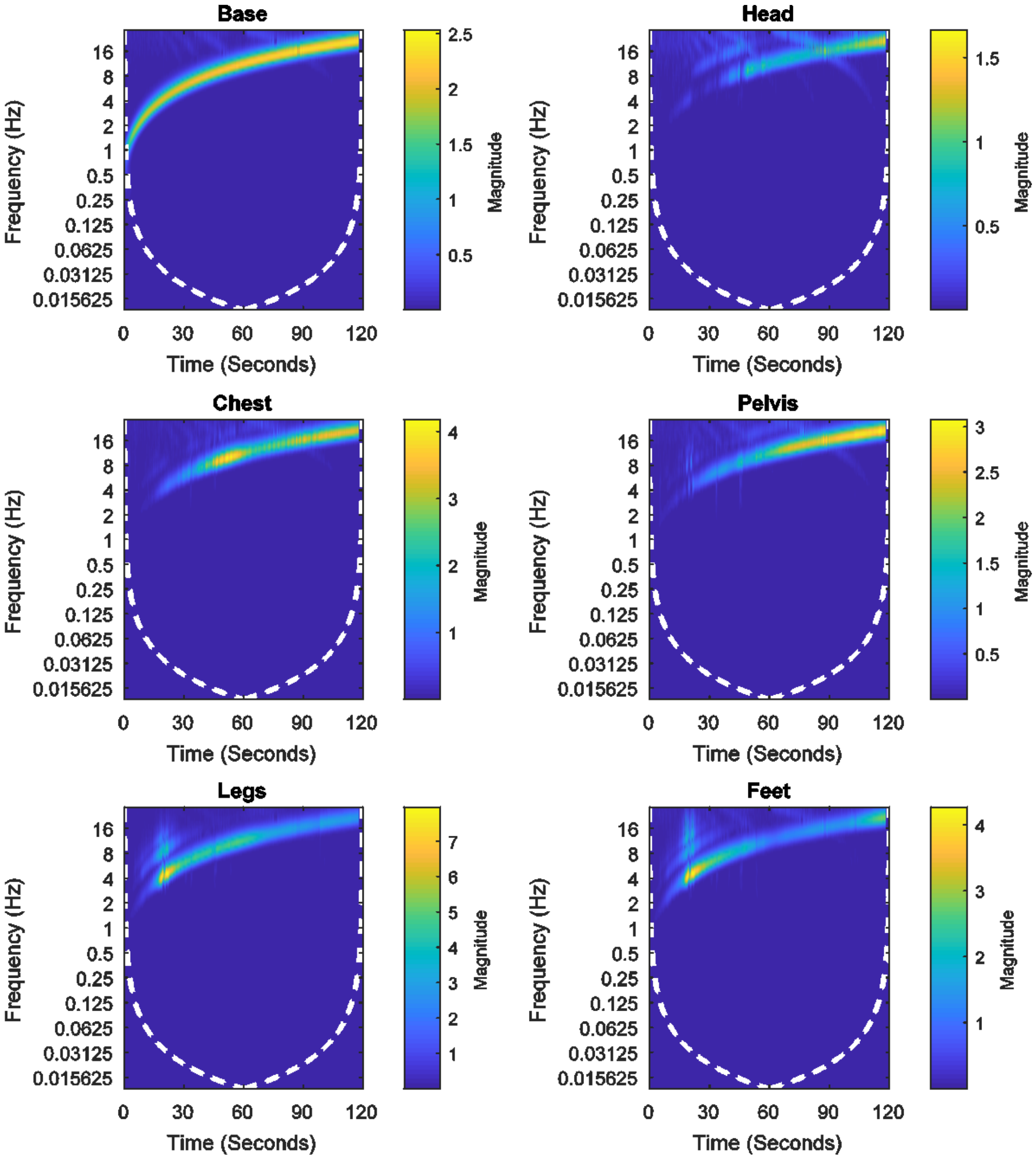

Figure (5.7) Magnitude scalogram with Morlet wavelet of the base motion acceleration and the head, chest, pelvis, legs, and feet acceleration relative to the base motion for Subject 8; the white dashed curve indicates the COI

Under the sine-sweep input base motion shown in Figure (5.7), the squared wavelet coherence between the acceleration of the legs and feet relative to the base motion for Subject 8 is plotted in Figure (5.8). The arrows at the area where the squared wavelet coherence is larger than 0.7, as shown by the colored bar on the right of Figure (5.8), are given to indicate the phase lag between legs and feet. The horizontal arrows indicate no lag between the motions of the segments, and the arrows with angles indicate a lag. The high magnitude of the wavelet transform band shown in Figure (5.7) is indicted by the red curves in Figure (5.8). The wavelet coherences between the acceleration of legs and feet relative to the base for the other subjects are shown in Appendix D.

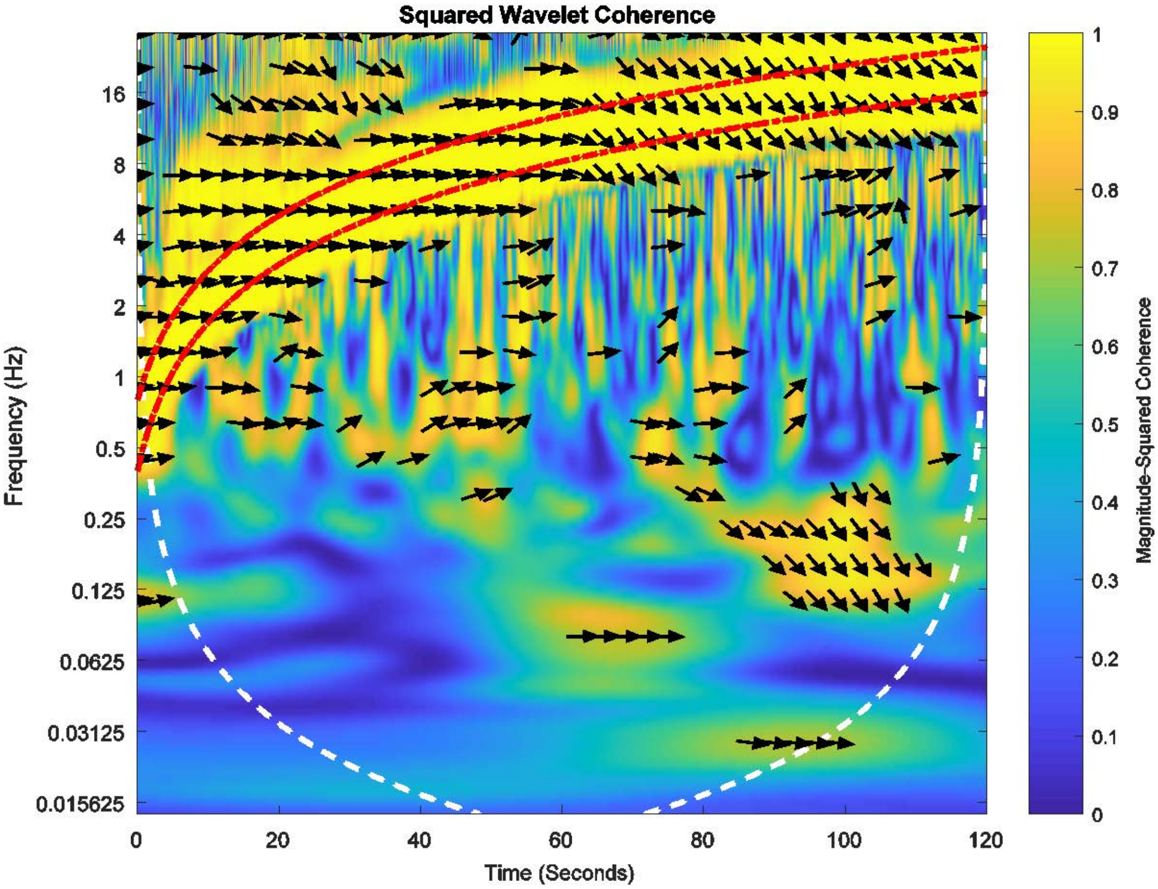

Figure (5.8) Squared wavelet coherence between the acceleration of the legs and feet relative to base motion for Subject 8; the white dashed curve indicates the COI, the red dashed curves indicate the high-value band of the base motion, and the direction of the arrows indicates the phase lag between legs and feet

5.4. Discussion

As shown in Table (5.1), only four modes can be identified in the frequency range of 0-20 Hz. Other modes can exist in that range of frequency, however, they may be indistinguishable using the current techniques. It can also be seen that the damping ratios from feet were comparable with the damping ratios from other body segments. From Figure (5.3), it’s obvious that the magnitude of the mode shape component at the feet was smaller than that at the legs under the four modes of the geometrical mean, and that the feet were moving in a similar direction to that of the legs.

Figure (5.4) and Figure (5.5) show distinct variations in the magnitude of the transmissibility between the different body segments at frequencies below 10 Hz; high peaks are obvious in the graphs. The transmissibility of the legs to feet for six subjects (Figure (5.5i), on the other hand, didn’t show obvious peaks below 15 Hz. In addition, the transmissibility magnitude for all subjects was lower than 1 at that range of frequency. Figure (5.5j) also showed no obvious differences between the phase of the feet relative to the legs as compared with the other segments in Figure (5.4) and Figure (5.5).

Besides the overall frequency analysis using the transmissibility of the legs to feet, the relationship between these two body segments can be analyzed locally in the time and frequency domain by the wavelet transform. There were six subjects in the transmissibility analysis and wavelet transform analysis. Inside the band where the sine-sweep of the base motion contained the particular dominant frequency with time, shown in Figure (5.7) and indicted by red curves in Figure (5.8), the wavelet coherence between legs and feet stayed close to 1. This means that these two body segments have a strong coherence in the frequency range of 0-20 Hz. In addition, it’s clear that, in the first 60 seconds (when the sine-sweep base motion shifted from 0 to 10 Hz in frequency domain), the orientation of the arrows was toward the right, indicating no phase lag between the legs and feet. This phase relationship can be verified by the phase of the transmissibility of the legs to feet shown in Figure (5.5j) in the frequency range of 0-10 Hz. Similarly, after the first 60 seconds (when the sine-sweep base motion shifted from 10 to 20 Hz in the frequency domain), the orientation of the arrows showed that there was a phase shift and then the phase lag stayed around 55° for the legs with respect to the feet.

Generally, there was a phase shift after 60 seconds and 10 Hz among the six subjects. This indicates that during the vertical input base motion vibration, with a low frequency content (0-10

Hz), the legs and feet moved together without obvious phase lag between them. In the relatively higher-frequency motion (10-20 Hz), the legs had a phase lag behind the feet.

5.5. Conclusion

When the feet were considered as an additional segment by separating them from the legs, five inertial sensors were attached to five locations at well-spaced distances along the supine human body. Still, the experimental modal analysis showed only four modes in the frequency range of 0-20 Hz.

The transmissibility with the legs and feet showed similar behavior in magnitude and phase among the six subjects. The wavelet coherence between the legs and feet kept a large value with a stable phase except with a phase shift just after 60 seconds and 10 Hz. This phase shift can also be tracked by the phase of the transmissibility of the legs to feet.

Given all of that, it is suggested that the two human body segments, the legs and feet, be modeled as one rigid segment for the consideration of supine human models under vertical whole-body vibration (WBV). Because the mass ratio of feet to legs is 9.9% [59], it’s reasonable to lump the legs and feet together for further analysis, in the frequency range of 0-10 Hz, under vertical WBV.

CHAPTER 6. FUTURE WORK

The following issues will be studied in future work.

6.1. Analysis Including Angular Motion

In this work, the experimental modal analysis of supine humans was conducted under vertical whole-body vibration (WBV). The subjects were exposed to two types of vertical vibration: a sine-sweep vibration and a random vibration. Only vertical motions were considered in this work; rotational motions were not included in the analysis. Future work will consider investigating human response under rotational input motions.

6.2. Analysis Including Nonlinear Behaviors

For the supine human, all the analysis and modeling were conducted based on the linearity assumption. However, nonlinear factors, such as the contributions from internal viscera, soft tissues, and muscles, cannot be ignored. Furthermore, the effect of vibration magnitude was also not taken into consideration. Taking these nonlinear factors into consideration is a challenge that can be considered in future work.

6.3. Complex Model Considering Angular Motion

In Chapter 4, a four-DOF model of a supine human was presented. In this model, for each human body segment, only the vertical translational motion was considered; angular motion was not considered. Because of the geometry and connectivity between different human segments, rotational motions are expected to take place even under vertical input motions. Therefore, a more complex model than that of a four-DOF model seems necessary to consider the angular motion of the supine human. Future work will consider the effect of including the angular motion of the segments in the analysis.

APPENDIX A: TIME HISTORY AND TRANSMISSIBILITY OF THE RESULTING VERTICAL ACCELERATION OF THE INDIVIDUAL SEGMENTS

The time history of the resulting vertical accelerations of individual segments and their transmissibility magnitude and phase are shown below for the other fourteen subjects.

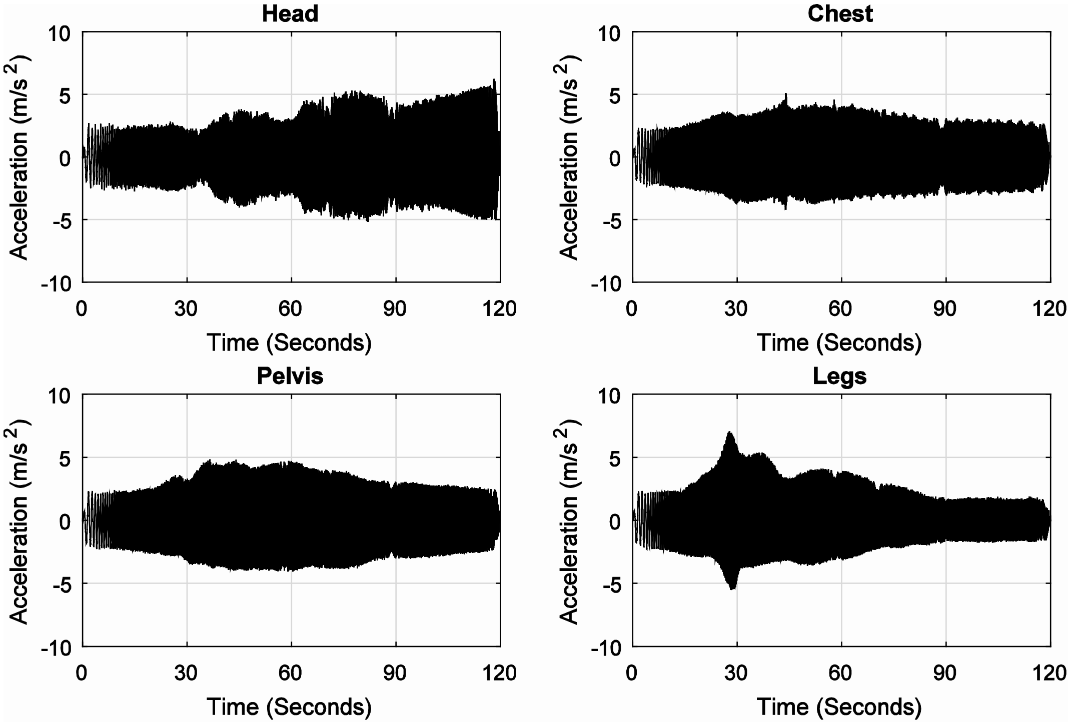

Figure (A.1) Time history of the resulting vertical acceleration signals measured at the head, chest, pelvis, and legs as result of the vertical input sinusoidal motion of Subject 1

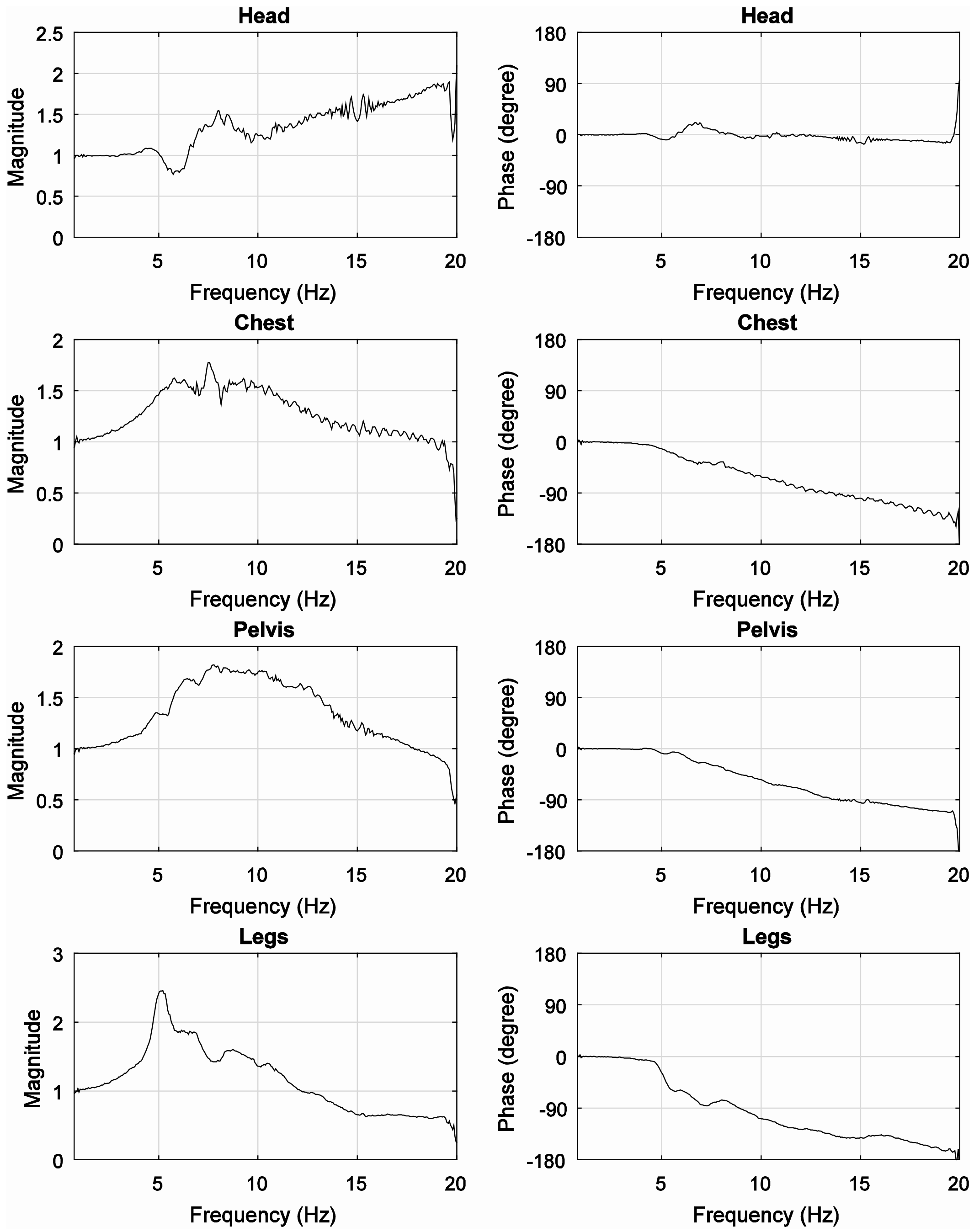

Figure (A.2) Transmissibility magnitude and phase between the vertical output motion at the head, chest, pelvis, and legs of Subject 1, and the vertical input sinusoidal motion at the rigid-base level

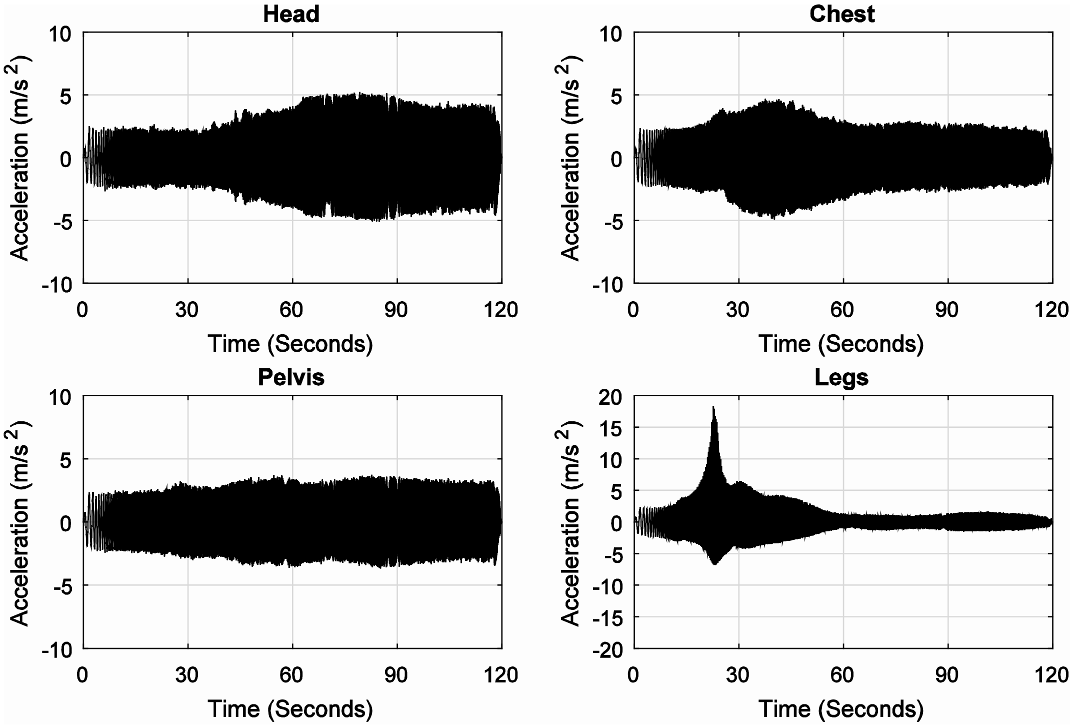

Figure (A.3) Time history of the resulting vertical acceleration signals measured at the head, chest, pelvis, and legs as result of the vertical input sinusoidal motion of Subject 2

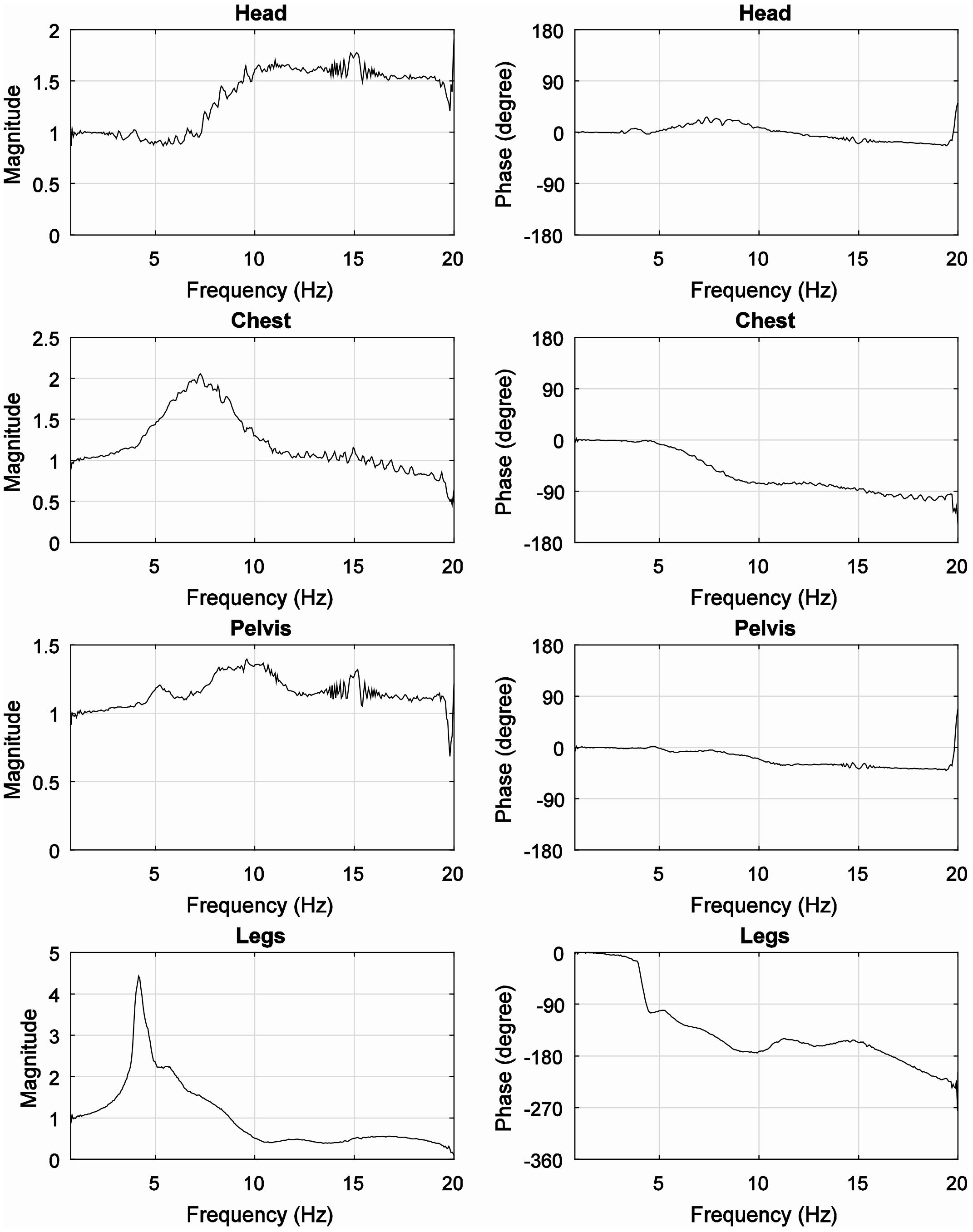

Figure (A.4) Transmissibility magnitude and phase between the vertical output motion at the head, chest, pelvis, and legs of Subject 2, and the vertical input sinusoidal motion at the rigid-base level

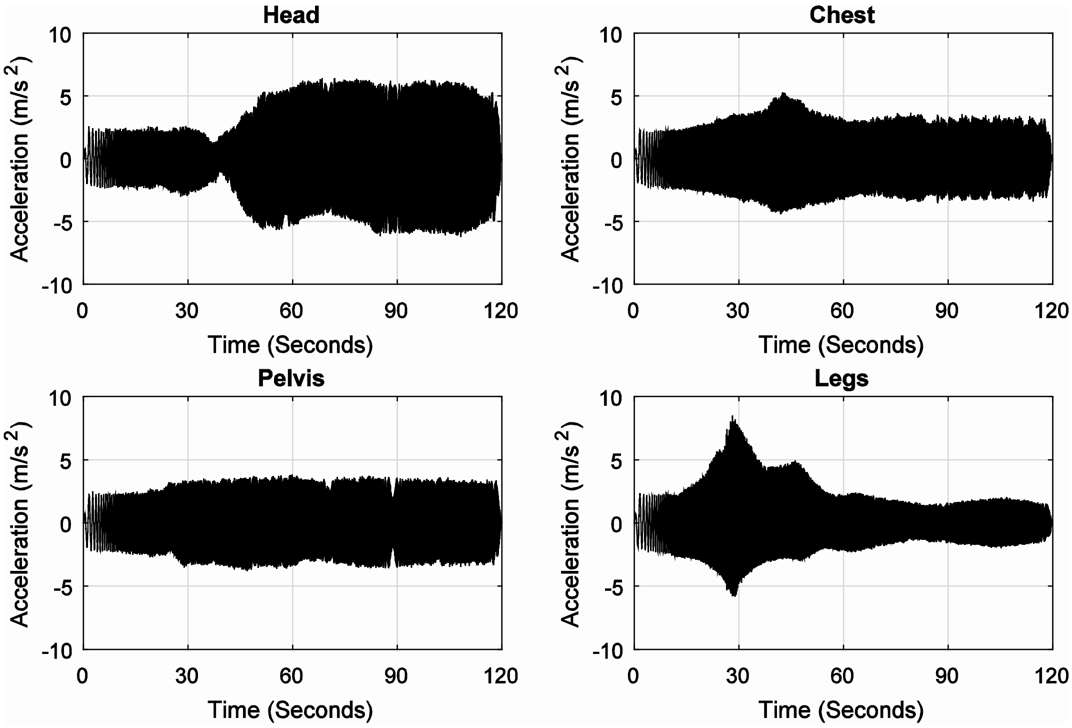

Figure (A.5) Time history of the resulting vertical acceleration signals measured at the head, chest, pelvis, and legs as result of the vertical input sinusoidal motion of Subject 4

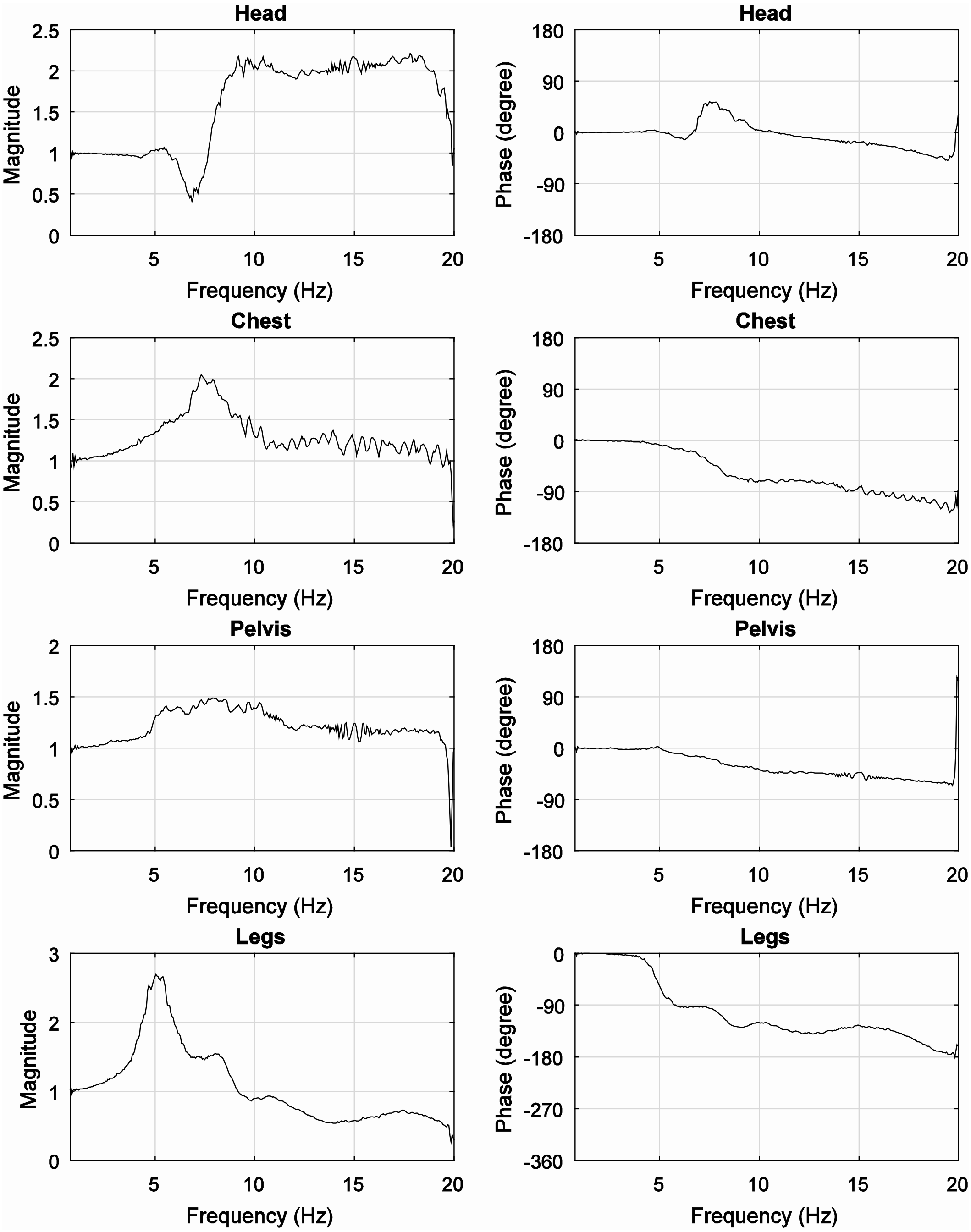

Figure (A.6) Transmissibility magnitude and phase between the vertical output motion at the head, chest, pelvis, and legs of Subject 4, and the vertical input sinusoidal motion at the rigid-base level

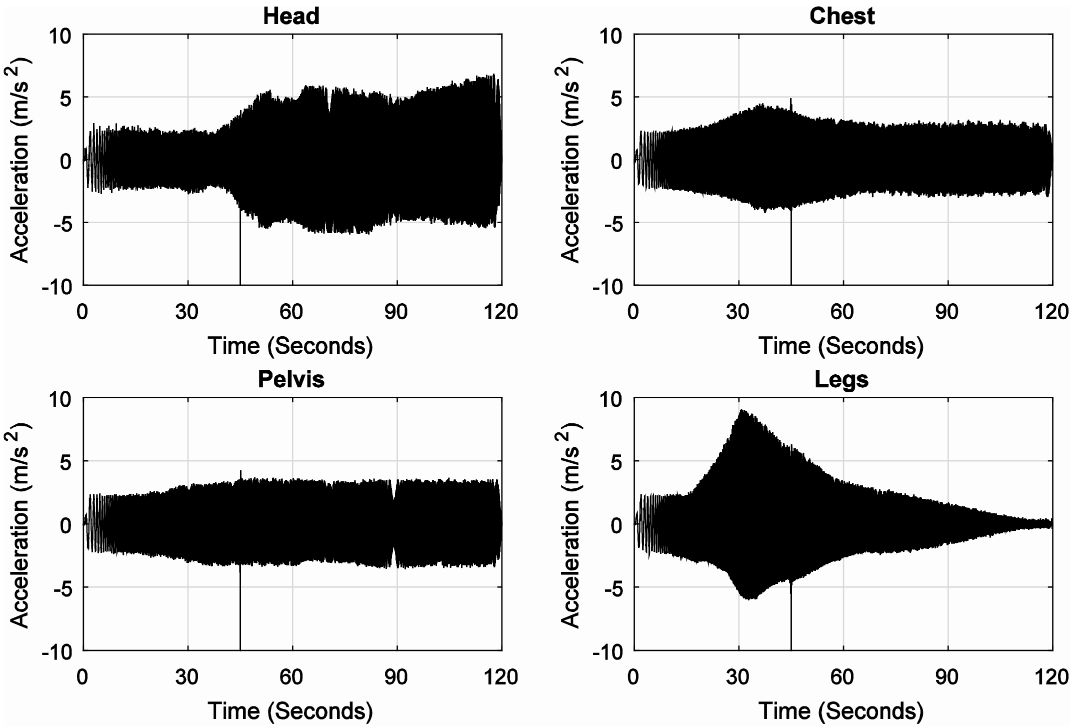

Figure (A.7) Time history of the resulting vertical acceleration signals measured at the head, chest, pelvis, and legs as result of the vertical input sinusoidal motion of Subject 5

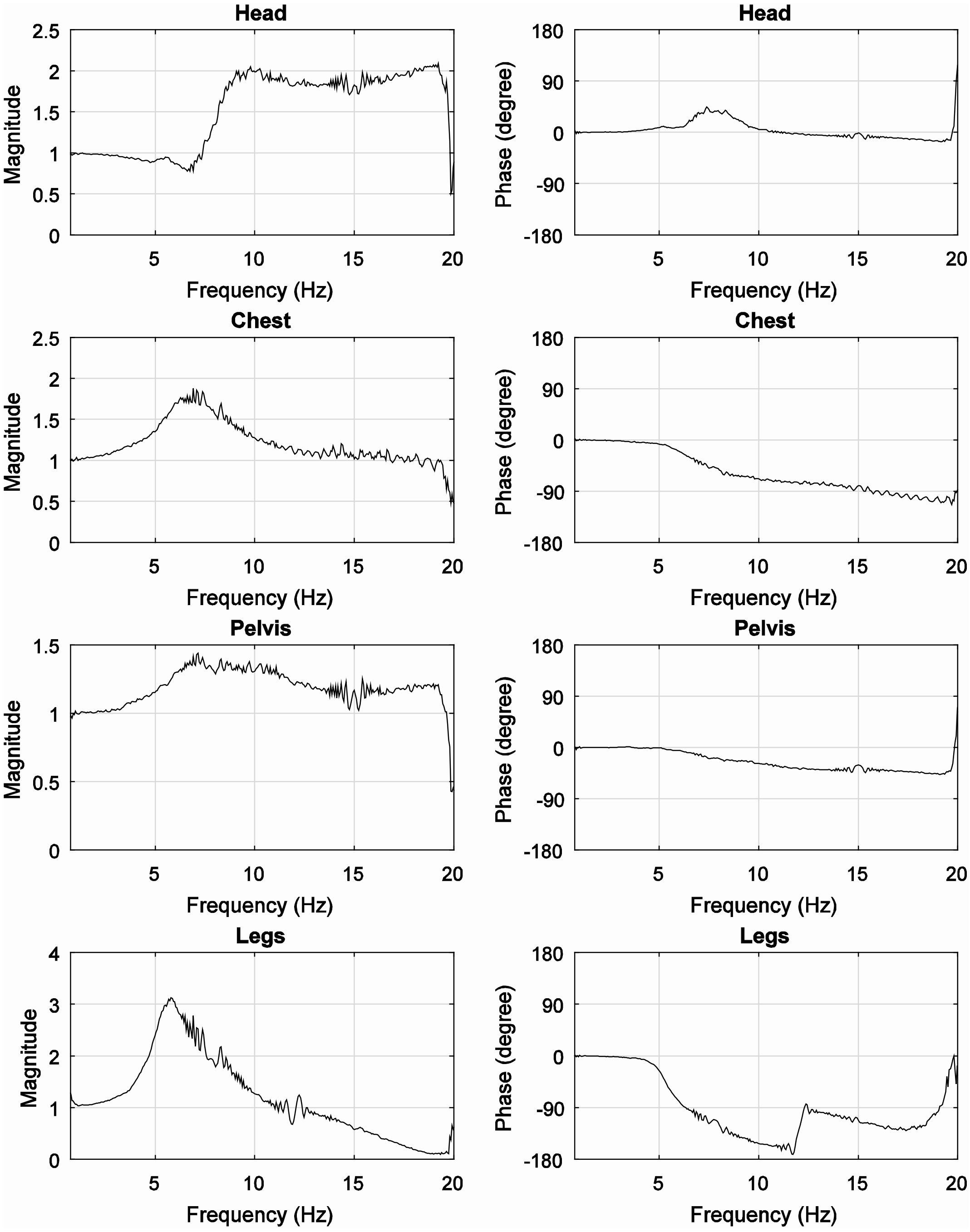

Figure (A.8) Transmissibility magnitude and phase between the vertical output motion at the head, chest, pelvis, and legs of Subject 5, and the vertical input sinusoidal motion at the rigid-base level

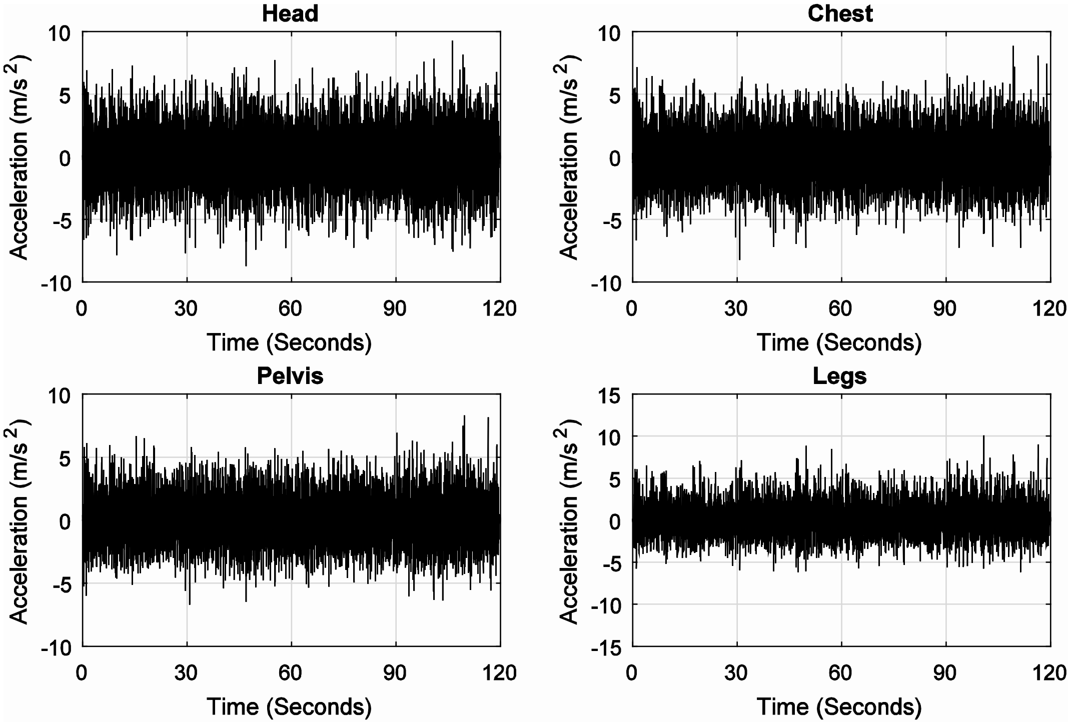

Figure (A.9) Time history of the resulting vertical acceleration signals measured at the head, chest, pelvis, and legs as result of the vertical input random motion of Subject 6

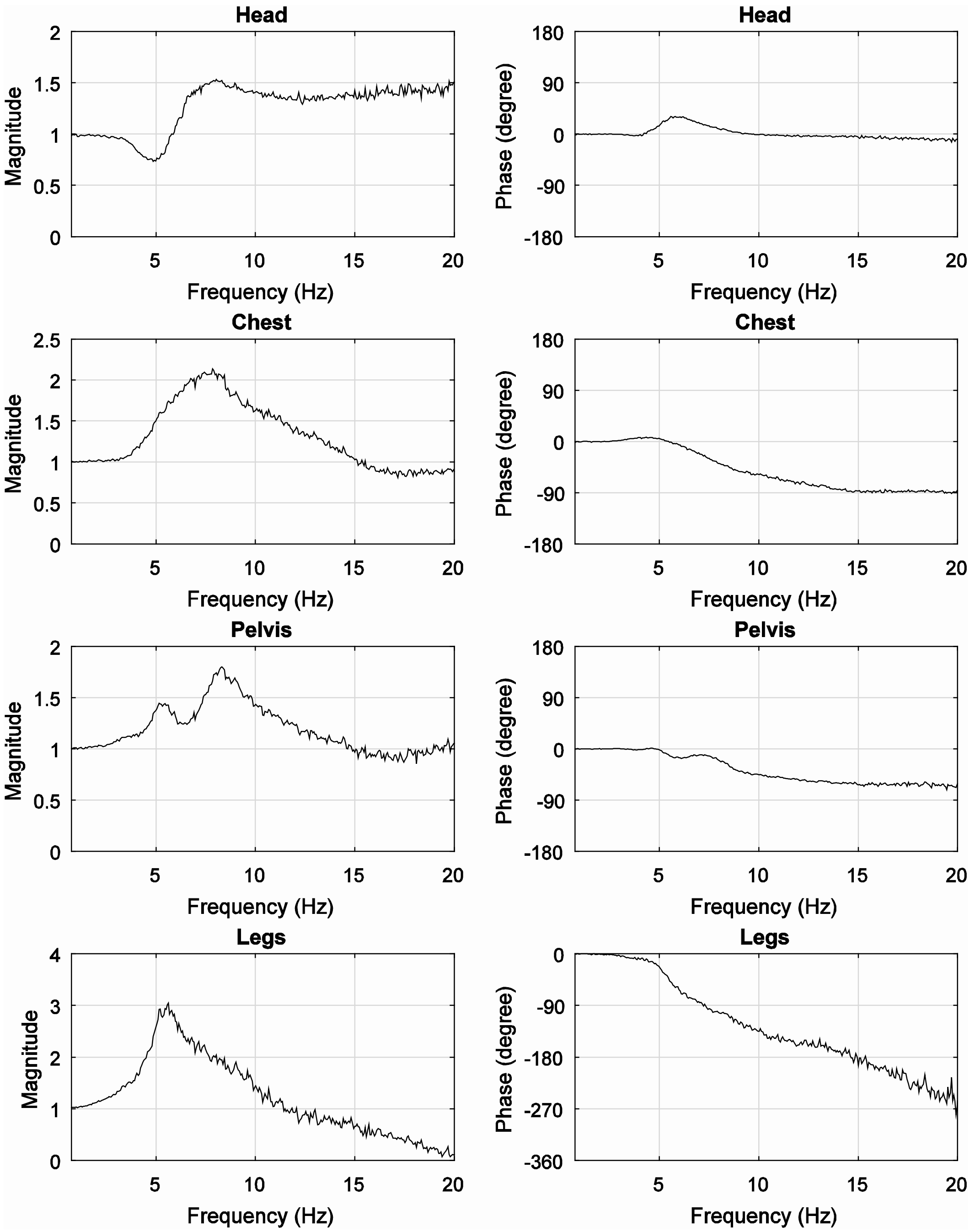

Figure (A.10) Transmissibility magnitude and phase between the vertical output motion at the head, chest, pelvis, and legs of Subject 6, and the vertical input random motion at the rigid-base level

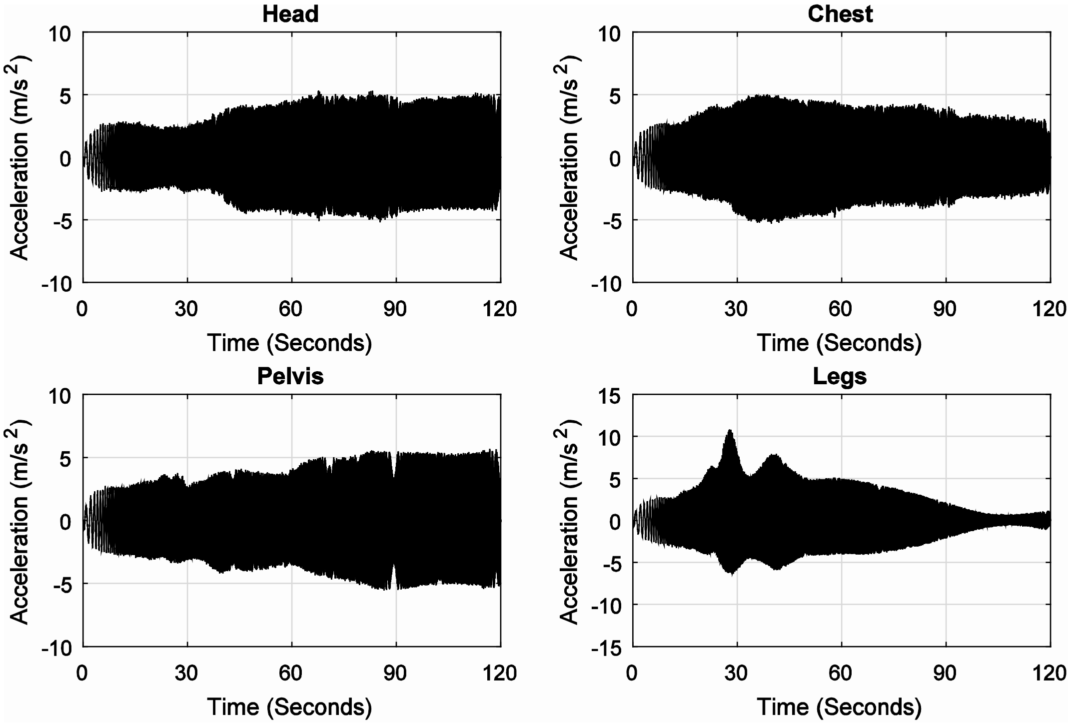

Figure (A.11) Time history of the resulting vertical acceleration signals measured at the head, chest, pelvis, and legs as result of the vertical input sinusoidal motion of Subject 7

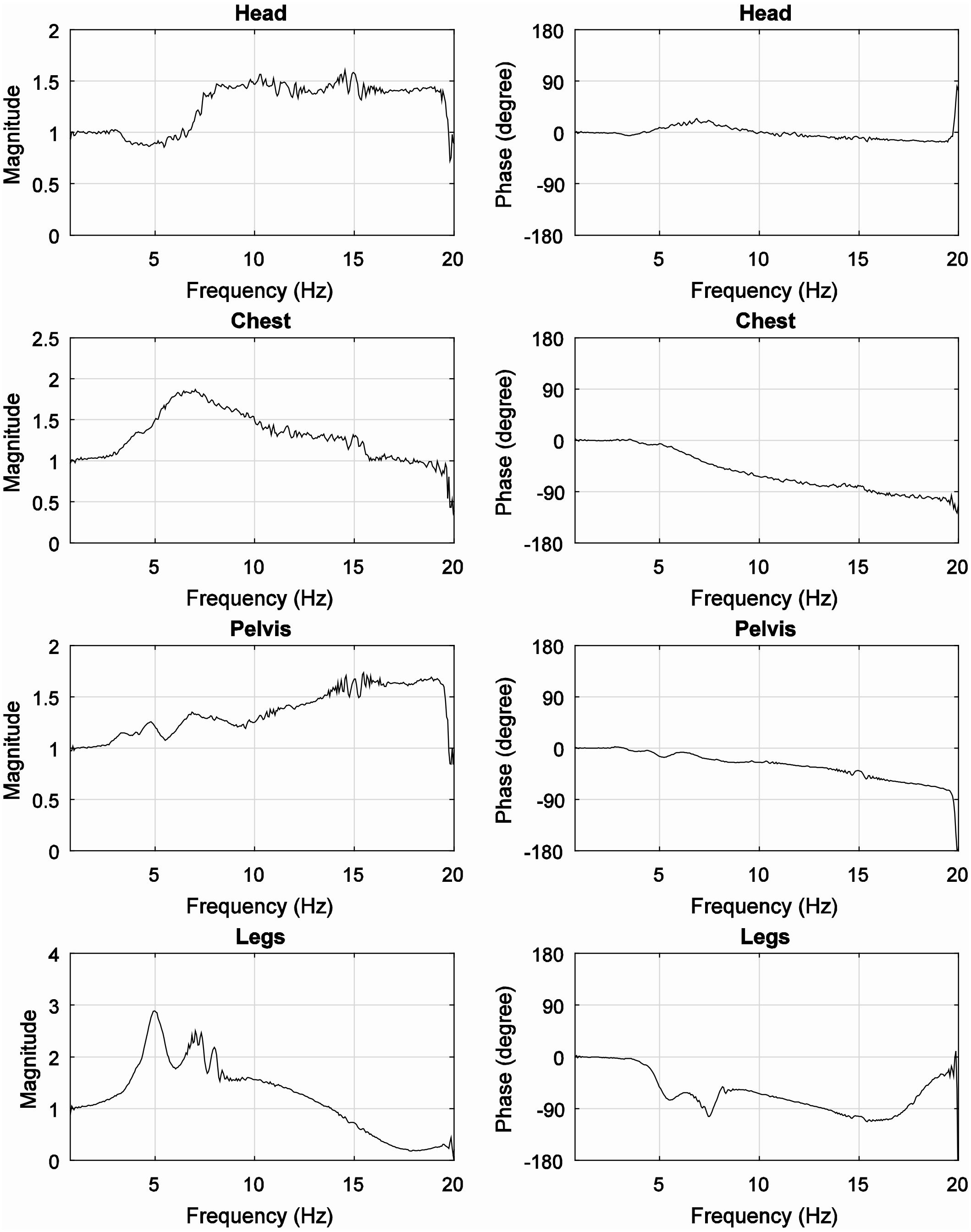

Figure (A.12) Transmissibility magnitude and phase between the vertical output motion at the head, chest, pelvis, and legs of Subject 7, and the vertical input sinusoidal motion at the rigid-base level

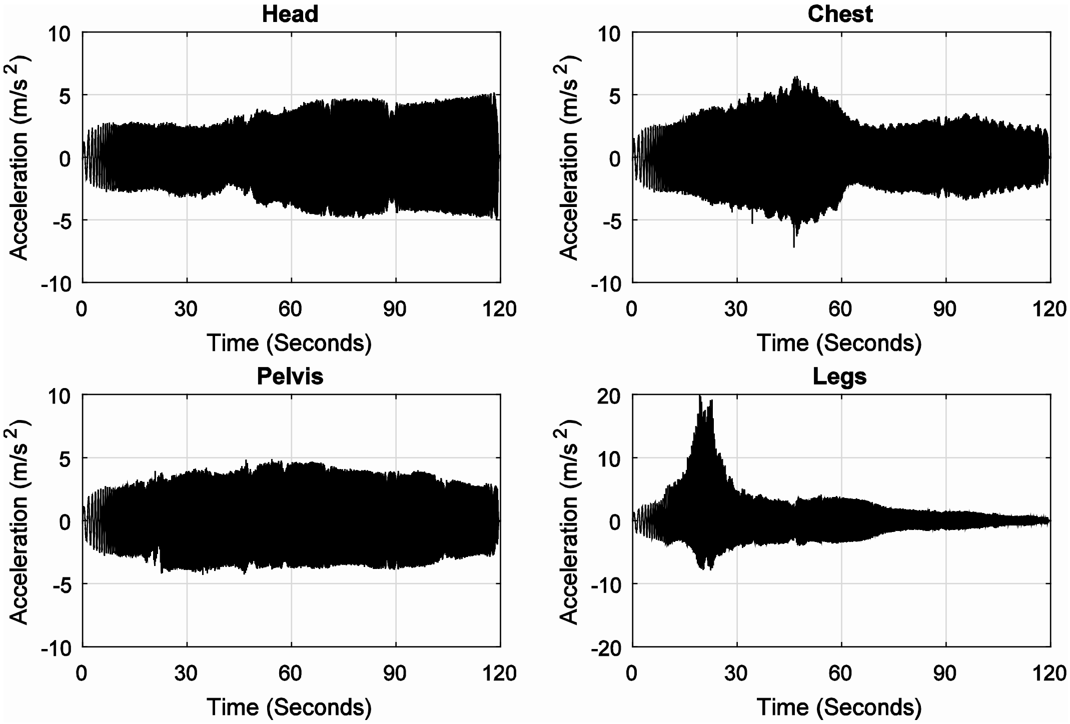

Figure (A.13) Time history of the resulting vertical acceleration signals measured at the head, chest, pelvis, and legs as result of the vertical input sinusoidal motion of Subject 8

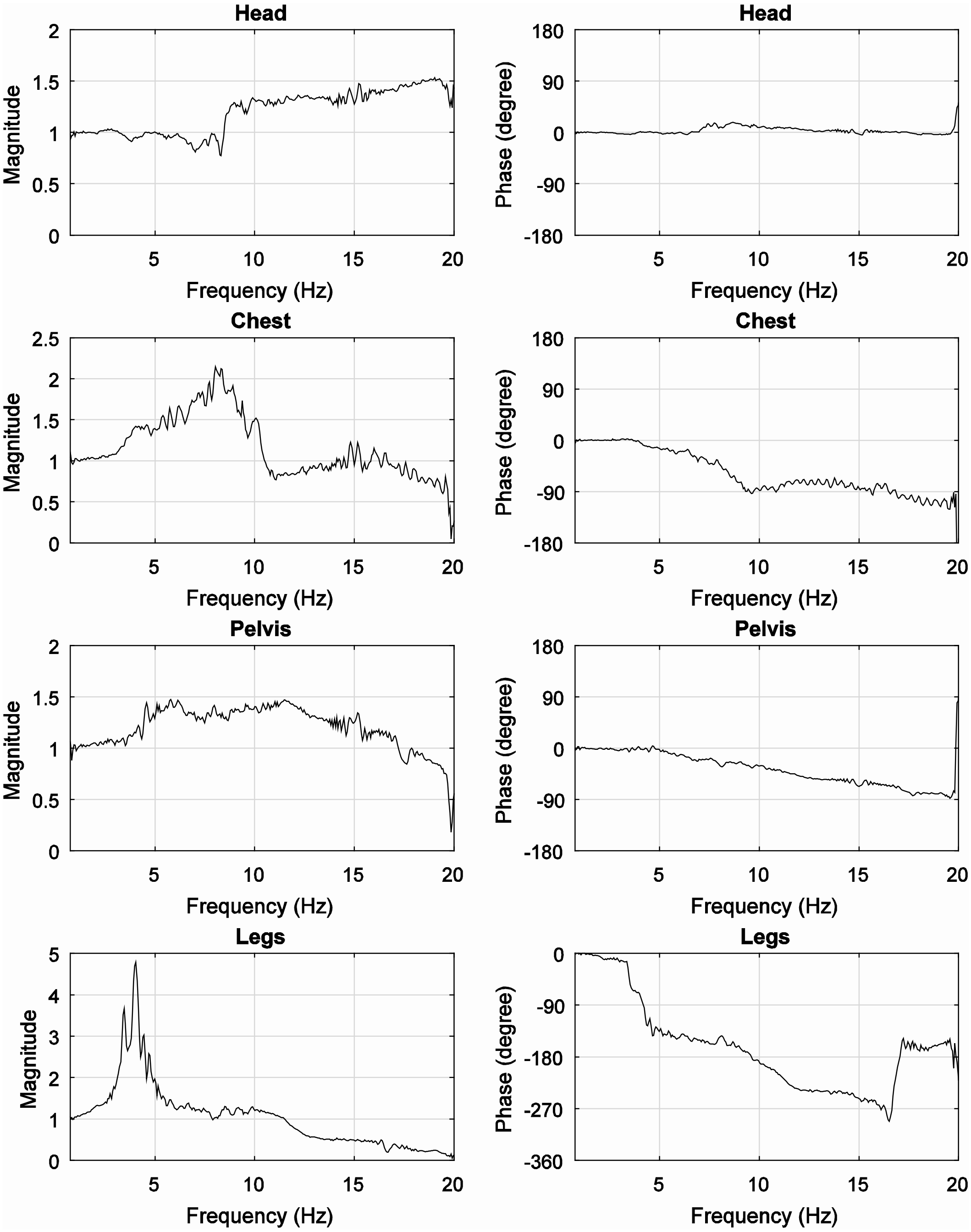

Figure (A.14) Transmissibility magnitude and phase between the vertical output motion at the head, chest, pelvis, and legs of Subject 8, and the vertical input sinusoidal motion at the rigid-base level

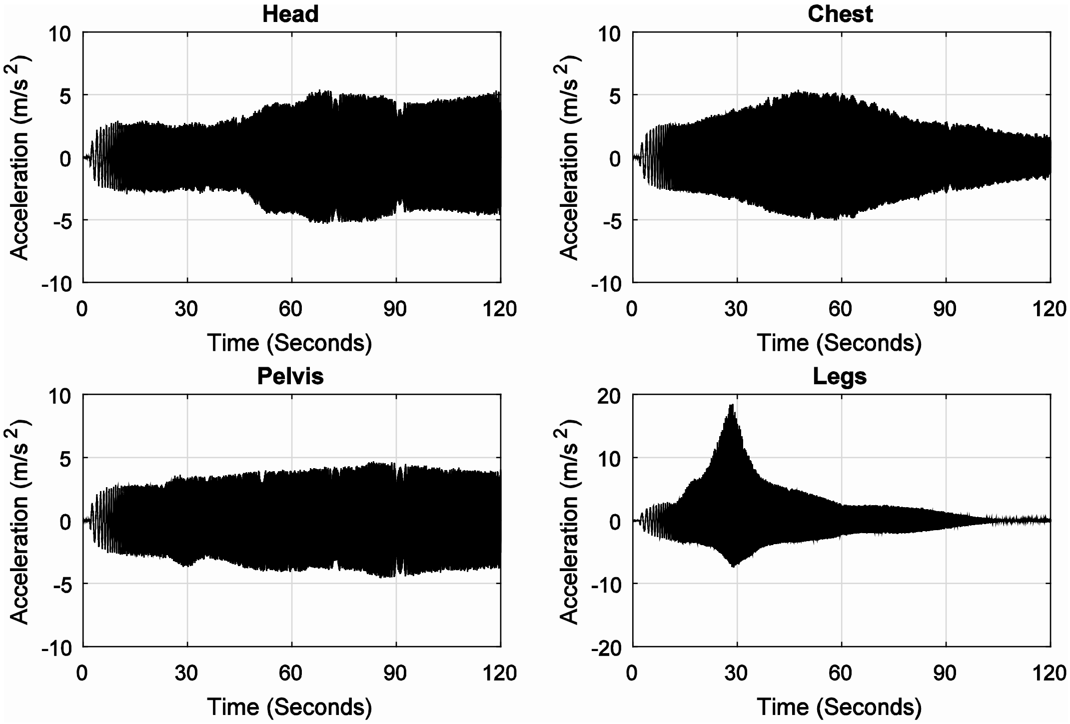

Figure (A.15) Time history of the resulting vertical acceleration signals measured at the head, chest, pelvis, and legs as result of the vertical input sinusoidal motion of Subject 9

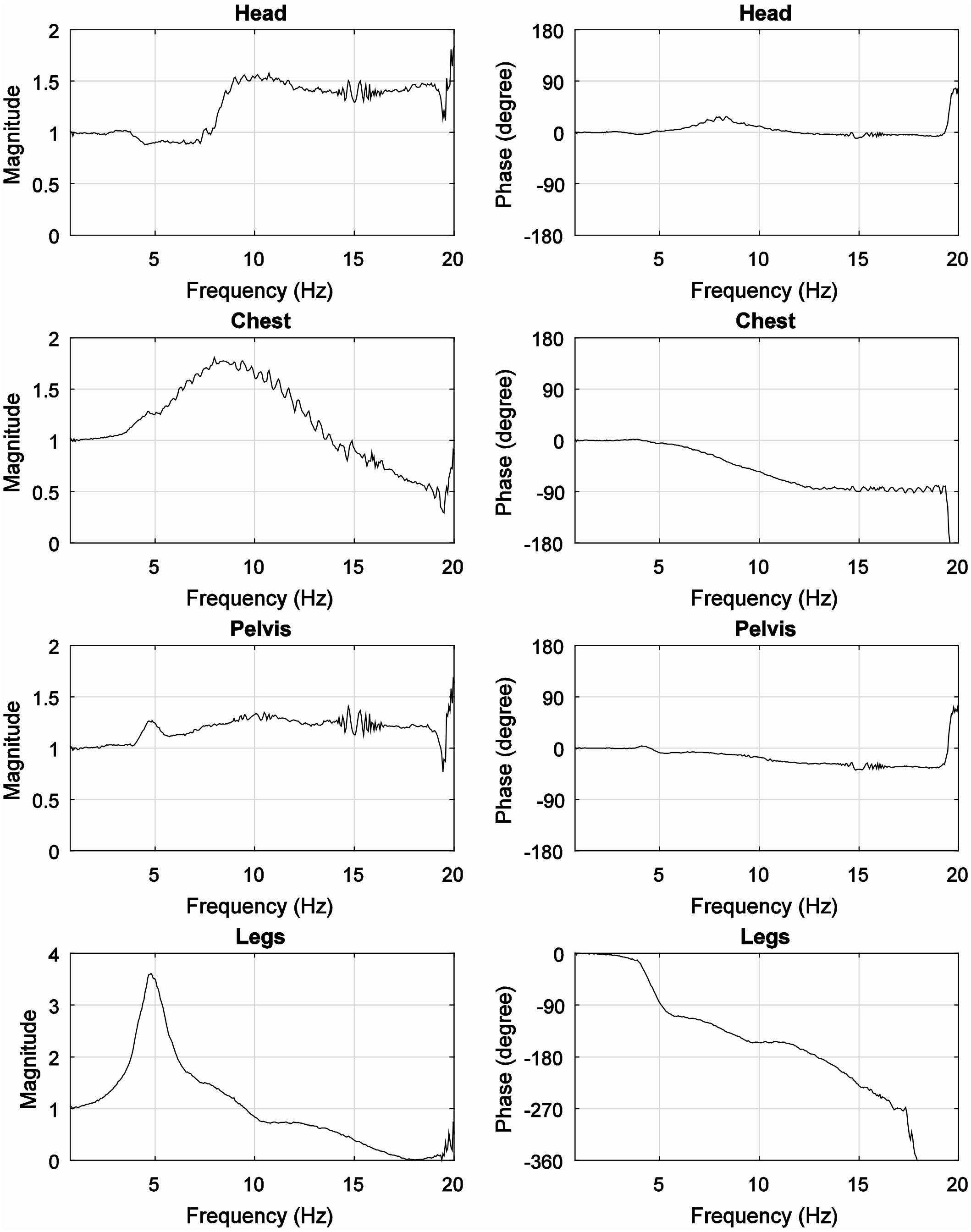

Figure (A.16) Transmissibility magnitude and phase between the vertical output motion at the head, chest, pelvis, and legs of Subject 9, and the vertical input sinusoidal motion at the rigid-base level

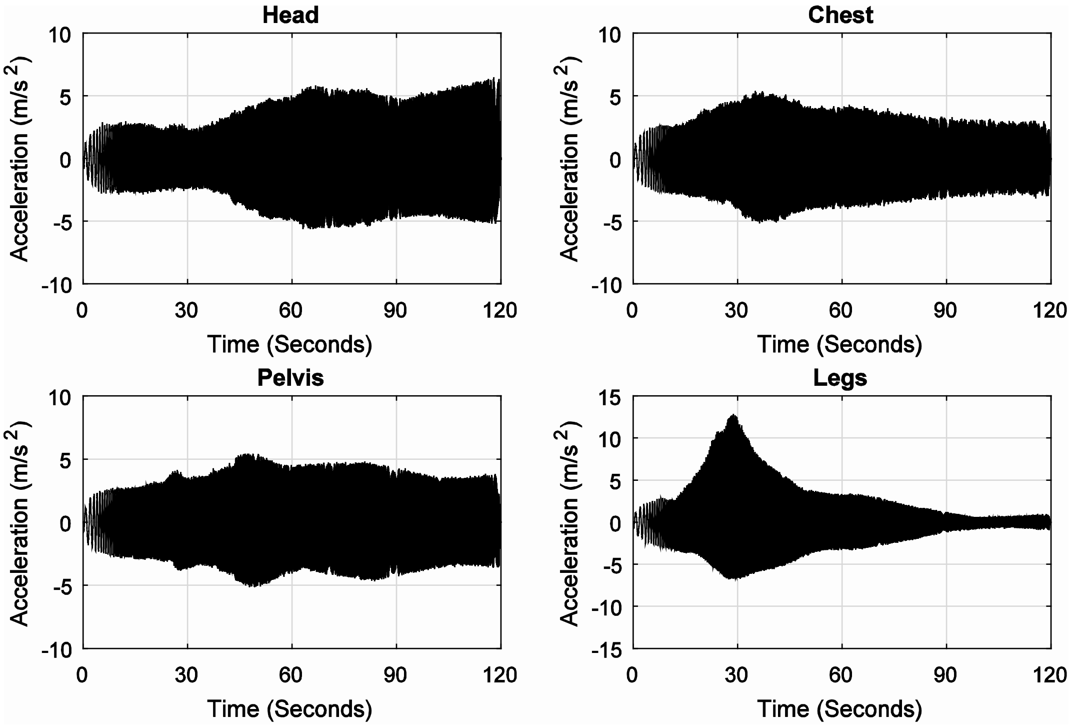

Figure (A.17) Time history of the resulting vertical acceleration signals measured at the head, chest, pelvis, and legs as result of the vertical input sinusoidal motion of Subject 10

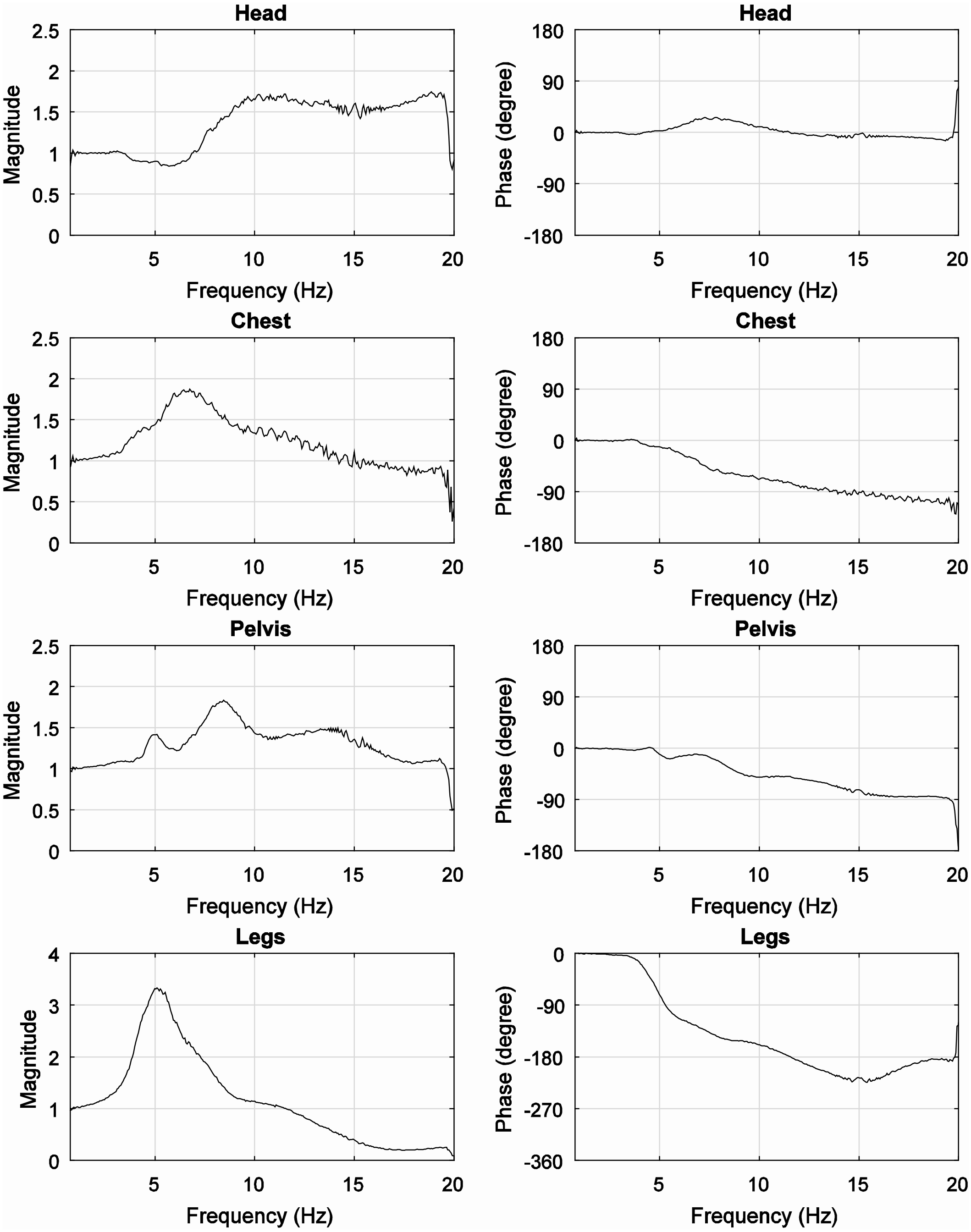

Figure (A.18) Transmissibility magnitude and phase between the vertical output motion at the head, chest, pelvis, and legs of Subject 10, and the vertical input sinusoidal motion at the rigid-base level

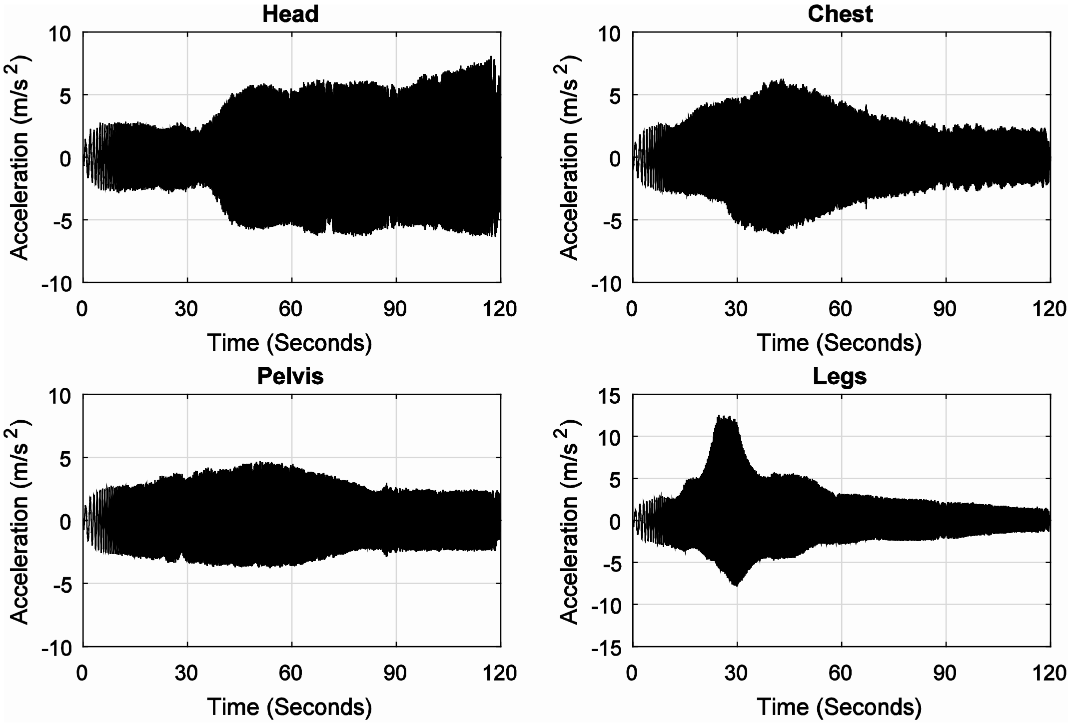

Figure (A.19) Time history of the resulting vertical acceleration signals measured at the head, chest, pelvis, and legs as result of the vertical input sinusoidal motion of Subject 11

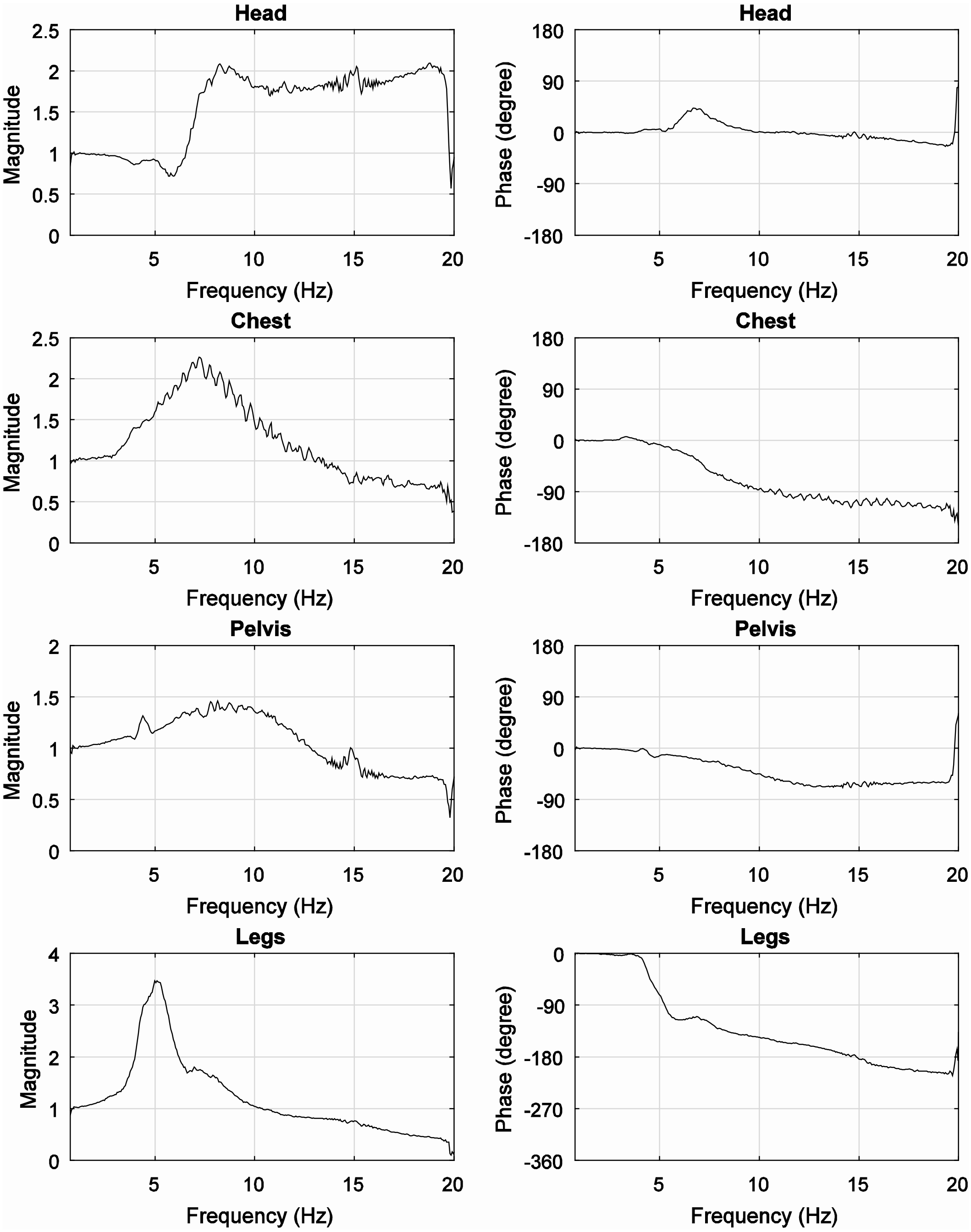

Figure (A.20) Transmissibility magnitude and phase between the vertical output motion at the head, chest, pelvis, and legs of Subject 11, and the vertical input sinusoidal motion at the rigid-base level

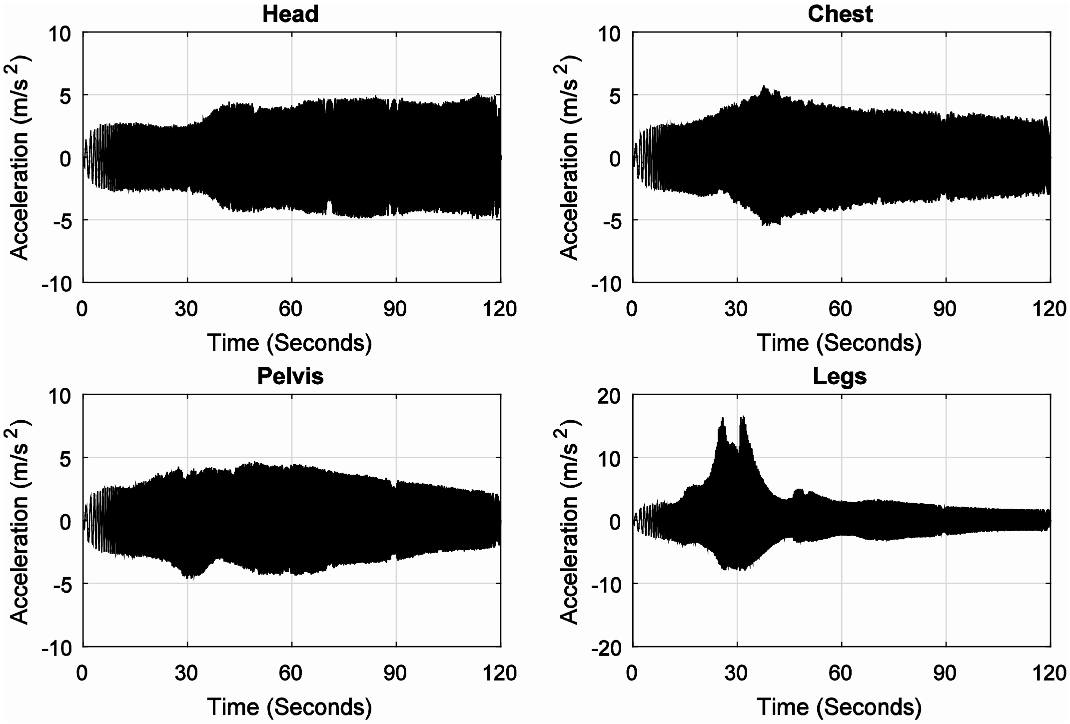

Figure (A.21) Time history of the resulting vertical acceleration signals measured at the head, chest, pelvis, and legs as result of the vertical input sinusoidal motion of Subject 12

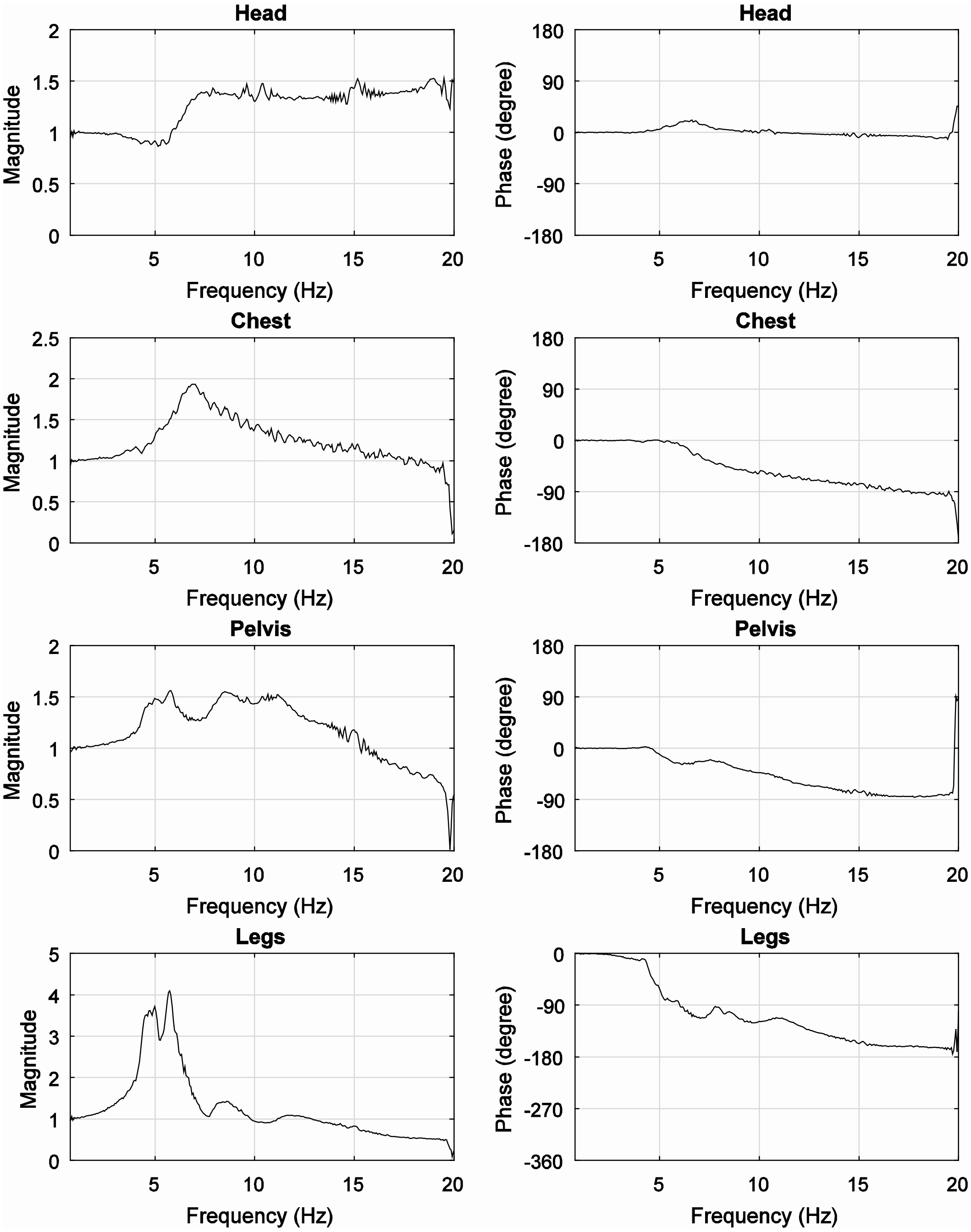

Figure (A.22) Transmissibility magnitude and phase between the vertical output motion at the head, chest, pelvis, and legs of Subject 12, and the vertical input sinusoidal motion at the rigid-base level

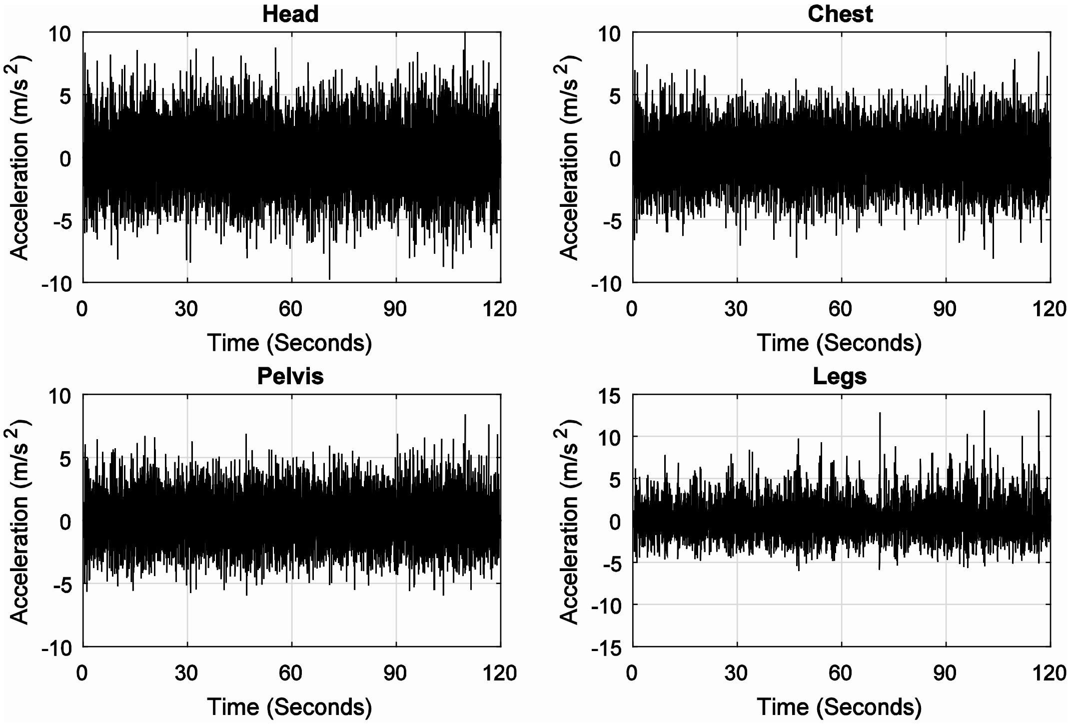

Figure (A.23) Time history of the resulting vertical acceleration signals measured at the head, chest, pelvis, and legs as result of the vertical input random motion of Subject 13

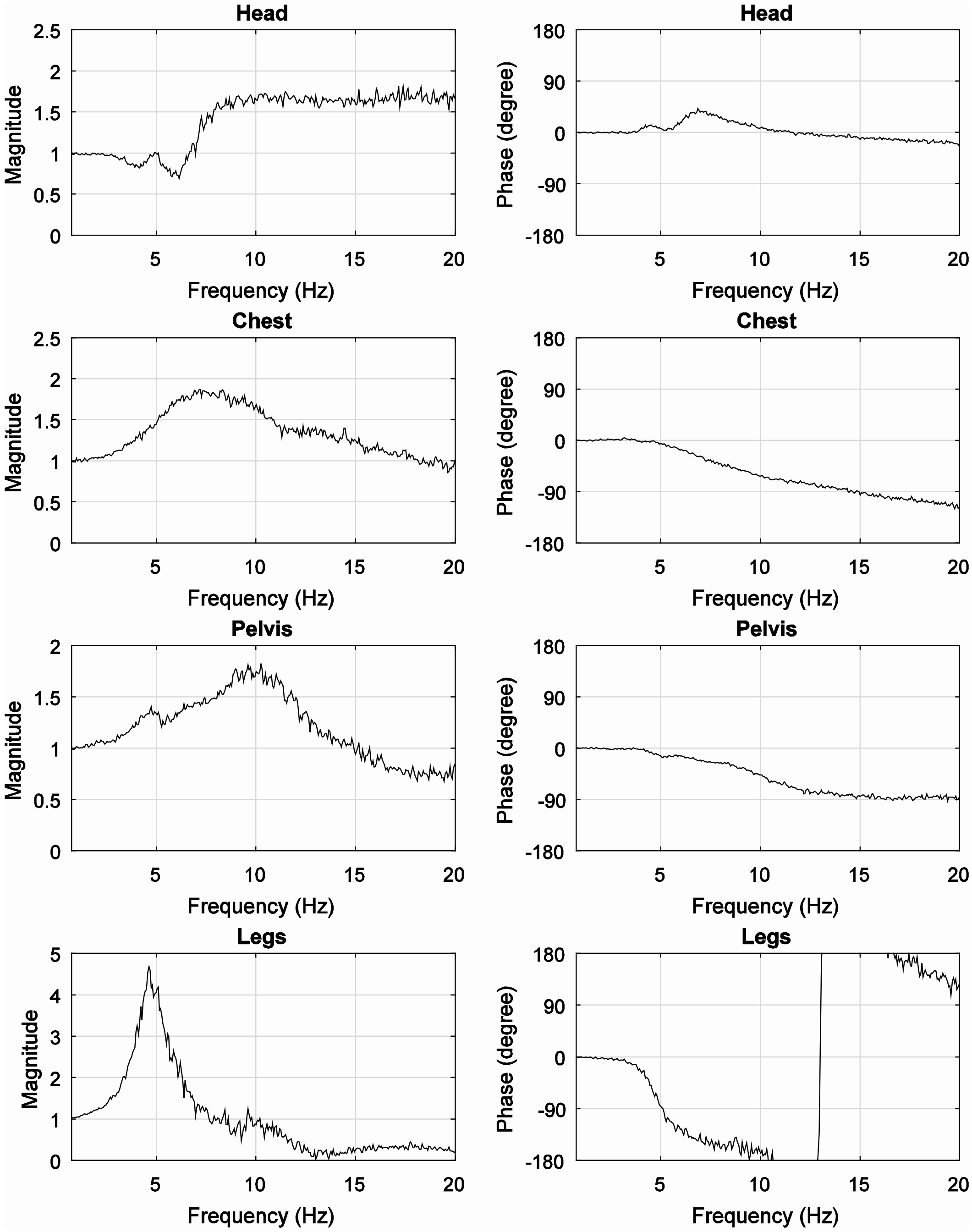

Figure (A.24) Transmissibility magnitude and phase between the vertical output motion at the head, chest, pelvis, and legs of Subject 13, and the vertical input random motion at the rigid-base level

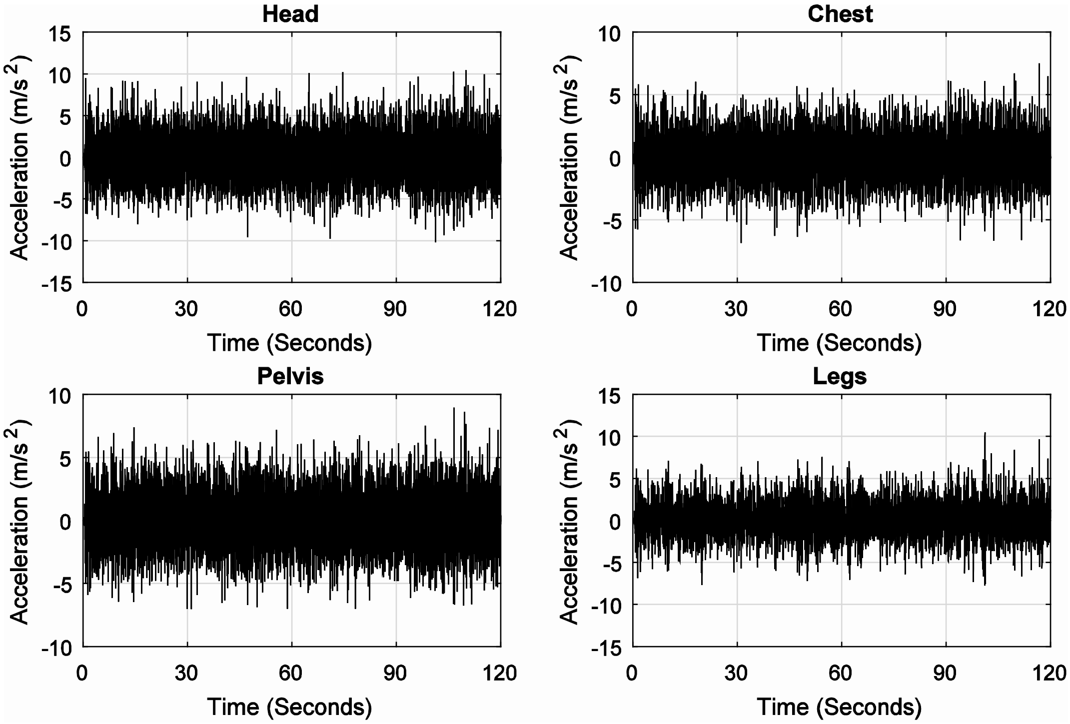

Figure (A.25) Time history of the resulting vertical acceleration signals measured at the head, chest, pelvis, and legs as result of the vertical input random motion of Subject 14

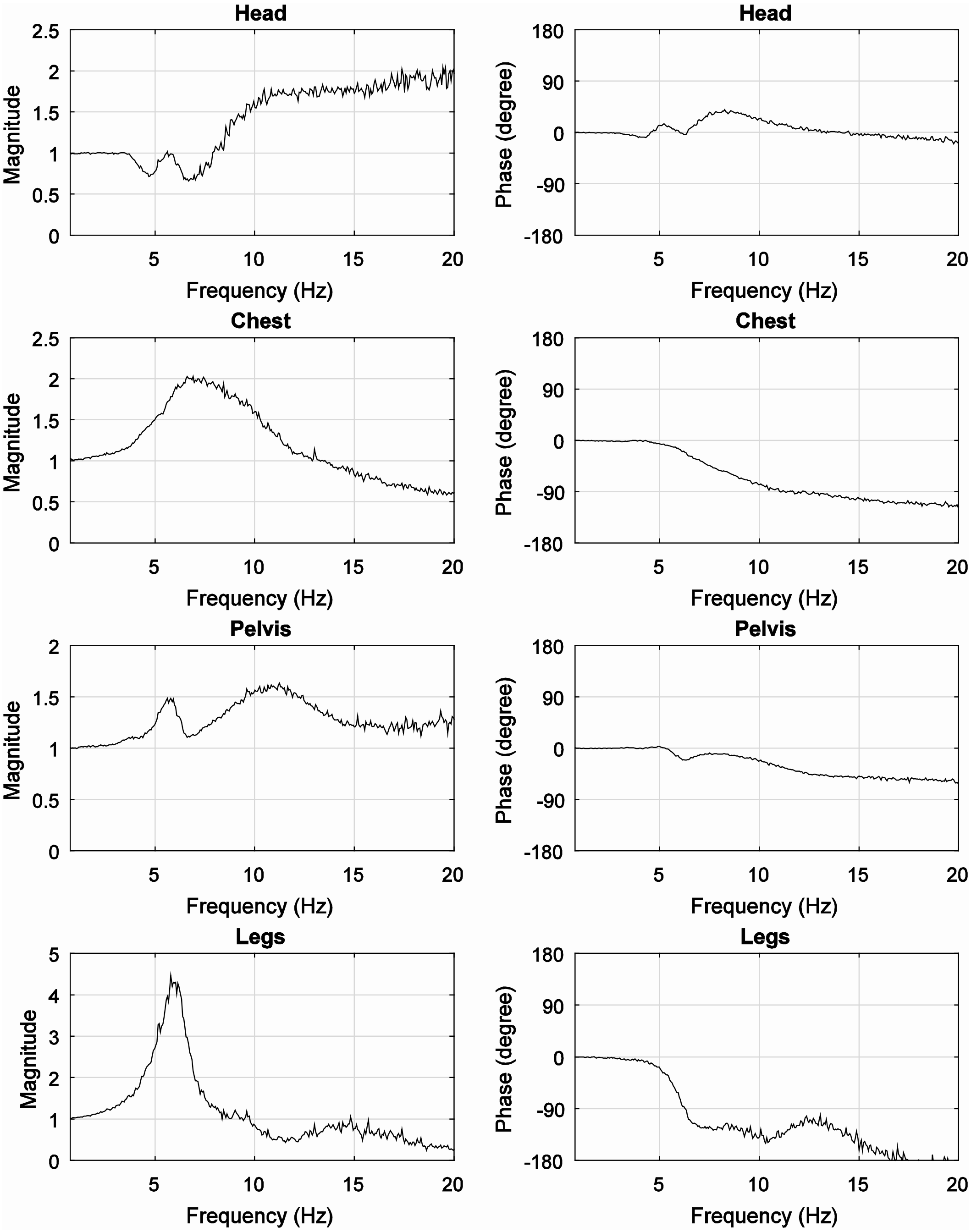

Figure (A.26) Transmissibility magnitude and phase between the vertical output motion at the head, chest, pelvis, and legs of Subject 14, and the vertical input random motion at the rigid-base level

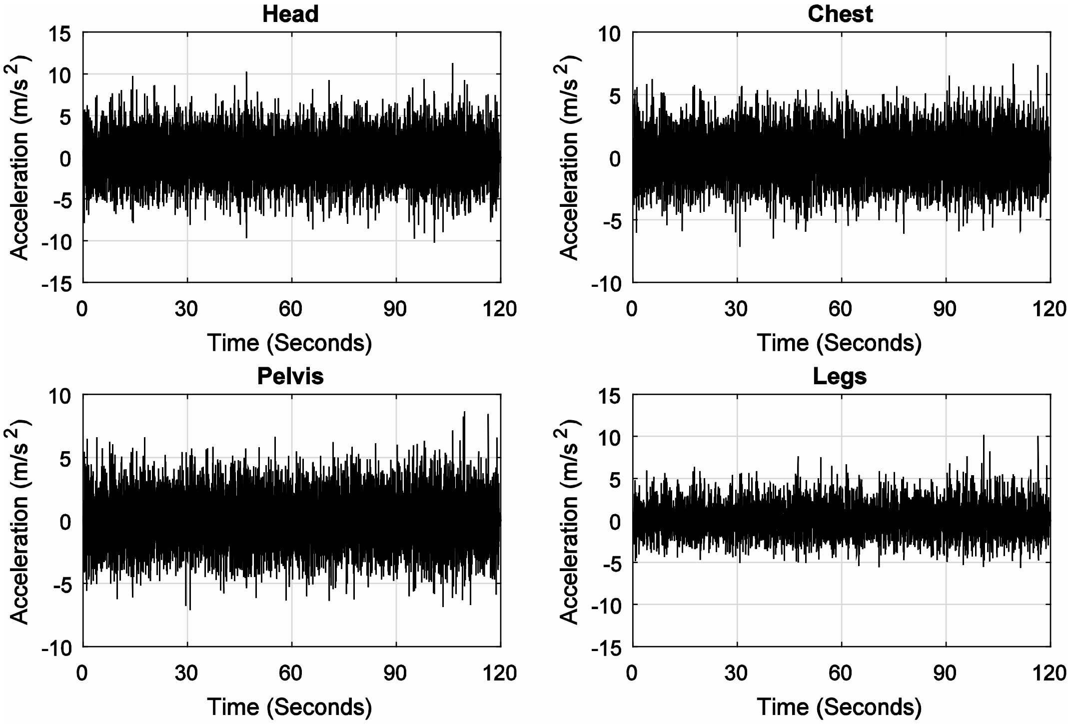

Figure (A.27) Time history of the resulting vertical acceleration signals measured at the head, chest, pelvis, and legs as result of the vertical input random motion of Subject 15

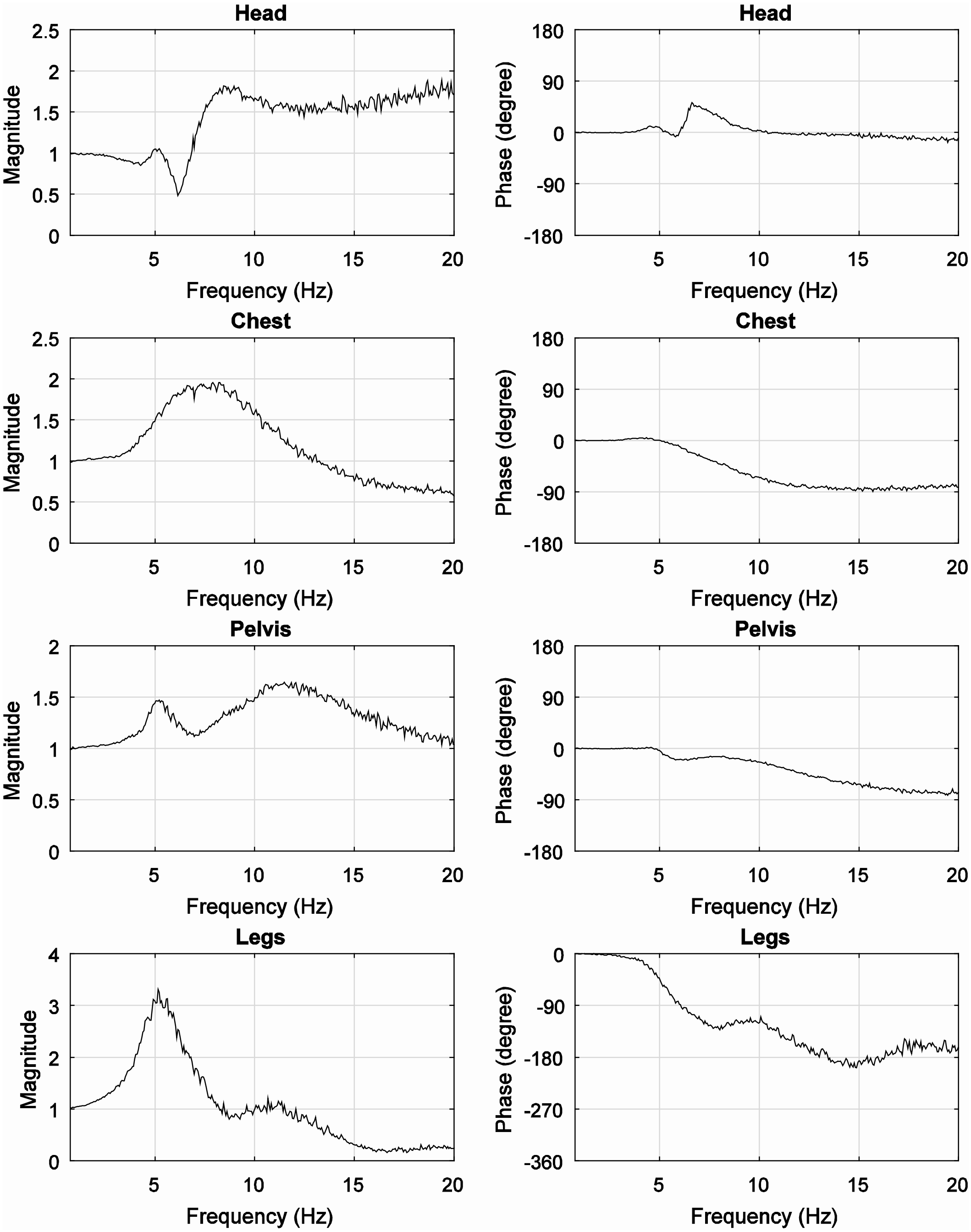

Figure (A.28) Transmissibility magnitude and phase between the vertical output motion at the head, chest, pelvis, and legs of Subject 15, and the vertical input random motion at the rigid-base level

APPENDIX B: THE RELATIONSHIPS BETWEEN THE ARMAX MODEL PREDICTION AND THOSE OF THE EXPERIMENTS IN THE FREQUENCY DOMAIN

The relationships between the ARMAX model prediction and those of the experiments in the frequency domain for the different body segments are shown below for the other fourteen subjects.

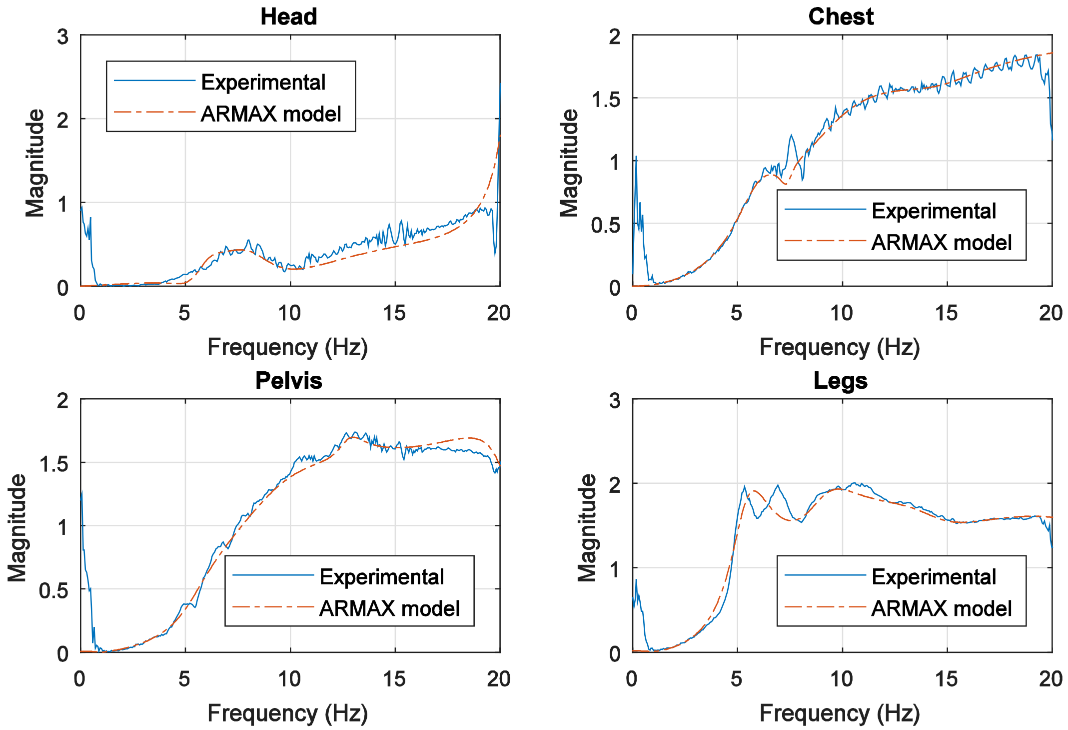

Figure (B.1) EPFRF magnitude predicted by ARMAX at the head, chest, pelvis, and legs, and those measured by the experiments of Subject 1

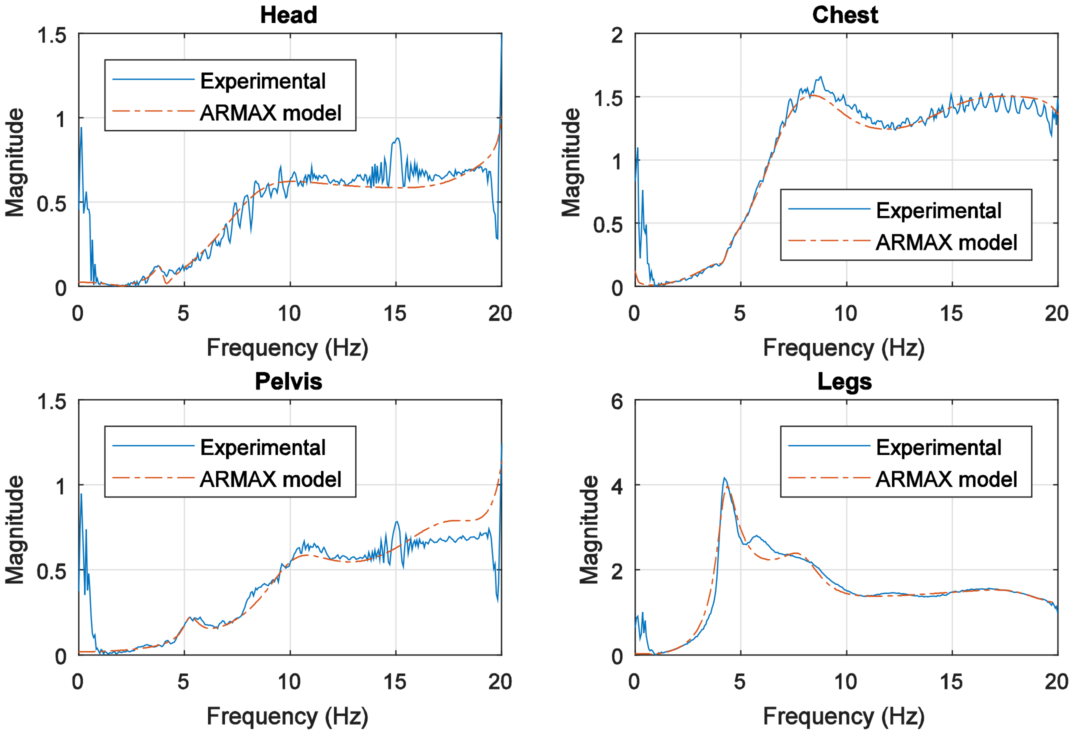

Figure (B.2) EPFRF magnitude predicted by ARMAX at the head, chest, pelvis, and legs, and those measured by the experiments of Subject 2

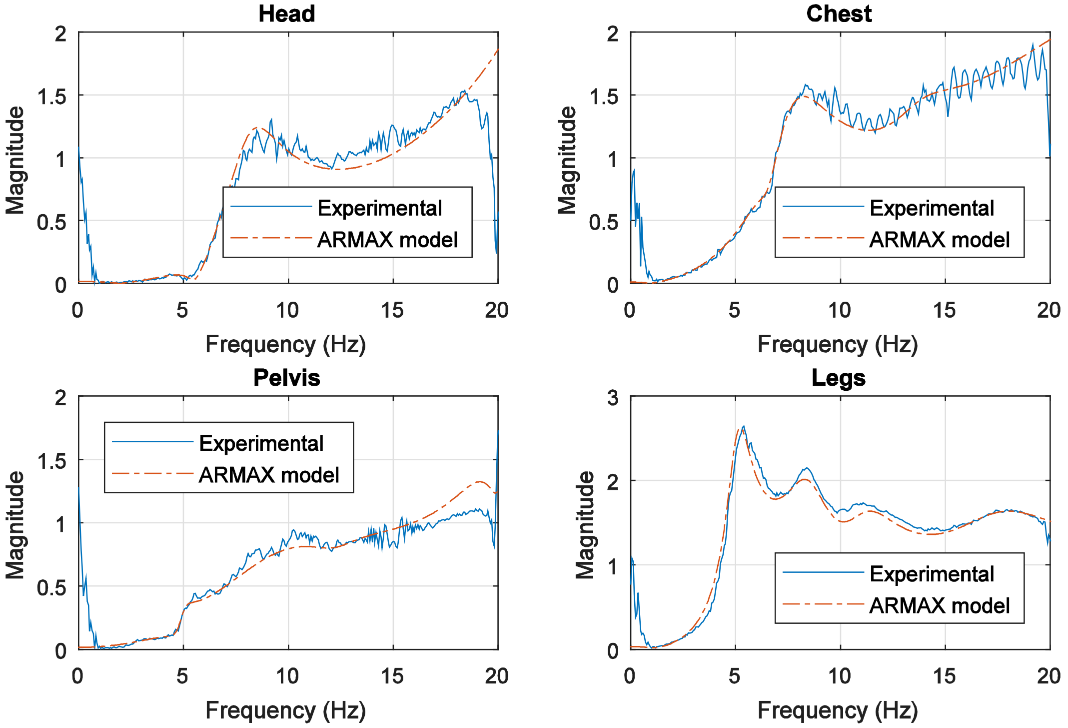

Figure (B.3) EPFRF magnitude predicted by ARMAX at the head, chest, pelvis, and legs, and those measured by the experiments of Subject 4

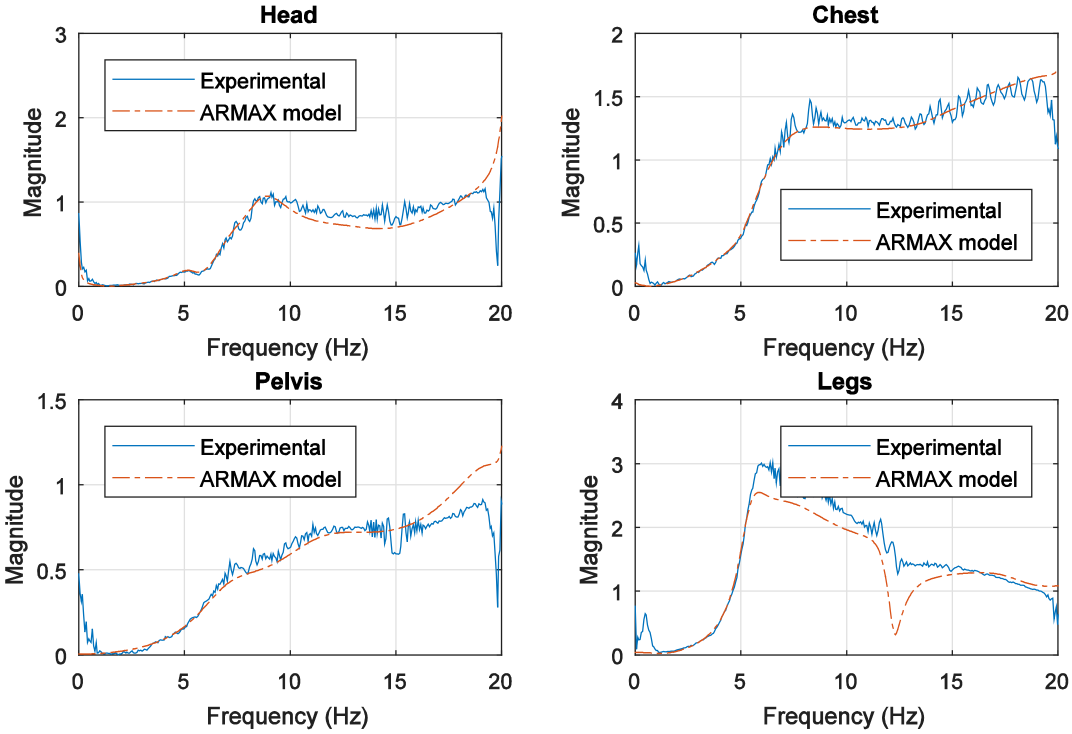

Figure (B.4) EPFRF magnitude predicted by ARMAX at the head, chest, pelvis, and legs, and those measured by the experiments of Subject 5

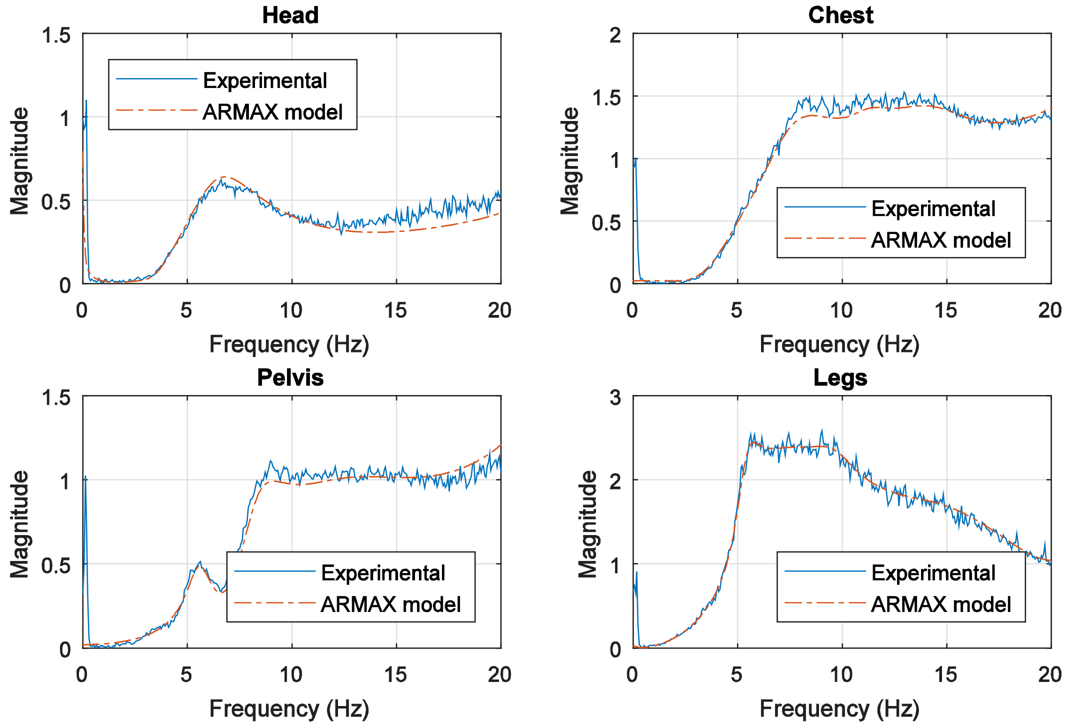

Figure (B.5) EPFRF magnitude predicted by ARMAX at the head, chest, pelvis, and legs, and those measured by the experiments of Subject 6

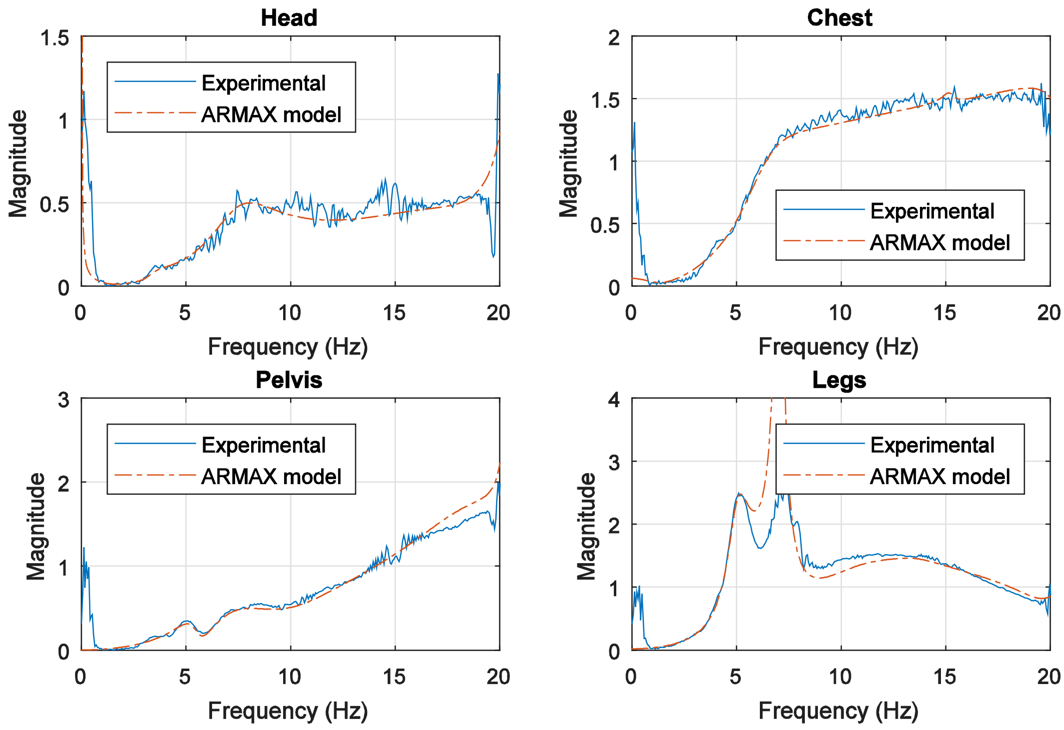

Figure (B.6) EPFRF magnitude predicted by ARMAX at the head, chest, pelvis, and legs, and those measured by the experiments of Subject 7

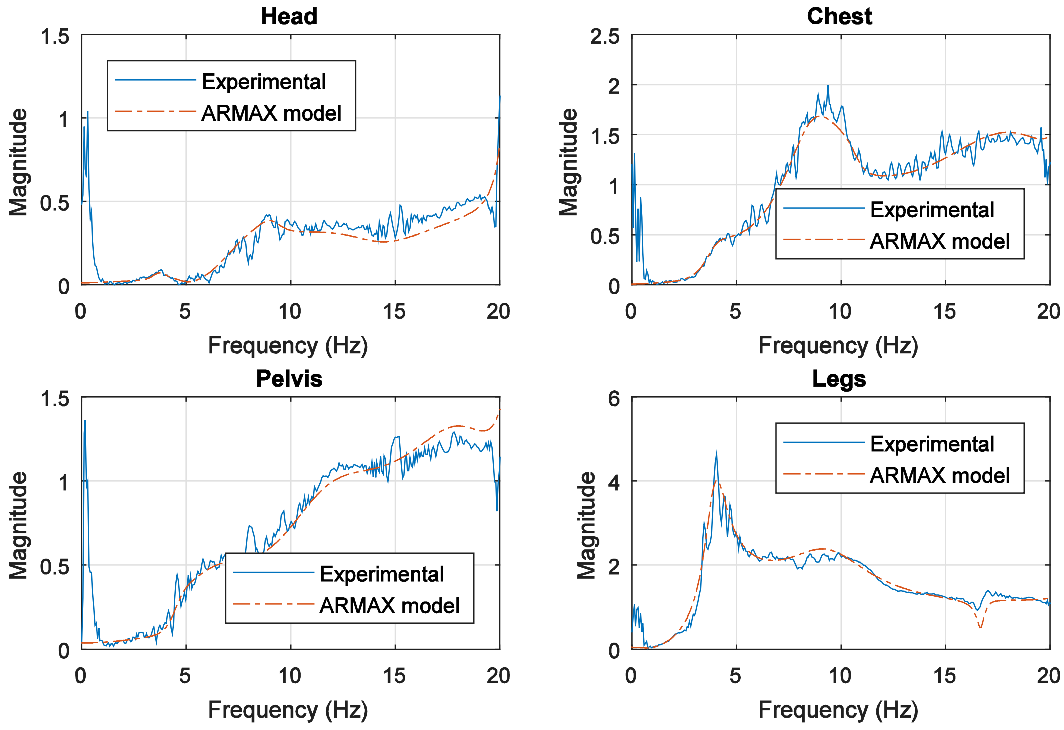

Figure (B.7) EPFRF magnitude predicted by ARMAX at the head, chest, pelvis, and legs, and those measured by the experiments of Subject 8

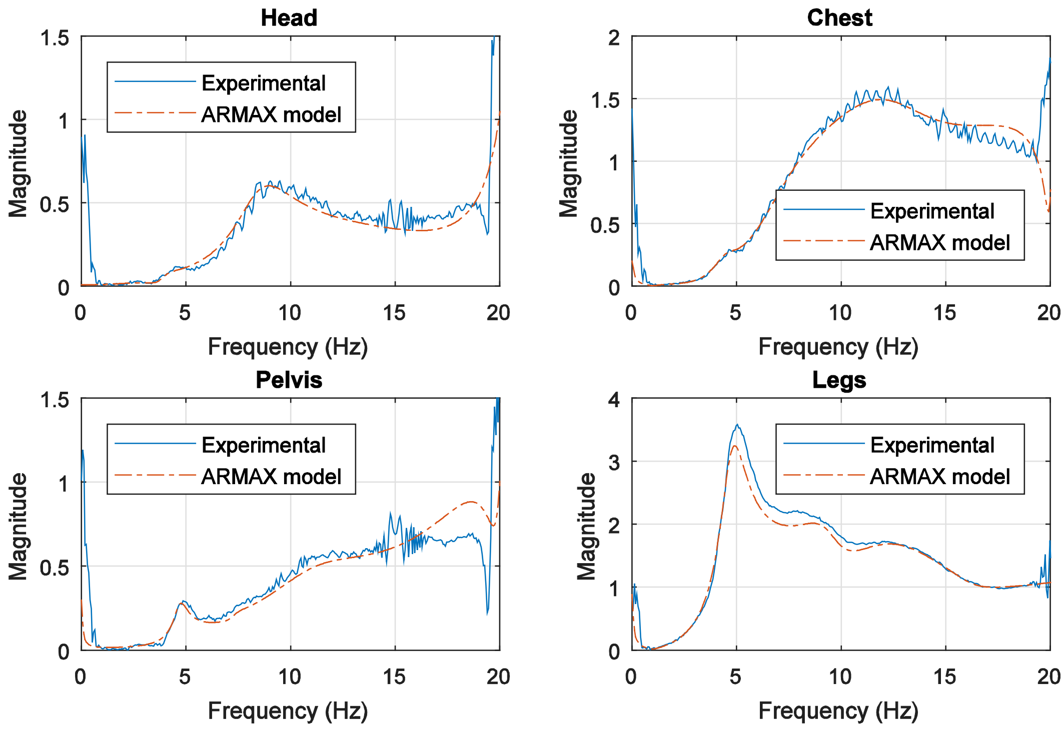

Figure (B.8) EPFRF magnitude predicted by ARMAX at the head, chest, pelvis, and legs, and those measured by the experiments of Subject 9

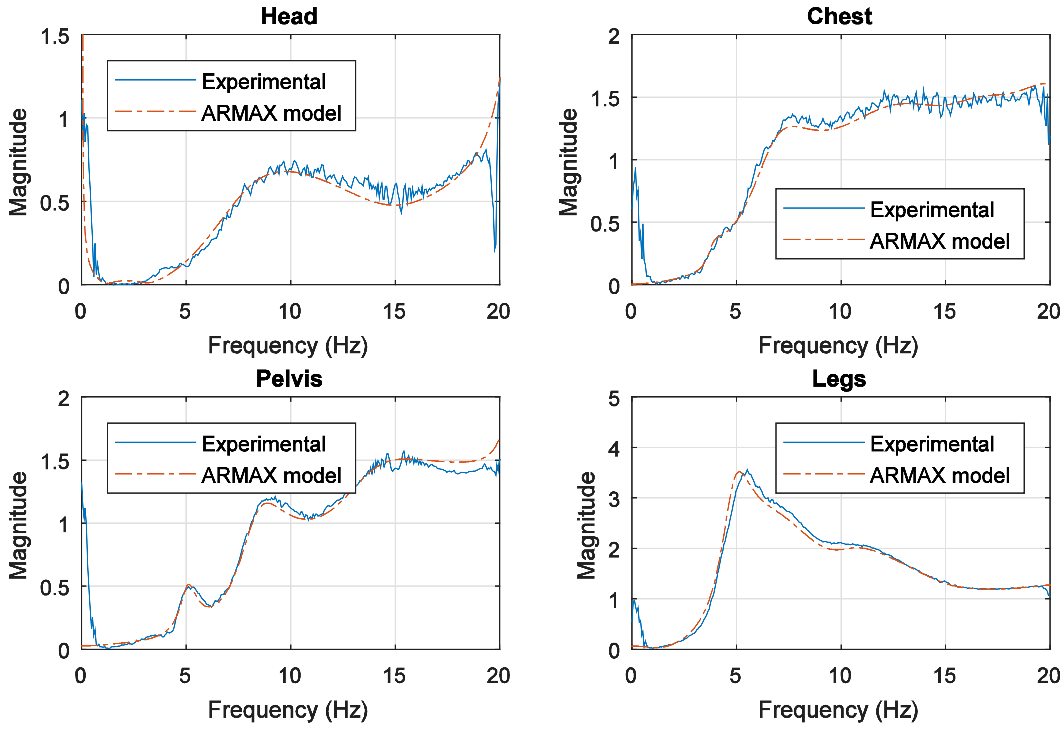

Figure (B.9) EPFRF magnitude predicted by ARMAX at the head, chest, pelvis, and legs, and those measured by the experiments of Subject 10

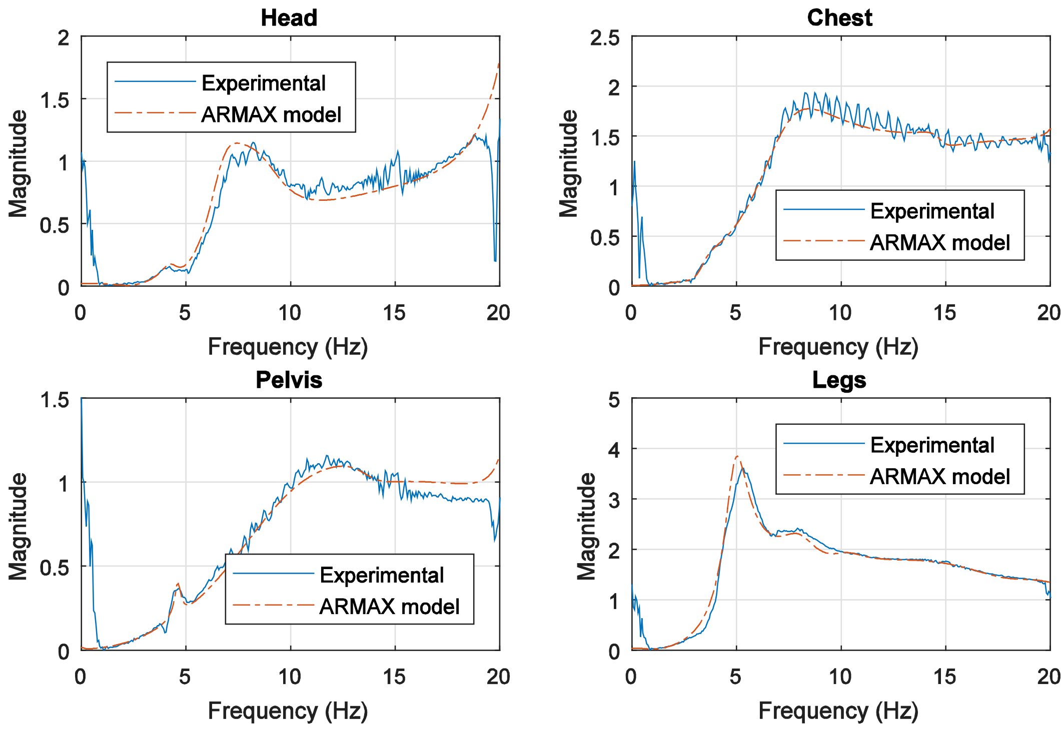

Figure (B.10) EPFRF magnitude predicted by ARMAX at the head, chest, pelvis, and legs, and those measured by the experiments of Subject 11

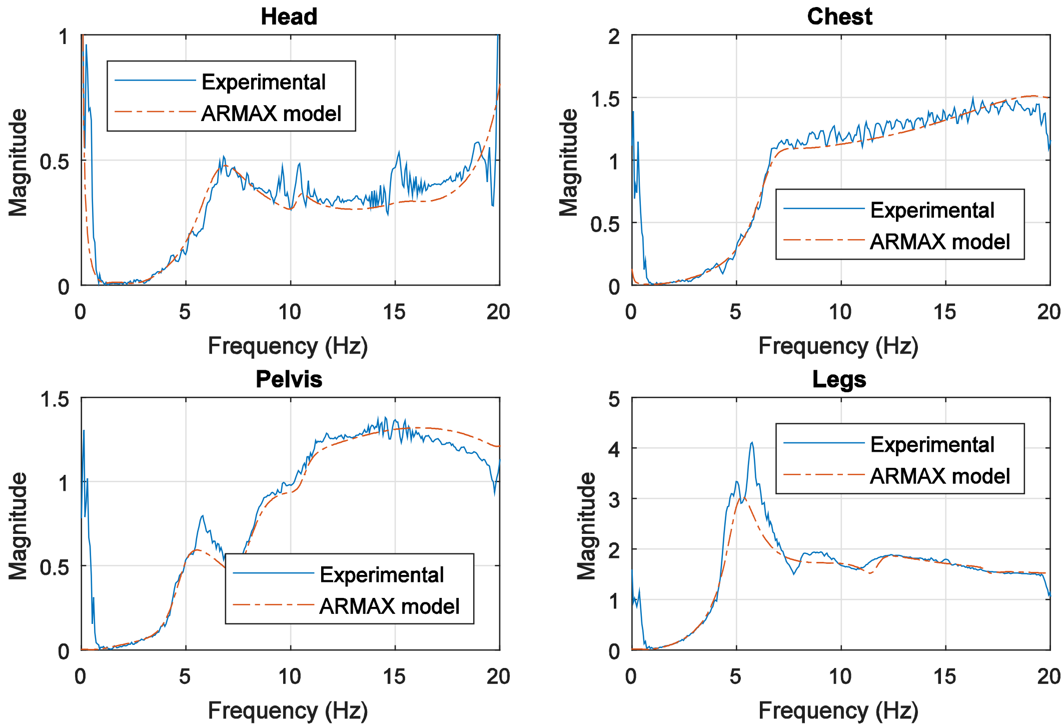

Figure (B.11) EPFRF magnitude predicted by ARMAX at the head, chest, pelvis, and legs, and those measured by the experiments of Subject 12

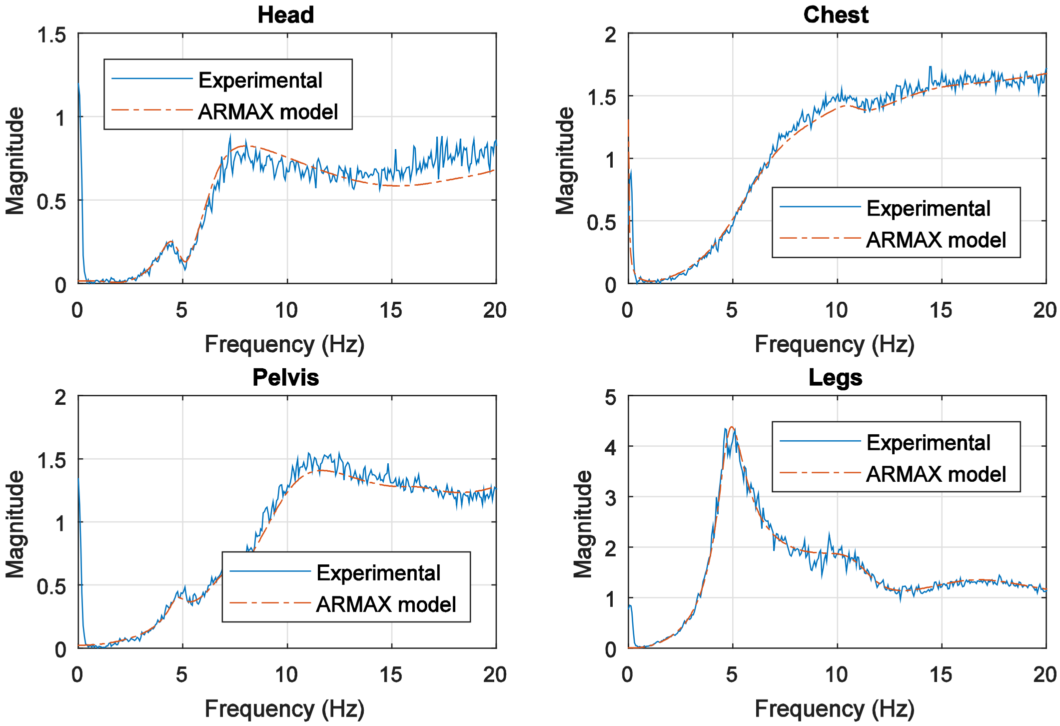

Figure (B.12) EPFRF magnitude predicted by ARMAX at the head, chest, pelvis, and legs, and those measured by the experiments of Subject 13

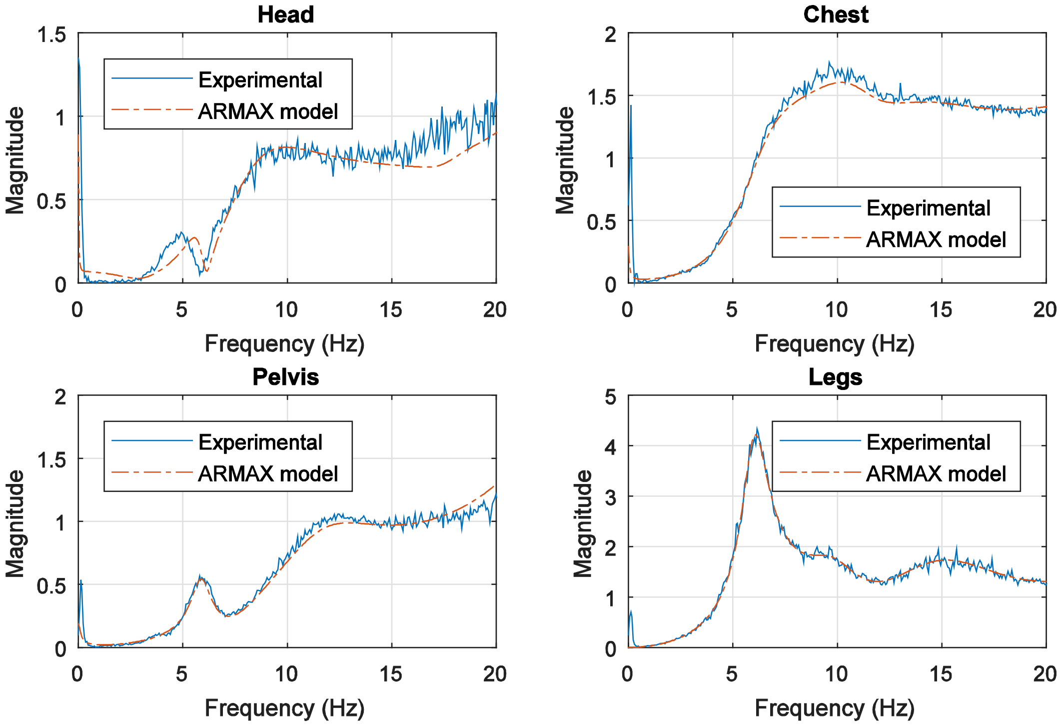

Figure (B.13) EPFRF magnitude predicted by ARMAX at the head, chest, pelvis, and legs, and those measured by the experiments of Subject 14

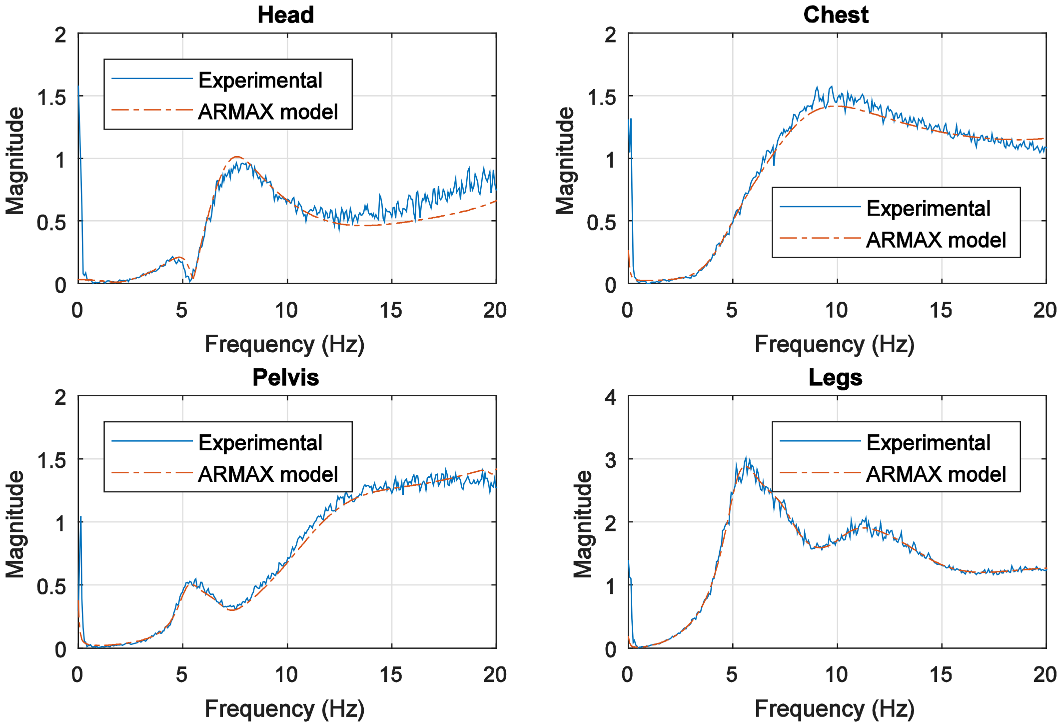

Figure (B.14) EPFRF magnitude predicted by ARMAX at the head, chest, pelvis, and legs, and those measured by the experiments of Subject 15

APPENDIX C: TIME HISTORY OF THE VERTICAL ACCELERATION AT FEET AND ITS ARMAX MODEL

The time history of the vertical acceleration at the feet, the magnitude, and the relationship between the ARMAX model prediction and those of the experiments in the frequency domain for the feet are shown below for the other nine subjects (Subjects 6-7,9-15).

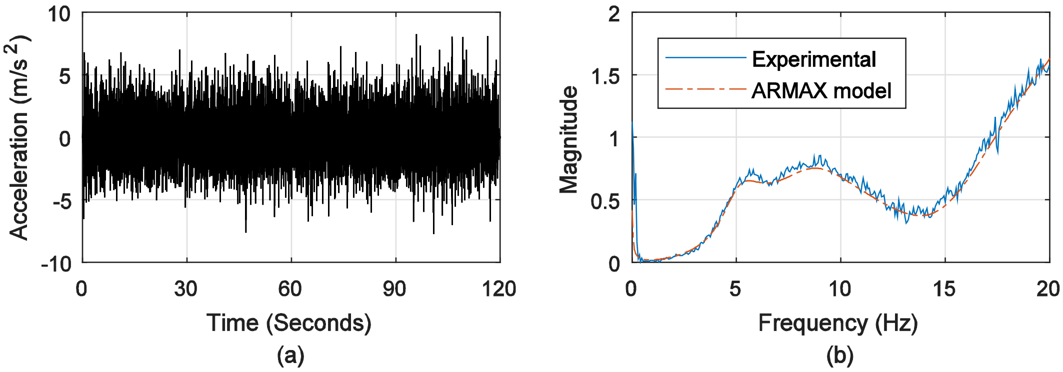

Figure (C.1) (a) Time history of the resulting vertical acceleration signals measured at the feet as a result of the vertical input random motion of Subject 6, (b) EPFRF magnitude predicted by ARMAX and measured by the experiment

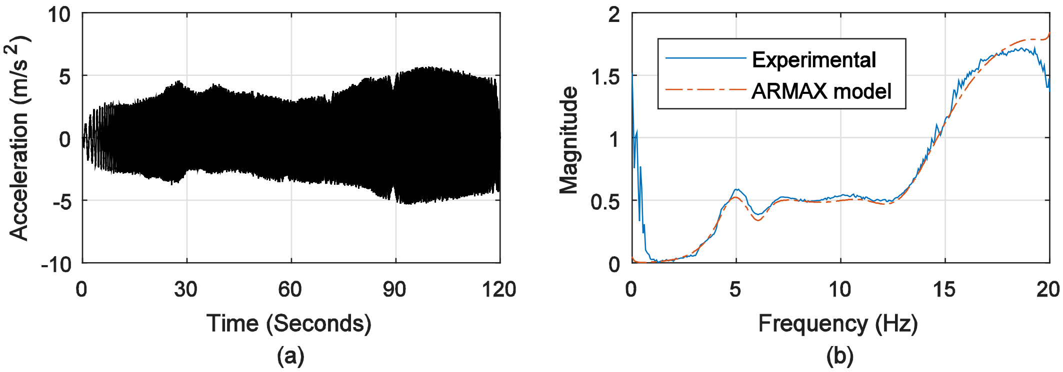

Figure (C.2) (a) Time history of the resulting vertical acceleration signals measured at the feet as a result of the vertical input sinusoidal motion of Subject 7, (b) EPFRF magnitude predicted by ARMAX and measured by the experiment

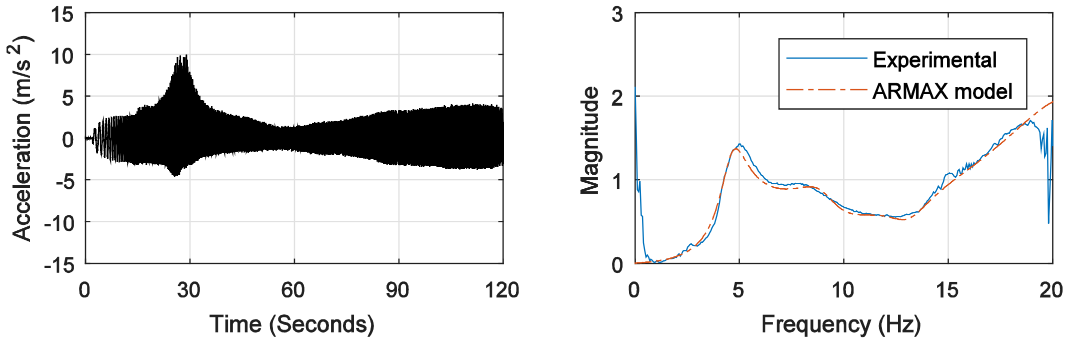

(a) (b)

Figure (C.3) (a) Time history of the resulting vertical acceleration signals measured at the feet as a result of the vertical input sinusoidal motion of Subject 9, (b) EPFRF magnitude predicted by ARMAX and measured by the experiment

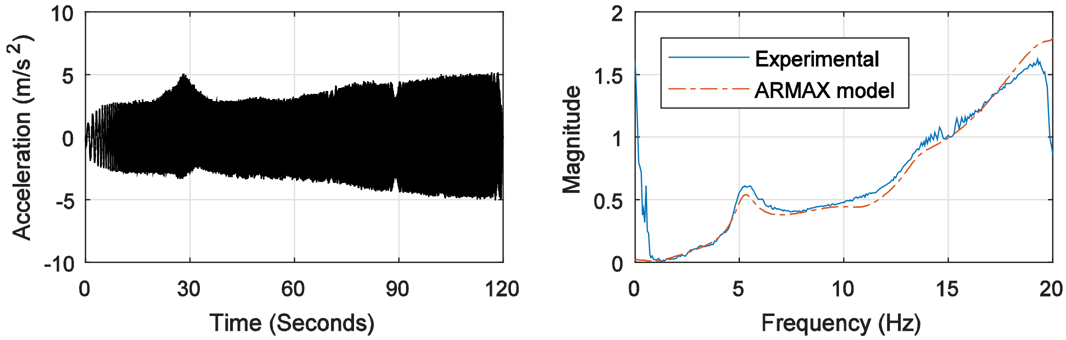

(a) (b)

Figure (C.4) (a) Time history of the resulting vertical acceleration signals measured at the feet as a result of the vertical input sinusoidal motion of Subject 10, (b) EPFRF magnitude predicted by ARMAX and measured by the experiment

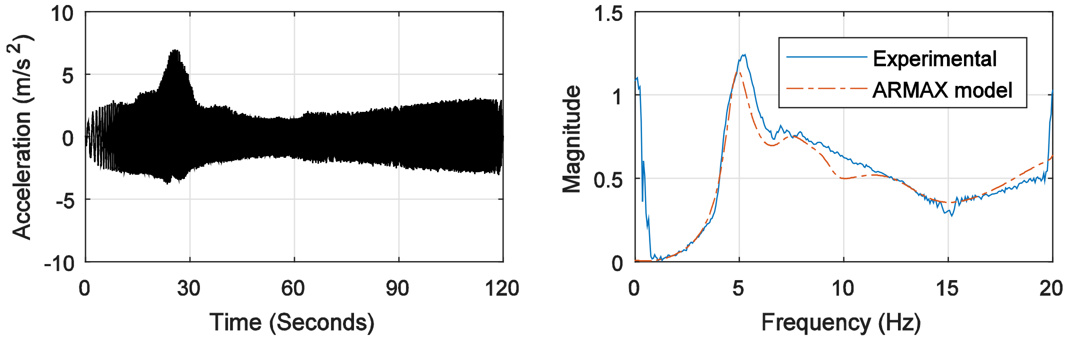

(a) (b)

Figure (C.5) (a) Time history of the resulting vertical acceleration signals measured at the feet as a result of the vertical input sinusoidal motion of Subject 11, (b) EPFRF magnitude predicted by ARMAX and measured by the experiment

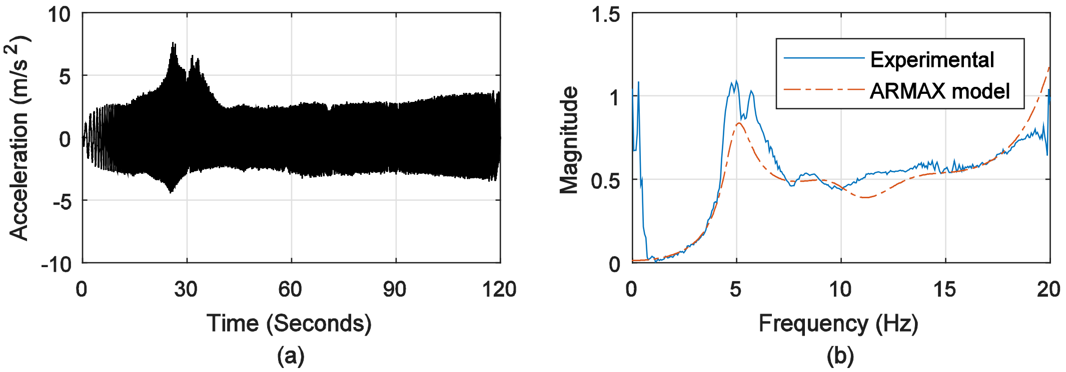

Figure (C.6) (a) Time history of the resulting vertical acceleration signals measured at the feet as a result of the vertical input sinusoidal motion of Subject 12, (b) EPFRF magnitude predicted by ARMAX and measured by the experiment

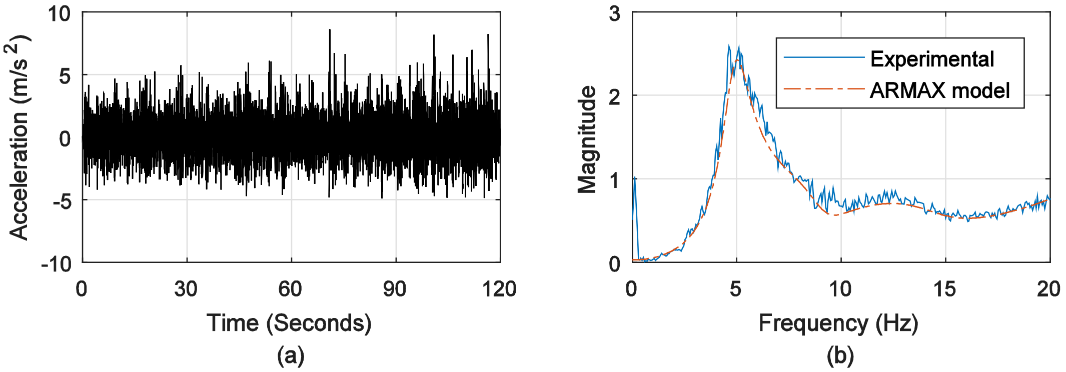

Figure (C.7) (a) Time history of the resulting vertical acceleration signals measured at the feet as a result of the vertical input random motion of Subject 13, (b) EPFRF magnitude predicted by ARMAX and measured by the experiment

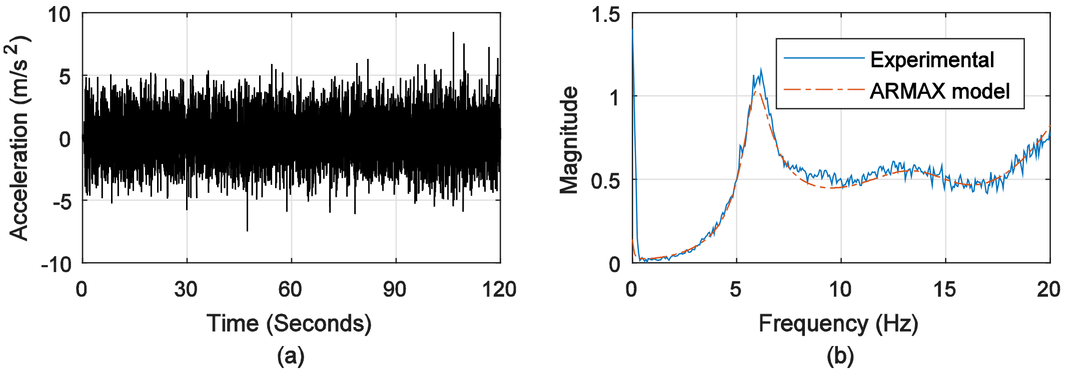

Figure (C.8) (a) Time history of the resulting vertical acceleration signals measured at the feet as a result of the vertical input random motion of Subject 14, (b) EPFRF magnitude predicted by ARMAX and measured by the experiment

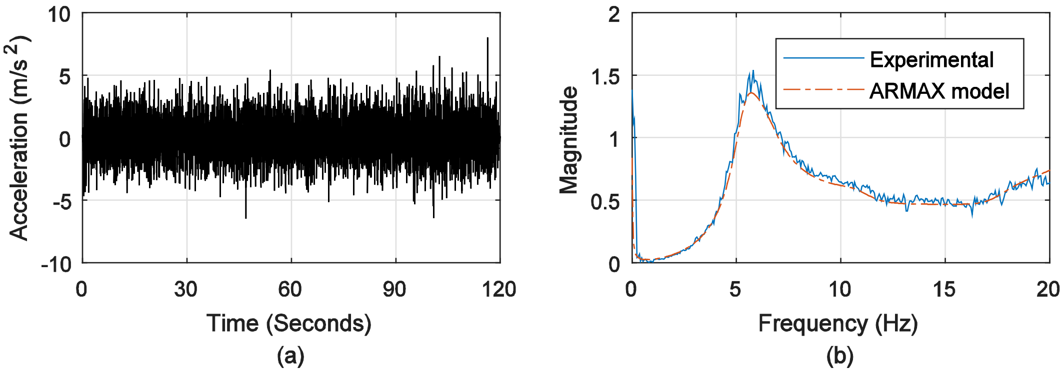

Figure (C.9) (a) Time history of the resulting vertical acceleration signals measured at the feet as a result of the vertical input random motion of Subject 15, (b) EPFRF magnitude predicted by ARMAX and measured by the experiment

APPENDIX D: MAGNITUDE SCALOGRAMS OF BASE MOTION AND THE INDIVIDUAL SEGMENTS, AND WAVELET COHERENCES BETWEEN LEGS AND FEET

The magnitude scalograms with the Morlet wavelet of the base motion acceleration and the head, chest, pelvis, legs, and feet accelerations relative to the base motion are shown below for the other five subjects (Subjects 7, 9-12). The wavelet coherences between the acceleration of the legs and feet relative to the base are also shown below for the same five subjects.

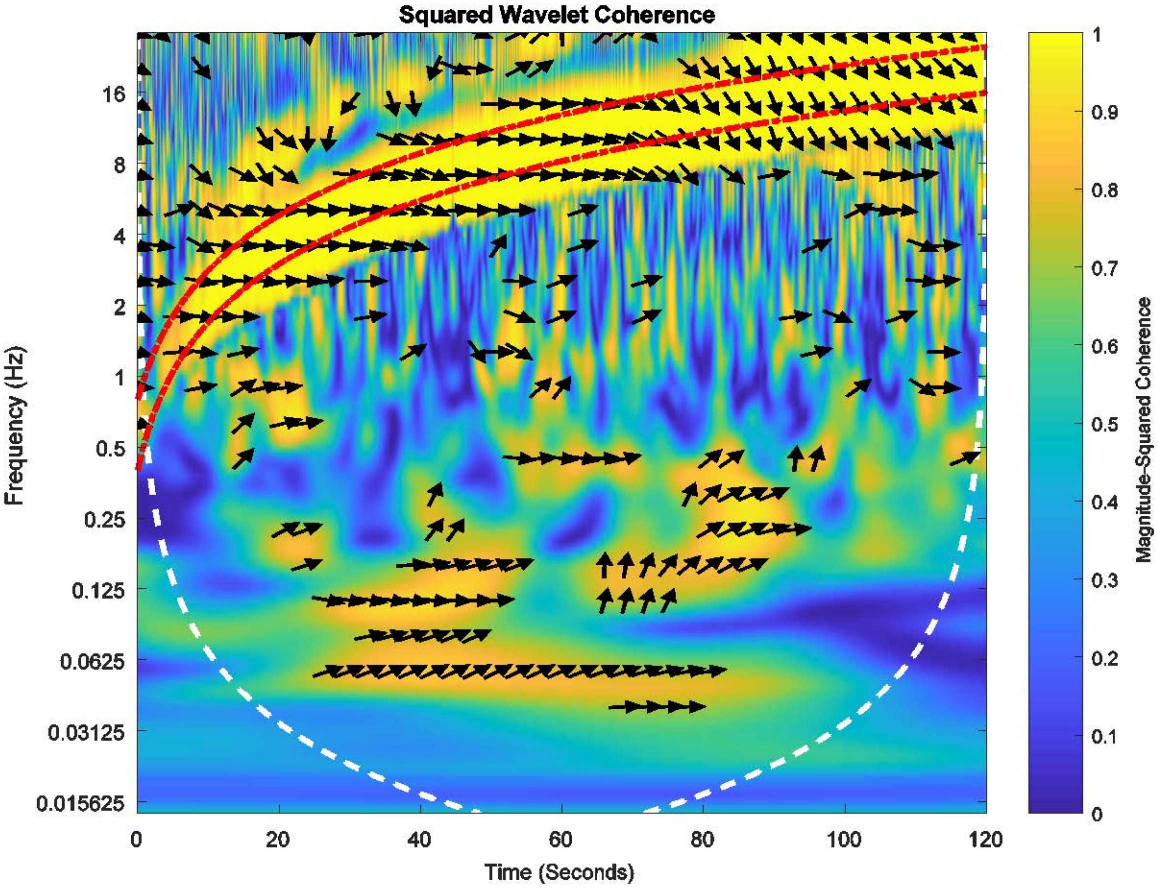

Figure (D.1) Squared wavelet coherence between the acceleration of the legs and feet relative to base motion for Subject 7; the white dashed curve indicates the COI, the red dashed curves indicate the high-value band of the base motion, and the direction of the arrows indicates the phase lag between legs and feet

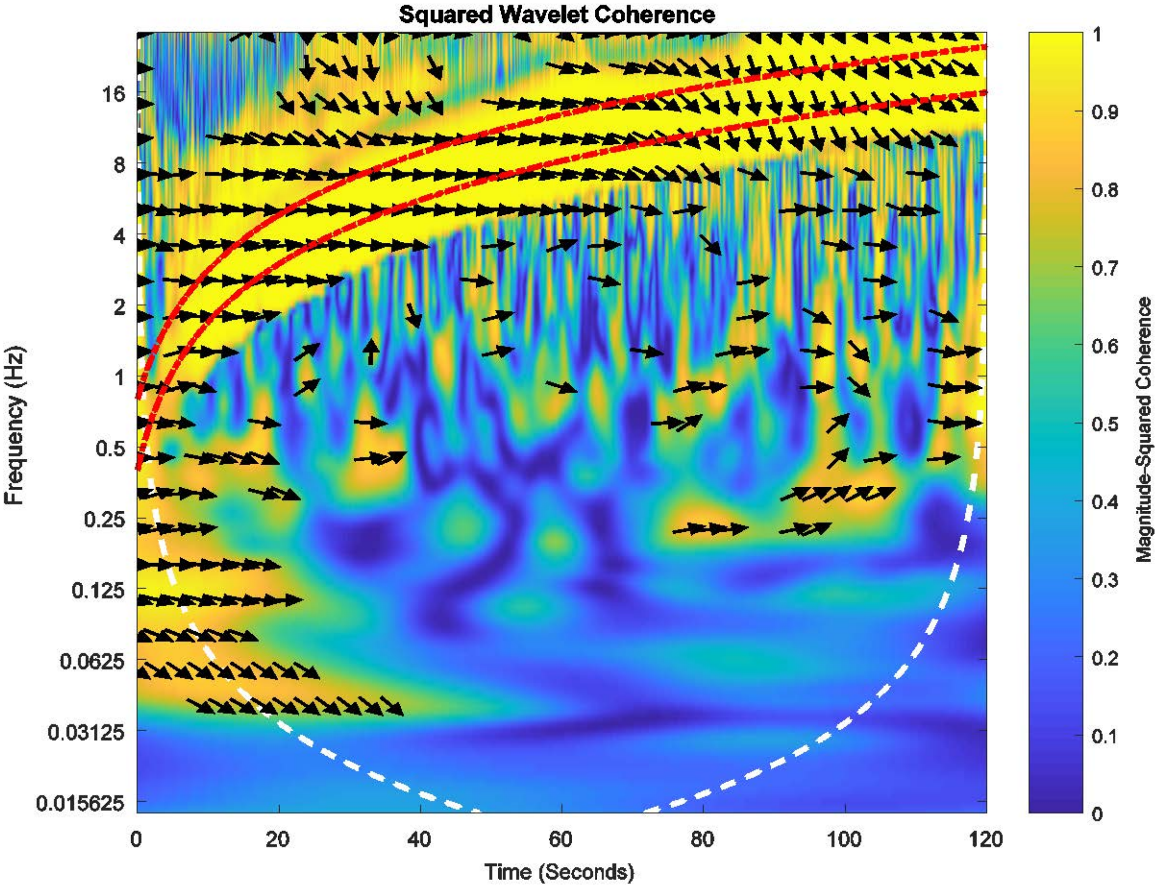

Figure (D.2) Squared wavelet coherence between the acceleration of the legs and feet relative to base motion for Subject 9; the white dashed curve indicates the COI, the red dashed curves indicate the high-value band of the base motion, and the direction of the arrows indicates the phase lag between legs and feet

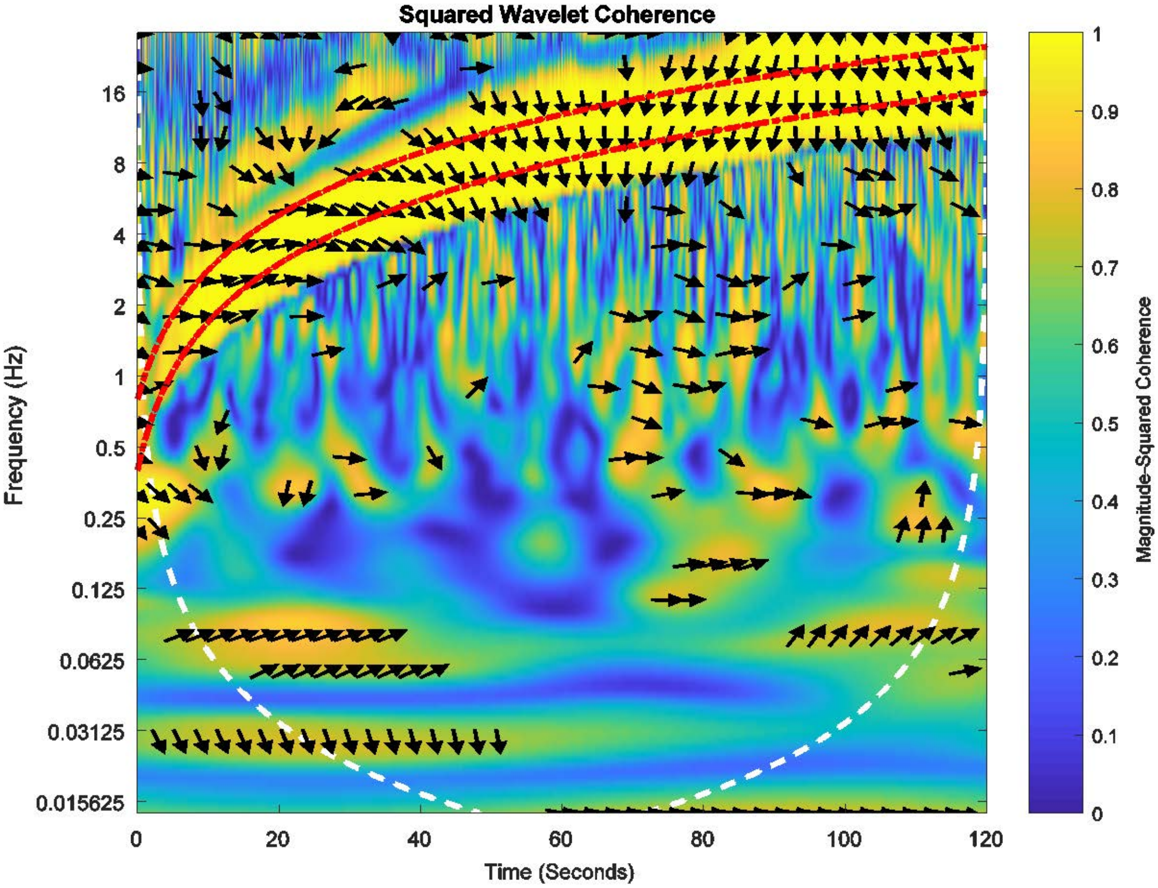

Figure (D.3) Squared wavelet coherence between the acceleration of the legs and feet relative to base motion for Subject 10; the white dashed curve indicates the COI, the red dashed curves indicate the high-value band of the base motion, and the direction of the arrows indicates the phase lag between legs and feet

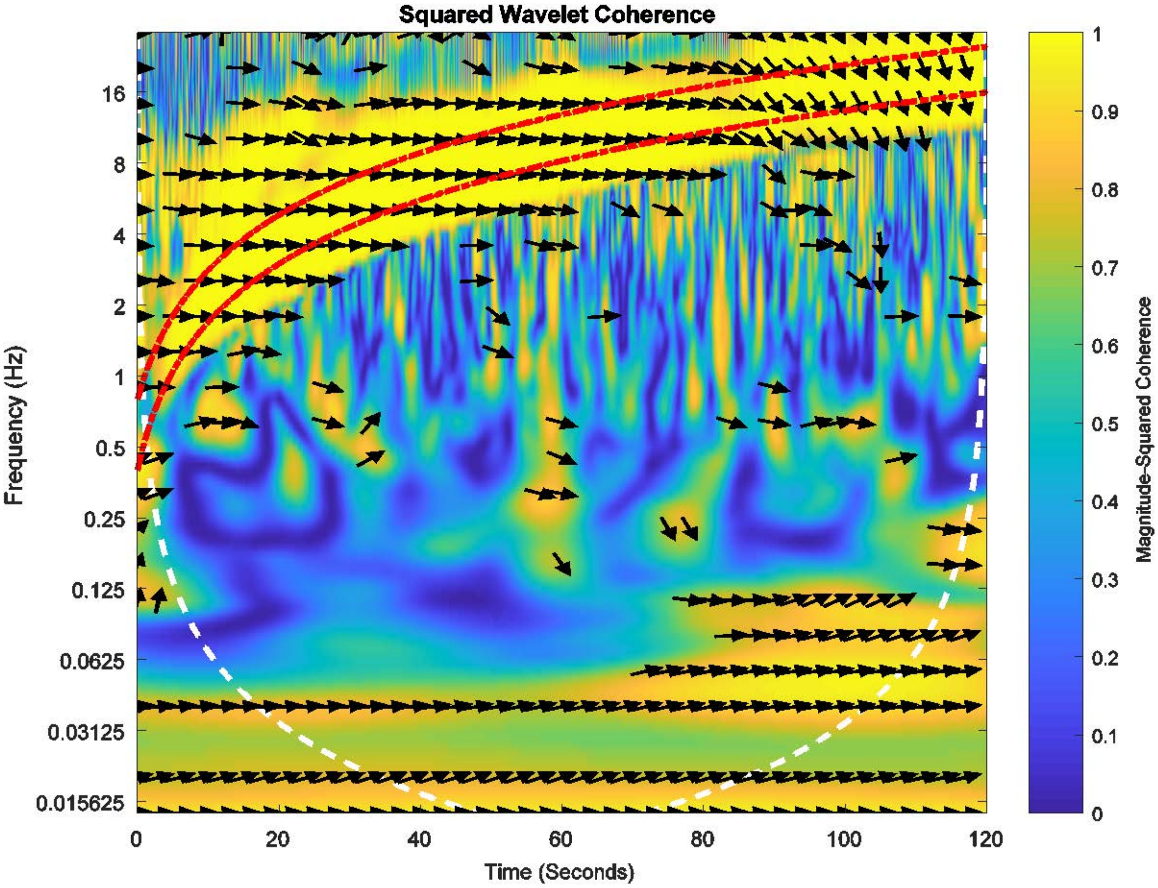

Figure (D.4) Squared wavelet coherence between the acceleration of the legs and feet relative to base motion for Subject 11; the white dashed curve indicates the COI, the red dashed curves indicate the high-value band of the base motion, and the direction of the arrows indicates the phase lag between legs and feet

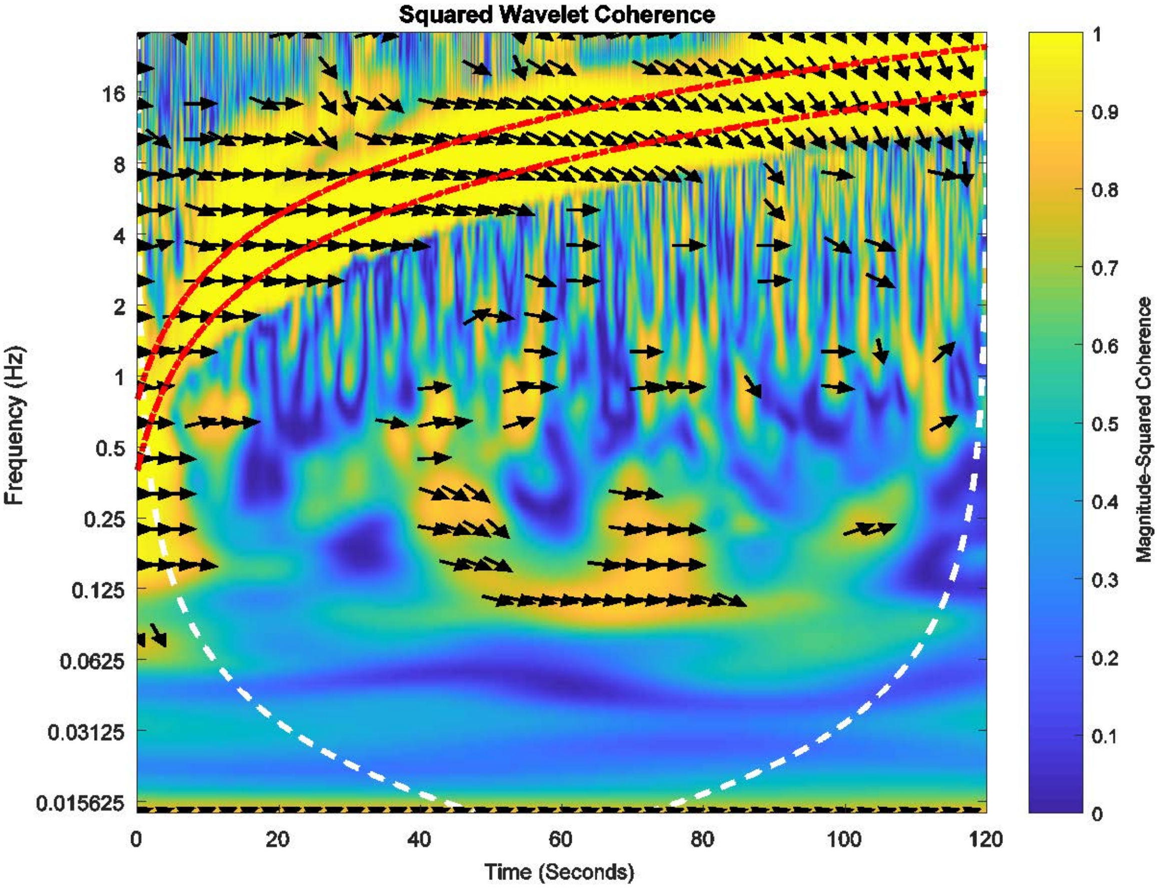

Figure (D.5) Squared wavelet coherence between the acceleration of the legs and feet relative to base motion for Subject 12; the white dashed curve indicates the COI, the red dashed curves indicate the high-value band of the base motion, and the direction of the arrows indicates the phase lag between legs and feet

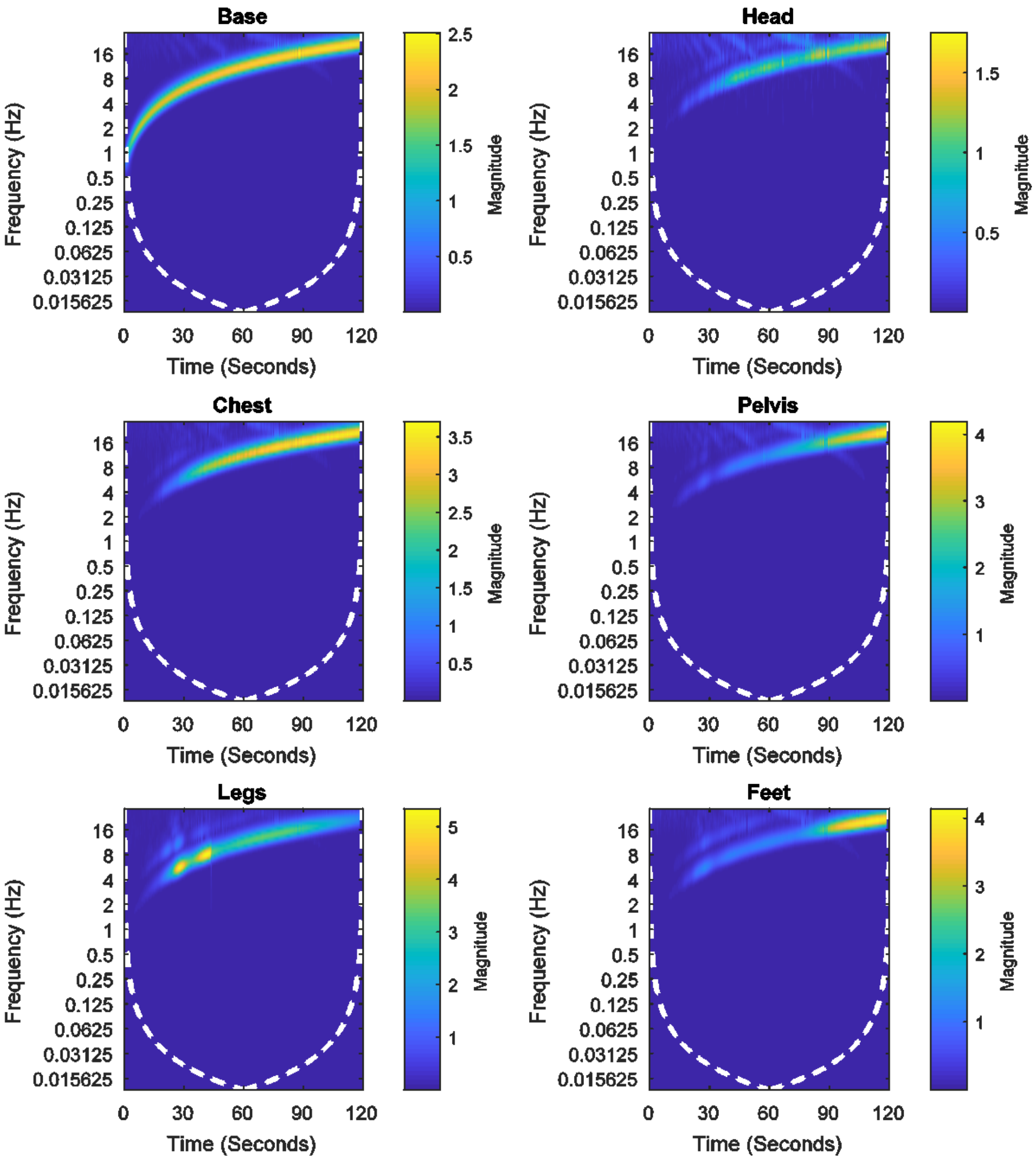

Figure (D.6) Magnitude scalogram with Morlet wavelet of the base motion acceleration and the head, chest, pelvis, legs, and feet acceleration relative to the base motion for Subject 7; the white dashed curve indicates the COI

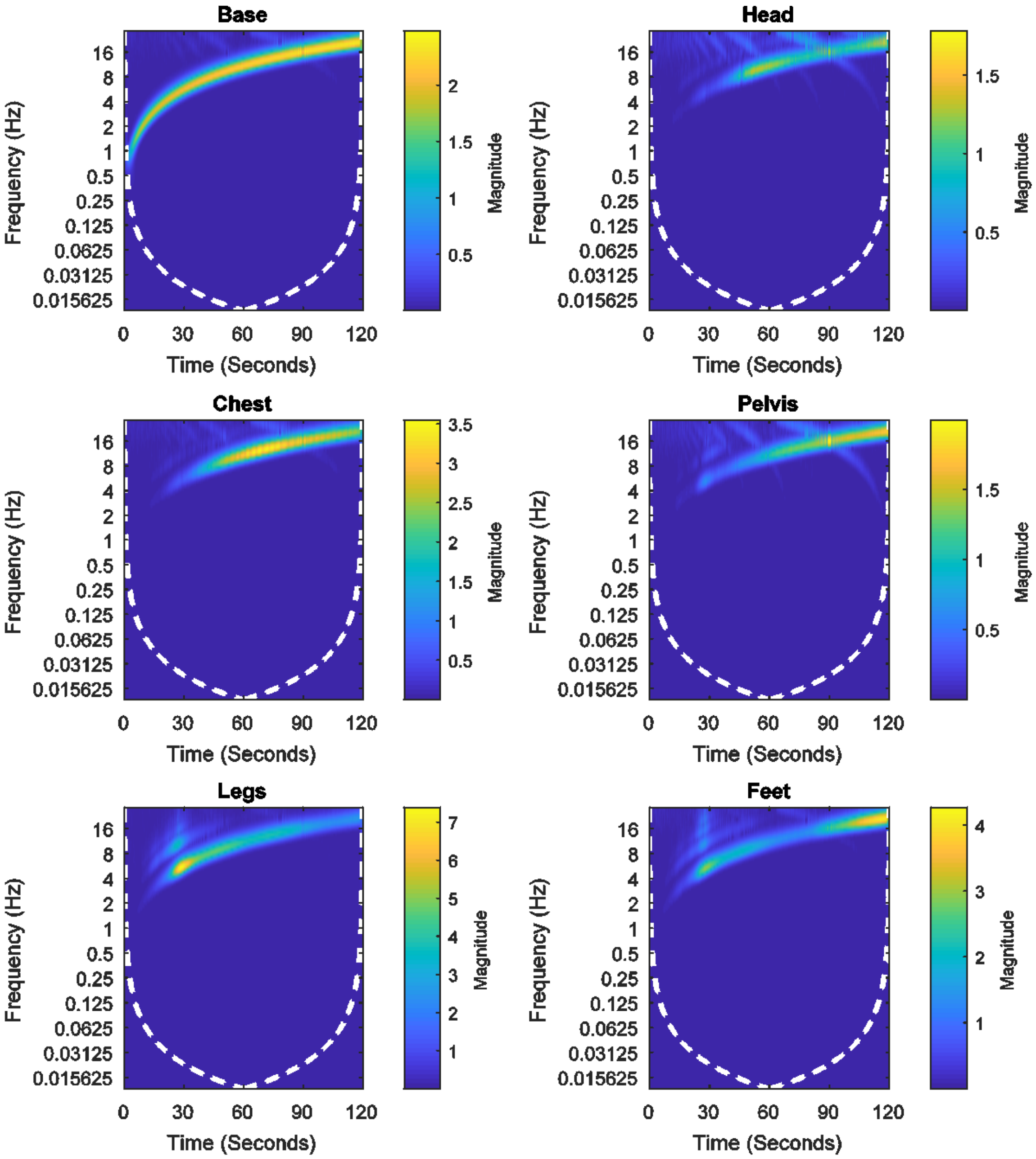

Figure (D.7) Magnitude scalogram with Morlet wavelet of the base motion acceleration and the head, chest, pelvis, legs, and feet acceleration relative to the base motion for Subject 9; the white dashed curve indicates the COI

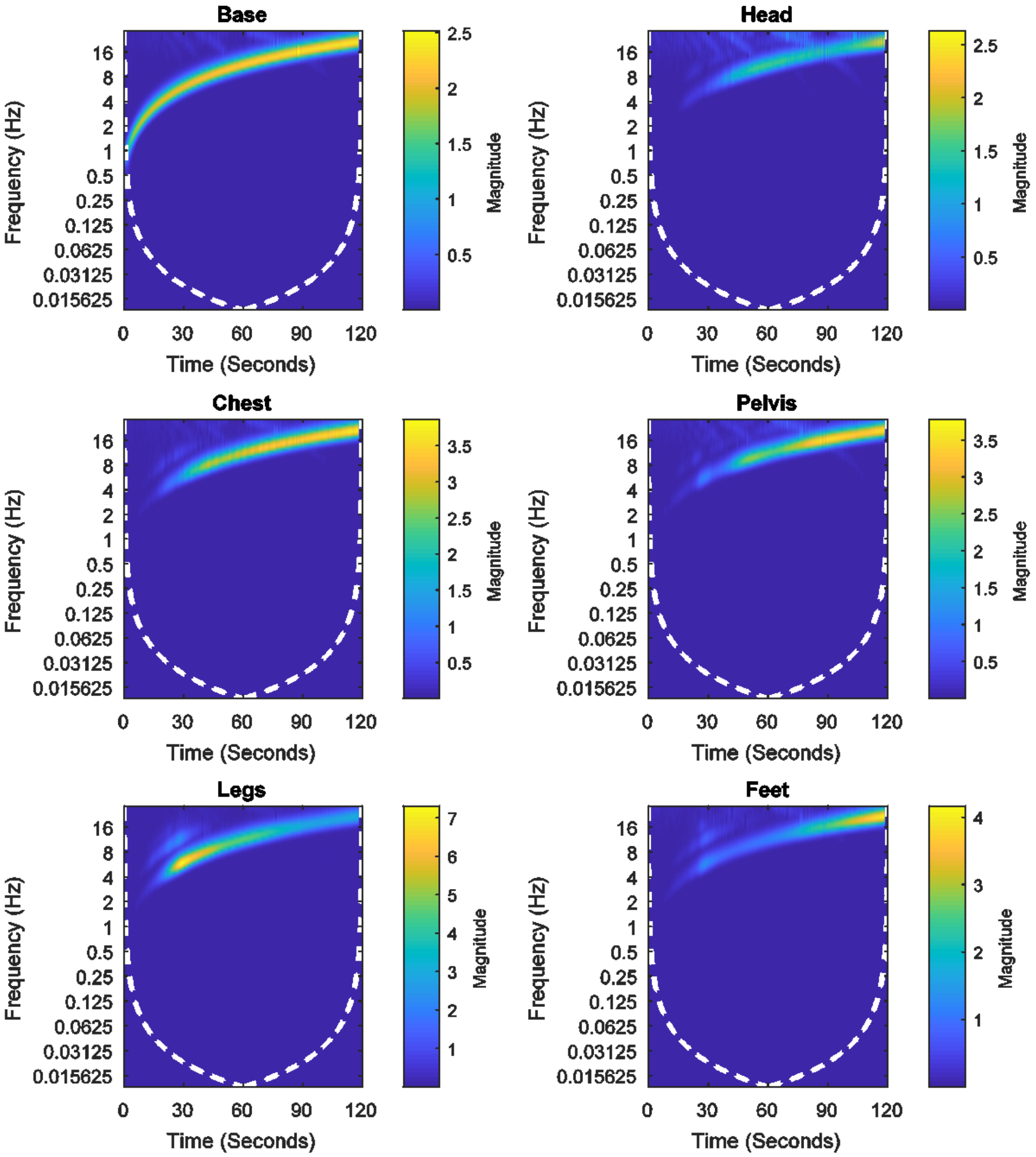

Figure (D.8) Magnitude scalogram with Morlet wavelet of the base motion acceleration and the head, chest, pelvis, legs, and feet acceleration relative to the base motion for Subject 10; the white dashed curve indicates the COI

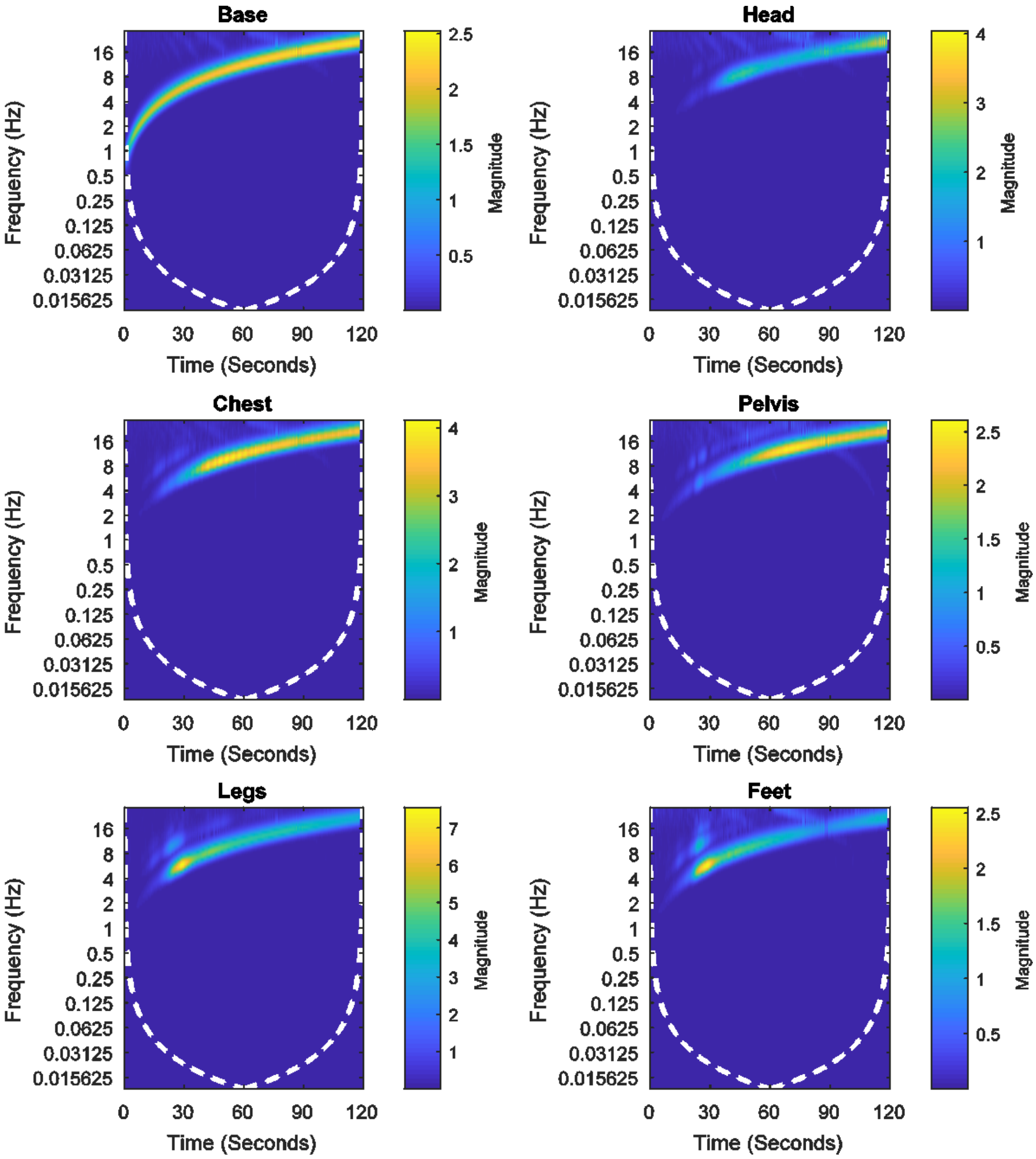

Figure (D.9) Magnitude scalogram with Morlet wavelet of the base motion acceleration and the head, chest, pelvis, legs, and feet acceleration relative to the base motion for Subject 11; the white dashed curve indicates the COI

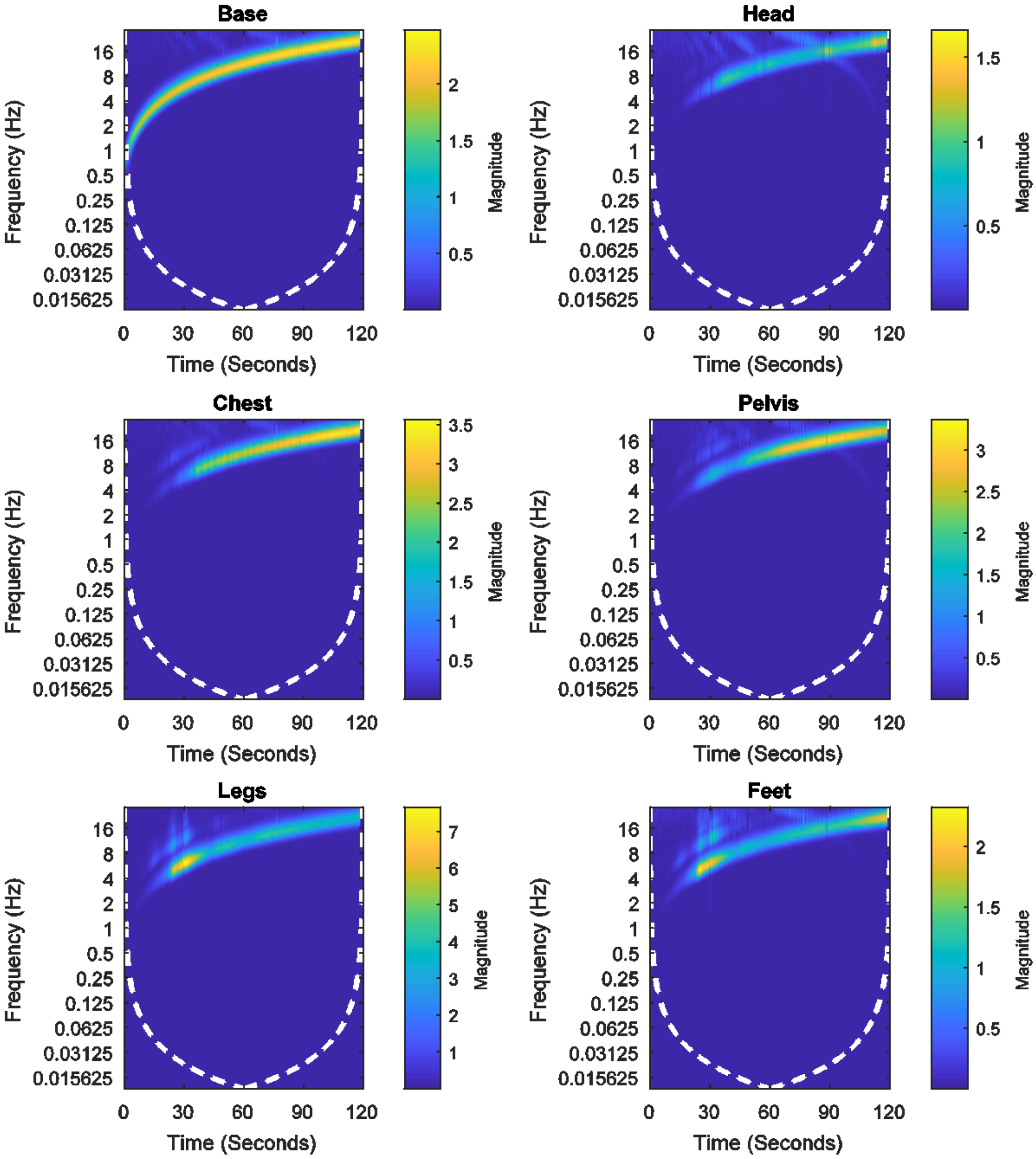

Figure (D.10) Magnitude scalogram with Morlet wavelet of the base motion acceleration and the head, chest, pelvis, legs, and feet acceleration relative to the base motion for Subject 12; the white dashed curve indicates the COI

APPENDIX E: INFORMED CONSENT DOCUMENT

The following pages reflect an unsigned informed consent document:

FOR IRB USE ONLY
APPROVED BY: IRB-02
IRB ID #: 200811705
APPROVAL DATE: 08/06/11
EXPIRATION DATE: 08/05/12

INFORMED CONSENT DOCUMENT

Project Title: **Comfort Weighting Curve for Seated Machine Operators**

Principal Investigator: **Salam Rahmatalla**

Research Team Contact: **Salam Rahmatalla, 1 319 335-5614**

John Meusch
Jonathan DeShaw

This consent form describes the research study to help you decide if you want to participate. This form provides important information about what you will be asked to do during the study, about the risks and benefits of the study, and about your rights as a research subject.

- If you have any questions about or do not understand something in this form, you should ask the research team for more information.
- You should discuss your participation with anyone you choose such as family or friends.
- Do not agree to participate in this study unless the research team has answered your questions and you decide that you want to be part of this study.

WHAT IS THE PURPOSE OF THIS STUDY?

This is a research study. We are inviting you to participate in this research study because you are a healthy, adult who does not have a history of muscle or bone disease or injury.

The purpose of this research study is to determine a proper shape of the comfort weighting curve for seated machine operators. This comfort curve will serve seat manufacturer in understanding the impact of machine changes on human comfort in single and multiple directions and therefore, help them in designing better and safer seats.
The study may also investigate the motion of people in supine position during emergency transportation with the goal of achieving better litter designs.

HOW MANY PEOPLE WILL PARTICIPATE?

Approximately 100 people will take part in this study at the University of Iowa.

HOW LONG WILL I BE IN THIS STUDY?

If you agree to take part in this study, your involvement will last for 3-6 hours in a single visit with no follow-up. If there are technical problems, you may be scheduled for second visit to complete the study procedures.

WHAT WILL HAPPEN DURING THIS STUDY?

If you agree to participate, you will be scheduled to return to the Engineering Research Facility, 330 South Madison Street, Iowa City, Iowa the morning of the test day. Inside the facility, you will change in to shorts and a tank-top so that the motion measurements can be obtained. The clothing will be supplied to you at the test site.

Preparation and Set-Up

Marker placement and calibration: Your body motion will be monitored using infrared cameras (VICON). Up to 90 reflective markers will be attached to your body. Each marker is about a half inch sphere attached to a soft rubber base of about 1 ½ inch x 1 ½ inch. The rubber base will be attached to your body using non-allergenic, double-sided tape. The markers on your head will be attached to an adjustable head band which you will wear on your head. Markers will be attached to your skin over bony landmarks, such as the elbow, the knee, the collar bone, or back bone. If you have considerable body hair, we will shave the small area of skin under each marker to minimize pain with removal of the markers. Markers may also be attached using athletic pre-wrap instead of adhesive tape. In some parts of the experiment, you may be dressed in a motion capture suit (a black cloth suit to which markers will be attached); in this case, the markers will be directly stuck to the suit instead of your skin.

Inertial sensors: Inertial sensors are devices that can measure acceleration in three and six directions. Inertial sensors are small devices that can sense movement. Inertial sensors will also be attached to your body at the same time the above markers are attached. Inertial sensors will be placed on you on up to 8 locations. The Inertial sensors will be attached to your skin using medical-grade, double-sided adhesive tapes, after cleaning your skin with rubbing alcohol.

The placement of the markers and inertial sensors will take about one to two hours.

In addition to the recordings for motion tracking, we will videotape the study procedure.

Testing

After this preparation stage, you will be instructed to sit on a chair or lay on a litter similar to those used in patient's transportation that is attached to a table that vibrates, called a shaker table. During the experiments, you will experience the physical conditions of a heavy construction machinery operator who is performing tasks in the real world or a person on a litter in an emergency transport vehicle.

Motion Capture Calibration: The first step in the motion capture process is to calibrate the system and ensure that the cameras see only the reflected markers (no artifact). The second step involves calibrating you by having you stand still for 30 seconds. The motion capture system will use this information to obtain your measurements, such as the length of your legs and arms.

Task Simulation: In order for you to keep your attention focused, we may provide a task for you to work on. The task consists of a video-game like simulation of the operation of a piece of heavy equipment. You will control the piece of equipment using the arm-rest controls you will be holding during the testing.

FOR IRB USE ONLY
APPROVED BY: IRB-02
IRB ID #: 200811705
APPROVAL DATE: 08/06/11
EXPIRATION DATE: 08/05/12

Experimental Protocol:
You will be tested under one of the following conditions:

Condition A) You will be asked to sit in the shaker table chair. The experiments to be conducted will include using a shaker table to provide vibration typical of operation of common heavy equipment.

You may be tested under the following scenarios:

1. Back on seatback and hands on armrests
2. Back on seatback and hands on lap
3. Back on seatback and hands on steering wheel
4. Back off seatback and hands on lap, and looking back (twisted posture)
5. Back off seatback and hands on armrests, and looking back (twisted posture)
6. Back off seatback and hands on lap
7. Back off seatback and hands on steering wheel
8. Back off seatback and hands on armrests
9. In some of the above cases, you may be asked to sit on a seat with your trunk constrain to the seatback using a life-Vest jacket; however, your arms will be freely to move. The reason for these cases is to isolate your head-neck motion from your trunk motion. By doing this, we will be able to more accurately analyzing the contribution of your head-motion to your discomfort level.

In all above cases, your feet will remain on the ground/pedals.

Condition B) You will be asked to take a supine position on a litter with a backboard similar to those in patient's transportation.
The following procedure will be used as recommended by the Local EMS provider (Johnson County):

1. Apply an appropriate, effective and properly fitted/sized cervical collar.
2. Position participant on the long spine board and center.
3. Place straps in an x-pattern over the shoulders and under the armpits to secure the upper chest.
4. Additional straps are placed across the iliac crest and above the knees to prevent movement.
5. Normal Anatomical Alignment of the spine should be maintained.
6. Immobilize the head in the normal anatomical position. 1-1.5 inches of non-compressive occipital padding may be used.
7. Towel rolls or other bulky, lightweight material may be placed around the head to stabilize.
8. Place a wide strip of adhesive tape across the forehead to form an "X" securing the head.
9. Secure the feet with tape to prevent leg motion.

The following cases will be considered:

i. Using traditional backboard.
ii. Using traditional backboard with cushions.

We will conduct a series of tests to collect information about your body's responses to the movement of the shaker table seat and to test whether or not we are tracking the markers attached to you. You will experience up to 200 bouts of typical ride vibration on the shaker table each lasting up to 60 seconds with total of up to 100 minutes. The test will be repeated for each of the above twoconditions.. The "rides" will consist of vibration in one or multiple directions. Normally, up to 100 minutes (for each of the two above mentioned conditions) of that time will consist of exposure to typical "ride" vibration. If up to half of the tests need to be repeated, you could be exposed to up to 150 minutes of "ride" vibration.

In the event a test is stopped before all the data are collected or data are lost due to computer failure, the test will be repeated, up to a maximum of half of the possible tests. It is unlikely that more than one or two tests will actually require repetition, but all estimates of total daily vibration and shock exposure have included these additional tests. In the event data recording systems fail to acquire data during a test, the test will be repeated. This may take an additional six hours during a separate visit.

As mentioned above, it is possible that some tests may need to be further repeated in the event results are not stored properly (data lost due to computer error, etc.). The duration of the testing procedures should require no longer than 6 hours (with breaks). The expected total duration of exposure to the vibration is 100 minutes, but could be as high as 150 minutes in the event half of the tests require repeating.

During the tests, you will be asked by the investigators to rate your discomfort level either using verbal forms or paper based forms.

You may be asked to complete more visits if additional testing is required.

Audio/Video Recording or Photographs

One aspect of this study involves taking some pictures and video movies during the testing procedures. The motion capture cameras can only "see" infrared light reflected from markers. In addition to the motion capture camera images, we will take photographs and video of you using traditional still and video cameras to know where the markers are located on your body. The pictures and video movies will help us in identifying the location of the markers on the body during the experiments; otherwise, it would be very difficult to recognize the real markers' locations on the body by just looking to the motion capture data. In the event these materials are used in reports or publications, the images will be altered so that no personally-identifiable information will appear.

These recordings and photographs will be used to document the test protocol. These recordings will not be erased or destroyed as they will provide valuable documentation of the study.

WHAT ARE THE RISKS OF THIS STUDY?

You may experience one or more of the risks indicated below from being in this study. In addition to these, there may be other unknown risks, or risks that we did not anticipate, associated with being in this study.

You may feel some irritation from the preparation for, the use of, and the removal of the reflective markers, and accelerometers. We will try to minimize this risk by using only medical-grade tape meant for use on human skin and shaving any areas that have substantial hair. We will try to make the time that the devices are attached as short as possible consistent with the data to be gathered. We will monitor you carefully by sight and by asking questions about how you feel. We will ask you if you are allergic to adhesive tape before placing the markers and accelerometers on your skin.

You may be at risk for developing dizziness. You will have a switch that will immediately stop the ride in the event you feel you need to stop. You can also take breaks as needed throughout the test protocol. We will monitor you carefully by sight and by asking questions about how you feel. If you are prone to motion sickness, have a history of vestibular (inner ear) problems, or do not tolerate simulation rides at Amusement Parks, you should not enroll in this study.

The vibration involved in this study may pose a risk for muscle or back pain with extended exposures. However, one day of testing is unlikely to result in any chronic vibration or shock injuries. The front to back vibrations you will experience should be no worse than those felt while riding a tractor on a rough field or operating typical heavy construction equipment for a period of time. We have analyzed the vibration for the conditions you will experience using international standards to be sure that the total exposure is within acceptable levels. If you have a history of neck or back pain, you should tell the researchers before enrolling in the study.

There is a risk that you could faint during the test. Sitting for extended periods of time, coupled with the simulated ride, could result in feeling like you could faint. Before fainting, people have reported experiencing weakness, lightheadedness, nausea, sweating, hyperventilation, blurred vision and/or impaired hearing. Sitting or lying down can reverse the symptoms. To minimize the risk of fainting, regular rest intervals are planned, where you will be asked to get up out of the seat and stand and move your arms and legs. Further you will be monitored closely for any signs of intolerance listed above, by sight and by asking questions about how you feel throughout the test. If you have any history of fainting or have a cardiac condition you should not enroll in this study.

If you have a history of neck or back pain, heart problems, neurological problems, balance problems or dizziness, motion sickness, or are taking over-the-counter drugs, prescribed drugs, or have consumed alcohol or recreational drugs within 24 hours of the study, you should not enroll in this study.

There is a risk that you may experience a fear of falling or being unable to maintain your balance in the seat. We will minimize this situation by monitoring you carefully by sight and by asking questions about how you feel. If you have any history of fear, then you should not enroll in this study.

WHAT ARE THE BENEFITS OF THIS STUDY?

You will not benefit from being in this study. However, we hope that, in the future, other people might benefit from this study because the result of this study may help seat and machine designers to develop more comfortable seats for heavy machinery operators.

WILL IT COST ME ANYTHING TO BE IN THIS STUDY?

You will not have any cost for being in this research study.

WILL I BE PAID FOR PARTICIPATING?

You will be paid for being in this research study. You will need to provide your social security number (SSN) in order for us to pay you. You may choose to participate without being paid if you do not wish to provide your social security number (SSN) for this purpose. You may also need to provide your address if a check will be mailed to you. If your social security number is obtained for payment purposes only, it will not be retained for research purposes.
You will be paid at a rate of $12 per hour of a total of up to $72. The average amount per visit is $48.

DO THE RESEARCHERS HAVE PERSONAL FINANCIAL INTEREST IN THIS STUDY?

No.

WHO IS FUNDING THIS STUDY?

Departmental Funding from the University of Iowa, Center for computer aided design.

WHAT IF I AM INJURED AS A RESULT OF THIS STUDY?

- If you are injured or become ill from taking part in this study, medical treatment is available at the University of Iowa Hospitals and Clinics.
- No compensation for treatment of research-related illness or injury is available from the University of Iowa unless it is proven to be the direct result of negligence by a University employee.
- If you experience a research-related illness or injury, you and/or your medical or hospital insurance carrier will be responsible for the cost of treatment.

WHAT ABOUT CONFIDENTIALITY?

We will keep your participation in this research study confidential to the extent permitted by law. However, it is possible that other people such as those indicated below may become aware of your participation in this study and may inspect and copy records pertaining to this research. Some of these records could contain information that personally identifies you.

- federal government regulatory agencies,
- auditing departments of the University of Iowa, and
- the University of Iowa Institutional Review Board (a committee that reviews and approves research studies)

To help protect your confidentiality, we will assign you an identification number that does not include any personally identifiable information. All data will be stored on password-protected computer files using this number and not your name. Your name and personal information will be linked to your study identification number in a separate document and kept by the principal investigator in electronic and hard-copy formats separately from the rest of the data. All data will be kept in a locked lab or office or in password protected computer files, with appropriate backup. The motion data will be available to other researchers for future model development; however no personal identification of any kind will be linked to the data sets.

If we write a report or article about this study or share the study data set with others, we will do so in such a way that you cannot be directly identified.

IS BEING IN THIS STUDY VOLUNTARY?

Taking part in this research study is completely voluntary. You may choose not to take part at all. If you decide to be in this study, you may stop participating at any time. If you decide not to be in this study, or if you stop participating at any time, you won't be penalized or lose any benefits for which you otherwise qualify.

Will I Receive New Information About the Study while Participating?

If we obtain any new information during this study that might affect your willingness to continue participating in the study, we'll promptly provide you with that information.

Can Someone Else End my Participation in this Study?

Under certain circumstances, the researchers might decide to end your participation in this research study earlier than planned. This might happen because in our judgment it would not be safe for you to continue or because the funding for the research study has ended.

WHAT IF I HAVE QUESTIONS?

We encourage you to ask questions. If you have any questions about the research study itself, please contact: Salam Rahmatalla at (319) 335-5614 or salam-rahmatalla@uiowa.edu If you experience a research-related injury, please contact Salam Rahmatalla at (319) 335-5614 or salam-rahmatalla@uiowa.edu

If you have questions, concerns, or complaints about your rights as a research subject or about research related injury, please contact the Human Subjects Office, 105 Hardin Library for the Health Sciences, 600 Newton Road, University of Iowa, Iowa City, IA 52242-1098, (319) 335-6564, or e-mail irb@uiowa.edu. General information about being a research subject can be found by clicking "Info for Public" on the Human Subjects Office web site, http://research.uiowa.edu/hso. To offer input about your experiences as a research subject or to speak to someone other than the research staff, call the Human Subjects Office at the number above.

This Informed Consent Document is not a contract. It is a written explanation of what will happen during the study if you decide to participate. You are not waiving any legal rights by signing this Informed Consent Document. Your signature indicates that this research study has been explained to you, that your questions have been answered, and that you agree to take part in this study. You will receive a copy of this form.

FOR IRB USE ONLY
APPROVED BY: IRB-02
IRB ID #: 200811705
APPROVAL DATE: 08/06/11
EXPIRATION DATE: 08/05/12

Subject's Name (printed): ____

Do not sign this form if today's date is on or after **EXPIRATION DATE: 08/05/12** .

_______________________________________ (Signature of Subject)

_______________________________ (Date)

Statement of Person Who Obtained Consent

I have discussed the above points with the subject or, where appropriate, with the subject's legally authorized representative. It is my opinion that the subject understands the risks, benefits, and procedures involved with participation in this research study.

_______________________________________ (Signature of Person who Obtained Consent)

_______________________________ (Date)

REFERENCES

1. Schwarz, B.J. and M.H. Richardson, *Experimental modal analysis.* CSI Reliability week, 1999. **35**(1): p. 1-12.
2. Sestieri, A. and S. Ibrahm, *Analysis of errors and approximations in the use of modal co-ordinates.* Journal of sound and vibration, 1994. **177**(2): p. 145-157.
3. Caughey, T.K., *Classical Normal Modes in Damped Linear Dynamic Systems.* Journal of Applied Mechanics, 1960. **27**(2): p. 269-271.
4. Caughey, T.K. and M.E.J. O'Kelly, *Classical Normal Modes in Damped Linear Dynamic Systems.* Journal of Applied Mechanics, 1965. **32**(3): p. 583-588.
5. Lancaster, P., *Expressions for Damping Matrices in Linear Vibration Problems.* Journal of the Aerospace Sciences, 1961. **28**(3): p. 256-256.
6. Pilkey, D.F. and D.J. Inman. *An iterative approach to viscous damping matrix identification*. in *Proceedings of SPIE, the International Society for Optical Engineering*. 1997. Society of Photo-Optical Instrumentation Engineers.
7. Datta, B.N., et al., *Partial eigenstructure assignment for the quadratic pencil.* Journal of Sound and Vibration, 2000. **230**(1): p. 101-110.
8. Chu, M.T., Y.-C. Kuo, and W.-W. Lin, *On inverse quadratic eigenvalue problems with partially prescribed eigenstructure.* SIAM Journal on Matrix Analysis and Applications, 2004. **25**(4): p. 995-1020.
9. Lancaster, P. and U. Prells, *Inverse problems for damped vibrating systems.* Journal of Sound and Vibration, 2005. **283**(3–5): p. 891-914.
10. Dong, B., M.M. Lin, and M.T. Chu, *Parameter reconstruction of vibration systems from partial eigeninformation.* Journal of Sound and Vibration, 2009. **327**(3–5): p. 391-401.
11. Chu, M. and S.-F. Xu, *Spectral decomposition of real symmetric quadratic λ-matrices and its applications.* Mathematics of Computation, 2009. **78**(265): p. 293-313.
12. Pilkey, D.F. and D.J. Inman. *A survey of damping matrix identification*. in *Proceedings-spie the international society for optical engineering*. 1998. Spie International Society For Optical.
13. Adhikari, S., *Lancaster's Method of Damping Identification Revisited.* Journal of Vibration and Acoustics, 2002. **124**(4): p. 617-627.
14. Imregun, M. and D. Ewins. *Complex modes-origins and limits*. in *Proceedings of the 13th International Modal Analysis Conference*. 1995.
15. Garvey, S.D., J.E.T. Penny, and M.I. Friswell, *The relationship between the real and imaginary parts of complex modes.* Journal of Sound and Vibration, 1998. **212**(1): p. 75-83.
16. Balmés, E., *New results on the identification of normal modes from experimental complex modes.* Mechanical Systems and Signal Processing, 1997. **11**(2): p. 229-243.
17. Chu, M. and G. Golub, *Inverse Eigenvalue Problems: Theory, Algorithms, and Applications.* 2005: OUP Oxford.
18. Chu, M.T., N. Del Buono, and B. Yu, *Structured quadratic inverse eigenvalue problem, I. Serially linked systems.* SIAM Journal on Scientific Computing, 2007. **29**(6): p. 2668-2685.
19. Todd, M.J., *Semidefinite optimization.* Acta Numerica 2001, 2001. **10**: p. 515-560.
20. Lofberg, J. *YALMIP: A toolbox for modeling and optimization in MATLAB.* in *Computer Aided Control Systems Design, 2004 IEEE International Symposium on*. 2004. IEEE.

21. Toh, K.-C., M.J. Todd, and R.H. Tutuncu, *On the implementation and usage of SDPT3-a MATLAB software package for semidefinite-quadratic-linear programming, version 4.0*. 2010.

22. Chu, M.T., et al., *Spillover phenomenon in quadratic model updating.* AIAA journal, 2008. **46**(2): p. 420-428.

23. Lin, M.M., B. Dong, and M.T. Chu, *Semi-definite programming techniques for structured quadratic inverse eigenvalue problems.* Numerical Algorithms, 2010. **53**(4): p. 419-437.

24. Ibrahim, S. and A. Sestieri. *Existence and normalization of complex modes in post experimental use in modal analysis*. in *Proceedings of the 13th International Modal Analysis Conference*. 1995.

25. Byrd, R.H., M.E. Hribar, and J. Nocedal, *An interior point algorithm for large-scale nonlinear programming.* SIAM Journal on Optimization, 1999. **9**(4): p. 877-900.

26. Willinger, R., et al., *Modal analysis of the human neck in vivo as a criterion for crash test dummy evaluation.* Journal of Sound and Vibration, 2005. **287**(3): p. 405-431.

27. Jaishi, B., et al., *Dynamic and seismic performance of old multi-tiered temples in Nepal.* Engineering Structures, 2003. **25**(14): p. 1827-1839.

28. Kitazaki, S. and M.J. Griffin, *Resonance behaviour of the seated human body and effects of posture.* Journal of Biomechanics, 1997. **31**(2): p. 143-149.

29. Kitazaki, S. and M.J. Griffin, *A modal analysis of whole-body vertical vibration, using a finite element model of the human body*. Journal of Sound and Vibration, 1997. **200**(1): p. 83-103.

30. Matsumoto, Y. and M.J. Griffin, *Movement of the upper-body of seated subjects exposed to vertical whole-body vibration at the principal resonance frequency*. Journal of Sound and Vibration, 1998. **215**(4): p. 743-762.

31. Matsumoto, Y. and M.J. Griffin, *Modelling the dynamic mechanisms associated with the principal resonance of the seated human body.* Clinical Biomechanics, 2001. **16, Supplement 1**: p. S31-S44.

32. Muksian, R. and C.D. Nash, *On frequency-dependent damping coefficients in lumped-parameter models of human beings.* Journal of Biomechanics, 1976. **9**(5): p. 339-342.

33. Subashi, G.H.M.J., Y. Matsumoto, and M.J. Griffin, *Modelling resonances of the standing body exposed to vertical whole-body vibration: Effects of posture*. Journal of Sound and Vibration, 2008. **317**(1–2): p. 400-418.

34. H. E. Krause and K.O. Lange, *Nonlinear behavior of biomechanical systems.* ASME, 1967.

35. Vogt, L., H. Mertens, and H. Krause, *Model of the supine human body and its reactions to external forces.* Aviation, space, and environmental medicine, 1978. **49**(1 Pt. 2): p. 270-278.

36. Griffin, M.J., *Handbook of Human Vibration*. 1990: Academic Press.

37. Mansfield, N.J. and S. Maeda, *The apparent mass of the seated human exposed to single-axis and multi-axis whole-body vibration*. Journal of Biomechanics, 2007. **40**(11): p. 2543-2551.

38. Newland, D.E., *An introduction to random vibrations and spectral analysis*. 1984: Longman.

39. Rahmatalla, S. and J. DeShaw, *Effective seat-to-head transmissibility in whole-body vibration: Effects of posture and arm position.* Journal of Sound and Vibration, 2011. **330**(25): p. 6277-6286.

40. Wang, W., S. Rakheja, and P.É. Boileau, *Relationship between measured apparent mass and seat-to-head transmissibility responses of seated occupants exposed to vertical vibration*. Journal of Sound and Vibration, 2008. **314**(3–5): p. 907-922.

41. Boileau, P.É. and S. Rakheja, *Whole-body vertical biodynamic response characteristics of the seated vehicle driver: Measurement and model development.* International Journal of Industrial Ergonomics, 1998. **22**(6): p. 449-472.

42. Buck, B. and H. Woelfel, *Dynamic three-dimensional finite element model of a sitting man with a detailed representation of the lumbar spine and muscles.* Comput. Methods Biomech. Biomed. Eng, 1998. **2**: p. 379-386.

43. Wang, Y. and S. Rahmatalla, *Human head–neck models in whole-body vibration: Effect of posture.* Journal of Biomechanics, 2013. **46**(4): p. 702-710.

44. Eman, K.F. and K.J. Kim, *Modal Analysis of Machine Tool Structures Based on Experimental Data.* Journal of Engineering for Industry, 1983. **105**(4): p. 282-287.

45. Park, B.-H. and K.-J. Kim, *Vector ARMAX modeling approach in multi-input modal analysis.* Mechanical Systems and Signal Processing, 1989. **3**(4): p. 373-387.

46. Ljung, L., *System Identification: Theory for the User*. 1999: Prentice Hall PTR.

47. DeShaw, J. and S. Rahmatalla, *Comprehensive measurement in whole-body vibration.* Low Frequency Noise, Vibration and Active Control, 2012. **31**(2): p. 63-74.

48. Brincker, R. and C. Ventura, *Introduction to Operational Modal Analysis*. 2015: Wiley.

49. Fassois, S.D. and J.E. Lee, *On the problem of stochastic experimental modal analysis based on multiple-excitation multiple-response data, part II: The modal analysis approach.* Journal of Sound and Vibration, 1993. **161**(1): p. 57-87.

50. Moore, S.M., J.C.S. Lai, and K. Shankar, *ARMAX modal parameter identification in the presence of unmeasured excitation—I: Theoretical background.* Mechanical Systems and Signal Processing, 2007. **21**(4): p. 1601-1615.

51. Florakis, A., S.D. Fassois, and F.M. Hemez, *MIMO LMS-ARMAX identification of vibrating structures—part II: a critical assessment.* Mechanical Systems and Signal Processing, 2001. **15**(4): p. 737-758.

52. Devriendt, C. and P. Guillaume, *Identification of modal parameters from transmissibility measurements.* Journal of Sound and Vibration, 2008. **314**(1–2): p. 343-356.

53. Rützel, S., B. Hinz, and H.P. Wölfel, *Modal description—A better way of characterizing human vibration behavior.* Journal of Sound and Vibration, 2006. **298**(3): p. 810-823.

54. Tarabini, M., et al., *Analysis of non-linear response of the human body to vertical whole-body vibration.* Ergonomics, 2014. **57**(11): p. 1711-1723.

55. Panjabi, M.M., R.A. Brand, and A.A. White, *Three-dimensional flexibility and stiffness properties of the human thoracic spine.* Journal of Biomechanics, 1976. **9**(4): p. 185-192.

56. van Engelen, S.J.P.M., et al., *Validation of vibration testing for the assessment of the mechanical properties of human lumbar motion segments.* Journal of Biomechanics, 2012. **45**(10): p. 1753-1758.

57. van Engelen, S.J.P.M., et al., *The feasibility of modal testing for measurement of the dynamic characteristics of goat vertebral motion segments.* Journal of Biomechanics, 2011. **44**(8): p. 1478-1483.

58. Qiao, G. and S. Rahmatalla, *Eigenvectors phase correction in inverse modal problem.* Journal of Sound and Vibration, 2017. **410**(Supplement C): p. 151-168.

59. Winter, D.A., *Biomechanics and Motor Control of Human Movement*. 2009: Wiley.

60. Schoukens, J. and R. Pintelon. *Measurement of frequency response functions in noisy environments*. in *Instrumentation and Measurement Technology Conference, 1990. IMTC-90. Conference Record., 7th IEEE*. 1990. IEEE.

61. White, A.A. and M.M. Panjabi, *Clinical Biomechanics of the Spine*. 1990: Lippincott.

62. McGlashen, K., et al., *Load displacement behavior of the human Lumbo‐sacral joint.* Journal of orthopaedic research, 1987. **5**(4): p. 488-496.

63. Moroney, S.P., et al., *Load-displacement properties of lower cervical spine motion segments.* Journal of Biomechanics, 1988. **21**(9): p. 769-779.

64. Miller, J., A. Schultz, and G. Andersson, *Load‐displacement behavior of sacroiliac joints.* Journal of orthopaedic research, 1987. **5**(1): p. 92-101.

65. Markolf, K.L. *Stiffness and damping characteristics of the thoracic-lumbar spine*. in *Proceedings of Workshop on Bioengineering Approaches to the Problems of the Spine*. 1970.

66. DeShaw, J. and S. Rahmatalla, *Effect of lumbar support on human-head movement and discomfort in whole-body vibration.* Occupational Ergonomics, 2016. **13**(1): p. 3-14.

67. van Niekerk, J.L., W.J. Pielemeier, and J.A. Greenberg, *The use of seat effective amplitude transmissibility (SEAT) values to predict dynamic seat comfort.* Journal of Sound and Vibration, 2003. **260**(5): p. 867-888.

68. van der Westhuizen, A. and J.L. van Niekerk, *Verification of seat effective amplitude transmissibility (SEAT) value as a reliable metric to predict dynamic seat comfort.* Journal of Sound and Vibration, 2006. **295**(3): p. 1060-1075.

69. Huang, Y. and M.J. Griffin, *Nonlinearity in apparent mass and transmissibility of the supine human body during vertical whole-body vibration.* Journal of Sound and Vibration, 2009. **324**(1): p. 429-452.

70. Daubechies, I., *Ten lectures on wavelets*. 1992: SIAM.

71. Addison, P.S., *The illustrated wavelet transform handbook: introductory theory and applications in science, engineering, medicine and finance*. 2017: CRC press.

72. Kijewski, T. and A. Kareem, *Wavelet transforms for system identification in civil engineering.* Computer‐Aided Civil and Infrastructure Engineering, 2003. **18**(5): p. 339-355.

73. Kaiser, G., *A friendly guide to wavelets*. 2010: Springer Science & Business Media.

74. Grinsted, A., J.C. Moore, and S. Jevrejeva, *Application of the cross wavelet transform and wavelet coherence to geophysical time series.* Nonlinear processes in geophysics, 2004. **11**(5/6): p. 561-566.

75. Maraun, D., J. Kurths, and M. Holschneider, *Nonstationary Gaussian processes in wavelet domain: Synthesis, estimation, and significance testing.* Physical Review E, 2007. **75**(1): p. 016707.

76. Torrence, C. and P.J. Webster, *Interdecadal changes in the ENSO–monsoon system.* Journal of Climate, 1999. **12**(8): p. 2679-2690.

77. Torrence, C. and G.P. Compo, *A practical guide to wavelet analysis.* Bulletin of the American Meteorological society, 1998. **79**(1): p. 61-78.